Semiconductors, Vol. 38, No. 5, 2004, pp. 495–498. Translated from Fizika i Tekhnika Poluprovodnikov, Vol. 38, No. 5, 2004, pp. 513–515.

ATOMIC STRUCTURE AND NONELECTRONIC PROPERTIES OF SEMICONDUCTORS

Dependence of Dicarbon Annealing Temperature in *n*-Si on Oxygen Concentration in the Crystal

N. I. Boyarkina* and S. A. Smagulova**

**Institute of Semiconductor Physics, Siberian Division, Russian Academy of Sciences, pr. Akademika Lavrent'eva 13, Novosibirsk, 630090 Russia*

***Yakutsk State University, Yakutsk, 677891 Russia*

e-mail: smagulova@mail.ru

Submitted April 24, 2003; accepted for publication May 15, 2003

Abstract—The role of oxygen in the mechanism of dissociation of the dicarbon complex in *n*-Si into components is considered. It is assumed that released interstitial carbon atoms C_i migrate through the crystal and react with both substitutional carbon C_s and interstitial oxygen with the resulting formation of complexes C_iC_s and C_iO_i, respectively. The solution of a system of equations describing the formation of interstitial carbon atoms in the course of annealing of dicarbon show that the rate constant for the reaction of annealing of the C_iC_s complex (the *G* center) depends on the oxygen concentration. This dependence is treated as the dependence of the activation energy for annealing of a C_iC_s complex and, consequently, the dissociation energy of this complex on oxygen concentration. A more accurate value of dissociation energy for the *G* center was determined as 1.08 ± 0.03 eV. © *2004 MAIK "Nauka/Interperiodica".*

1. INTRODUCTION

Experiments with annealing of C_iC_s (dicarbon) complexes, or *G* centers, in *n*-Si (see, for example, [1, 2]) showed that the temperature of annealing of this center depends on the oxygen concentration in the crystal. The aforementioned *G* centers are annealed out at lower temperatures in silicon grown by the Czochralski method (Cz-Si) than in silicon grown by the floating-zone method (FZ-Si).

The dissociation energy for a C_iC_s complex ($E_{C_iC_s} = 1.10 \pm 0.05$ eV) reported by Boyarkina *et al.* [3] was determined from comparison of the calculated kinetics of annealing for this complex with experimental data [1, 4] on the isochronous heat treatment of irradiated *n*-Si. It was assumed in the calculations that the reaction of annealing of a C_iC_s complex proceeds via the scheme of decomposition of this center into its constituent components with the subsequent migration of the released interstitial carbon atom C_i through the crystal. The involvement of oxygen in this reaction was not taken into account.

The aim of this study is to calculate the annealing kinetics for a C_iC_s complex taking into account the effect of oxygen on the rate constant for the reaction of decomposition of the center under consideration.

2. INVOLVEMENT OF OXYGEN IN THE REACTION OF DECOMPOSITION OF A C_iC_s COMPLEX (THE *G* CENTER)

Interstitial carbon atoms released as a result of decomposition of *G* centers migrate and can be trapped by interstitial oxygen O_i with the resulting formation of C_iO_i centers [6] or be retrapped by carbon at the Si lattice sites (substitutional carbon C_s) with the resulting formation of C_iC_s complexes [5]. The trapping of C_i atoms by atoms of substitutional carbon C_s with the formation of new C_iC_s complexes leads to an increase in the characteristic time of decomposition of these complexes [2], which is equivalent to an increase in the activation energy for annealing out of these centers.

We write a system of equations that describe the variation in the concentrations of atoms of interstitial carbon C_i and the *G* centers in the course of heat treatment as

$$\begin{cases} \dfrac{dN_G}{dt} = -\nu_G N_G + k_{C_iC_s} N_{C_i} N_{C_s}, \\ \dfrac{dN_{C_i}}{dt} = \nu_G N_G - k_{C_iC_s} N_{C_i} N_{C_s} - k_{C_iO_i} N_{C_i} N_{O_i}, \end{cases} \quad (1)$$

where N_G, N_{C_i}, N_{C_s}, and N_{O_i} are the concentrations of *G* centers, interstitial carbon atoms C_i, substitutional carbon atoms C_s, and interstitial oxygen atoms O_i; ν_G is the rate constant for the reaction of decomposition of a *G* center; and $k_{C_iC_s}$ and $k_{C_iO_i}$ are the probabilities of trapping of interstitial carbon atoms by atoms of substitutional carbon and interstitial oxygen, respectively.

Experiments with isochronous annealing of interstitial carbon atoms and C_iC_s complexes in *n*-Si irradiated with ^{60}Co gamma-ray photons [1] showed that the con-

centration of interstitial carbon atoms became negligible ($\leq 10^{12}$ cm^{-3}) even at temperatures that were lower than the temperatures corresponding to annealing out of the C_iC_s complex (310 K for Cz-Si and 380 K for FZ-Si). Therefore, we assume that the concentration of interstitial carbon atoms remains unchanged in the course of annealing the *G* centers; i.e., we have

$$\frac{dN_{C_i}}{dt} = 0. \quad (2)$$

By solving the system of Eqs. (1), we obtain

$$N_{C_i} = \frac{v_G N_G}{k_{C_iC_s} N_{C_i}\left(1 + \frac{k_{C_iO_i} N_{O_i}}{k_{C_iC_s} N_{C_s}}\right)}, \quad (3)$$

$$\frac{dN_G}{dt} = -v_G N_G \frac{k_{C_iO_i} N_{O_i}/k_{C_iC_s} N_{C_s}}{1 + k_{C_iO_i} N_{O_i}/k_{C_iC_s} N_{C_s}}. \quad (4)$$

It was ascertained previously [5] that the probability that an interstitial carbon atom will be trapped by an oxygen atom exceeds the probability of its being trapped by substitutional carbon by approximately a factor of 3; i.e.,

$$\frac{k_{C_iO_i}}{k_{C_iC_s}} \approx 3. \quad (5)$$

As a result, we derive the following equation that describes the annealing out of the *G* centers:

$$\frac{dN_G}{dt} = -v_G N_G \frac{3N_{O_i}/N_{C_s}}{1 + 3N_{O_i}/N_{C_i}}. \quad (6)$$

It can be seen that the effective rate constant for the reaction of decomposition of the *G* center depends on the oxygen concentration; i.e.,

$$v_G^{\text{eff}} = v_G \frac{3N_{O_i}/N_{C_s}}{1 + 3N_{O_i}/N_{C_s}}. \quad (7)$$

3. DISCUSSION OF THE RESULTS OF CALCULATION

The concentration of substitutional carbon atoms $N_{C_s} = (1–5) \times 10^{16}$ cm^{-3} both in FZ- and Cz-Si. In Cz-Si, the concentration of interstitial oxygen $N_{O_i(Cz)} \leq 10^{18}$ cm^{-3}; i.e., the ratio $N_{O_i(Cz)}/N_{C_s} \gg 1$. The concentration of interstitial carbon atoms is defined as

$$N_{C_i(Cz)} = \frac{v_G N_G}{k_{C_iO_i} N_{O_i(Cz)}}. \quad (8)$$

For FZ-Si, the corresponding relations are written as

$$N_{O_i(FZ)} = (1–3) \times 10^{16} \text{ cm}^{-3}, \quad N_{O_i(FZ)}/N_{C_s} \approx 1,$$
$$N_{C_i(FZ)} = \frac{v_G N_G}{k_{C_iC_s} N_{C_s}}. \quad (9)$$

The ratio between the concentration of interstitial carbon atoms in FZ-Si and that in Cz-Si is given by

$$\frac{N_{C_i(Cz)}}{N_{C_i(FZ)}} = \frac{k_{C_iC_s} N_{C_s}}{k_{C_iO_i} N_{O_i(Cz)}} \ll 1. \quad (10)$$

In the Cz-Si crystals, the concentration of interstitial carbon atoms is low; as a result, almost all these atoms are involved in the formation of the C_iO_i complexes, taking into account that there is a sufficient amount of oxygen in the crystals. At the same time, the concentration of interstitial carbon in FZ-Si is much higher and is sufficient for the formation of both C_iO_i complexes and new *G* centers, which entails an increase in the decomposition time for these centers. As a result, the activation energy for annealing out of *G* centers E_{aG} is higher in FZ-Si than in Cz-Si.

The activation energy for annealing out of a *G* center (by decomposition into its components) E_{aG} is the sum of the *G*-center dissociation energy $E_{C_iC_s}$, the energy of rearrangement of the electronic subsystem of the crystal $W^{\text{el}}_{C_iC_s}$, and the migration energy for the released interstitial carbon atom W_{C_i} [3]:

$$E_{aG} = E_{C_iC_s} + W^{\text{el}}_{C_iC_s} + W_{C_i}. \quad (11)$$

A variation in the rate constant for the reaction of decomposition of the C_iC_s complex (the *G* center), which is described by formula (7), can be treated as a variation in the activation energy of this process by the quantity δE_{aG}; i.e.,

$$v_G^{\text{eff}} = v_G \exp\left(\frac{-\delta E_{aG}}{kT}\right). \quad (12)$$

Comparing (7) and (12), we obtain

$$\exp\left(\frac{-\delta E_{aG}}{kT}\right) = \frac{3N_{O_i}/N_{C_s}}{1 + 3N_{O_i}/N_{C_s}}; \quad (13)$$

therefore,

$$\delta E_{aG} = kT \ln \frac{1 + 3N_{O_i}/N_{C_s}}{3N_{O_i}/N_{C_s}} = kT \ln\left(1 + \frac{N_{C_s}}{3N_{O_i}}\right). \quad (14)$$

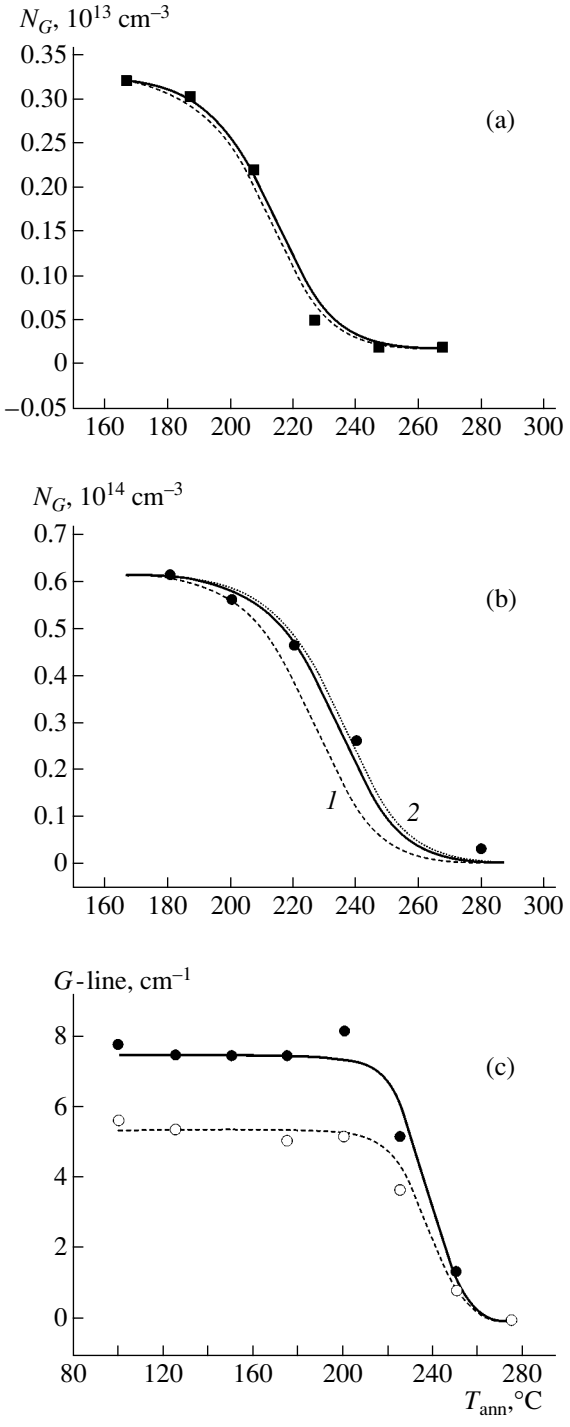

Fig. 1. Calculated dependences of dicarbon concentration on the temperature of isochronous annealing of *n*-Si [(a) corresponds to Cz-Si, (b, c) corresponds to FZ-Si] irradiated with (a, c) gamma-ray photons and (b) fast electrons. The values of the *G*-center dissociation energy E_{aG} used in calculations were equal to (a) 1.06 eV, (b) 1.11 eV for curve *1* and 1.15 eV for curve *2*, and (c) 1.08 eV. The concentration of interstitial oxygen N_{O_i} was taken as equal to (a) 9×10^{17}, (b) 10^{16}, and (c) 2×10^{16} cm^{-3}. Squares and circles represent experimental data taken from (a) [4, Fig. 1], (b) [4, Fig. 3a], and (c) [2, Fig. 8].

If $N_{O_i} \gg N_{C_s}$, as in Cz-Si, this addition is nearly equal to zero. However, for FZ-Si, where $N_{O_i} \approx 10^{16}$ cm^{-3} and $N_{C_i} \approx (1–5) \times 10^{16}$ cm^{-3}, we obtain $\delta E_{aG} \approx kT \ln 2.7 \approx 0.04$ eV for annealing temperature $T \approx 500$ K.

Therefore, in order to fit the results of calculations (with the effect of oxygen disregarded) to experimental data on the kinetics of annealing of C_iC_s complexes in FZ-Si, we had to use a larger value of dissociation energy for this center than that in Cz-Si [3]. The range of the values of dissociation energy $E_{C_iC_s}$ determined from comparison of the results of calculations with experimental data was equal to 1.05–1.15 eV. Evidently, the upper limit of this range corresponds to "oxygen-free" FZ-Si, where $N_{O_i} = (1–3) \times 10^{16}$ cm^{-3}. If the effect of oxygen on the annealing of C_iC_s complexes is taken into account, this upper limit should be decreased by $\delta E_{aG} = 0.04$ eV. As a result, we obtain the following range for dissociation energies for C_iC_s complexes: 1.05–1.11 eV. In other words, we define this energy as $E_{C_iC_s} = 1.08 \pm 0.03$ eV.

In Figs. 1a and 1b, we show the calculated dependences of the *G*-center concentration on the temperature of isochronous annealing (T_{ann}) of irradiated *n*-Si; these dependences were obtained by solving Eq. (4). The rate constant for the *G*-center dissociation reaction ν_G was calculated using expression (6) from [3] as

$$\nu_G = \nu_{0C_iC_s} \exp \frac{-E_{C_iC_s} - W^{el}_{C_iC_s} - W_{C_i}}{kT}. \qquad (15)$$

The values of the dissociation energy $E_{C_iC_s}$ were taken to be equal to 1.06 eV (Fig. 1a, solid curve), 1.11 eV (Fig. 1b, solid curve), and 1.08 eV (Fig. 1c, both curves). The data for Cz-Si are shown in Fig. 1a, and the data for FZ-Si are shown in Figs. 1b and 1c.

Calculated dependences of the *G*-center concentration on the temperature of isochronous annealing are obtained with the effect of oxygen on the annealing out of these centers disregarded and are represented by dashed lines with $E_{C_iC_s} = 1.06$ eV (Fig. 1a) and $E_{C_iC_s} = 1.11$ and 1.15 eV for the lower and upper curves in Fig. 1b, respectively.

The squares and circles correspond to experimental data obtained as a result of annealing *n*-Si irradiated with ^{60}Co gamma-ray photons [4, 2] (Figs. 1a, 1c) and with fast electrons [4] (Fig. 1b).

4. CONCLUSION

We explained the dependences of the annealing temperature for dicarbon (the *G* center) in *n*-Si on the oxygen concentration in the crystal taking into account the involvement of oxygen in the trapping of the interstitial

carbon atom released as a result of the decomposition of the aforementioned center. We obtained a more accurate value of dissociation energy for the *G* center (the C_iC_s complex), $E_{C_iC_s} = 1.08 \pm 0.03$ eV.

ACKNOWLEDGMENTS

We thank I.V. Antonova and L.S. Smirnov for their interest in this study and for fruitful discussions.

REFERENCES

1. L. I. Murin, Phys. Status Solidi A **93**, K147 (1986).
2. G. Davies, T. K. Kwok, and T. Reade, Phys. Rev. B **44**, 12146 (1991).
3. N. I. Boyarkina, S. A. Smagulova, and A. A. Artem'ev, Fiz. Tekh. Poluprovodn. (St. Petersburg) **36**, 907 (2002) [Semiconductors **36**, 845 (2002)].
4. I. F. Medvedeva, L. F. Makarenko, V. P. Markevich, and L. I. Murin, Izv. Akad. Nauk BSSR, Ser. Fiz.–Mat. Nauk, No. 3, 19 (1991).
5. T. K. Kwok, Phys. Rev. B **51**, 17188 (1995).
6. V. P. Markevich and L. I. Murin, Fiz. Tekh. Poluprovodn. (Leningrad) **22**, 911 (1988) [Sov. Phys. Semicond. **22**, 574 (1988)].

Translated by A. Spitsyn

Semiconductors, Vol. 38, No. 5, 2004, pp. 499–504. Translated from Fizika i Tekhnika Poluprovodnikov, Vol. 38, No. 5, 2004, pp. 516–521.

ELECTRONIC AND OPTICAL PROPERTIES OF SEMICONDUCTORS

Equilibrium Characteristics and Low-Temperature Photoluminescence of CdTe:Pb Single Crystals

A. V. Savitsky, O. A. Parfenyuk, M. I. Ilashchuk, A. Ĭ. Savchuk, and S. N. Chupyra*

Fed'kovich National University, ul. Kotsyubinskogo 2, Chernovtsy, 58012 Ukraine

**e-mail: sergiy_ch@mail.ru*

Submitted August 5, 2003; accepted for publication September 18, 2003

Abstract—Using the Bridgman–Stockbarger method, CdTe:Pb single crystals with various dopant concentrations in the solution ($C^0_{Pb} = 5 \times 10^{18}$, 10^{19}, and 5×10^{19} cm^{-3}) were grown. Equilibrium characteristics of the material are controlled by deep acceptors with energy $E_v + (0.39 \pm 0.02)$ eV. The hole concentration decreases as the dopant concentration increases over the entire range of variation in C^0_{Pb}. The band caused by transitions in donor–acceptor pairs, as well as the edge emission band, is observed in the low-temperature photoluminescence spectra. As C^0_{Pb} increases, the intensity of the band associated with transitions from the conduction band to an acceptor in the edge region increases abruptly. The peak of the zero-phonon line of this radiation shifts to shorter wavelengths. The possible nature of transitions and the dynamics of variation in the photoluminescence spectra are analyzed in relation to the doping level. © *2004 MAIK "Nauka/Interperiodica".*

1. INTRODUCTION

It is well known that doping of CdTe with Group IV elements leads to the formation of a high-resistivity material [1]. Our previous research showed that the equilibrium characteristics of Ge-, Sn-, and Pb-doped CdTe crystals are controlled by corresponding deep levels: $E_v + (0.60 – 0.65)$ eV, $E_c – (0.60–0.90)$ eV, and $E_v + (0.39–0.43)$ eV [1–4]. Similar physical processes occur in such crystals with identical variation in the photoexcitation conditions and temperature, and it is possible to explain them in the context of the same model [5]. As a result, we may assume that the defects associated with Ge, Sn, and Pb in CdTe have a similar structure.

If we assume that a high-resistivity state of CdTe crystals doped with Group IV elements is caused by pinning the equilibrium Fermi level at a corresponding deep donor, it is difficult to understand the following experimental data. It was shown that, as the Pb concentration in the solution C^0_{Pb} increases from 10^{18} to 5×10^{19} cm^{-3}, the hole concentration decreases by more than three orders of magnitude with the invariable depth of the deep acceptor level $E_v + (0.4 \pm 0.02)$ eV [1]. This may indicate that the concentration of acceptor defects formed in the crystal as a result of self-compensation with doping with Pb_{Cd} donors exceeds the concentration of these donors.

The complex character of interaction of Group IV atoms with the CdTe lattice is confirmed by the results of study [6], in which magnetooptical investigations of CdTe:Ge crystals were carried out. In addition to simple donor centers $Ge^{+/0}$, complex acceptors $A^{-/0}$ were also found.

This study is devoted to the investigation of electrical properties and low-temperature photoluminescence (PL) of compensated CdTe:Pb single crystals in relation to the concentration of the impurity introduced. In contrast to Ge- and Sn-doped CdTe samples, such crystals have been investigated in less detail.

2. EXPERIMENTAL

Using the Bridgman–Stockbarger method, three CdTe ingots with various Pb concentrations in the melt were grown: $C^0_{Pb} = 5 \times 10^{18}$, 10^{19}, and 5×10^{19} cm^{-3}. The total concentration of residual impurities in starting Te and Cd was no higher than 10^{-4} at %. Prior to the synthesis, the materials were additionally purified in hydrogen. The ingots were of identical size with a length of ~12 cm and a diameter of 2.2 cm. The free space in the cell was approximately equal to the volume of the crystal.

The crystals grown consisted of three to four single-crystal blocks. The samples for electrical measurements and PL investigations were prepared from neighboring parts of the wafers, which were cut from the initial (I), middle (M), and last (L) portions of the ingots. To prepare the samples and to deposit the contacts, the standard procedures were used [7]. The PL spectra were

Equilibrium characteristics of the CdTe:Pb samples at 300 K

No.	Sample	Impurity concentration in the melt C^0_{Pb}, cm^{-3}	Relative length $\Delta l/l_0$	Conduction type	Hall mobility μ_H, cm^2/(V s)	Resistivity ρ, Ω cm	$h\nu_0^{BA}$, eV for band–acceptor transitions
1	901 P-I	5×10^{18}	0.22	*p*	60	1.86×10^7	1.544
2	901 P-M	5×10^{18}	0.44	*p*	62	6.38×10^3	–
3	901 P-L	5×10^{18}	0.88	*p*	56	3.66×10^4	1.548
4	902 P-I	10^{19}	0.30	*p*	990	19.6	1.546
5	902 P-M	10^{19}	0.58	*p*	67	3.43×10^4	1.545
6	902 P-L	10^{19}	0.84	*p*	66	7.76×10^4	1.547
7	903 P-I	5×10^{19}	0.26	*p*	72	1.64×10^6	1.552
8	903 P-M	5×10^{19}	0.57	*p*	67	2.88×10^5	1.552
9	903 P-L	5×10^{19}	0.87	*p*	32	1.26×10^6	1.554

measured on as-cleaved surfaces. The electrical parameters (the conductivity σ and the Hall coefficient R_H) were measured using a dc current in the temperature range 80–450 K.

The PL was investigated at 4.2 K according to the standard procedure using a setup based on an MDR-23 monochromator. The excitation source was a He–Ne laser with a power of 40 mW. The resolution was no lower than 1 meV. The spectral range of measurements was 7700–9300 Å.

3. RESULTS

We determined from electrical measurements that, except for the initial region of ingot 902P, all the samples had *p*-type conduction (see table).

The energy of a deep level for all *p*-CdTe:Pb samples was in the range of $E_v + (0.39 \pm 0.02)$ eV. Resistivity increased as C^0_{Pb} increased (see table and Fig. 1).[1] One can see that the lowest-resistivity material was formed in the central part of ingot 903P, and the resistivity of the crystal increased as one approached its ends. The resistivity of the middle parts of ingots 901P and 902P was also lower compared with their end parts. The initial parts of these ingots had considerably lower hole concentrations (low enough to invert the conduction type in sample 902P-I). The cause of this phenomenon will be considered below.

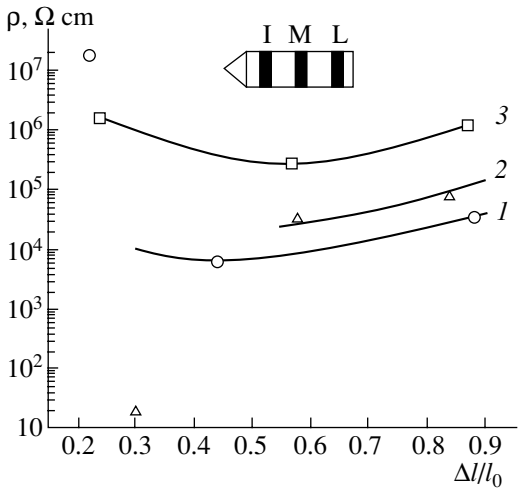

Fig. 1. Resistivity ρ of the CdTe:Pb samples at 300 K as a function of the relative length of the ingots $\Delta l/l_0$: (*1*) 901P, (*2*) 902P, and (*3*) 903P.

Measuring the mobility, we failed to determine its dependence on C^0_{Pb} (see table). A certain decrease in the value of μ_H is observed in the end parts of ingots. The run of the $\mu_H(T)$ dependence (Fig. 2) indicates that the charge carriers are scattered mainly at lattice vibrations.

Three emission bands can be distinguished in the PL spectra (Fig. 3).[2] These are the region associated with donor–acceptor pairs (DAPs), i.e., the band at 1.4 eV in the wavelength range λ = 8400–9300 Å; the edge-emission band (λ = 7920–8400 Å); and the excitonic band. The first two bands are dominant for samples 901P-I and 901P-M with lower Pb concentrations. An increase in the impurity concentration in the end part of ingot 901P causes an abrupt increase in the near-edge emission (Fig. 4, curve *1*).

The PL spectra for all parts of ingot 902P were approximately identical; specifically, the edge emission band with phonon replicas was dominant, and a considerably weaker emission region associated with DAPs

[1] The relative length (see table and abscissa in Fig. 1) is defined as the ratio $\Delta l/l_0$. Here, Δl is the distance from the starting point of the ingot to the point where the wafer is cut, and l_0 is the total length of the ingot.

[2] The use of normalized dependences makes it possible to compare absolute values of emission intensities for various samples. The magnitudes I_{max} correspond to peak values of the signal in the PL-detecting device. For the *a* and *b* spectra (Fig. 3), as well as for *1*, *2*, and *3* spectra (Fig. 4), the ratio between these peaks is 2 : 1 and 22 : 29 : 5, respectively.

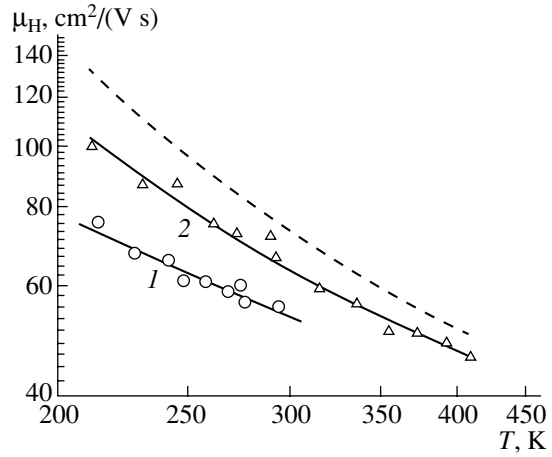

Fig. 2. Temperature dependences of mobility μ_H for end parts of the CdTe:Pb ingots: (*1*) 901P-L and (*2*) 902P-L. The dashed line corresponds to the calculated dependence $\mu_H(T)$ for scattering at optical phonons.

was observed. Similar spectra were also obtained for ingot 903P. However, the total PL intensity was lower, and the half-width of the bands increased for the I and L parts of the ingot. Figure 4 shows typical PL spectra for ingots 902P and 903P that were obtained for their central parts. The exact peak positions for zero-phonon lines ($h\nu_0^{BA}$) in the edge-emission region of the samples are given in the table.

The excitonic emission band for samples 901P-I and 901P-M is peaked at $h\nu$ = 1.592 eV (Fig. 3), which is close to the line associated with the recombination of excitons bounded at a neutral donor ($h\nu$ = 1.593 eV [8]). As the impurity concentration C_{Pb} in the sample increases, the intensity of this band decreases. In the subsequent consideration, we will analyze only the DAP-associated bands and edge emission.

A wide PL spectral feature peaked at $h\nu \approx 1.4$ eV (Fig. 3) is typical of CdTe. In addition to the purely electronic transition, it contains a series of peaks, which correspond to the emission of various numbers of longitudinal optical (LO) phonons (for CdTe $h\nu_{LO}$ = 0.021 eV [8]).

The intensity of phonon replicas can be described by the Poisson distribution:

$$I_n = I_0 e^{-s}\frac{S^n}{n!}, \qquad (1)$$

where S is the Huang–Rhys factor, which characterizes the magnitude of the electron–phonon interaction, and I_0 is the intensity of the zero-phonon line. The common emission band can be approximated by the Poisson distribution with Gaussian lines for each single peak. Due to this approximation procedure for samples 901P-I and 901P-M, the best agreement with the experiment was obtained at S = 2.01 and S = 1.96, respectively, and

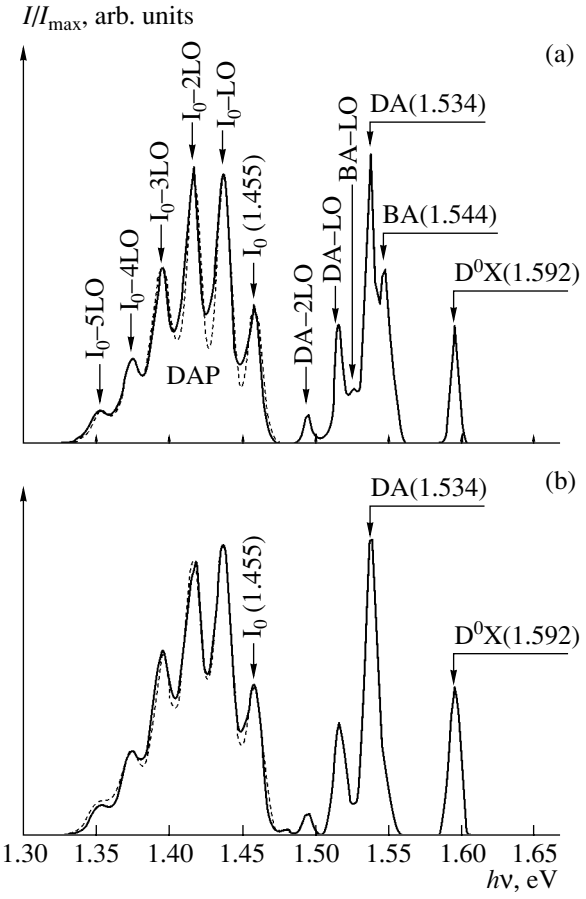

Fig. 3. Normalized spectra of low-temperature photoluminescence at T = 4.2 K for samples (a) 901P-I and (b) 901P-M. The dashed lines correspond to the result of approximation based on formula (1). The symbol I_0 designates the position of the zero-phonon DAP-line (in the text $h\nu_0^{DAP}$).

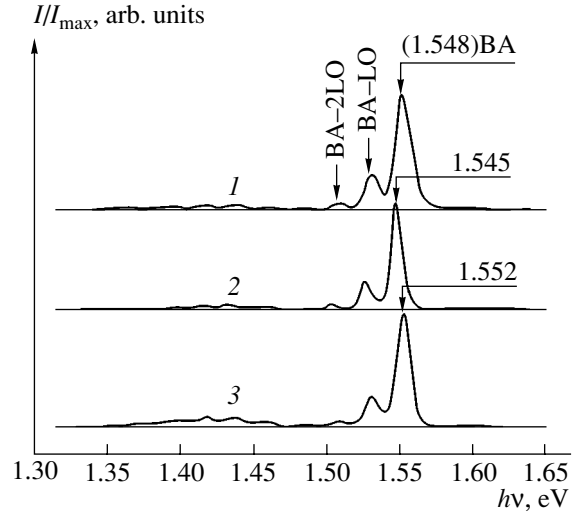

Fig. 4. Normalized spectra of low-temperature photoluminescence for samples (*1*) 901P-L, (*2*) 902P-M, and (*3*) 903P-M; T = 4.2 K.

with the position of the zero-phonon line $h\nu_0^{DAP}$ = 1.455 eV (Fig. 3).

The edge emission band for sample 901P-I (Fig. 3a) consists of five lines, which correspond to two series of transitions. The first series (DA) is formed by transitions from shallow donor centers to acceptors. Its zero-phonon line position $h\nu_0^{DA}$ is 1.534 eV. The shorter-wavelength series (BA) peaked at $h\nu_0^{BA}$ = 1.544 eV is formed by electron transitions from the conduction band to the same acceptor center.

For radiative transitions from the conduction band to the acceptor defect, the depth of the latter can be found from the relationship [9]

$$E_A^{BA} = E_g - h\nu_0^{BA} + \frac{kT}{2}, \quad (2)$$

where T is the electron temperature, which coincides with the lattice temperature for low excitation levels, and E_g is the band gap. Using the values E_g(4.2 K) = 1.606 eV [10] and $h\nu_0^{BA}$ = 1.544 eV (sample 901P-I), we obtain $E_A \approx 0.062$ eV.

In the middle part of ingot 901P (Fig. 3b), the BA band vanishes, whereas the edge emission consists of only the DA transitions with the same position of the zero-phonon line $h\nu_0^{DA}$ = 1.534 eV.

For the material with a higher Pb concentration (ingots 902P, 903P, and the end of ingot 901P), only the very intense line with phonon replicas emerges in the edge-emission regions of the PL spectra. This line is caused by the BA transition (Fig. 4). The peak of the main line of this series $h\nu_0^{BA}$ is shifted to shorter wavelengths proportionally to the impurity concentration (see table and Fig. 4).

4. DISCUSSION

The equilibrium characteristics of the crystals investigated agree well with the data [1]. As C_{Pb} increases, the hole concentration decreases. Therefore, the more compensated material in parts I of ingots 901P and 902P can form due to the higher Pb concentration in these regions. Radiometry investigations of Ge-doped CdTe crystals showed that the Ge concentration in their initial parts was anomalously high [11, 12]. This could even lead to the formation of inclusions of the second phase. We may assume that the situation for Pb-doped CdTe is similar. The PL spectrum of the initial part of ingot 901P includes the band of BA transitions, which is typical of the samples with a higher impurity concentration. This is indicative of a high Pb content in this part of the ingot.

Our investigations of numerous crystals allow us to suggest that a Pb impurity cannot lead to the formation of a low-resistivity *n*-type material. We may assume that this is caused by a high content of interstitial Cd, whose concentration decreases as the growth temperature increases [13]. In some cases, during growth by the Bridgman–Stockbarger method, Cd can saturate the lower part of the crystal, even forming Cd precipitates [14].

The PL band peaked at 1.4 eV is attributed to transitions to the acceptor centers, whose depth is 0.12–0.17 eV. The nature of these acceptors has been discussed for a long time (see, for example, [15]). It is generally believed that these defects have a complex nature and include both shallow donors and Cd vacancies (*A* centers).

The *A*-center depth can be determined from formula (2) with allowance made for the fact that the DAP band is caused by the electron transitions to the conduction band. Using the value of $h\nu_0^{DAP}$ = 1.455 eV, we obtain E_A^{DAP} = 0.15 eV.

In our opinion, the *A* centers in the crystals investigated are formed with the involvement of background donor impurities. The total concentration of uncontrollable impurity in CdTe can exceed 10^{16} cm^{-3} [16]. The value of E_A^{DAP} obtained coincides with the *A*-center depth ($E_A \approx 0.16$ eV) quite well for *n*-type crystals, whose conductivity is determined by the presence of hydrogen-like donors formed by Group III elements [17]. Therefore, we believe that uncontrollable donors located at Cd sites are incorporated into the *A* centers in our crystals as well.

In analyzing the edge emission, the considerable increase in the intensity of BA transitions and the shifts of the peak of the zero-phonon line of this series to shorter wavelengths at a higher Pb content should be considered.

Self-compensation is characteristic of CdTe. Therefore, as the concentration of the Pb_{Cd} donors increases, the concentration of intrinsic acceptor defects of V_{Cd} type increases accordingly. These defects can be isolated or incorporated into complexes. The transitions to these centers form the BA PL band in the crystals under study. We determined the value E_A^{BA} = 0.062 eV. This is close to the depth of the intrinsic acceptor, which is formed in CdTe by annealing in vacuum (E_A = 0.05 eV). Loreuz and Segall [18] relate the intrinsic acceptor to the first charge state of the V_{Cd} vacancy.

The shift of peaks of the edge PL bands of CdTe to shorter wavelengths with increasing doping level is well known and is attributed to the increasing role of the Coulomb component, which governs the magnitude of the interimpurity interaction [8]. In this case, only the position of the DA lines, which are caused by donor–acceptor recombination, should vary, as was observed by Agrinskaya *et al.* [19]. For the material under study, the situation is different, as the line arrangement varies during BA transitions (Fig. 5).

In the case under consideration, this shift may be caused by the complex character of the acceptor center.

The ionization energy of the V_{Cd} vacancy, which is subjected to Coulomb interaction with the donor, depends on the distance from the donor. We assume that such donors are Pb atoms. The large energy depth of Pb donors excludes their immediate involvement in the formation of the BA band; however, they can affect V_{Cd} electrostatically.

The peak of the zero-phonon line of BA transitions for the crystals under investigation shifts by 0.01 eV as C_{Pb}^0 increases (see table). Let us assume that the Coulomb interaction between Pb_{Cd} and V_{Cd} for a sample with a low Pb content (901P-I) can be disregarded. We can then find the average distance between these defects in the material with highest C_{Pb}^0 (sample 903P-L). Using the well-known expression for the Coulomb interaction energy

$$\Delta W = \frac{e^2}{\varepsilon R},$$

for $\Delta W = 0.01$ eV we obtain $R = 1.5 \times 10^{-6}$ cm. Knowing the average size of pairs, we can determine their concentration:

$$N = \left(\frac{4}{3}\pi R^3\right)^{-1};$$

thus, we obtain $N \approx 6.6 \times 10^{16}$ cm^{-3}. It is clear that the concentration of the Pb_{Cd} donors interacting electrostatically with V_{Cd} is the same in sample 903P-L. In the material with lower C_{Pb}^0, the distance between the components of a pair will be larger, and the shift of the peak of the $h\nu_0^{BA}$ band will be smaller.

In addition to the pairs with large R, the complexes with the involvement of Pb atoms and V_{Cd}, which occupy neighboring Cd sites, are present in the CdTe:Pb crystals. The existence of such complexes, whose constituents are bound by the ionic–covalent bond, accounts for the high photosensitivity of the crystals under investigation [20].

To estimate the total amount of Pb-related electrically active defects (isolated or in the composition of stable complexes), the concentration of complexes should be found. Taking into account the fact that the specific photosensitivities of the CdTe:Ge and CdTe:Pb crystals are almost the same [19], we may assume that such materials have an approximately identical amount of photosensitivity-controlling defects (M_{Cd}–V_{Cd}, where M are the Ge or Pb atoms), which is equal to $(3–8) \times 10^{16}$ cm^{-3}. This value was obtained by Nikonyuk *et al.* from the investigation of photoelectric properties of CdTe:Ge [21]. Thus, the concentration of the Pb impurity in the CdTe lattice ($\sim 10^{17}$ cm^{-3}) is considerably lower than the concentration of Pb atoms in the melt.

Doping CdTe with Pb affects the state of background impurities only slightly. This inference follows from a comparison of absolute intensities of the DAP band for the samples with different C_{Pb}. As was noted above, this emission emerges with the transition to complex acceptors, which are formed with the involvement of uncontrollable donors. The ratio of intensities of the DAP emission for ingots 901P and 902P is no larger than 2.5, whereas for the BA transition in the edge-emission region this ratio can be as large as 150.

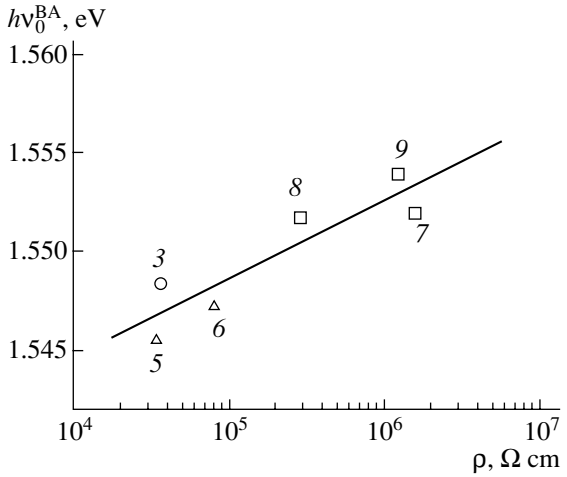

Fig. 5. Peak position of the zero-phonon line versus resistivity ρ for the BA transitions in the CdTe:Pb samples. Numbers correspond to sample numbers in the table.

5. CONCLUSION

Doping CdTe with Pb yields *p*-type material; the compensation effect of Pb increases proportionally to the impurity content. The properties of the CdTe:Pb crystals differ substantially from the characteristics of the Ge-doped and Sn-doped CdTe, for which the material properties are virtually independent of C_{Ge} or C_{Sn} when a certain critical concentration of Ge or Sn is attained [2].

A considerable fraction of the Pb impurity is electrically inactive and probably forms inclusions. The magnitude and temperature run of mobility show that these inhomogeneities do not form drift barriers for current.

In the CdTe lattice, the Pb_{Cd} donors can interact with intrinsic defects V_{Cd}. If the distances between them are considerable, this leads to a decrease in the ionization energy of V_{Cd} proportionally to the impurity concentration. As they arranged at neighboring sites of the Cd sublattice, these defects form stable complexes.

REFERENCES

1. A. V. Savitskiĭ, O. A. Parfenyuk, M. I. Ilashchuk, and P. A. Pavlin, Izv. Akad. Nauk SSSR, Neorg. Mater. **25**, 1848 (1989).
2. V. V. Matlak, M. I. Ilashchuk, O. A. Parfenyuk, *et al.*, Fiz. Tekh. Poluprovodn. (Leningrad) **11**, 2287 (1977) [Sov. Phys. Semicond. **11**, 1345 (1977)].

3. O. A. Parfenyuk, A. V. Savitskiĭ, P. A. Pavlin, and A. L. Al'bota, Izv. Vyssh. Uchebn. Zaved., Fiz., No. 4, 66 (1986).
4. O. Panchuk, O. Savitsky, P. Fochuk, *et al.*, J. Cryst. Growth **197**, 607 (1999).
5. A. Rose, *Concepts in Photoconductivity and Allied Problems* (Interscience, New York, 1963; Mir, Moscow, 1966).
6. K. Shcherbin, S. Odulov, F. Ramaz, B. Farid, B. Briat, H. J. Bardeleben, I. Rarenko, Z. Zakharuk, O. Panchuk, and P. Fochuk, *Optics and Optoelectronics*, Vol. 2: *Theory Devices and Applications* (Narosa, Dehradun, India, 1998).
7. A. V. Savitsky, O. A. Parfenyuk, M. I. Ilashchuk, *et al.*, Semicond. Sci. Technol. **15**, 263 (2000).
8. Zh. R. Panosyan, Tr. Fiz. Inst. im. P. N. Lebedeva, Akad. Nauk SSSR **68**, 147 (1973).
9. D. M. Eagles, J. Phys. Chem. Solids **16**, 75 (1960).
10. G. Fonthal, L. Tirado-Mejia, J. I. Marin-Hurtado, *et al.*, J. Phys. Chem. Solids **61**, 579 (2000).
11. L. P. Shcherbak, E. S. Nikonyuk, O. É. Panchuk, *et al.*, Izv. Akad. Nauk SSSR, Neorg. Mater. **13**, 415 (1977).
12. P. Feichuk, L. Shcherbak, D. Pluta, *et al.*, Proc. SPIE **3182**, 100 (1997).
13. F. A. Kröger, *The Chemistry of Imperfect Crystals* (North-Holland, Amsterdam, 1964; Mir, Moscow, 1969).
14. K. R. Zanio, in *Semiconductors and Semimetals*, Vol. 13: *Cadmium Telluride*, Ed. by R. K. Willardson and A. C. Beer (Academic, New York, 1978), p. 235.
15. M. Somimi, B. Biglari, M. Hage-Ali, *et al.*, Phys. Status Solidi A **100**, 251 (1987).
16. P. Rudolph, M. Muhlberg, M. Neubert, *et al.*, J. Cryst. Growth **118**, 204 (1992).
17. N. V. Agrinskaya, E. N. Arkad'eva, and O. A. Matveev, Fiz. Tekh. Poluprovodn. (Leningrad) **5**, 869 (1971) [Sov. Phys. Semicond. **5**, 767 (1971)].
18. M. R. Loreuz and B. Segall, Phys. Lett. **7**, 18 (1963).
19. N. V. Agrinskaya, E. N. Arkad'eva, and O. A. Matveev, Fiz. Tekh. Poluprovodn. (Leningrad) **5**, 863 (1971) [Sov. Phys. Semicond. **5**, 762 (1971)].
20. P. Gorley, J. Vorobiev, V. Makhniy, *et al.*, Mater. Sci. Eng. (in press).
21. E. S. Nikonyuk, O. A. Parfenyuk, V. V. Matlak, *et al.*, Fiz. Tekh. Poluprovodn. (Leningrad) **9**, 1271 (1975) [Sov. Phys. Semicond. **9**, 840 (1975)].

Translated by N. Korovin

Semiconductors, Vol. 38, No. 5, 2004, pp. 505–506. Translated from Fizika i Tekhnika Poluprovodnikov, Vol. 38, No. 5, 2004, pp. 522–523.

ELECTRONIC AND OPTICAL PROPERTIES OF SEMICONDUCTORS

Electrical Properties of Layered $FeGaInS_4$ Single Crystals

N. N. Niftiev

Azerbaijani State Pedagogical Institute, Baku, 370000 Azerbaijan

Submitted September 24, 2003; accepted for publication October 6, 2003

Abstract—The temperature dependence of conductivity and current–voltage characteristics of a layered $FeGaInS_4$ single crystal have been studied in various conditions. It is shown that the nonlinearity of the current–voltage characteristic is due to the space-charge-limited current. The activation energies of impurity levels in $FeGaInS_4$ single crystals are determined. © *2004 MAIK "Nauka/Interperiodica".*

Considerable attention has been given recently to studies of semimagnetic semiconductors of the $II–III_2–VI_4$ type (where II stands for Mn, Fe, Ni, or Co; III, for Ga or In; and VI, for S, Se, or Te) [1–4]. These compounds are promising for the development of lasers, light modulators, photodetectors and other magnetic-field-controlled functional devices. In [5], new layered semimagnetic semiconductors of $CoIn_2S_4$ composition were obtained at a 1 : 1 ratio of the starting materials of spinel structure ($CoIn_2S_4$, $Fd3m$ space group) and tetragonal structure ($CoGa_2S_4$, $I\bar{4}$ space group), and their structural and magnetic properties were studied. The fact that layered compounds are formed in the interaction of semimagnetic semiconducting compounds prompted us to try to obtain layered semimagnetic semiconductors on the basis of other transition elements. As was done in [5], we obtained new layered semimagnetic semiconductors of $MnGaInS_4$ composition and studied their optical properties and photoconductivity [6, 7]. In studying the phase diagram of the system $FeGa_2S_4$–$FeIn_2S_4$, we obtained for the first time the layered compound $FeGaInS_4$.

In this paper, we report the results obtained in studying the temperature dependence of conductivity $\sigma(T)$ and current–voltage ($I–U$) characteristics of $FeGaInS_4$ single crystals.

The $FeGaInS_4$ single crystals were grown by the Bridgman method. An X-ray diffraction analysis demonstrated that $FeGaInS_4$ crystallizes as a one-packet polytype of $ZnIn_2S_4$ [8], with lattice constants a = 3.81 Å, c = 12.17 Å, and z = 1 ($P3m1$ space group). The contacts for $I–U$ measurements were fabricated by fusing-in indium on the opposite surfaces of the samples (sandwich structure). The interelectrode spacing was varied within the range 15–200 μm.

Figure 1 shows $I–U$ characteristics of In–$FeGaInS_4$–In structures obtained at different temperatures. The $I–U$ characteristics exhibit two portions: an ohmic region ($I \propto U$) and a region with a steeper rise in current ($I \propto U^n$, $n > 1$).

Figure 2 shows the temperature dependence of conductivity with an electric field strength of 77 V/cm. It can be seen that the curve that describes the dependence $\log\sigma = f(10^3/T)$ comprises two linear portions with different slopes. The activation energies of impurity levels, determined from these slopes, are E_1 = 0.14 eV and E_2 = 0.25 eV.

In order to explain the mechanism of current transport in the nonlinearity region, we studied $I–U$ characteristics of samples with different interelectrode spac-

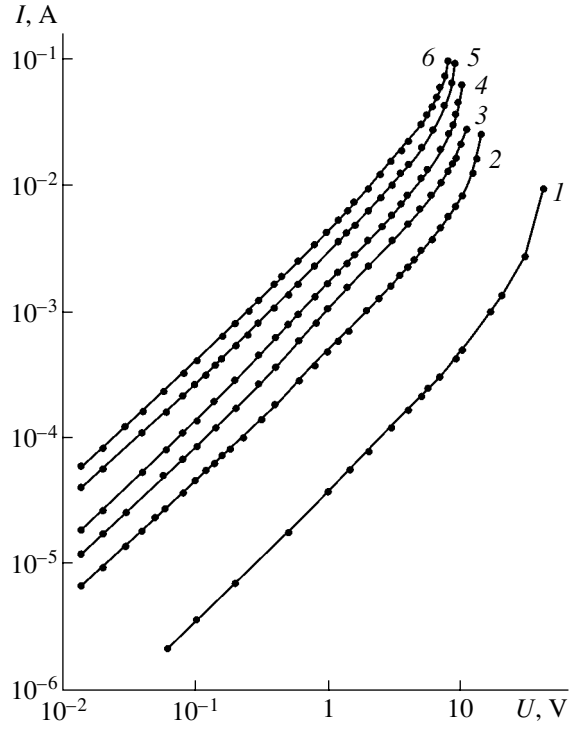

Fig. 1. Dark $I–U$ characteristics of In–$FeGaInS_4$–In structures obtained at temperatures T: (*1*) 193, (*2*) 290, (*3*) 315, (*4*) 340, (*5*) 365, and (*6*) 385 K.

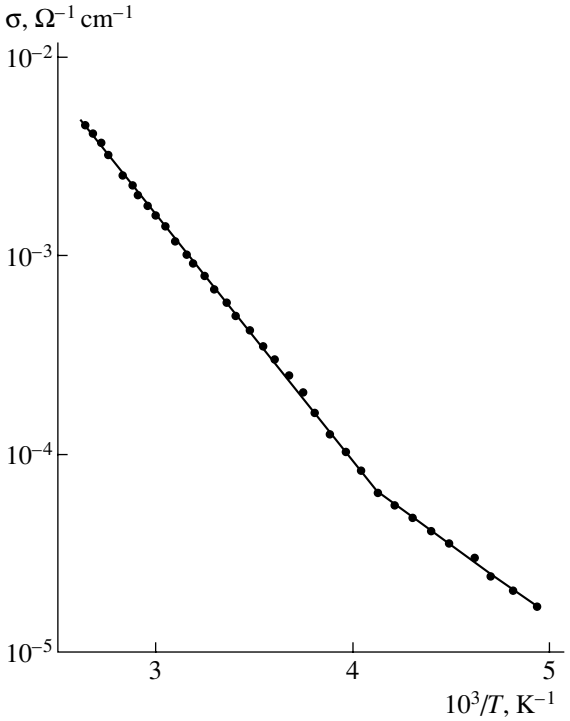

Fig. 2. Temperature dependence of conductivity of a $FeGaInS_4$ single crystal with an electric field strength of 77 V/cm.

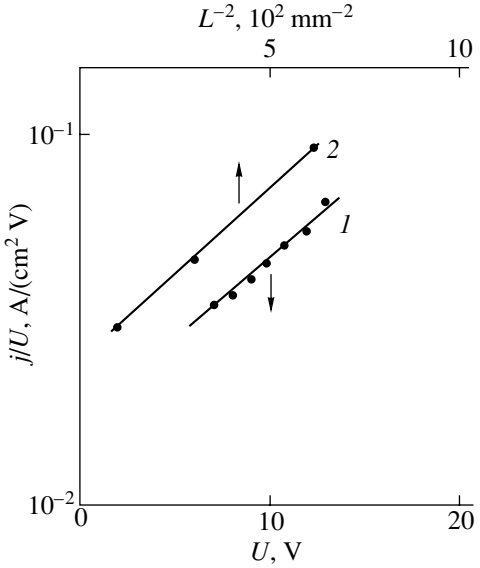

Fig. 3. j/U vs. (*1*) voltage U at T = 290 K and (*2*) L^{-2} at a voltage of 10 V.

ings L. It was found that the following dependences are observed for the layers studied:

$$\ln\frac{j}{U} \propto U \quad \text{and} \quad \ln\frac{j}{U} \propto \frac{1}{L^2}$$

(Fig. 3, curves *1* and *2*, respectively), which indicates that the space-charge-limited current (SCLC) [9] is the reason why the *I–U* characteristics are nonlinear. Here, j is the current density and U is the bias.

According to [10], if the ohmic-to-nonlinear transition voltage is temperature-independent, the crystals are weakly compensated. Analysis of the data we obtained shows that the transition voltage from ohmic conductivity to the SCLC mode is shifted to higher voltages as the temperature is decreased; i.e., $FeGaInS_4$ crystals are strongly compensated.

Thus, our study of the *I–U* characteristics and $\sigma(T)$ dependences demonstrated that the current in the nonlinear portion of the *I–U* characteristic is due to monopolar injection. The activation energies of impurity levels in $FeGaInS_4$ single crystals were determined.

REFERENCES

1. T. Kanomata, H. Ido, and T. Kaneko, J. Phys. Soc. Jpn. **34**, 554 (1973).
2. R. N. Bekimbetov, Yu. V. Rud', and M. A. Tairov, Fiz. Tekh. Poluprovodn. (Leningrad) **21**, 1051 (1987) [Sov. Phys. Semicond. **21**, 642 (1987)].
3. G. A. Medvedkin, Yu. Rud, and M. A. Tairov, Phys. Status Solidi A **3**, 289 (1989).
4. N. N. Niftiev, Solid State Commun. **92**, 781 (1994).
5. C. Battistoni, L. Gastaldi, G. Mattogno, *et al.*, Solid State Commun. **61**, 43 (1987).
6. N. N. Niftiev, A. G. Rustamov, O. B. Tagiev, and G. M. Niftiev, Opt. Spektrosk. **75**, 351 (1993) [Opt. Spectrosc. **75**, 206 (1993)].
7. N. N. Niftiev, O. B. Tagiev, and G. M. Niftiev, Neorg. Mater. **32**, 291 (1996).
8. A. Hulliger, *Structural Chemistry of Layer-Type Phases*, Ed. by F. Levy (Reidel, Dordrecht, 1976).
9. J. A. Rose, *Concepts in Photoconductivity and Allied Problems* (Interscience, New York, 1963; Mir, Moscow, 1966).
10. A. V. Malovichko, V. G. Chalaya, and E. P. Shul'ga, Ukr. Fiz. Zh. **20**, 209 (1975).

Translated by M. Tagirdzhanov

Semiconductors, Vol. 38, No. 5, 2004, pp. 507–511. Translated from Fizika i Tekhnika Poluprovodnikov, Vol. 38, No. 5, 2004, pp. 524–528.

ELECTRONIC AND OPTICAL PROPERTIES OF SEMICONDUCTORS

Features of Thermal Radiation of Plane-Parallel Semiconductor Wafers

K. Yu. Guga, A. G. Kollyukh*, A. I. Liptuga, V. A. Morozhenko, and V. I. Pipa

Institute of Semiconductor Physics, National Academy of Sciences of Ukraine, Kiev, 03028 Ukraine

**e-mail: kollyukh@isp.kiev.ua*

Submitted July 1, 2003; accepted for publication October 8, 2003

Abstract—The spectra and angular distribution of thermal radiation from semitransparent plane-parallel semiconductor wafers are theoretically and experimentally investigated. It is shown that the spectrum of thermal radiation from these objects is oscillatory due to multiple-beam interference, and the radiation pattern has the lobes. The measurements are performed in the region of free-carrier absorption of *n*-GaAs and *n*-Si. It is concluded that the results of this study can be used for calculating new controlled IR-radiation sources. © *2004 MAIK "Nauka/Interperiodica".*

1. INTRODUCTION

The thermal radiation (TR) of heated solids typically has a wide continuous spectrum and a quasi-isotropic angular distribution. These TR characteristics of opaque solids differ little from blackbody radiation. Therefore, in contrast to highly monochromatic and narrow-beam laser radiation, TR is conventionally considered noncoherent. However, as shown in studies [1–3], the TR from certain periodic structures exhibits coherent properties in certain spectral regions. Spectral peaks and narrow radiation patterns were observed in the TR of Si and SiC crystals on the surface of which a grating was formed. Such features arise near the surface-plasmon frequency (in Si) or the phonon-polariton frequency (in SiC).

In this study, we theoretically and experimentally investigate the TR from semitransparent plane-parallel semiconductor wafers. It is shown that the TR from these systems also exhibits an antenna effect, i.e., sharp spectral peaks and a radiation pattern with lobes. However, this effect arises here because of resonant properties of the radiating solid and, in contrast to the data in [1–3], is not related to the excitation of surface waves and manifests itself without the grating. The resonant properties of the radiating wafers are caused by their plane-parallel shape, which gives rise to the multiple-beam interference. The interference pattern in the luminescence spectra of thin layers was observed previously [4, 5]; however, this effect was not experimentally investigated for TR. The features of TR in thin plane-parallel layers were theoretically predicted in [6]. In this study, we measured the TR in the spectral region of the free-carrier absorption of light in *n*-GaA and *n*-Si. To quantitatively describe the results of the measurements of the spectral, angular, and polarization characteristics of the radiation, we used Kirchhoff's law. The interference oscillations in the TR spectra observed along the surface normal of a plane-parallel wafer are described in terms of this law in [7].

2. THEORY

We consider the plane-parallel wafer of a homogeneous semiconductor ($0 \le z \le l$) in free space. The semiconductor is at a temperature T and has the frequency-dependent complex permittivity $\varepsilon(\omega) = \varepsilon' + i\varepsilon''$.

Let $dJ = J(\omega, \vartheta)d\omega d\Omega dS$ designate the intensity of light emission from an area dS of the solid surface at an angle ϑ to its normal into a solid-angle element $d\Omega$ in the frequency range ω, $\omega + d\omega$. According to Kirchhoff's law,

$$J(\omega, \vartheta) = A(\omega, \vartheta)\frac{\hbar\omega^3 N(\omega)}{4\pi^3 c^2}\cos\vartheta, \qquad (1)$$

where $A(\omega, \vartheta)$ is the emissivity of a solid equal to its absorptivity and $N(\omega)$ is the Planck distribution function at the temperature T.

The absorptivity $A(\omega, \vartheta)$ is defined as the fraction of the radiation energy flux incident on the solid surface which is absorbed by this solid:

$$A = 1 - R_l - D_l. \qquad (2)$$

Here, $R_l(\omega, \vartheta)$ is the optical reflectance from a wafer and $D_l(\omega, \vartheta)$ is the wafer transmittance. In formulas (1) and (2), we take into account both independent polarizations of light. The polarization properties depend on the partial absorptivity A_ν ($\nu = s, p$) for *s*-polarized radiation (the electric-wave vector is perpendicular to the incidence plane) and *p*-polarized radiation (the magnetic-wave vector is perpendicular to the incidence plane):

$$A_\nu = 1 - |r_{l\nu}|^2 - |d_{l\nu}|^2. \qquad (3)$$

Here, r_{lv} and d_{lv} are the amplitudes of optical reflectance and transmittance of the wafer, respectively. The factor $A(\omega, \vartheta)$ in formula (1) is defined as

$$A = \frac{A_s + A_p}{2}. \quad (4)$$

For a linearly polarized plane wave incident from vacuum on the wafer surface at an angle ϑ to the normal, the amplitudes r_{lv} and d_{lv} are described by the expressions [8]

$$r_{lv} = \frac{r_v(1-e^{i\varphi})}{1-r_v^2 e^{i\varphi}}, \; d_{lv} = \frac{1-r_v^2}{1-r_v^2 e^{i\varphi}} e^{i\varphi/2}, \quad (5)$$

where r_v are the amplitudes of reflectances from the surface of a semi-infinite medium with permittivity ε. These amplitudes have the form

$$r_s = \frac{k_{1z}-k_{2z}}{k_{1z}+k_{2z}}, \; r_p = \frac{\varepsilon k_{1z}-k_{2z}}{\varepsilon k_{1z}+k_{2z}}. \quad (6)$$

We introduce the following designations into expressions (5) and (6): $k_{1z} = k_1\cos\vartheta$, $k_{2z} = k_1\sqrt{\varepsilon - \sin^2\vartheta} = k'_{2z} + ik''_{2z}$, $\varphi = 2k_{2z}l$, and $k_1 = \omega/c$.

Expression (3), in which the amplitudes r_{lv} and d_{lv} are calculated from Eqs. (5) and (6), defines the absorptivity in terms of the macroscopic electrodynamics. This expression is valid if the wafer thickness is much greater than the atomic dimensions, while the relation between the radiation wavelength and the wafer thickness can be arbitrary. It is also noteworthy that the absorption of light is not assumed to be weak.

If the absorption of light in a semiconductor is weak ($\varepsilon'' \ll \varepsilon'$) and the wavelengths in the wafer are short ($\delta = 2k'_{2z}l \gg 1$), formula (3) can be simplified as

$$A_v = \frac{(1-R_v)(1+\eta R_v)(1-\eta)}{1-2\eta R_v\cos\delta + \eta^2 R_v^2}, \quad (7)$$

where $R_v = |r_v|^2$ and $\eta = \exp(-2k''_{2z}l)$. The parameter η specifies the reduction of the TR intensity due to the absorption during a single pass of the wave through the wafer. The phase δ and the transmittance η can be expressed in terms of the real refractive index n, the absorptivity α, and the angle of refraction ϑ_2 ($n\sin\vartheta_2 = \sin\vartheta$) using the relations $\alpha = 2k''_{2z}\cos\vartheta_2$ and $k'_{2z} = (2\pi/\lambda)n\cos\vartheta_2$. Here, $\lambda = 2\pi c/\omega$ is the radiation wavelength in free space.

It can be seen from (1) and (7) that the intensity of TR from a plane-parallel wafer oscillates as a function of the wavelength λ at the fixed observation angle ϑ. For a given λ, the intensity oscillates as a function of the angle ϑ. The oscillations of the radiation intensity are governed by the oscillatory dependence of the emissivity $A(\lambda, \vartheta)$ of the plane-parallel wafer and are caused by the interference of waves multiply reflected from the interfaces. If n and α vary only slightly over the oscillation period, the positions of the $A(\lambda)$ extrema are determined by the interference conditions

$$\lambda_{\max} = \frac{2nl}{m}\cos\vartheta_2, \; \lambda_{\min} = \frac{4nl}{2m-1}\cos\vartheta_2, \quad (8)$$

where $m = 1, 2, \ldots$.

The averaging of (7) over the phase δ leads to the absorptivity

$$\bar{A}_v = \frac{(1-R_v)(1-\eta)}{1-\eta R_v}, \quad (9)$$

which coincides with that of the wafer if the interference is disregarded [9].

3. EXPERIMENTAL

In the experimental investigation, we used plane-parallel wafers of single-crystal GaAs with the concentration of uncompensated donors N_d–$N_a = 9.6 \times 10^{17}$ cm^{-3} and single-crystal Si with N_d–$N_a = 6 \times 10^{17}$ cm^{-3}. The plane-parallel wafers were obtained by mechanical grinding and subsequent polishing of the wide faces. The flatness and parallelism of the faces were checked by conventional optical methods. For the measurements, we selected wafers whose planes deviated from parallelism by 5″–10″ to ensure that their flatness was close to ideal. The wafers had an area of 10×15 mm^2 and a thickness of 111 μm (GaAs) and 92 μm (Si). The measurements were carried out in the spectral region of the free-carrier optical absorption, and the wafers were heated to temperature $T = 360$ K.

The spectra were investigated using a Fourier spectrometer with a resolution of 1 cm^{-1}. We detected the nonpolarized TR from the plane-parallel and non-plane-parallel GaAs samples that propagated close to the normal to the surface of the crystals. The entrance optical aperture of the spectrometer amounted to less than 2.5°. The radiation from the GaAs wafers was normalized to the blackbody radiation measured under the same experimental conditions. The TR from the plane-parallel wafers was compared to the radiation from identical non-plane-parallel wafers that had the same average thickness and temperature.

The angular dependences of TR were investigated on Si samples at a wavelength of $\lambda = 10.57$ μm. We detected *s*- and *p*-polarized radiation, as well as nonpolarized TR. The radiation from the plane-parallel Si wafers was normalized to the radiation from the identical non-plane-parallel wafers; i.e., we measured the ratio $A_v(\vartheta)/\bar{A}_v(\vartheta)$ of the emissivities.

4. RESULTS AND DISCUSSION

Figure 1 shows the experimental spectral dependences for the emissivities of the plane-parallel GaAs wafers (oscillating curve *1*) and the non-plane-parallel

wafers (steadily increasing curve *2*). Curve *3* shows the measured variance of the optical thickness αl of these wafers. It can be seen that the maxima and minima of the emission from the plane-parallel wafer are arranged virtually symmetrically relative to the curve of the radiation from the non-plane-parallel wafer.

To analyze the experimental data, we compared them to the results of the calculation performed using formulas (3), (7), and (9). In this calculation, we took into account the absorptance α and the refractive index n of the wafers in relation to λ; the corresponding values were determined from our measurements and verified with the published data [10, 11]. It was found that the results of calculations agree well with the experiment within the entire investigated spectral range (λ = 4–16 μm). The calculations with formulas (3) and (7) yield virtually identical results because the absorption of light in the semiconductor is weak in the investigated case, while the wavelengths in the wafer are much less than its thickness.

For a descriptive comparison of experimental and theoretical results, in Fig. 2 we show the emissivities for the plane-parallel wafer (curves *1*, *2*) and the non-plane-parallel wafer (curves *3*, *4*) in a narrow spectral range (the experimental curves *2* and *3* are portions of curves *1* and *2* in Fig. 1). One can see that the theoretical and experimental results virtually coincide for the non-plane-parallel wafer. The small difference in the calculated and measured amplitudes of the oscillations (curves *1*, *2*) in the plane-parallel wafer may be attributed to a decrease in the oscillation amplitude caused by the imperfect parallelism of the surfaces of the experimental sample.

From the viewpoint of the practical use of the results obtained, it is expedient to investigate the dependence of the oscillation amplitude of the emissivity $\Delta A = A_{max} - A_{min}$ of plane-parallel wafers on the parameters R and η. Here, A_{max} and A_{min} are the amplitudes of the neighboring maxima and minima, respectively. Using formulas (7) and (8) and assuming that $\vartheta_2 = 0$ (i.e., $R_s = R_p = R$ and $A_s = A_p = A$), we obtain

$$\Delta A = \frac{4\eta R(1-R)(1-\eta)}{(1-\eta R)^2(1+\eta R)}. \qquad (10)$$

The analysis shows that ΔA attains a maximum near R and η close to unity. In this case, A_{max} is close to 0.5 and A_{min} is virtually equal to zero, which corresponds to the most pronounced interference pattern. In Fig. 2, we show the calculated emissivity of a highly transparent (η = 0.89) plane-parallel GaAs wafer (curve *5*) and a non-plane-parallel GaAs wafer (curve *6*) with R = 0.9. The reflectance can be increased by depositing dielectric coatings on the wafer surface (a variation in the phase δ, which governs the positions of the interference extrema positions, was disregarded). It can be seen that the spectrum of the plane-parallel wafer includes narrower emission peaks in this case and features much greater oscillation amplitude in comparison with

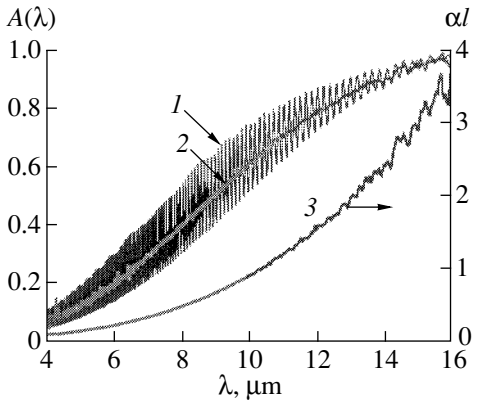

Fig. 1. Experimental spectral dependences of the emissivity $A(\lambda)$ (curves *1*, *2*) and the optical thickness αl (curve *3*) for *n*-GaAs wafers; *1* is a plane-parallel wafer, and *2* is an identical wafer that is not plane-parallel.

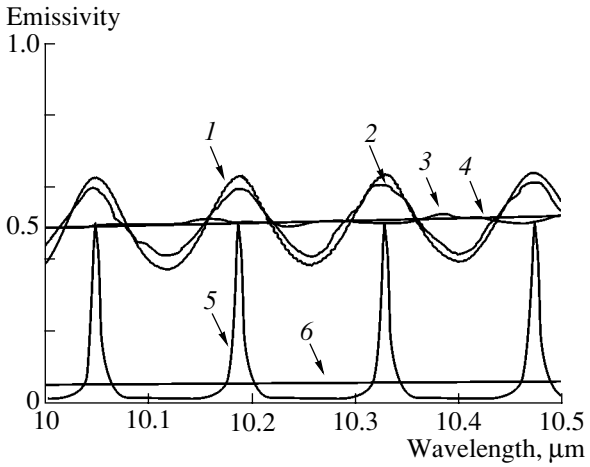

Fig. 2. Spectral dependences of the emissivities of plane-parallel (*1*, *2*, *5*) and non-plane-parallel (*3*, *4*, *6*) *n*-GaAs wafers. Curves *2* and *3* represent experimental data, and the remaining curves correspond to the calculation with the parameters n = 3.3 (curves *1*, *4–6*); R = 0.29 (*1*, *4*), 0.9 (*5*, *6*); and η = 0.4 (*1*, *4*) and 0.89 (*5*, *6*).

curves *1* and *2*. The dependences $\Delta A(\eta)$ for R = const and $\Delta A(R)$ for η = const are described by nonmonotonic curves with a peak. Dependences $\Delta A(\eta)$ can be observed in experiment. Figure 1 shows that, in the spectral regions $\lambda < 6$ μm and $\lambda > 14$ μm for which high ($\alpha l < 0.2$) and low ($\alpha l > 2$) transparencies of the wafers are characteristic, respectively, the oscillation amplitude ΔA is smaller than that in the remaining spectral region. The largest oscillations are observed near $\eta = \exp(-\alpha l) \approx 0.56$, which corresponds to $\lambda \approx 8.4$ μm. In Fig. 3, the dots correspond to the experimental dependence ΔA on η, and the solid line represents the results of calculation. For each dot, we plot an average value of η in the spectral region A_{max}–A_{min} on the vertical axis. Taking into account that the variation in η in these

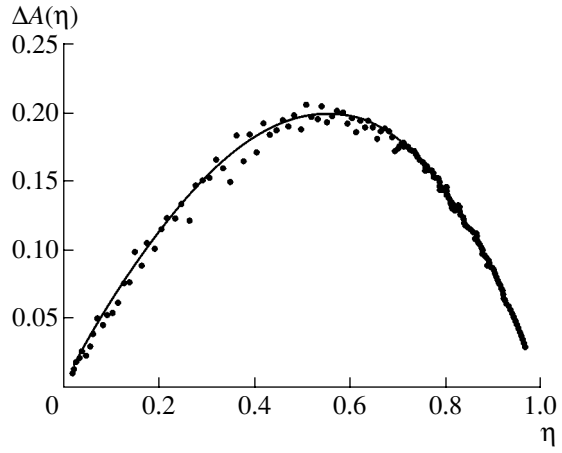

Fig. 3. Experimental (dots) and calculated (solid line) emissivity modulation ΔA of *n*-GaAs wafers vs. the transmittance η.

regions is less than 6%, the error of this representation is considered negligible.

In the calculation, we took into account the slight tapering of the wafer. It was assumed that the wafer thickness linearly increased along the *x* axis; i.e.,

$$l(x) = l_0 + x\tan\gamma,$$

where $\gamma \ll 1$ is the angle between the emitting faces, and l_0 is the wafer thickness for $x = 0$. Replacing l by $l(x)$ in formula (7), we obtain the local emissivity $A(x)$. Then, the emissivity for the tapered wafer of a length L can be written as the mean value:

$$\langle A\rangle = \frac{1}{L}\int_0^L A(x)dx. \qquad (11)$$

The dependence of the oscillation amplitude on η was calculated using the oscillatory functions $\langle A(\lambda)\rangle$. The agreement between the experimental and theoretical data shown in Fig. 3 was obtained for $L = 15$ mm, $l_0 = 111$ μm, and $\gamma = 6''$.

The angular distributions of the TR from the plane-parallel Si wafers are shown in Figs. 4a and 4b. The solid curves show the calculated ratios between the emissivities $A_\nu(\vartheta)$ and $\bar{A}_\nu(\vartheta)$ of the plane-parallel and non-plane-parallel wafers, respectively, with different directions of polarizations and $\lambda = 10.57$ μm ($\alpha = 8$ cm^{-1}). It can be seen that, as a result of the multiple-beam interference, the radiation acquires directivity with a number of pronounces lobes. The angular dependences $A_\nu(\vartheta)/\bar{A}_\nu(\vartheta)$ for the *s*- and *p*-polarized emission (Fig. 4b and the left-hand side of the pattern in Fig. 4a) markedly differ from one another. In the range of 55°–75°, the extrema for the *p*-polarized radiation virtually disappear, which is related to a decrease in the reflectance R_p almost to zero. The angular dependences for the *s*-

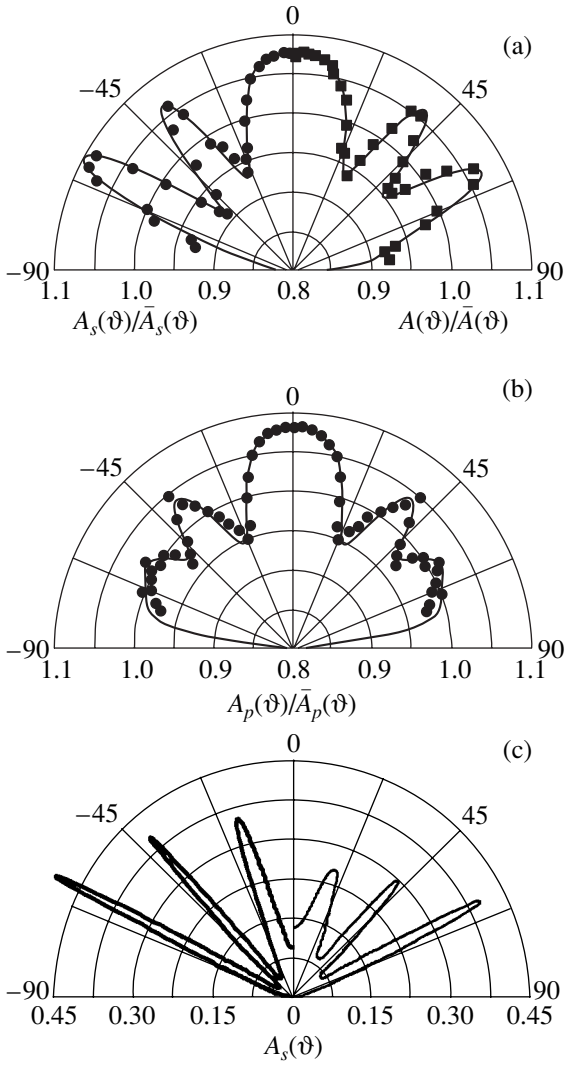

Fig. 4. Angular distributions of the thermal radiation of semiconductor wafers for $\lambda = 10.57$ μm. The solid lines correspond to the calculation, and the circles and squares correspond to the experiment; (a) and (b) are the ratios between the emissivities of plane-parallel and identical non-plane-parallel wafers, and (c) is the emissivities of plane-parallel wafers. The left-hand side of the radiation pattern in Fig. 4a corresponds to *s* polarization; the right-hand side, to nonpolarized radiation. Figure 4b corresponds to *p* polarization; Fig. 4c, to *s* polarization. The parameters used in the calculation: (a, b) $\eta = 0.93$, $l = 92$ μm, $n = 3.4$, *n*-Si wafer; (c) $\eta = 0.87$, $l = 179$ μm, a wafer with $n = 6$ (left-hand side of the pattern) and a wafer with $n = 3.4$ (right-hand side).

polarized and nonpolarized emission are similar in many respects (Fig. 4a). In Figs. 4a and 4b, the circles and squares show the experimental results. One can see that the calculated and experimental data are in good agreement.

As in the radiation spectra, a more pronounced TR pattern can be obtained in the angular dependences if R of the plane-parallel wafer is increased. This effect can be seen from Fig. 4c, which shows the calculated angu-

lar dependences for the emissivities $A_s(\vartheta)$ of a wafer with the refractive index $n = 6$ (the left-hand side of the pattern) and a wafer with the refractive index $n = 3.4$ (the right-hand side of the pattern). For both wafers, $l = 179$ μm and $\eta = 0.87$ (for $\vartheta = 0$).

Nowadays, semiconductor luminescent light emitting diodes (LEDs) are widely used in the near IR region. It is a complicated problem to significantly expand their operating spectral range (to the region $\lambda > 4.5$ μm) because the external quantum efficiency [12] falls drastically as the radiation wavelength increases. In contrast to luminescent LEDs, thermal sources can usually operate in an arbitrary spectral region; however, they require an external modulating device. Certain types of semiconductor thermal sources [13, 14] are an exception because their emission intensity can be modulated by the current flowing through a crystal.

A source using thermal radiation from thin plane-parallel layers can have a narrow-band radiation spectrum in the medium- and far-IR range. Modifying the optical parameters of a semiconductor emitting element by external effects allows one to carry out spectral and amplitude modulation of its radiation.

5. CONCLUSION

We showed theoretically and experimentally that multiple-beam interference manifests itself in the thermal radiation of semiconductor plane-parallel semitransparent wafers. The thermal-radiation spectrum of the plane-parallel wafer differs markedly from that of identical non-plane-parallel wafers and is oscillatory. The amplitude of the oscillation of the emissivity depends on the transmittance and reflectance of the wafer and increases as they increase. The thermal-radiation intensity in the ranges corresponding to the interference maxima for a plane-parallel wafer can far exceed the radiation intensity from an identical non-plane-parallel wafer. Due to the resonant properties of the plane-parallel wafer, the directivity pattern of its thermal radiation has lobes. The width and number of the lobes in the radiation pattern are governed by the optical parameters of the wafer. The experimental data of the spectral dependences of the thermal radiation and its angular distributions agree well with the theoretical data. The results of this study can be used to design new controlled IR-radiation sources.

REFERENCES

1. P. J. Hesketh, J. N. Zemel, and B. Gebhart, Nature **325**, 549 (1986); Phys. Rev. B **37**, 10803 (1988).
2. J. Le Gall, M. Oliver, and J.-J. Greffet, Phys. Rev. B **55**, 10105 (1997).
3. J.-J. Greffet, R. Carminati, K. Joulain, *et al.*, Nature **416**, 61 (2002).
4. N. A. Vlasenko, V. K. Miloslavskiĭ, and I. N. Shklyarevskiĭ, Opt. Spektrosk. **11**, 403 (1961).
5. T. Weber, H. Stoltz, W. von der Ostern, *et al.*, Semicond. Sci. Technol. **10**, 1113 (1995).
6. V. S. Pekar, Zh. Éksp. Teor. Fiz. **67**, 471 (1974) [Sov. Phys. JETP **40**, 233 (1975)]; Zh. Éksp. Teor. Fiz. **88**, 667 (1985) [Sov. Phys. JETP **61**, 392 (1985)].
7. A. I. Liptuga and N. B. Shishkina, Infrared Phys. Technol. **44**, 85 (2003).
8. L. D. Landau and E. M. Lifshitz, *Course of Theoretical Physics*, Vol. 8: *Electrodynamics of Continuous Media*, 2nd ed. (Nauka, Moscow, 1982; Pergamon, New York, 1984).
9. T. S. Moss, G. J. Burrel, and B. Ellis, *Semiconductor Opto-Electronics* (Butterworths, London, 1973; Mir, Moscow, 1976).
10. P. I. Baranskiĭ, V. P. Klochkov, and I. V. Potykevich, *Semiconductor Electronics* (Naukova Dumka, Kiev, 1975).
11. Yu. I. Ukhanov, *Optical Properties of Semiconductors* (Nauka, Moscow, 1977).
12. T. Ashley, C. T. Elliott, N. T. Gordon, *et al.*, Appl. Phys. Lett. **64**, 2433 (1994).
13. R. M. Mindock, Proc. SPIE **783**, 77 (1987).
14. A. I. Liptuga and V. K. Malyutenko, Avtometriya **6**, 108 (1991).

Translated by V. Bukhanov

Semiconductors, Vol. 38, No. 5, 2004, pp. 512–513. Translated from Fizika i Tekhnika Poluprovodnikov, Vol. 38, No. 5, 2004, pp. 529–531.

ELECTRONIC AND OPTICAL PROPERTIES OF SEMICONDUCTORS

Nonlinear Absorption of Light by $Zn_{0.37}Cd_{0.63}Se$ Solid Solutions

A. Baĭdullaeva, A. I. Vlasenko, P. E. Mozol', and L. F. Shcherbonos

Institute of Semiconductor Physics, National Academy of Sciences of Ukraine, Kiev, 03028 Ukraine

e-mail: baidulla@yahoo.com

Received September 22, 2003; accepted for publication October 17, 2003

Abstract—Nonlinear absorption spectra of $Zn_{0.37}Cd_{0.63}Se$ crystals were measured using the method of two light sources. At high levels of excitation by neodymium laser pulses, both fundamental two-photon absorption and absorption by excess free carriers are observed. At low excitation, impurity centers with energy levels spaced 0.72, 0.63, 0.53, 0.42, 0.36, 0.25, and 0.20 eV from the edge of the band gap are detected. © *2004 MAIK "Nauka/Interperiodica".*

The development of high-intensity tunable laser sources has stimulated further advances in the main areas of the classical spectroscopy of solids and revealed fundamentally new possibilities of spectroscopic methods.

The laser-induced excitation of crystals under the condition $\hbar\omega > \Delta_{CV}/2$, where Δ_{CV} is the band-gap width, is known to result not only in two-photon absorption (TPA) but also in a number of other competitive intense nonlinear absorption processes, such as (1) two-stage transitions (TSTs) via local deep levels of impurities or defects in the band gap; (2) absorption by excess free carriers excited during the TPA process; and (3) stimulated absorption and stimulated blooming induced by a change in the population of the impurity levels [1].

The superposition of all these effects hinders the interpretation of experimental data on changes in the intensity of radiation that passes through a crystal. However, investigation of these effects may provide new information on the impurity centers and the energy spectrum of the crystal.

Nonlinear absorption spectra can be studied by analyzing the dependence $\beta = f(2\hbar\omega - \Delta_{CV})$ as a function of photon energy, where $\beta = KI^{-1}$ is the nonlinear absorption coefficient, I is the intensity of radiation, and K is the absorption factor.

One technical difficulty of this method lies in obtaining light beams with isotype parameters at different photon energies. Moreover, the result significantly depends on the statistical properties of light [2, 3] and on possible manifestations of size effects [4].

The possibilities of studying the nonlinear absorption spectra by varying the band gap width Δ_{CV} are also limited since a considerable change in Δ_{CV} can be attained only for crystals of solid solutions, for example, Cd_xSe_{1-x}, $Zn_xCd_{1-x}Se$.

The method of two light sources is considered the most informative technique. This method uses a beam of high-intensity laser radiation at a given photon energy $\hbar\omega_1$ and a beam of broadband radiation of lower intensity, from which an almost monochromatic beam with a variable photon energy $\hbar\omega_2$ is selected [5].

On the basis of experimental data, the absorption factor $K(\omega_2)$ can be determined as

$$K(\omega_2) = \frac{1}{X}\ln\frac{1}{[1 + \Delta I(\omega_2)/I_0(\omega_2)]}, \qquad (1)$$

where $\Delta I(\omega_2) = I(\omega_2) - I_0(\omega_2)$; $I_0(\omega_2)$ and $I(\omega_2)$ are the intensities of light incident on the sample surface at the instants $t = 0$ and $t > 0$, respectively; and X is the sample thickness. Taking into account that $\Delta I/(\omega_2)/I_0(\omega_2) = \Delta h(\omega_2)/h_0(\omega_2)$, where $h_0(\omega_2)$ is the deviation of the electron beam on the oscilloscope display from the zero level induced by the probe beam at $t = 0$ and $\Delta h(\omega_2)$ is the deviation of the electron beam from $h_0(\omega_2)$ at $t > 0$, we obtain the expression for the calculations in the form

$$K(\omega_2) = \frac{1}{X}\ln\frac{1}{[1 + \Delta h(\omega_2)/h_0(\omega_2)]}. \qquad (2)$$

It is known that II–VI solid solutions are widely used in the production of planar optical waveguides, which are thin-film analogs of optical fibers in integrated optics. Therefore, it is of interest to investigate the nonlinear absorption spectra of $Zn_{0.37}Cd_{0.63}Se$ exposed to high-intensity laser radiation with photon energy $\hbar\omega_1 = 1.17$ eV and pulse width $1.5 \cdot 10^{-8}$ s.

Figure 1 shows the experimental dependences of the absorption factor of two $Zn_{0.37}Cd_{0.63}Se$ crystals (with a band-gap width of 2.16 eV) from different growth cells versus the probe photon energy $\hbar\omega_2$ for linear polarization and the $\hbar\omega_1$-beam intensity equal to 7 (curve *1*) and 17 (curve *2*) MW/cm^2. Each point of the spectra was obtained by averaging over a large amount of experimental data.

It can be seen that, at a lower level of laser illumination (curve *1*), the nonlinear absorption spectrum shows seven peaks with amplitudes that are different for samples taken from different sets.

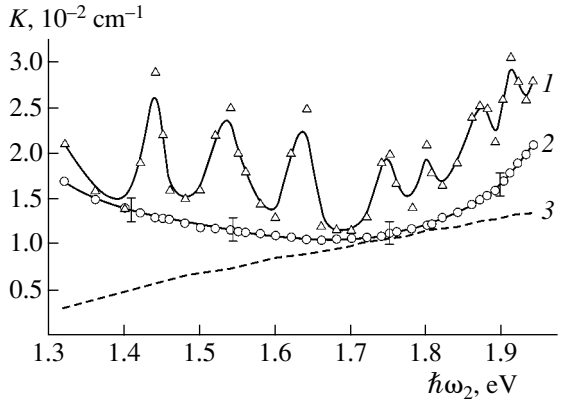

Fig. 1. Absorption spectra of $Zn_{0.37}Cd_{0.63}Se$ for a laser pulse power of (*1*) 7 and (*2*) 17 MW/cm^2; (*3*) calculation of the fundamental two-photon absorption.

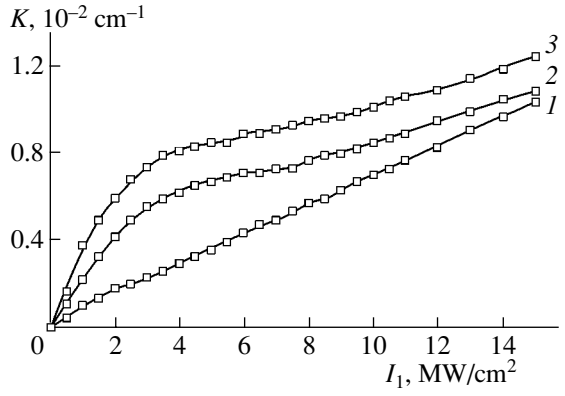

Fig. 2. Absorption factor K vs. the intensity of neodymium laser radiation for probe photon energy $\hbar\omega_2$ = (*1*) 1.75, (*2*) 1.55, and (*3*) 1.43 eV.

When the intensity of laser radiation is as high as 17 MW/cm^2, a smooth curve of nonlinear absorption is observed. The absorption by excess free carriers manifests itself when the photon energies $\hbar\omega_2$ are less than 1.75 eV. Impurity and (or) defect levels in the band gap can be involved in the TPA both as virtual and real states. In the former case, fundamental TPA occurs; in the latter, a resonant TPA or TST process.

One of the simplest ways to separate TPA and TST is to analyze the time change in the shape of the probe pulse with frequency $\hbar\omega_2$. Its relaxation after the laser irradiation is switched off indicates the occurrence of TST. However, the shape of the additional reduction in time of the probe-beam intensity is often identical to the laser pulse shape within the entire spectral range. Thus, these data appeared to be insufficient to separate the processes under study. To improve the situation, we also measured the dependences $K = f(I_1)$, where I_1 is the intensity of radiation with $\hbar\omega_1$, for different photon energies $\hbar\omega_2$. The resulting curves are shown in Fig. 2. At $\hbar\omega_2$ = 1.75 eV, the dependence is linear, which may be indicative of a fundamental TPA process. At lower energies $\hbar\omega_2$, the dependences are nonlinear, which indicates resonant TST or TPA processes.

The dependence $K = f(\hbar\omega_2)$ calculated for the case of a fundamental TPA process and allowed–forbidden transitions taking account of the Coulomb electron–hole interaction is shown in Fig. 1 (curve *3*).

When the level of excitation $\hbar\omega_1$ is low, the real levels that are present in the band gap of $Zn_xCd_{1-x}Se$ give rise to a resonance increase in nonlinear absorption in the form

$$\frac{1}{\Delta_i - \hbar\omega_2 - (\mu/m_V)(\hbar\omega_1 + \hbar\omega_2 - \Delta_{CV})},$$

$$\mu = \left(\frac{1}{m_V} - \frac{1}{m_C}\right)^{-1},$$

where Δ_i is the depth of the impurity level in the band gap and m_C and m_V are the effective masses of electrons and holes, respectively [6, 7].

Using the peaks in the nonlinear absorption curve obtained at low excitation, we estimated the energies of the deep levels in the band gap with an accuracy up to the term $(\mu/m_V)(\hbar\omega_1 + \hbar\omega_2 - \Delta_{CV})$: 0.72, 0.63, 0.53, 0.42, 0.36, 0.25, and 0.20 eV. Note that the bands at 0.72 and 0.36 eV in the nonlinear absorption spectrum of $Zn_{0.37}Cd_{0.63}Se$ coincide in position with the energy levels of copper in ZnSe. The value of 0.42 eV is close to the energy of spin–orbital splitting of the valence band in ZnSe [6].

Since the nonlinear absorption signal repeats the laser pulse shape, these levels can act as fast nonradiative recombination centers, thus hindering the observation of photoluminescence in these crystals.

Thus, the method of two light sources proved to be the most informative way to study the nonlinear absorption processes in crystals under laser excitation and to obtain new data on the impurity centers and band structure of the crystals.

REFERENCES

1. P. E. Mozol', I. I. Patskun, E. A. Sal'kov, and L. S. Martsenyuk, Fiz. Tekh. Poluprovodn. (Leningrad) **17**, 1861 (1983) [Sov. Phys. Semicond. **17**, 1188 (1983)].
2. B. R. Mollow, Phys. Rev. **175**, 1555 (1968).
3. D. A. Kleiman, R. C. Miller, and W. A. Nordland, Appl. Phys. Lett. **23**, 243 (1973).
4. I. P. Herman and J. Ducuing, Phys. Rev. A **5**, 2557 (1972).
5. P. E. Mozol', I. I. Patskun, E. A. Sal'kov, *et al.*, Fiz. Tekh. Poluprovodn. (Leningrad) **14**, 902 (1980) [Sov. Phys. Semicond. **14**, 532 (1980)].
6. E. J. Johnson, in *Semiconductors and Semimetals*, Vol. 3: *Optical Properties of III–V Compounds*, Ed. by R. Willardson and A. Beer (Academic, New York, 1967; Mir, Moscow, 1970).
7. V. I. Bredikhin and V. N. Galkin, Fiz. Tverd. Tela (Leningrad) **13**, 1329 (1971) [Sov. Phys. Solid State **13**, 1110 (1971)].

Translated by A. Sidorova

Semiconductors, Vol. 38, No. 5, 2004, pp. 514–519. Translated from Fizika i Tekhnika Poluprovodnikov, Vol. 38, No. 5, 2004, pp. 532–537.

ELECTRONIC AND OPTICAL PROPERTIES OF SEMICONDUCTORS

Mobility of Minority Charge Carriers in *p*-HgCdTe Films

V. S. Varavin*, S. A. Dvoretskiĭ*, V. Ya. Kostyuchenko, V. N. Ovsyuk*, and D. Yu. Protasov*^**

**Institute of Semiconductor Physics, Siberian Division, Russian Academy of Sciences, pr. Akademika Lavrent'eva 13, Novosibirsk, 630090 Russia*

^e-mail: protasov@thermo.isp.nsc.ru

***Siberian State Geodesy Academy, Novosibirsk, 630108 Russia*

Submitted September 23, 2003; accepted for publication October 17, 2003

Abstract—Temperature dependences of electron mobility in *p*-$Hg_{1-x}Cd_xTe$ films (x = 0.210–0.223) grown by molecular beam epitaxy are investigated. In the temperature range 125–300 K, mobility was found by the mobility-spectrum method, and for the range 77–125 K, it was found using a magnetophotoconductivity method suggested in this study. The method is based on the measurement of the magnetic-field dependence of photoconductivity. The magnetic field is parallel to the radiation and normal to the sample surface. The electron mobility is determined using the simple expression μ_n [m^2/(V s)] = 1/B_H [T]. Here, B_H is the induction of the magnetic field corresponding to a half-amplitude of the photoconductivity signal under zero magnetic field. In the temperature range 100–125 K, the results obtained by the magnetophotoconductivity and mobility-spectrum methods coincide. For the samples investigated, the electron mobility at 77 K is in the range 5–8 m^2/(V s).

1. INTRODUCTION

$Hg_{1-x}Cd_xTe$ solid solution (cadmium–mercury telluride, CMT) is one of main materials for detectors of infrared (IR) radiation in a wide wavelength range from the near-IR region (1–2 μm) to the far-IR region (8–12 μm). One of the main parameters of the material that largely determines the characteristics of photodetectors is the diffusion length of minority carriers, which in turn depends on their mobility. Therefore, minority-carrier mobility can be used to evaluate the suitability a material for the fabrication of photodetectors with required characteristics. Knowledge of the mobility is also necessary in analyzing the measurements of the steady-state lifetime, which along with mobility determines the diffusion length.

To determine the minority-carrier mobility in *p*-CMT grown by different methods, a series of methods is developed. For example, the mobility and concentration of equilibrium minority carriers were determined by the method of multiband fitting of theoretical magnetic-field dependences of the Hall coefficient and magnetoresistance to the experimental data. More sophisticated methods of analysis of similar measurements are the mobility-spectrum method [4–6] and the quantitative mobility-spectrum method [7]. These methods allow one to determine the mobility and concentration of carriers without preliminary knowledge of the number of carrier types in the sample under investigation. However, for temperatures (T) at which the electron concentration becomes too low, which is observed at T < 100 K for *p*-CMT with x = 0.22, these methods yield a large error [8].

The differential methods based on determining the electron mobility from the peak position in the derivative of magnetoresistance with respect to the magnetic field [9] or from the reflectance module for the microwave signal [10] are more sensitive. In these methods, the equilibrium minority-carrier mobility is measured. Therefore, the temperature region of their application is restricted because the carriers are frozen when the sample is cooled. The complexity of the experimental equipment used should also be noted.

The electron mobility in *p*-CMT was also determined from measurements of the photomagnetic effect [11], photomagnetic effect and photoconductivity [12], and photo-Hall measurements [13]. Since the mobility of nonequilibrium photoexcited carriers was measured in this case, these methods can be used at lower temperatures. The carrier mobility is found by fitting the theoretical expressions describing the effects listed to the experimental data. The disadvantage of these methods consists in the fact that a large number of simultaneously fitted parameters (as many as six) are used, which decreases the reliability of the data obtained. The method of determining electron mobility from photo-Hall magnetic-field dependences was suggested in [14]. At low temperatures, when the electron concentration is much lower than the hole concentration, the voltage measured is described by the expression

$$\Delta U_H = \frac{k(\mu_p, \mu_n, p, \langle \hat{p} \rangle)B}{1 + \mu_n^2 B^2}, \qquad (1)$$

where μ_p and μ_n are the hole and electron mobilities, p and $\langle \hat{p} \rangle$ are the concentrations of equilibrium and nonequilibrium holes, and k is the proportionality coefficient independent of the magnetic field B. From the slope of the straight line plotted in the coordinates $B/\Delta U_H$ versus B^2, the electron mobility can be found by fitting. In this method, two parameters are also fitted simultaneously, i.e., the electron mobility and hole concentration averaged by the sample thickness, which decreases the accuracy of fitting.

We suggested a direct method of determining minority-electron mobility based on the measurements of magnetic-field dependences of photoconductivity in the geometry of the Hall effect (magnetophotoconductivity, MPC). Using this method, we plotted the temperature dependences of the electron mobility for *p*-CMT films.

2. EXPERIMENTAL

Samples prepared from films grown by molecular beam epitaxy on GaAs(013) substrates were investigated [15]. The films' thickness was 7–10 μm, and the composition corresponded to x = 0.21–0.23. After growth, the samples had *n*-type conduction, and they were annealed in helium to convert them to *p*-type conduction. High-quality photodetectors were fabricated using similar samples [16, 17]. The parameters of the samples (composition, film thickness d, hole concentration p, and mobility μ_p) are given in Table 1.

To measure MPC, the Hall effect, and magnetoresistance, samples were cut out in the form of rectangular strips 10 mm long and 1.5 mm wide. Then the samples were mounted on a sapphire substrate, and indium contacts were formed. The sample geometry is shown in Fig. 1.

For four CMT samples, the magnetic-field dependences of the MPC signal were measured in the temperature range T = 77–125 K. The Hall effect and magnetoresistance were measured at T = 77–300 K. For temperatures of 77–125 K, the electron mobility was determined from the analysis of MPC, and at higher temperatures it was determined by the mobility-spectrum method.

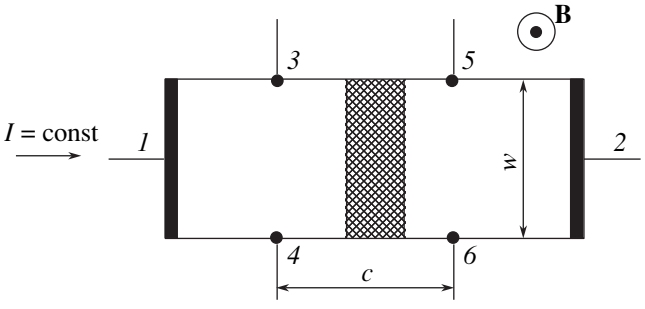

Fig. 1. Schematic representation of magnetophotoconductivity measurements. The illuminated part of the sample is hatched. The current *I* passes through the contacts *1* and *2*; magnetophotoconductivity and magnetoresistance are measured using contacts *3* and *5* or *4* and *6*; the Hall effect is measured using contacts *3* and *4* or *5* and *6*.

Table 1. Parameters of CMT samples

Sample	Composition, x	d, μm	p, 10^{22} m^{-3}	μ_p, $m^2/(V\ s)$
971124	0.220	7.7	0.94	0.036
001123	0.215	7.1	6.3	0.026
010629-1	0.210	9.5	2.3	0.032
020528	0.223	8.75	1.3	0.040

The layout of the setup used to measure the Hall effect, magnetoresistance, and MPC is shown in Fig. 2. Sample *1* in liquid-nitrogen cryostat *2* was placed between the poles of electromagnet *3*. The induction of the magnetic field varied from 0 to 2 T. Its magnitude was measured using Hall sensor *4* powered from source *5*. To measure the Hall effect, magnetoresistance, and MPC, the dc current from source *7* was passed through the sample. The position K_1 of a switch K corresponds to the measurement of the Hall effect and magnetoresistance. To measure MPC (the position K_2 of the switch K), the sample was additionally illuminated using LED *10* (wavelength $\lambda \approx 0.94$ μm), powered by an ac voltage generator *11*. The signal measured was detected using lock-in amplifier *12* at the reference frequency of generator *11*. The sample temperature was varied from 77 to 300 K using heater *8* and temperature controller *9*. The signals from the sample and the Hall sensor were recorded using a computer.

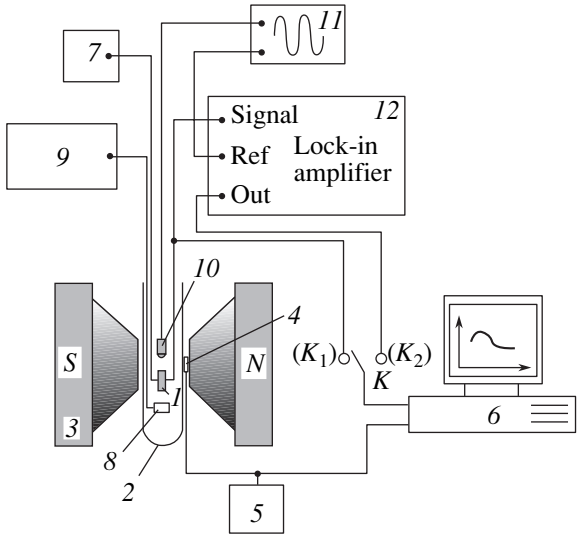

Fig. 2. Experimental setup.

3. THEORY

For the samples shaped like a Hall bridge and subjected to electric and magnetic fields directed as shown in Fig. 1, the longitudinal voltage U_σ measured from contacts *3* and *5* (or *4* and *6*) in the ac generator mode is given by the expression [18]

$$U_\sigma(B) = \frac{cI}{wd}\frac{1}{\sigma(B)}, \tag{2}$$

where c is the distance between potential contacts *3* and *5* (or *4* and *6*), w and d are the sample width and thickness, and I is the current across the sample.

The expression for conductivity in the magnetic field with the presence of electrons and holes takes the form [18]

$$\sigma(B) = q\left[\frac{n^2\mu_n^2(1+\mu_p^2B^2)+p^2\mu_p^2(1+\mu_n^2B^2)}{n\mu_n(1+\mu_p^2B^2)+p\mu_p(1+\mu_n^2B^2)} + \frac{2np\mu_n\mu_p(1-\mu_n\mu_pB^2)}{n\mu_n(1+\mu_p^2B^2)+p\mu_p(1+\mu_n^2B^2)}\right], \tag{3}$$

where p and n are the concentrations of electrons and holes, and μ_p and μ_n are the mobilities of electrons and holes, respectively.

The conductivity of the sample varies due to the generation of nonequilibrium carriers by light. The light is directed onto the sample through a narrow rectangular diaphragm that excludes the effect of the contacts, since the distance from the diaphragm edges to contacts considerably exceeds the diffusion length of nonequilibrium carriers. In contrast to [14], the measurement of MPC does not require uniform exposure of the sample as a whole.

For a small variation in the carrier concentration (Δn, Δp), the increment of longitudinal voltage can be obtained by expanding expression (2) into the series and retaining the term proportional to the variation in mobility $\Delta\sigma$,

$$\Delta U_\sigma(B) = -\frac{cI}{wd}\frac{\Delta\sigma(B)}{\sigma^2(B)}. \tag{4}$$

To find $\Delta\sigma(B)$, let us substitute $n = n_0 + \Delta n$, $p = p_0 + \Delta p$ (n_0 and p_0 are the equilibrium concentrations of electrons and holes) in formula (3). Since the excitation level is low, we may disregard the terms of the order Δn^2, Δp^2, and $\Delta n\Delta p$; as a result, we obtain

$$\Delta\sigma(B) = 2q\frac{n_0\Delta n\mu_n^2(1+\mu_p^2B^2)+p_0\Delta p\mu_p^2(1+\mu_n^2B^2)}{n_0\mu_n(1+\mu_p^2B^2)+p_0\mu_p(1+\mu_n^2B^2)} + \frac{(n_0\Delta p+p_0\Delta n)\mu_n\mu_p(1-\mu_n\mu_pB^2)}{n_0\mu_n(1+\mu_p^2B^2)+p_0\mu_p(1+\mu_n^2B^2)} - \sigma_0(B)\frac{\Delta n\mu_n(1+\mu_p^2B^2)+\Delta p\mu_p(1+\mu_n^2B^2)}{n_0\mu_n(1+\mu_p^2B^2)+p_0\mu_p(1+\mu_n^2B^2)}. \tag{5}$$

At low temperatures, when $n_0 \ll p_0$, and for values of induction of the magnetic field for which $\mu_p^2B^2 \ll 1$ and $\mu_n\mu_pB^2 \ll 1$, expression (5) can be written in the form

$$\Delta\sigma(B) = \frac{q}{1+\mu_n^2B^2}[\Delta n\mu_n + \Delta p\mu_p(1+\mu_n^2B^2)]. \tag{6}$$

For *p*-CMT, the main recombination mechanism at low temperatures is the recombination through the traps [19]. Then, for the steady-state case, the electroneutrality equation can be written as

$$\Delta n(1+K) = \Delta p, \tag{7}$$

where K is the coefficient characterizing the variation in the electron concentration at the traps. In this case, the expressions for $\Delta\sigma(B)$ and $\Delta U_\sigma(B)$ can be written as

$$\Delta\sigma(B) = \frac{q\Delta n\mu_n}{1+\mu_n^2B^2} + q\Delta n\mu_pK, \tag{8}$$

$$\Delta U_\sigma(B) = -\frac{cI}{wd}\frac{\Delta n}{q}\frac{\mu_n}{p_0^2\mu_p^2(1+\mu_n^2B^2)} - \frac{cI}{wd}\frac{\Delta n}{q}\frac{K}{p_0^2\mu_p}. \tag{9}$$

As one can see from expression (9), allowance made for the effect of traps leads to the emergence of an additional term that is independent of the magnetic field. Since the magnitude of this term is smaller than the MPC signal in the absence of magnetic field by a factor of $\mu_n/\mu_p \approx 100$, it can be discarded:

$$\Delta U_\sigma(B) = \frac{cI}{wd}\frac{\Delta n}{q}\frac{-\mu_n}{p_0^2\mu_p^2(1+\mu_n^2B^2)} = \frac{\Delta U_\sigma(0)}{(1+\mu_n^2B^2)}. \tag{10}$$

The mobility can be determined from the magnetic-field dependence of the signal $\Delta U_\sigma(B)$, which is described by expression (10). For this purpose, the magnetic induction B_H corresponding to the signal level $\Delta U_\sigma(0)/2$ should be measured. At this point, the condition $1 + \mu_n^2B_H^2 = 2$ is met; as a result, the formula for mobility is easily derived:

$$\mu_n\ [\mathrm{m^2/(V\ s)}] = 1/B_H\ [\mathrm{T}]. \tag{11}$$

The error in determining the mobility includes four components. These are the error in determining the magnetic induction B_H, the error in determining half of the photoconductivity signal $\Delta U_\sigma(B)/\Delta U_\sigma(0) = 1/2$, the error caused by the presence of more than two types of

carriers in the sample, and the error associated with the violation of the condition $n_0 \ll p_0$.

Since the form of expression (10) is simple, it is possible to show that the first two errors are small and are no greater than a few percent.

When deriving formula (10), we assumed that only two types of carriers exist in the sample, namely, electrons and heavy holes. It is known from studies [1, 2, 6] that, along with heavy holes with the concentration p_h, light holes with the concentration p_l exist in CMT. Numerical calculations showed that the effect of light holes on MPC becomes noticeable at the concentration $p_l = 0.05p_h$, which considerably exceeds their actual concentration ($p_l \le 0.001p_h$ according to the data [1]). Consequently, when analyzing MPC, the effect of light holes can be disregarded.

Violation of the condition $n_0 \ll p_0$ affects the mobility measured to a much greater extent. To determine the temperature dependence of the error, numerical calculations were carried out. It is found that the error is strongly temperature-dependent. At 77–90 K, it is very small, specifically, less than 1%. At 100 K, this error is 2% and increases to 22% at 125 K. Let us estimate the limiting error for this temperature. Figure 3 shows the theoretical dependence $\Delta U_\sigma(B)$ (solid line). This dependence was calculated with formulas (2) and (5) under the following conditions: $x = 0.21$, $T = 125$ K, $p = 2.3 \times 10^{22}$ m^{-3}, $\mu_p = 0.03$ m^2/(V s), and $\mu_n = 4.0$ m^2/(V s). The dashed curve is obtained using formula (10) for $\mu_n = 3.3$ m^2/(V s). As can be seen from Fig. 3, the magnetic-field dependence $\Delta U_\sigma(B)$ calculated with formulas (2) and (5) is well described by formula (10), although for another value of mobility. As a result, the error in determining the mobility from relationship (11) arises. The error is systematic and causes a decrease in the determining electron mobility.

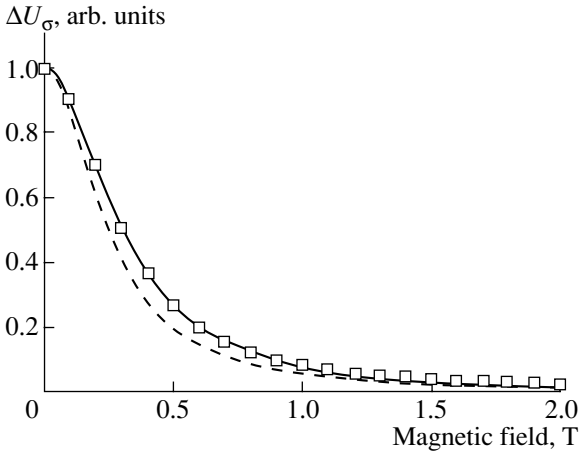

Fig. 3. Deviation of $\Delta U_\sigma(B)$ in approximation (10) from the calculation by formulas (2) and (5). The solid line represents the calculation by formulas (2) and (5); the dashed line represents the calculation by formula (10) for the electron mobility $\mu_n = 4.0$ m^2/(V s). Squares correspond to the calculation by formula (10) for the electron mobility $\mu_n = 3.3$ m^2/(V s).

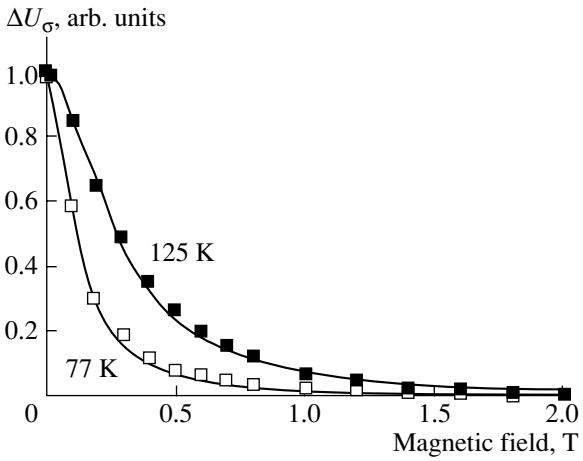

Fig. 4. Magnetophotoconductivity for sample 010629-1 at 77 and 125 K. Squares correspond to the experiment; lines represent the calculation from formula (10).

4. RESULTS

Figure 4 shows the results of MPC measurements (the $\Delta U_\sigma(B)$ signal) for sample 010129-1 at 77 and 125 K. Plotted theoretical curves calculated from formula (10) include experimental points. The electron mobility determined from formula (11) is $\mu_n = 8.1$ m^2/(V s) at 77 K and 3.6 m^2/(V s) at 125 K.

One can see from Fig. 4 that, at 77–125 K, the experimental data are well described by expression (10). Compared with 77 K, the MPC signal at $T = 125$ K decreases more slowly as the magnetic field increases due to a decrease in the electron mobility.

At 100–130 K, the mixed conduction is observed for *p*-CMT with $x = 0.22$, and the parameters of nonequilibrium carriers can be determined using the mobility-spectrum method. The electron mobilities determined by various methods were compared for sample 971124. Figure 5 shows the mobility spectra for this sample. The carrier mobility is along the abscissa, and the conductivity is along the ordinate. Carriers manifest themselves in the spectrum by forming the conductivity peaks. The carrier mobility is determined from the peak position, and the concentration is determined from the peak height. The electron mobility is taken as negative, and the hole mobility is taken as positive. In Fig. 5, the highest peak in the region of low positive mobilities corresponds to majority carriers, specifically, heavy holes. At 100 and 125 K, the positions of electron peaks are indicated by arrows. No electron peak is observed in the spectrum at 77 K since the electron concentration is too low.

The electron mobilities for all the samples studied at 100 and 125 K, which were determined by the MPC and mobility spectrum methods, are listed in Table 2.

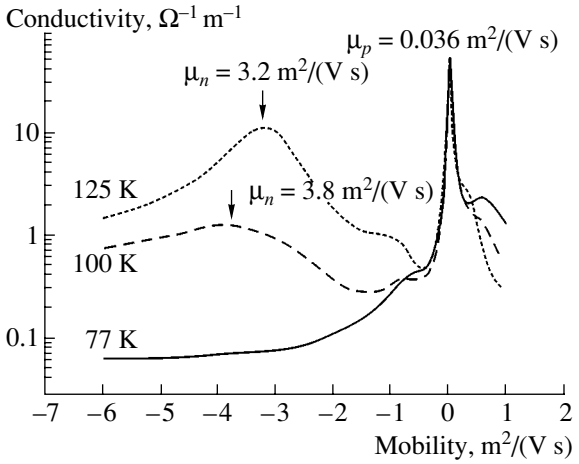

Fig. 5. Mobility spectra for sample 971124. Mobilities corresponding to spectral peaks are indicated.

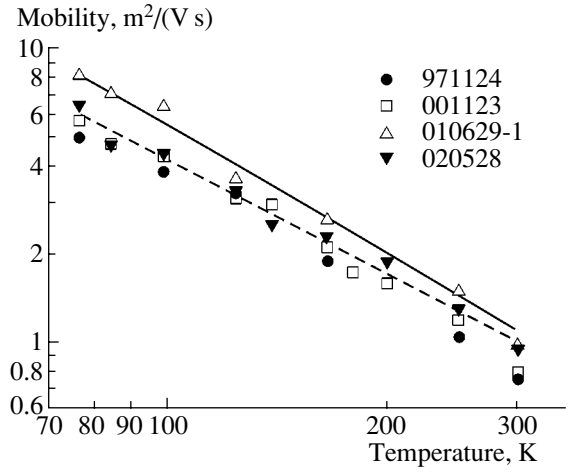

Fig. 6. Temperature dependences of mobility. The solid line is the law $T^{-1.5}$ for sample 010629-1; the dashed line, the law $T^{-1.3}$ for sample 020528.

As can be seen from Fig. 5 and Table 2, the results obtained by different methods agree well with each other; i.e., the mobilities of nonequilibrium minority carriers coincide with the mobility of equilibrium carriers. At temperatures higher than 77 K, lattice scattering is dominant in CMT [20] and photoexcited electrons lose the excess energy in a short time (compared to the electron lifetime) and become indistinguishable from equilibrium electrons.

Table 2. Electron mobilities

Sample	μ_n, m²/(V s)			
	mobility spectrum	MPC	mobility spectrum	MPC
	100 K		125 K	
971124	3.8	3.7	3.2	3.1
001123	–	4.3	3.1	3.2
010629-1	–	6.3	4.2	3.7
020528	–	4.4	3.0	3.3

Figure 6 shows the temperature dependences of the electron mobility. In the temperature range 77–125 K, the mobility was determined from MPC measurements, and in the range 140–300 K, it was determined from the mobility spectrum.

It is well known (see, for example, [21]) that the temperature dependence of mobility in the case of lattice scattering follows the law T^{-m}, where $m = 1.5$–2 [22]. It turned out that the temperature dependence of electron mobility for sample 010629-1 follows the law $\mu_n \propto T^{-1.5}$ (the solid line in Fig. 6). For three other samples, it follows the law $\mu_n \propto T^{-1.3}$ (the dashed line in Fig. 6 plotted for sample 020528). The exponent m is out of the range given in [22]. This is apparently caused by the fact that the approximation was carried out in a wide range (77–300 K). In the vicinity of 77 K, the mobility starts to be affected by scattering by ionized impurities, which follows the law $\propto T^{3/2}$. As follows from the Matthiessen rule [21], this effect should decrease the total value of m. Therefore, the accuracy of the approximation decreases at high temperatures (~300 K), which is observed in Fig. 6.

5. CONCLUSION

The electron mobilities in *p*-CMT films with the composition $x = 0.210$–0.223 grown by molecular beam epitaxy are measured in the range 77–300 K.

To determine the electron mobility in the range 77–125 K, a direct method of determining the mobility from the magnetic-field dependence of photoconductivity is suggested. The error of the method depends on the measurement temperature. The error is a few percent in the range 77–100 K and is as large as 25% at 125 K. In the range 125–300 K, the electron mobility was determined by the mobility-spectrum method.

For the samples studied, the mobility at 77 K is in the range 5–8 m²/(V s). The temperature dependence of mobility follows the law T^{-m}, where $m = 1.3$–1.5.

In the region of mixed conductivity, the mobility of equilibrium electrons determined by the mobility-spectrum method coincides with the mobility of nonequilibrium electrons determined by the MPC method.

REFERENCES

1. M. C. Gold and D. A. Nelson, J. Vac. Sci. Technol. A **4**, 2040 (1986).
2. N. Z. Talipov, V. N. Ovsyuk, V. G. Remesnik, and V. V. Schaschkin, Mater. Sci. Eng. B **44**, 278 (1997).
3. P. Moravec, R. Grill, J. Franc, *et al.*, Semicond. Sci. Technol. **16**, 7 (2001).

4. W. A. Beck and J. R. Anderson, J. Appl. Phys. **62**, 541 (1987).
5. J. Antoszewski and L. Faraone, J. Appl. Phys. **80**, 3881 (1996).
6. Yongsheng Gui, Biao Li, Guozhen Zheng, *et al.*, J. Appl. Phys. **84**, 4327 (1998).
7. J. R. Meyer, C. A. Hoffman, J. Antoszewski, and L. Faraone, J. Appl. Phys. **81**, 709 (1997).
8. S. Barton, P. Capper, C. L. Jones, *et al.*, Semicond. Sci. Technol. **10**, 56 (1995).
9. V. N. Ovsyuk, D. Yu. Protasov, and N. Kh. Talipov, Avtometriya, No. 5, 99 (1998).
10. T. I. Baturina, P. A. Borodovski, S. A. Buldygin, and S. A. Studenikin, Mater. Sci. Eng. B **44**, 283 (1997).
11. G. Sarussi, A. Zemel, and D. Eger, J. Appl. Phys. **72**, 2312 (1992).
12. S. A. Studenikin, I. A. Panaev, V. Ya. Kostyuchenko, and Kh.-M. Z. Torchinov, Fiz. Tekh. Poluprovodn. (St. Petersburg) **27**, 748 (1993) [Semiconductors **27**, 409 (1993)].
13. C. A. Hoffman, J. R. Meyer, E. R. Youngdale, *et al.*, Phys. Rev. B **37**, 6933 (1988).
14. S. E. Schacham and E. Finkman, J. Appl. Phys. **60**, 2860 (1986).
15. Yu. G. Sidorov, S. A. Dvoretsky, N. N. Mikhailov, *et al.*, Proc. SPIE **4355**, 228 (2001).
16. V. V. Vasiliev, V. N. Ovsyuk, and Yu. G. Sidorov, Proc. SPIE **5065**, 39 (2001).
17. F. F. Sizov, V. V. Vasiliev, D. G. Esaev, *et al.*, Opto-Electron. Rev. **9** (4), 391 (2001).
18. E. V. Kuchis, *Galvanomagnetic Effects and Methods for Studying Them* (Radio i Svyaz', Moscow, 1990).
19. V. C. Lopes, A. S. Syllaios, and M. C. Chen, Semicond. Sci. Technol. **8**, 824 (1993).
20. Sang Dong Yoo and Kae Dal Kwack, J. Appl. Phys. **81**, 719 (1997).
21. F. J. Blatt, *Theory of Mobility of Electrons in Solids* (Academic, New York, 1957; Fizmatgiz, Moscow, 1963); Solid State Phys. **4**, 1999 (1957).
22. L. F. Lou and W. H. Frye, J. Appl. Phys. **56**, 2253 (1984).

Translated by N. Korovin

Semiconductors, Vol. 38, No. 5, 2004, pp. 520–523. Translated from Fizika i Tekhnika Poluprovodnikov, Vol. 38, No. 5, 2004, pp. 538–542.

ELECTRONIC AND OPTICAL PROPERTIES OF SEMICONDUCTORS

Optical Properties of Synthetic Diamond Single Crystals

A. V. Mudryĭ*^, T. P. Larionova*, I. A. Shakin*, G. A. Gusakov, G. A. Dubrov**, and V. V. Tikhonov****

**Institute of Solid State and Semiconductor Physics, Belarussian Academy of Sciences, ul. Brovki 17, Minsk, 220072 Belarus*

^e-mail: mudriy@ifttp.bas-net.by

***Institute of Applied Physical Problems, Belarussian State University, Minsk, 220108 Belarus*

Submitted October 7, 2003; accepted for publication October 17, 2003

Abstract—Synthetic diamond single crystals were grown by the thermal gradient method in a high-pressure apparatus in the presence of solvent catalysts (nickel, iron). Absorption, luminescence, and photoluminescence excitation measurements were performed in order to determine the nature of impurity–defect complexes in both as-grown crystals and crystals treated at high temperature ($T \approx$ 2000–2200 K) and high pressure ($P \approx$ 6.0–6.5 GPa). Different luminescence and absorption bands were assigned to impurity centers containing nitrogen and nickel atoms. © *2004 MAIK "Nauka/Interperiodica".*

1. INTRODUCTION

The combination of unique physical (optical, electrical, thermal, and mechanical) properties and the high radiative and chemical durability of diamond opens up wide possibilities for using this material in instrument making (optical windows, heat removal, ultraviolet and thermal sensors, detectors of ionizing radiation, active media for lasers, optoelectronic devices, and so on). However, the development of this line of research is hindered by the lack of high-quality crystals with the required parameters. In this context, the synthesis of large diamond single crystals with a high-quality structure, based on new processing techniques and complex research into the physical (primarily, optical) properties of the synthesized crystals, is an urgent scientific and engineering problem [1]. In this study, we report new experimental data obtained by studying the absorption, luminescence, and luminescence excitation spectra of synthetic diamonds grown under different conditions and subjected to thermobaric treatment in different modes.

2. EXPERIMENTAL

Diamond single crystals were synthesized by the thermal gradient method in the temperature range 1750–1800 K at pressures of ~(5.4–5.5) GPa in a split-sphere high-pressure apparatus. Single crystals 4–7 mm in diameter were grown in a Ni–Fe–C system. In some cases, a stabilizing thermobaric treatment of crystals was performed at temperatures in the range $T \approx$ (2000–2200) K and pressures $P \approx$ (6.0–6.5) GPa for 3–24 h. The initial crystals had a saturated yellow color. The optical properties of diamonds were investigated in a wide temperature range from 78 to 300 K by measuring the absorption in the wavelength range 0.2–25 μm, photoluminescence (PL), and luminescence excitation spectra in the range 0.2–2 μm. Absorption spectra in the range 0.2–3.0 μm were recorded on a Carry 500 UV-VIS-NIR double-beam spectrometer (Varian, United States) and, in the range 1.4–25 μm, on a Protege-460 Fourier spectrometer (Nicolet, United States). Photoluminescence spectra were measured on an MDR-23M monochromator with 600–1200 groove/mm gratings. An FÉU-83 (or FÉU-100) photomultiplier and germanium *p–i–n* diode, cooled to liquid-nitrogen temperature, were used as detectors of optical signals. A DKSÉL-1000 xenon lamp (power 1000 W) with a set of ultraviolet (UV) light filters served as the light source. When luminescence excitation spectra were recorded, the radiation of the xenon lamp, resolved by the MDR-12 diffraction monochromator, was focused on the sample under study.

3. RESULTS AND DISCUSSION

In our experiments, we recorded a number of strong PL bands, including the electronic–vibrational bands due to residual unintentional impurities (nitrogen, nickel, and so on) and intrinsic structural defects in the synthetic diamond crystals. As an example, Fig. 1 shows the typical PL spectra of as-grown diamond crystals (Figs. 1a, 1b, sample 1811) and crystals subjected to thermobaric high-temperature treatment at T = 2173 K and $P \approx$ 6.5 GPa for 16 h (Figs. 1c, 1d, sample 2005). As can be seen, the luminescence spectra of the samples under investigation contain a strong wide band *A* with a maximum in the wavelength range 510–540 nm (the photon energy 2.30–2.45 eV), which is characteristic of growth pyramids on octahedral faces. At room temperature, this band has an extended long-wavelength wing and a half-width of about 370 meV.

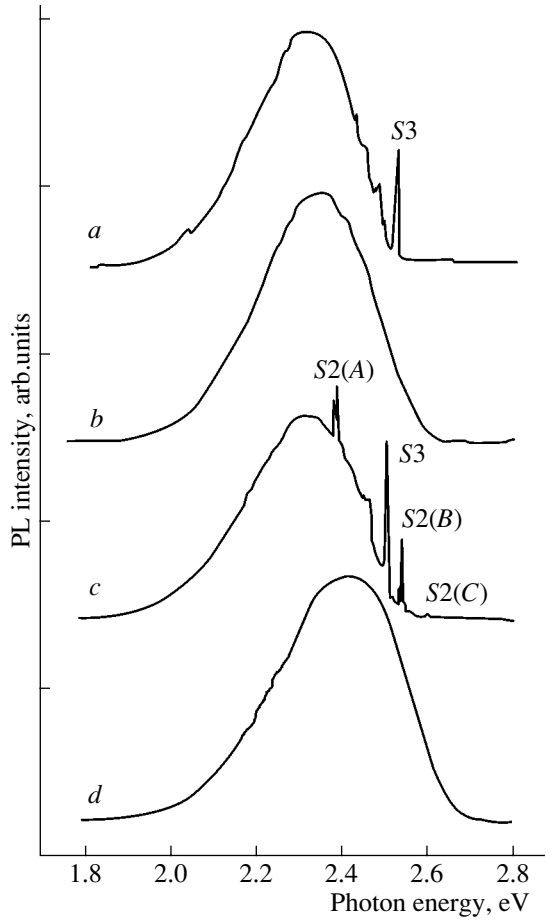

Fig. 1. PL spectra of diamond single crystals measured at (*a*, *c*) 78 and (*b*, *d*) 300 K. (*a*, *b*) Sample 1811 and (*c*, *d*) sample 2005.

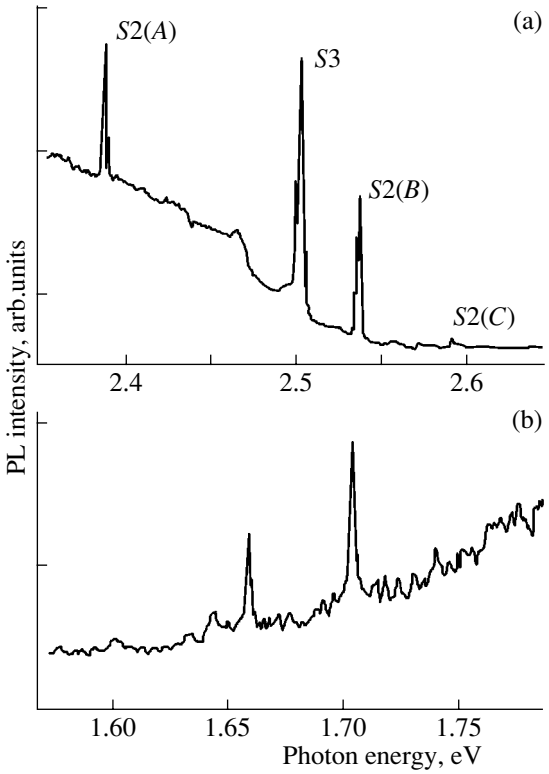

Fig. 2. Fine structure of the PL spectra of sample 2005 measured at 78 K. (a) and (b) show different spectral regions.

When the crystals are cooled to 78 K, an electronic–vibrational band with a leading zero-phonon line *S*3 at an energy (wavelength) of about 2.496 eV (496.7 nm) arises in the photoluminescence spectra. This line contains characteristic low-energy vibrational replicas at 2.457 eV (504.6 nm), 2.426 eV (511 nm), and 2.391 eV (518 nm). The energies of the corresponding phonons are 40, 70, and 105 meV, which is consistent with the data of [2–5]. The most distinct is the electronic transition involving a quasi-local phonon with an energy of ~40 meV (Fig. 2). The spectra also contain a weaker zero-phonon line at 2.621 meV (473.3 nm), which is due to the same luminescence center. In this case, the initial synthetic diamond crystals have a yellow-green saturated color. The experiments show that thermobaric high-temperature treatment at a pressure of 6.5 GPa and an annealing temperature of ~2173K for 20 h changes the color of synthetic diamonds: they become much lighter, with a characteristic soft green hue. The photoluminescence spectra of such crystals at liquid-nitrogen temperature show a richer quasi-linear structure, which is observed in the high-energy wing of the wide band. Several strong narrow zero-phonon lines are also observed in the luminescence spectra: *S*2(*A*) at ~2.369 eV (523.3 nm), *S*2(*B*) at ~2.535 eV (489.1 nm), *S*2(*C*) at ~2.594 eV (477.8 nm), and a number of weaker components associated with these lines, including vibrational replicas. The lines *A*, *B*, and *C*, observed after thermobaric treatment (see also the fine structure of the spectra in Fig. 2), can be assigned to the optical transitions in the electronic structure of so-called *S*2 centers [5]. It should be noted that the lines of the *S*2 group (*A*, *B*, *C*) also manifested themselves with a much lower intensity in the spectra of most of the starting synthetic diamonds under study. High-temperature thermobaric treatment of such samples led to an increase in the intensity of the *S*2 lines by a factor of 5–10. In general, these experiments showed that thermobaric treatment of diamonds leads to a significant increase in the intensity of both *S*3 and *S*2 electronic–vibrational bands. As was noted, an increase in the concentration of corresponding luminescence centers, *S*2 and *S*3, facilitates crystal bleach and enhances the luminescence intensity by a factor of 3–5 in comparison with starting samples at the same excitation levels. In our opinion, this fact indicates that annealing of nonradiative recombination centers takes place upon thermobaric treatment and active rearrangement of defects in a crystal matrix, which involves residual process impurities (mainly nitrogen and nickel). Previously, these luminescence centers were found in natural and synthetic diamonds and assigned to Ni atoms in a positively

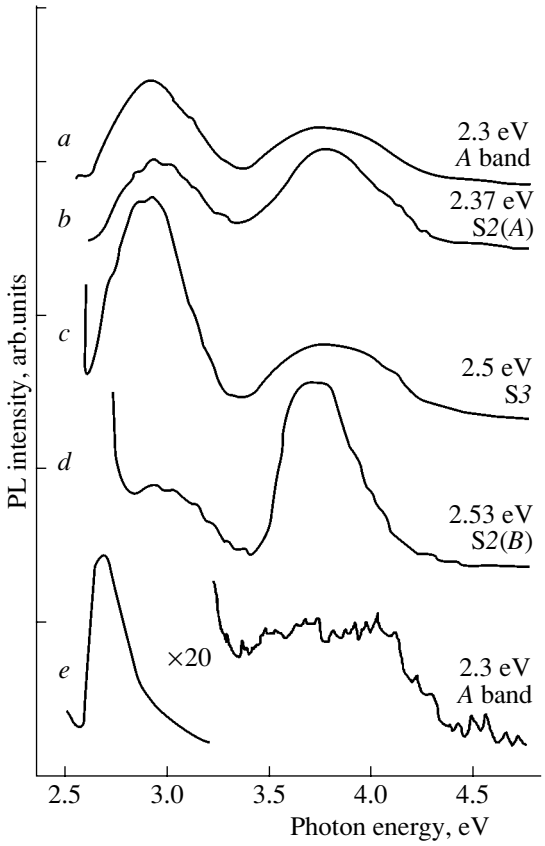

Fig. 3. Photoluminescence excitation spectra of diamond single crystals measured at 78 K. (*a–d*) Sample 2005 and (*e*) sample 1811. The photon energies at which the measurements were performed are indicated.

charged state (a positively charged Ni atom is associated with a divacancy and two or three neighboring N atoms in a complex) [2–5]. It is noteworthy that the relative intensity of the spectral groups *S*2 and *S*3 for different initial synthetic diamonds varied substantially: for example, in the PL spectra of sample 1811, the *S*2 system does not manifest itself at all (Fig. 1). Thermobaric treatment also significantly changes the relative ratio of the intensities of the spectral groups *S*2 and *S*3, although the general behavior of the spectra remains the same for all the treated samples (T = 2000–2200 K, $P \approx 6.5$ Gpa, 5–20 h). Nevertheless, the total increase and relative redistribution of the intensities of the electronic–vibrational bands *S*2 and *S*3 in the spectra indicates a significant transformation of defects containing Ni and N impurities, which leads to the change in the color of diamonds from saturated yellow-green to soft light green.

Figure 2b shows the long-wavelength region of the PL spectrum of sample 2005 that was subjected to thermobaric treatment. As can be seen, this spectral region contains a group of narrow lines at 1.704, 1.660, and 1.605 eV. Analysis of the relative intensities of these PL lines, in particular the lines at 1.704 and 1.660 eV, shows that they are dissimilar for different crystals and change with changing conditions of thermobaric treatment (temperature 2000–2200 K, pressure 6.5 GPa, duration 5–20 h). These facts indicate that the noted lines are due, at least, to several independent luminescence centers containing background Ni and N impurities. The fact that the intensities of the lines at 1.704 and 1.660 eV are significantly higher in the PL spectra measured from the region adjacent to the crystal seed supports the view that these lines should be assigned to nickel-containing (nitrogen-containing) centers. These lines were found previously [4–6] and also assigned to nickel-containing (nitrogen-containing) centers.

Figure 3 shows luminescence excitation spectra recorded for two samples with the photon energies corresponding to the maximum intensity of bands and lines; the values of the photon energies at which the measurements were performed are indicated. As can be seen, the spectra contain wide excitation bands with maxima at ~2.8 eV (440 nm) and 3.6 eV (340 nm), whose relative intensity is governed to a great extent by the measurement conditions, i.e., if they belong to the corresponding PL bands or not. These facts indicate that the *S*2 (*A*) and *S*2 (*B*) lines and the corresponding luminescence centers are independent; i.e., these lines can be assigned to two defects of different nature, which is consistent with the assumption made in [3]. The luminescence excitation spectrum of sample 1811 contains a radically different main excitation band peaked at 2.66 eV (485 nm) and a weak band in the vicinity of 3.6 eV (340 nm) (the ratio of the intensities of the bands at 2.66 and 3.6 eV was 1 : 20). The data reported for samples 2005 and 1811 are proof that thermobaric treatment leads to a significant transformation of the structural defects in diamond crystals, which is also confirmed by independent measurements of the absorption spectra of the samples in the UV and visible regions.

Figure 4 shows the infrared (IR) absorption spectra of diamond crystals, both initial and those treated at high temperatures and pressures. For convenience, the spectra are shifted with respect to each other along the vertical axis. As can be seen, the spectral range from 1500 to 3500 cm^{-1} contains wide bands due to the natural vibrations of the atoms of a diamond lattice. These bands do not change during thermobaric treatment. The group of bands in the frequency range 1000–1400 cm^{-1} is due to the vibrational modes of impurity N atoms incorporated in various defect complexes. The absorption band peaked at 1130 cm^{-1} corresponds to the *C* defect, which is a single substitutional N atom. The band peaked at 1280 cm^{-1} is due to the *A* defect, which is a pair of neighboring substitutional N atoms. Along with the bands due to the N impurity, the spectrum of initial crystals also contains a wide band peaked at ~860 cm^{-1}, which, according to data in [7, 8], is due to Me–*X* centers. These defects arise at the boundaries of microscopic inclusions of a metal–solvent (Me). The component *X* may be carbon and/or nitrogen. The main

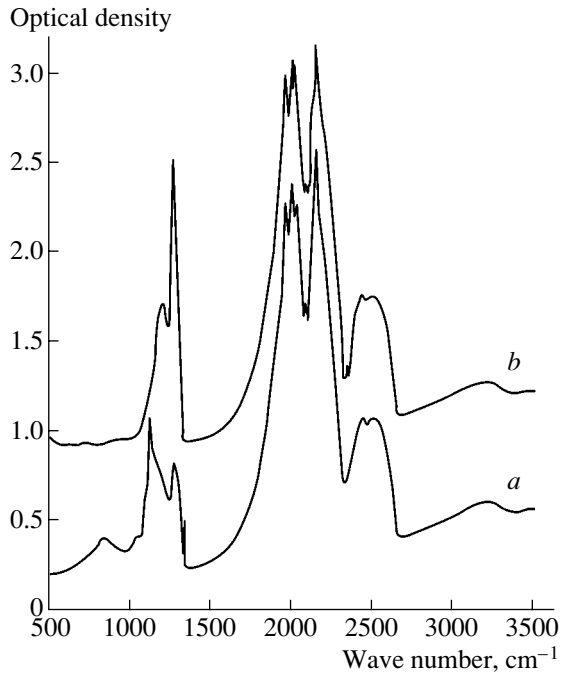

Fig. 4. IR absorption spectra of sample 2005 (*a*) prior to and (*b*) after thermobaric treatment.

changes that occur in the IR absorption spectra of diamond single crystals as a result of their thermobaric treatment are as follows: the bands at 1130 and 860 cm^{-1} nearly completely disappear and the intensity of the band at 1280 cm^{-1} increases. Thus, under the chosen conditions of thermobaric treatment, Me–*X* centers are annealed and N atoms aggregate to form pairs (*A* defects). Estimation of the concentration of N impurity in different forms, performed using the technique reported in [9], showed that the degree of aggregation of *C* defects in all the crystals under investigation exceeds 90%. It should also be noted that we did not observe any increase in the total concentration of N impurity in synthetic diamond single crystals subjected to thermobaric treatment. These results cast doubt on the suggestion [8] that the N impurity is incorporated into Me–*X* centers.

It is established that diamond crystals grown under different conditions have dissimilar photoluminescence spectra; the shape of the spectrum is controlled by the distribution of the impurities (N, Ni, etc.) over the growth sectors and faces of a crystal. It is shown that thermobaric treatment of synthetic diamond crystals in the temperature range 2000–2200 K at a stabilizing pressure of 6–6.5 GPa leads to the aggregation of a significant (more than 90%) fraction of *C* defects with formation of *A* defects and almost complete annealing of Me–*X* centers. At the same time, the color of the crystals changes from saturated yellow-green to light green and their transparency increases. As a result of thermobaric treatment, the luminescence intensity significantly increases (by a factor of 3–5) in comparison with initial crystals. Apparently, this phenomenon is related to the annealing of nonradiative recombination centers. Significant changes are also observed in the excitation spectrum of *A* luminescence, which indicates restructuring of the absorption spectra of the samples and is proof of the significant transformation of structural defects in the diamond crystals subjected to thermobaric treatment.

ACKNOWLEDGMENTS

This study was supported by GNTP Almazy, project no. 3412/2.41, and the Belarussian Foundation for Basic Research, project no. F03-031.

REFERENCES

1. V. S. Solov'ev, G. A. Gusakov, S. V. Reĭman, *et al.*, Poroshk. Metall. (Kiev) **23**, 23 (2000).
2. V. E. Il'in, E. V. Sobolev, and O. P. Yur'eva, Fiz. Tverd. Tela (Leningrad) **12**, 2159 (1970) [Sov. Phys. Solid State **12**, 1721 (1970)].
3. V. Nadolinny and A. Yelisseyev, Diamond Relat. Mater. **3**, 17 (1993).
4. A. Yelisseyev, Yu. Babich, V. Nadolinny, *et al.*, Diamond Relat. Mater. **11**, 23 (2002).
5. I. N. Kupriyanov, V. A. Gusev, Yu. M. Borzdov, *et al.*, Diamond Relat. Mater. **8**, 1301 (1999).
6. S. C. Lawson, H. Kanda, K. Watanabe, *et al.*, J. Appl. Phys. **79**, 4348 (1996).
7. V. G. Malogolovets, A. S. Vishnevskiĭ, and A. S. Povarennykh, Dokl. Akad. Nauk SSSR **243**, 111 (1978) [Sov. Phys. Dokl. **23**, 788 (1978)].
8. V. G. Malogolovets, S. A. Ivanchenko, and G. V. Chipenko, Sverkhtverd. Mater. **82** (1), 7 (1993).
9. H. Kanda and S. Yamaoka, Diamond Relat. Mater. **2**, 1420 (1993).

Translated by Yu. Sin'kov

Semiconductors, Vol. 38, No. 5, 2004, pp. 524–527. Translated from Fizika i Tekhnika Poluprovodnikov, Vol. 38, No. 5, 2004, pp. 543–546.

ELECTRONIC AND OPTICAL PROPERTIES OF SEMICONDUCTORS

Phase Conjugation on the Surface of Optically Excited ZnO

A. N. Gruzintsev and V. T. Volkov

Institute of Microelectronic Technology and Ultra-High-Purity Materials, Russian Academy of Sciences, Chernogolovka, Moscow oblast, 142432 Russia

e-mail: gran@ipmt-hpm.ac.ru

Submitted October 10, 2003; accepted for publication October 19, 2003

Abstract—The feasibility of phase conjugation in excited semiconductor media is shown both theoretically and experimentally. For the first time, phase conjugation of a light wave (nitrogen laser) with a photon energy equal to half the exciton radiative recombination energy in the medium (ZnO epitaxial films) at room temperature is revealed. The spectral dependences of the phase conjugation signal are studied. The quadratic interaction between the electromagnetic and exciton waves in a semiconductor is suggested as a possible mechanism of this effect. © *2004 MAIK "Nauka/Interperiodica".*

1. INTRODUCTION

Zinc oxide is a wide-gap (E_g = 3.39 eV) semiconductor; it has the highest (60 meV) exciton binding energy among the compounds of this class [1]. As a result, exciton luminescence of ZnO can be observed at temperatures of up to 55 K. The highly efficient radiative recombination in ZnO films made it possible to observe stimulated luminescence in the ultraviolet (UV) region at 397 nm upon nitrogen laser excitation of such films [2, 3]. This fact makes zinc oxide a promising material for the production of high-intensity diode-laser sources of UV radiation. The operation of a diode laser is to a large extent governed by the cavity mirrors, since they are responsible for its Q factor and lasing threshold, as well as the direction and spectral width of the laser radiation.

The application of phase-conjugating mirrors in gas laser cavities was considered in a number of studies [4–6]. The main advantage of such mirrors is their ability to correct the distortions induced by the active medium or the optical elements within the cavity and, thus, to provide for self-tuning of the cavity. In the case considered, an incident wave is reflected exactly in the reverse direction, and the parallelism of the cavity mirrors may not be strictly observed. In the experiments [6] on phase conjugation, the input power was about 1.6×10^7 W/cm^2 and the reflected wave power amounted to approximately 2×10^{-3} of the signal power (the mirror reflectance). In all the variants of the experiments mentioned above, the phase conjugation effect is based on three-wave mixing in a nonlinear crystal or gaseous medium. Because of this, the phase-conjugating mirrors used in this case are rather bulky, have low reflectivity, and are not applicable to diode lasers, which are rather small.

In this study, we revealed and investigated the phenomenon of phase conjugation by excitons that are present in zinc oxide upon high-power excitation by a UV laser. This process involves only two-wave mixing, whose probability in noncentrosymmetrical electro-optical semiconductors similar to ZnO is fairly high.

2. THEORY

In the tensor form, the expression for the polarization vector **P** in a semiconductor medium under the action of electromagnetic waves E_1 and E_2 with different frequencies Ω and ω can be written as [7]

$$P_i = \chi_{ij}^{(1)} E_j + \chi_{ijk}^{(2)} E_j E_k + \chi_{ijkl}^{(3)} E_j E_k E_l + \ldots, \qquad (1)$$

where the summation is over all equal indices (j, k, l = 1, 2, 3) corresponding to the three components of the total electric field; $\chi^{(1)}$, $\chi^{(2)}$, and $\chi^{(3)}$ are the linear, quadratic, and cubic parts of the optical susceptibility expanded in terms of the electric field, which are generally the second-, third-, and fourth-rank tensors, respectively.

Let us dwell on the quadratic susceptibility term in expansion (1), which is characteristic of noncentrosymmetrical crystals. This term is responsible for the second harmonic generation and the electro-optical effect (the latter is significant in ZnO that has a hexagonal wurtzite lattice). For simplicity, we assume that the polarization vector **P** and both electric field vectors E_1 and E_2 are directed along the crystal growth axis (z axis). The electromagnetic wave propagates along the x direction and has the form

$$E_2 = E_{20} \exp(-i\omega t + ikx) + E_{20}^* \exp(i\omega t - ikx).$$

The other electromagnetic wave in the material corresponds to the state of an exciton at rest (the wave vector **K** = 0) on the polariton dispersion curve and can be written as

$$E_1 = E_{10} \exp(-i\Omega t) + E_{10}^* \exp(i\Omega t).$$

Then, the second term in Eq. (1) appears as

$$\chi^{(2)}(E_1 + E_2)(E_1 + E_2) = 2\chi^{(2)}E_1E_2 + \chi^2E_1^{(2)} + \chi^{(2)}E_2^2. \quad (2)$$

Let us discuss the first term on the right-hand side of Eq. (2) in more detail and write it out with the assumption that the light wave frequency comprises half the frequency of the exciton wave; i.e., $\omega = \Omega/2$.

$$2\chi^{(2)}E_1E_2 = 2\chi^{(2)}[E_{10}E_{20}\exp(-i3\omega t + ikx) + E_{10}E_{20}^*\exp(-i\omega t - ikx) + \text{c.c.}], \quad (3)$$

where c.c. denotes the terms that are complex conjugate to the first two terms in Eq. (3). Expression (3) for the polarization of a semiconductor medium describes two electromagnetic waves: the first does not fit into the dispersion curve, while the second is a conjugate wave propagating towards the incident wave (E_2), regardless of the angle of incidence. The intensity of the second wave is proportional to the intensity of the incident wave, the intensity of excitonic oscillations, and the quadratic nonlinear optical susceptibility of the medium. Irradiating ZnO films by UV nitrogen laser radiation, which is absorbed in this material within a depth of about 0.1–0.2 μm, one can readily obtain the conditions for phase conjugation in a thin surface ZnO layer.

3. EXPERIMENTAL

ZnO films on (0001)-oriented sapphire were obtained by electron-beam high-vacuum deposition in an L-560 (Leubold Haereus) system. The resulting films 0.5 μm thick had high crystal quality; their growth axis was perpendicular to the surface [9]. The peak at 3.24 eV due to the exciton luminescence was predominant in the luminescence spectrum at room temperature. The photoluminescence (PL) spectra of the films were studied upon their excitation by pulses of an LGI-505 nitrogen laser (pulse width 10 ns, peak power 15 kW, wavelength 337.1 nm). The experimental setup designed to implement phase conjugation on a zinc oxide film is shown in Fig. 1. It is noteworthy that a Narva-100 incandescent dc lamp was used as the source of incident light, and the angle of incidence exceeded 45° in order to prevent the reflected light from entering the input of a detecting MDR-6 monochromator. After passing through an MDR-12 wide-aperture monochromator, the light of the incandescent lamp was continuous in time and had a spectral half-width of no more than 4 nm. The detection system was tuned to the repetition rate of the pumping LGI-505 laser and consisted of a Unipan-237 computer-controlled ac amplifier. The experiments were carried out at room temperature with a zinc oxide sample oriented so that both electromagnetic waves from the laser and the incandescent lamp had nonzero components along the film growth axis. The laser beam was focused onto a spot less than 100 μm in diameter on the film surface, which corresponded to a pump power density of about 10^8 W/cm^2. The overlap of the laser beam spot with the spot from the lamp on the sample surface was controlled by an optical microscope. A standard glass plate was used as a beam splitter (Fig. 1). The spectra of the reversed signal and the film luminescence were recorded using KS-15 and SZS-23 light filters, respectively, which cut off the second-order spurious signals of the double monochromator MDR-6 from the detected signals.

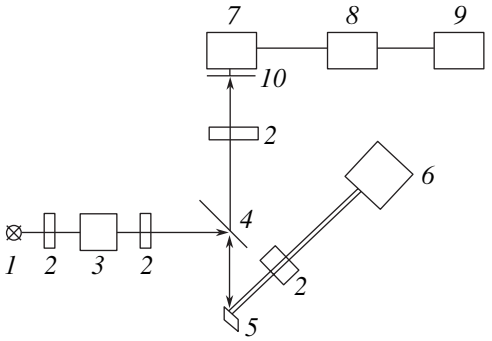

Fig. 1. Schematic of the setup used for phase conjugation on a zinc oxide film: (*1*) Narva-100 light source, (*2*) lenses, (*3*) MDR-12 monochromator, (*4*) beam splitter, (*5*) ZnO sample, (*6*) LGI-505 laser, (*7*) MDR-6 monochromator, (*8*) FÉU-79 photomultiplier, (*9*) recording system, and (*10*) light filter.

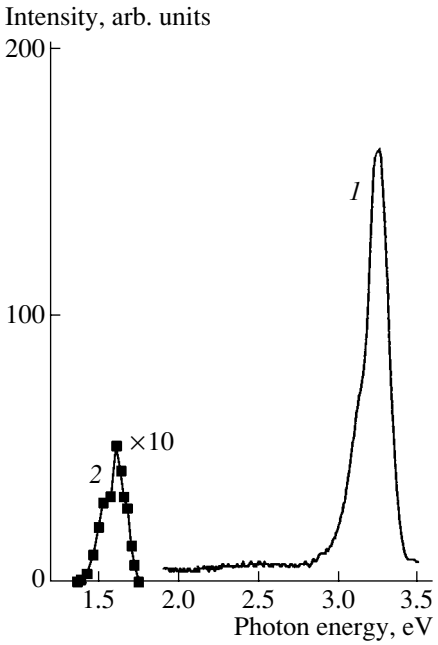

Fig. 2. (*1*) PL and (*2*) phase-conjugation spectra measured from a ZnO film on sapphire at 300 K.

4. RESULTS AND DISCUSSION

Figure 2 shows the PL spectrum (curve *1*) of the ZnO films under study recorded upon laser excitation

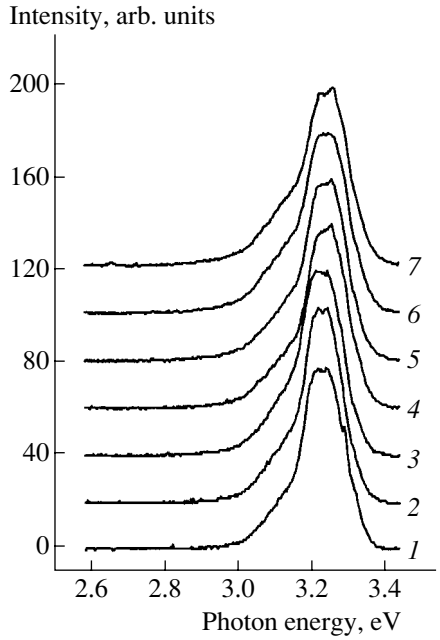

Fig. 3. PL and phase-conjugation spectra of a ZnO film on sapphire measured in the blue-violet region at 300 K under illumination with a photon energy of (*1*) 3.26, (*2*) 3.18, (*3*) 3.10, (*4*) 2.95, (*5*) 2.82, (*6*) 2.69, and (*7*) 2.58 eV.

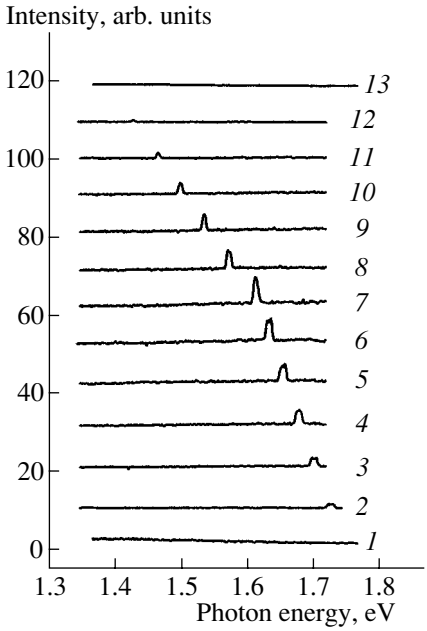

Fig. 4. Phase-conjugation spectra of a ZnO film on sapphire measured in the red region at 300 K for an incident photon energy of (*1*) 1.75, (*2*) 1.72, (*3*) 1.70, (*4*) 1.67, (*5*) 1.65, (*6*) 1.63, (*7*) 1.61, (*8*) 1.57, (*9*) 1.53, (*10*) 1.49, (*11*) 1.46, (*12*) 1.42, and (*13*) 1.39 eV.

without additional illumination. Only an exciton peak at 3.24 eV with a small shoulder in the long-wavelength region (at 3.12 eV) can be seen in the spectrum. These spectral features can be attributed to the radiative recombination of a free exciton with an exciton bound at a donor [2, 3].

Let us now consider a sample subjected to a combined action of nitrogen laser pulses and continuous blue-violet radiation with a photon energy ranging from 2.58 to 3.26 eV (Fig. 3). As can be seen from Fig. 3, the detected signal contains only a PL component peaked at 3.24 eV with a shoulder at 3.12 eV. Note that a change in the continuous light wavelength does not affect the shape and intensity of the spectral lines.

Much more interesting behavior is displayed by the signal detected in the red spectral region with a photon energy equal to half the energy of exciton radiative recombination in zinc oxide (Fig. 4). In this case, a KS-15 infrared filter was placed in front of the detecting monochromator MDR-6 so that neither the scattered light from the 337.1-nm laser nor the luminescence signal from the ZnO film could pass through the monochromator. This was done to cut off the second-order luminescence line that may arise in the monochromator. It is clearly seen that no phase-conjugated (time-reversed) signal is present in the red region in the case of illumination with a photon energy of 1.75 eV (Fig. 4, curve *1*). However, as the photon energy approaches half the exciton component (3.24/2 = 1.62 eV), a narrow spectral peak of the time-reversed signal appears at the energy of incident photons. The detection method is also evidence that, in contrast to the incident wave, the time-reversed signal is periodic with a frequency equal to the repetition rate of the pump. The half-width of the time-reversed signal coincides with that of the incident light wave, and its intensity depends on the spectral position.

Figure 2 (curve *2*) shows the intensity of the peak corresponding to the time-reversed wave plotted versus the spectral peak position. It can be seen that, as in Fig. 4, the intensity of the time-reversed signal peaks at an energy of incident photons of 1.61 eV, which is very close to half the energy of the exciton PL peak. Curve *2* in Fig. 2 has a characteristic long-wavelength shoulder, which is similar to the shoulder in the photoluminescence curve (curve *1*).

Note that, according to the mathematics given above, the phase-conjugation effect may occur in media with quadratic optical nonlinearity if the incident wave frequency comprises one half of the frequency of excitonic oscillations (3). The intensity of the resulting time-reversed signal is proportional to both the incident and the exciton wave intensities. In our case, the intensity of the incident red light is almost constant in the spectral range under study (1.4–1.7 eV). Therefore, the spectrum of the time-reversed signal repeats the spectral dependence of the exciton wave intensity (Fig. 2, curves *2* and *1*, respectively), and the process itself occurs only at the instant when the exciton density in a semiconductor becomes high. Since the radiative recombination time of excitons in ZnO films at room temperature is about a picosecond, excitonic oscilla-

tions can exist only within the pump pulse duration. As a result, the phase-conjugation process also has pulse character, which is confirmed by the detection of an alternating signal at the repetition rate of pump pulses in our experiments. In view of the pronounced spectral dependence of the time-reversed signal intensity (Fig. 2, curve *2*), the discovered process cannot be associated with the scattering of continuous light by polycrystalline grains of a ZnO film; at the same time, the signal of purely geometric reflection of light from the sample surface does not enter the detection system.

5. CONCLUSION

Phase conjugation of an electromagnetic wave on the surface of a ZnO film highly excited by a nitrogen laser is predicted theoretically (see expression (3)) and confirmed experimentally. It is shown that phase conjugation occurs when the energy of incident photons comprises one half of the exciton radiative recombination energy. Therefore, we may conclude that phase conjugation involves the exciton states of the semiconductor film. Assuming that, under the conditions of band-to-band excitation, laser radiation is absorbed in a submicron (0.1 μm) surface layer [8], one can easily obtain a high density of excitons by nitrogen laser pumping of semiconductor. It should be noted that thin ZnO films, which have high crystal quality and excellent luminescent properties, are especially suitable for phase conjugation. In our case, almost complete conversion of the laser pump energy into the energy of excitonic oscillations in zinc oxide was attained.

This mechanism of phase conjugation in a semiconductor medium significantly differs from the four-wave mixing of counterpropagating beams that occurs in optically nonlinear media [6]. In the latter case, phase conjugation of a signal wave also occurs, but a medium must have cubic optical nonlinearity and be transparent for all the light beams. Because of the low cubic optical susceptibility [7], the efficiency of phase conjugation is low and a large volume of nonlinear medium is required. In our case, the semiconductor medium is opaque for the pump wave and, thus, thin layers can be used. For a complete reconstruction of the phase in a time-reversed wave, optically thin mirrors should be used; i.e., their thickness should be of the same order of magnitude as the incident wavelength. This condition can be met only in the case of our study.

ACKNOWLEDGMENTS

This study was supported by INTAS, grant no. 2002-0796.

REFERENCES

1. Y. Chen, D. M. Bagnall, Z. Zhu, *et al.*, J. Cryst. Growth **181**, 165 (1997).
2. Ji. Chen and T. Fujita, Jpn. J. Appl. Phys., Part 2 **41**, L203 (2002).
3. A. N. Gruzintsev, V. T. Volkov, C. Barthou, and P. Benalloul, Fiz. Tekh. Poluprovodn. (St. Petersburg) **36**, 741 (2002) [Semiconductors **36**, 701 (2002)].
4. P. A. Belanger, A. Hardy, and A. E. Seigman, Appl. Opt. **19**, 602 (1980).
5. J. F. Lam and W. P. Brown, Opt. Lett. **5**, 61 (1980).
6. D. M. Bloom and G. C. Bjoklund, Appl. Phys. Lett. **31**, 592 (1977).
7. F. Kaczmarek, *Wstep do Fizyki Laserow* (PWN, Warszawa, 1978; Mir, Moscow, 1981).
8. *Zinc Oxide*, Ed. by W. Hirschwald *et al.*, Vol. 7 of *Current Topics in Materials Science*, Ed. by E. Kaldis (North-Holland, Amsterdam, 1981).
9. A. N. Gruzintsev, V. T. Volkov, and L. N. Matveeva, Mikroélektronika **31**, 227 (2002).

Translated by A. Sidorova

Semiconductors, Vol. 38, No. 5, 2004, pp. 528–530. Translated from Fizika i Tekhnika Poluprovodnikov, Vol. 38, No. 5, 2004, pp. 547–549.

ELECTRONIC AND OPTICAL PROPERTIES OF SEMICONDUCTORS

Paramagnetic Structural Defects and Conductivity in Hydrogenated Nanocrystalline Carbon-Doped Silicon Films

O. I. Shevaleevskii*^, A. A. Tsvetkov*, L. L. Larina*, S. Y. Myong, and K. S. Lim****

**Institute of Biochemical Physics, Russian Academy of Sciences, Moscow, 119991 Russia*

^e-mail: O_Chevale@Yahoo.com

***Korea Advanced Institute of Science and Technology, Daejeon 305-701, South Korea*

Submitted October 30, 2003; accepted for publication November 4, 2003

Abstract—The behavior of paramagnetic defects and dark conductivity in heterogeneous samples of hydrogenated nanocrystalline carbon-containing silicon (*nc*-SiC:H) prepared by the photo-CVD method is studied. It is shown that, with increasing carbon content in *nc*-SiC:H, a phase transition from a nanocrystalline to an amorphous structure occurs, producing a reduction in paramagnetic defect density and a significant decrease in the dark conductivity. *© 2004 MAIK "Nauka/Interperiodica".*

Thin films of nanocrystalline hydrogenated carbon-containing silicon *nc*-SiC:H are promising materials for use in solar cells as wide-gap optical windows [1] and buffer layers [2]. Compared to microcrystalline silicon (μ*c*-Si:H) [3], *nc*-SiC:H samples with a small carbon content have a wider optical transmission band. The structure of *nc*-SiC:H, the carbon content, the ratio of the amorphous phase to the crystalline phase, and the crystallite size are governed by the growth conditions. This circumstance provides an opportunity to control such parameters as the optical transmission band and conductivity [4].

In device-quality amorphous silicon (*a*-Si:H), the high conductivity ($\sim 10^{-3}\ \Omega^{-1}\ cm^{-1}$) is usually attributed to the low density ($N_S \approx 10^{16}\ cm^{-3}$) of paramagnetic defects, i.e., silicon dangling bonds (DBs) with uncompensated spins [5]. The conductivity of *a*-Si:H and *a*-SiC:H decreases by three to four orders of magnitude as N_S increases to $\sim 10^{18}\ cm^{-3}$ [6]; however, in heterogeneous samples containing both amorphous and nanocrystalline fractions, the relation between the DB density and conductivity is different. Thus, in μ*c*-Si:H films prepared by plasma-enhanced chemical vapor deposition (PECVD), the conductivity increases simultaneously with the DB defect density [7]. Compared to μ*c*-Si:H, *nc*-SiC:H samples are more complicated objects, in which the effect of adding small amounts of carbon has been inadequately studied. Moreover, there are no data on the behavior of paramagnetic defects. We performed structural investigations of *nc*-SiC:H samples prepared by the photo-CVD method and studied the effect of paramagnetic defects on electron transport.

Films of *nc*-SiC:H ~150 nm thick were deposited on glass substrates using the decomposition of monosilane SiH_4, hydrogen H_2, and ethylene C_2H_4 by high-intensity ultraviolet radiation. We have described in detail the photo-CVD method in [8, 9]. The paramagnetic defect density (N_S) was determined by analyzing the electron spin resonance (ESR) spectra. The absolute values of N_S and the *g*-factor were evaluated by comparing the signals from the sample and from standards with known parameters. The dark conductivity σ_D was measured in the temperature range 300–420 K.

We have previously confirmed the presence of a carbon-containing amorphous phase in *nc*-SiC:H films using infrared Fourier spectroscopy [9] and estimated the carbon density by Auger spectroscopy [10]. The carbon content *x* was estimated by the method suggested in [11] and based on the analysis of the ratio between the fluxes of the reacting gases.

The structure of the samples was studied by Raman spectroscopy, and the spectra were analyzed by resolving the experimental curve into Gaussian components that corresponded to the structural phases: crystalline silicon *c*-Si (~520 cm^{-1}), *a*-SiC:H with low carbon content (~480 cm^{-1}), and an intermediate phase in the region of microcrystallite boundaries (~506 cm^{-1}). Measurements in the range 750–950 cm^{-1} did not detect any signal from crystalline silicon carbide *c*-SiC, and we may assume that all the carbon atoms are localized in the amorphous phase. The crystallite size estimated from the X-ray diffraction data by using Scherrer's formula was ~12 nm. In Fig. 1, we present the resolution of the Raman spectrum of the *nc*-SiC:H sample with carbon content $x = 11$ at %. The relative content of the nanocrystalline fraction X_C was evaluated from the relative intensities of the Gaussian peaks obtained by resolving the Raman experimental curve,

$$X_C = \frac{I_{520} + I_{506}}{I_{520} + I_{506} + I_{480}}. \quad (1)$$

The inset in Fig. 1 shows X_C as a function of the carbon content *x*. For $[C_2H_4]/[SiH_4] = 0.07$, samples with a low carbon content ($x = 6$ at %) and maximum crys-

tallinity ($X_C \approx 86\%$) were obtained. A structural phase transition and the formation of a predominantly amorphous phase in the sample were observed with increasing carbon content.

ESR spectra for a series of *nc*-SiC:H samples with carbon content increasing from 6 to 11 at % is shown in Fig. 2. For all the samples, asymmetric ESR lines with a half-width ΔH_{pp} of about 20–30 G and a *g*-factor equal to 2.0065 (±0.0005) were observed. The densities N_S calculated from these ESR data are plotted in Fig. 3 as functions of the carbon content X_C. In the sample with high crystallinity ($X_C = 86\%$), the DB density was $N_S \approx 2 \times 10^{19}$ cm^{-3}, and in the sample in which the amorphous phase was dominant ($X_C \approx 48\%$) N_S was found to be an order of magnitude smaller.

In the course of film growth by the photo-CVD method, the increase in carbon content inhibited the formation of the crystalline phase, which appreciably decreased the DB defect density. The similar behavior of N_S indicates that the observed defects are related to nanocrystallites and are apparently localized at their surface. We have calculated the surface defect density N_{SQ} for the crystallites and obtained the value $N_{SQ} \approx 2 \times 10^{13}$ cm^{-2}. This is of the same order of magnitude as the surface defect density measured for homogeneous *a*-Si:H and *a*-SiC:H samples in [12], where N_{SQ} varied in the range 10^{12}–10^{13} cm^{-2}.

In addition to the established correlation between N_S and the content of the crystalline component, there is a similar correlation with the behavior of the conductivity. In Fig. 3 the dependence of σ_D on the crystallinity of the sample (at $T = 300$ K) is shown together with the corresponding dependence of N_S. The maximum conductivity $\sigma_D = 3.4 \times 10^{-6}\ \Omega^{-1}$ cm^{-1} corresponds to the film of the greatest crystallinity dropping to $\sigma_D = 3.2 \times 10^{-8}\ \Omega^{-1}$ cm^{-1} as the fraction of the amorphous phase increases. Measurements of the temperature dependence of σ_D and the analysis of the Arrhenius curves show that the conductivity in the temperature range 300–420 K is controlled by an activation mechanism. In the film with high X_C, the activation energy is small ($E_a = 0.37$ eV) and increases steadily to $E_a = 0.55$ eV as the fraction of the amorphous phase increases. We may assume that, for *nc*-SiC:H, the conductivity is governed by the dominant contribution of the states at the surface of the nanocrystalline phase and at the interfaces of microcrystallites, as shown for heterogeneous μ*c*-SiC:H films of similar composition [13].

In conclusion, we will discuss the behavior of DB defects in *nc*-SiC:H. We believe that the origin of the effect of the content of the crystalline component on the spin state density is quite complicated, and the observed effect is a superposition of two competitive processes. The increase in carbon content in the sample reduces the fraction of the crystalline phase. In this case, additional carbon DB defects are formed [14] and the observed value of N_S contains contributions from

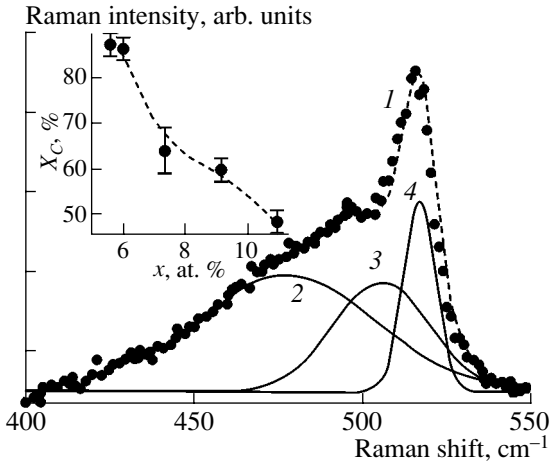

Fig. 1. (*1*) Experimental Raman spectrum for the *nc*-SiC:H sample with $X_C = 48\%$ resolved into Gaussian components with peaks in the regions of (*2*) ~480, (*3*) ~506, and (*4*) ~520 cm^{-1}. The inset shows X_C as a function of the relative carbon content *x*.

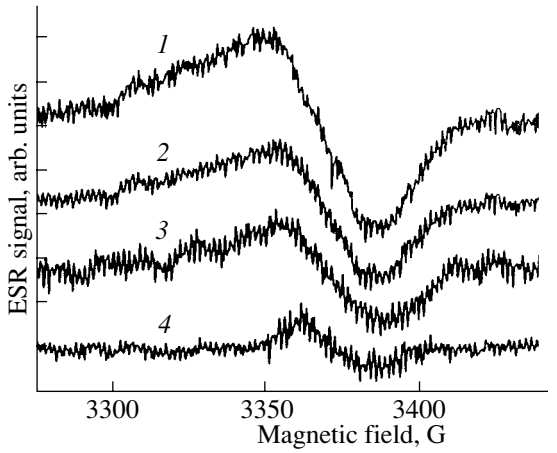

Fig. 2. The form of ESR absorption spectra in the *nc*-SiC:H samples with a crystalline phase content of X_C = (*1*) 86, (*2*) 64, (*3*) 60, and (*4*) 48%.

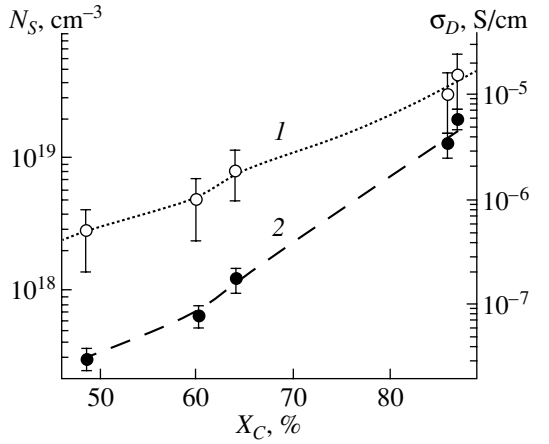

Fig. 3. (*1*) Density of paramagnetic defects N_S and (*2*) the dark conductivity σ_D of *nc*-SiC:H samples in relation to the crystalline fraction X_C.

two different components. Indirect evidence of the presence of signals from different DBs is an asymmetric wide ESR line. However, the decrease in the silicon DB defect density due to decreasing X_C dominates over the simultaneous increase in the number of carbon defects. Therefore, N_S varies by an order of magnitude with decreasing X_C. It is interesting to note that, in μ*c*-Si:H, where the only defects are silicon DBs, such a structural transition results in a decrease in N_S of more than two orders of magnitude [7].

Thus, using the ESR method, we studied for the first time paramagnetic defects in thin *nc*-SiC:H films with a low carbon content prepared by the photo-CVD method. We established a correlation between the degree of crystallinity of the samples, the DB defect density, and the conductivity.

REFERENCES

1. B. Goldstein and C. R. Dickson, Appl. Phys. Lett. **53**, 2672 (1988).
2. S. Y. Myong, S. S. Kim, O. Shevaleevskii, *et al.*, in *Proceedings of 29th IEEE Photovoltaic Specialists Conference* (New Orleans, USA, 2002), p. 1226.
3. A. G. Kazanskiĭ, P. A. Forsh, K. Yu. Khabarov, and M. V. Chukiev, Fiz. Tekh. Poluprovodn. (St. Petersburg) **37**, 1100 (2003) [Semiconductors **37**, 1076 (2003)].
4. S. Ghosh, A. Dasgupta, and S. Ray, J. Appl. Phys. **78**, 3200 (1995).
5. J. K. Rath, Sol. Energy Mater. Sol. Cells **76**, 431 (2003).
6. R. Schropp, Thin Solid Films **403–404**, 17 (2002).
7. A. L. Baia Neto, A. Lambertz, R. Carius, and F. Finger, Phys. Status Solidi **186**, R4 (2001).
8. J. W. Lee and K. S. Lim, J. Appl. Phys. **81**, 2432 (1997).
9. S. Y. Myong, H. K. Lee, E. Yoon, and K. S. Lim, J. Non-Cryst. Solids **298**, 131 (2002).
10. S. Y. Myong, H. K. Lee, E. Yoon, and K. S. Lim, Mater. Res. Soc. Symp. Proc. **557**, 603 (1999).
11. D. Kuhmann, S. Grammatica, and F. Jansen, Thin Solid Films **177**, 253 (1989).
12. U. K. Das, T. Yasuda, and S. Yamasaki, Phys. Rev. B **63**, 245204 (2001).
13. A. G. Kazanskiĭ, H. Mell, E. I. Terukov, and P. A. Forsh, Fiz. Tekh. Poluprovodn. (St. Petersburg) **34**, 373 (2000) [Semiconductors **34**, 367 (2000)].
14. F. Giorgis, C. F. Pirri, E. Tresso, *et al.*, Physica B (Amsterdam) **229**, 233 (1997).

Translated by I. Zvyagin

Semiconductors, Vol. 38, No. 5, 2004, pp. 531–532. Translated from Fizika i Tekhnika Poluprovodnikov, Vol. 38, No. 5, 2004, pp. 550–551.

ELECTRONIC AND OPTICAL PROPERTIES OF SEMICONDUCTORS

Electrical Properties of $MnIn_2Se_4$

N. N. Niftiev, M. A. Alidzhanov, O. B. Tagiev, F. M. Mamedov, and M. B. Muradov

Azerbaijani State Pedagogical Institute, Baku, 370000 Azerbaijan

Submitted October 13, 2003; accepted for publication November 4, 2003

Abstract—The temperature dependence of conductivity and current–voltage characteristics of $MnIn_2Se_4$ crystals have been studied. It is shown that the current in the nonlinear part of the current–voltage characteristic is due to the field effect. The activation energies of carriers and trap concentrations are determined. A relaxation of current with time is observed in $MnIn_2Se_4$. © *2004 MAIK "Nauka/Interperiodica".*

Ternary chalcogenide compounds possess a number of exceedingly important properties and find application in various fields of new technology. Of interest in this regard is the group of ternary compounds II–III_2–VI_4 (where II stands for Mn, Fe, Ni, or Co; III, for Ga or In; and VI, for S, Se, or Te), some of which have already been synthesized but have been insufficiently studied [1–5]. These compounds are promising for the development of lasers, light modulators, photodetectors and other magnetic-field-controlled functional devices.

$MnIn_2Se_4$ belongs to the class of II–III_2–VI_4 compounds, whose physical properties have been little studied [2, 3].

The present paper presents the results obtained in studying the temperature dependence of conductivity, $\sigma(T)$, and current–voltage (I–U) characteristics of $MnIn_2Se_4$ crystals.

$MnIn_2Se_4$ was obtained by direct fusion of high-purity (99.99%) elements taken in stoichiometric amounts. An X-ray diffraction analysis revealed that $MnIn_2Se_4$ polycrystals have a hexagonal structure with lattice constants a = 4.19 Å, c = 12.90 Å; c/a = 3.08. The samples studied were prepared by mechanical processing of the ingots obtained. The contacts were fabricated by fusing-in indium on the opposite surfaces of a sample (sandwich structure). The electrical properties of $MnIn_2Se_4$ were examined on plates with dimensions $2 \times 4 \times 6$ mm, cut from the ingots. $MnIn_2Se_4$ crystals have n-type conduction.

Figure 1 shows the temperature dependence of conductivity for $MnIn_2Se_4$. The curve describing the dependence $\sigma \propto \exp(10^3/T)$ comprises two linear portions with different slopes. The activation energies of impurity levels in $MnIn_2Se_4$, found from these slopes, are E_1 = 21 meV and E_2 = 27 meV.

Figure 2 shows I–U characteristics of In–$MnIn_2Se_4$–In structures, measured at different temperatures. The I–U characteristics exhibit two portions: a linear region ($J \propto U$) and a region with a steeper rise in current ($J \propto U^n$, $n > 1$).

It can be seen that, at low voltages, the current flowing through the sample obeys Ohm's law. As the voltage increases further, Ohm's law starts to be violated, and the current increases by the power law ($J \propto U^n$). In the nonlinear region, the current transport mechanism is determined by the field effect, since the experimental points in the dependence of the conductivity on electric field are in good agreement with Frenkel's theory of thermionic ionization [6]:

$$\sigma = \sigma_0 \exp(\beta\sqrt{F}),$$

where σ_0 is the weak-field conductivity and β is the Frenkel coefficient. The expression

$$N_t = \left(\frac{2e}{kT\beta}\sqrt{F_{cr}}\right)^3$$

was used to estimate (from the known minimum electric field strength at which σ starts to depend on F

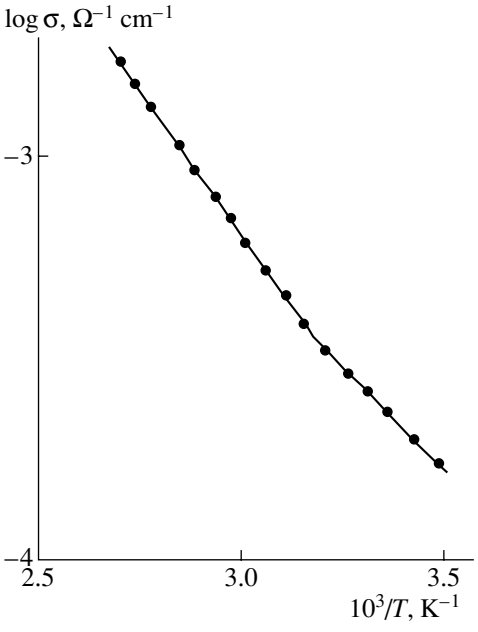

Fig. 1. Temperature dependence of conductivity of $MnIn_2Se_4$.

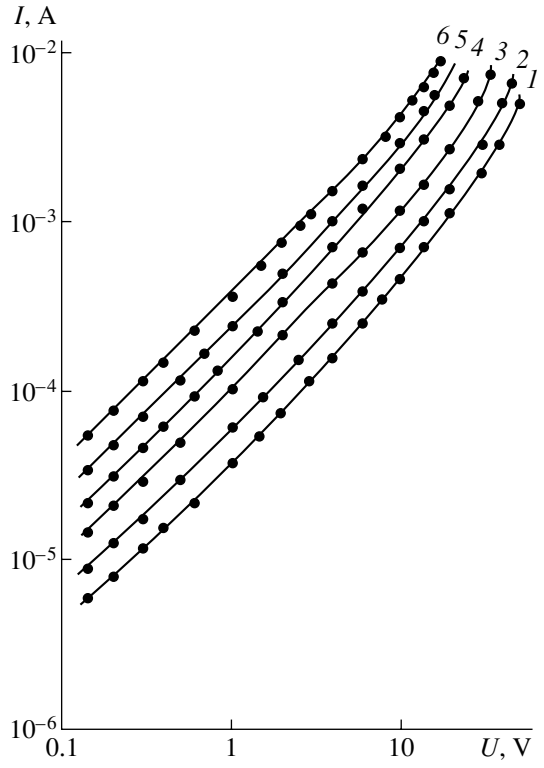

Fig. 2. Dark *I–U* characteristics of In–$MnIn_2Se_4$–In structures at different temperatures *T*: (*1*) 289, (*2*) 309, (*3*) 329, (*4*) 349, (*5*) 364, and (*6*) 379 K.

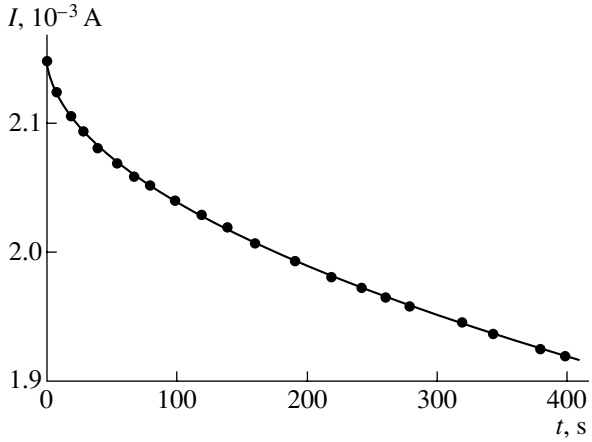

Fig. 3. Current flowing through the system at $U = 30$ V vs. time *t* during which the crystal is kept under bias.

(i.e., F_{cr})) the concentration of ionized centers ($N_t = 9.2 \times 10^{13}$ cm^{-3}) [7].

A relaxation of the current in the course of time was observed in $MnIn_2Se_4$. Figure 3 shows an experimental dependence of the current on time *t* at fixed voltage $U = 30$ V. It can be seen that the current rapidly decreases initially (0–50 s) and then more slowly at longer times (60–400 s).

It is assumed that the variation of the current with time is due to charge accumulation in a narrow region of the crystal (~10^{-4}–10^{-5} cm). This charge gives rise to a reverse electromotive force, which reduces the current that flows through the sample [8]. The relaxation process begins at a voltage of 1 V. However, the current shows a weaker dependence on time at high voltages and temperatures.

Thus, a study of the *I–U* characteristics and the $\sigma(T)$ dependence demonstrated that the current in the nonlinear region is due to the field effect. The activation energies of carriers and the trap concentrations were determined. A relaxation of the current in the course of time was observed in $MnIn_2Se_4$.

REFERENCES

1. T. Kanomata, H. Ido, and T. Kaneko, J. Phys. Soc. Jpn. **34**, 554 (1973).
2. B. K. Babaeva and M. R. Allazov, in *Studies in Inorganic and Physical Chemistry* (Nauka, Baku, 1977).
3. D. S. Azhdarova, *Semiconductors Based on Manganese Chalcogenides* (Nauka, Baku, 2001).
4. G. A. Medvedkin, Yu. V. Rud, and M. A. Tairov, Phys. Status Solidi A **3**, 289 (1989).
5. N. N. Niftiev, M. A. Alidzhanov, O. B. Tagiev, and M. B. Muradov, Fiz. Tekh. Poluprovodn. (St. Petersburg) **37**, 173 (2003) [Semiconductors **37**, 165 (2003)].
6. Ya. I. Frenkel', Zh. Éksp. Teor. Fiz. **8**, 1292 (1938).
7. R. H. Hill, Philos. Mag. **23**, 59 (1971).
8. B. L. Timan and A. P. Karpova, Fiz. Tekh. Poluprovodn. (Leningrad) **7**, 230 (1973) [Sov. Phys. Semicond. **7**, 167 (1973)].

Translated by M. Tagirdzhanov

Semiconductors, Vol. 38, No. 5, 2004, pp. 533–536. Translated from Fizika i Tekhnika Poluprovodnikov, Vol. 38, No. 5, 2004, pp. 552–555.

ELECTRONIC AND OPTICAL PROPERTIES OF SEMICONDUCTORS

Plasmon–Phonon–Polaritons in *p*-Doped Bi–Sb Alloys

N. P. Stepanov

Chita State Pedagogical University, Chita, 672000 Russia

e-mail: stepanov@academ.chita.ru

Submitted October 22, 2003; accepted for publication November 4, 2003

Abstract—The phonon spectra of Bi crystals and Bi–Sb alloys indicate the presence of phonon–polaritons caused by the polarization of valence electrons, which reduces the rigidity of the transverse mode of optical lattice vibrations and increases the rigidity of the longitudinal mode of vibrations. Doping Bi–Sb alloys with Sn (*p*-type impurity) decreases the difference in the energy of plasma oscillations of free charge carriers and the energy of longitudinal optical phonons. In this case, the behavior of the dielectric function is described in terms of the model corresponding to the excitation of plasmon–phonon–polaritons. © *2004 MAIK "Nauka/Interperiodica".*

The behavior of the dielectric function of bismuth in the far-infrared spectral region is governed mainly by free charge carriers [1]. The resonance frequencies of valence electrons, although shifted to the infrared region, are all still high [2]. In this case, the contribution of valence electrons to the dielectric function near the frequencies characteristic of the plasma resonance of free charge carriers can be described by the frequency-independent susceptibility $\chi_{v.c.}$, whose imaginary part can be disregarded: $\varepsilon_\infty = 1 + \chi_{v.c.} = \text{const}$. In principle, resonances of polar optical phonons may exist in the far-infrared region. Estimates based on the ratios of atomic masses and masses of valence electrons predict a frequency range from 10 to 150 cm^{-1} for the lattice resonances, i.e., precisely that spectral range where the plasma frequencies of free charge carriers in Bi crystals and Bi–Sb alloys lie. When investigating the optical functions in the immediate vicinity of the lattice resonances, one should take into account the dispersion due to particular excitations in a crystal, which are described as phonon–polaritons [3]. At the same time, it is well known that, from symmetry considerations, long-wavelength lattice excitations in elemental crystals with two atoms per unit cell do not contribute to polarization [3]. Silicon, germanium, and the semimetals arsenic, antimony, and bismuth are among such elements. Nevertheless, some results obtained by studying the spectra of optical functions of Bi crystals and Bi–Sb alloys in the far-infrared region indicate the activity of longitudinal optical phonons in bismuth, which is especially pronounced when the difference between the energy of plasma oscillations and the energy of phonons decreases.

For example, the investigations of the reflectance spectra of *p*-doped $Bi_{0.97}Sb_{0.03}$ crystals revealed the effect of energy transfer between independent anisotropic components of plasma oscillations via isotropic excitation of the crystal, whose frequency is close to that of longitudinal optical phonons at the point Γ of the Brillouin zone [4, 5]. Information on the activity of these optical phonons can be found in [6], where studies of the transmission spectra of Bi–Sb crystals are reported. Thus, the observed activity of longitudinal optical phonons in bismuth needs to be explained.

It is well known that close packing of atoms in a semiconductor crystal leads to strong interaction between valence electrons and to a decrease in the ionization energy. When the packing density is sufficiently high, this process leads to a polarization catastrophe—the transformation of the semiconductor into a metal. The intermediate position of semimetals accounts for the importance of the problem of the cooperative effect of all lattice atoms on the crystal polarizability.

The polarizability of condensed matter can be evaluated from the value of the ionization energy. This observation manifests itself in the empirical Moss relation: $nE_g = \text{const}$, where E_g is the band gap and n is the refractive index of a material. In Bi–Sb alloys, this relation is satisfied fairly well [7].

It was found in [7] (where the plasma reflection from $Bi_{1-x}Sb_x$ crystals with $x = 0$, 0.03, 0.065, 0.075, and 0.12 was studied) that the high-frequency permittivity ε_∞ is higher for $Bi_{0.97}Sb_{0.03}$ alloys, for which the band gap width is minimum at the point L of the Brillouin zone. It is known that a gapless state is observed in binary alloys $Bi_{1-x}Sb_x$ with $x = 0.04$ at liquid-helium temperatures [6]. The increase in ε_∞ in $Bi_{0.97}Sb_{0.03}$ alloys amounts to 30% of the value typical of bismuth ($\varepsilon_\infty = 100$). The increase in the high-frequency permittivity in the crystals with a minimum band gap width indicates an increase in the polarizability of valence electrons in $Bi_{0.97}Sb_{0.03}$ crystals, which is consistent with the Moss relation.

Due to the high polarizability of valence electrons, the electronic and lattice (phonon) properties turn out to be significantly dependent on each other, which leads to the formation of polaritons. This observation is confirmed by the investigations of the phonon spectrum of

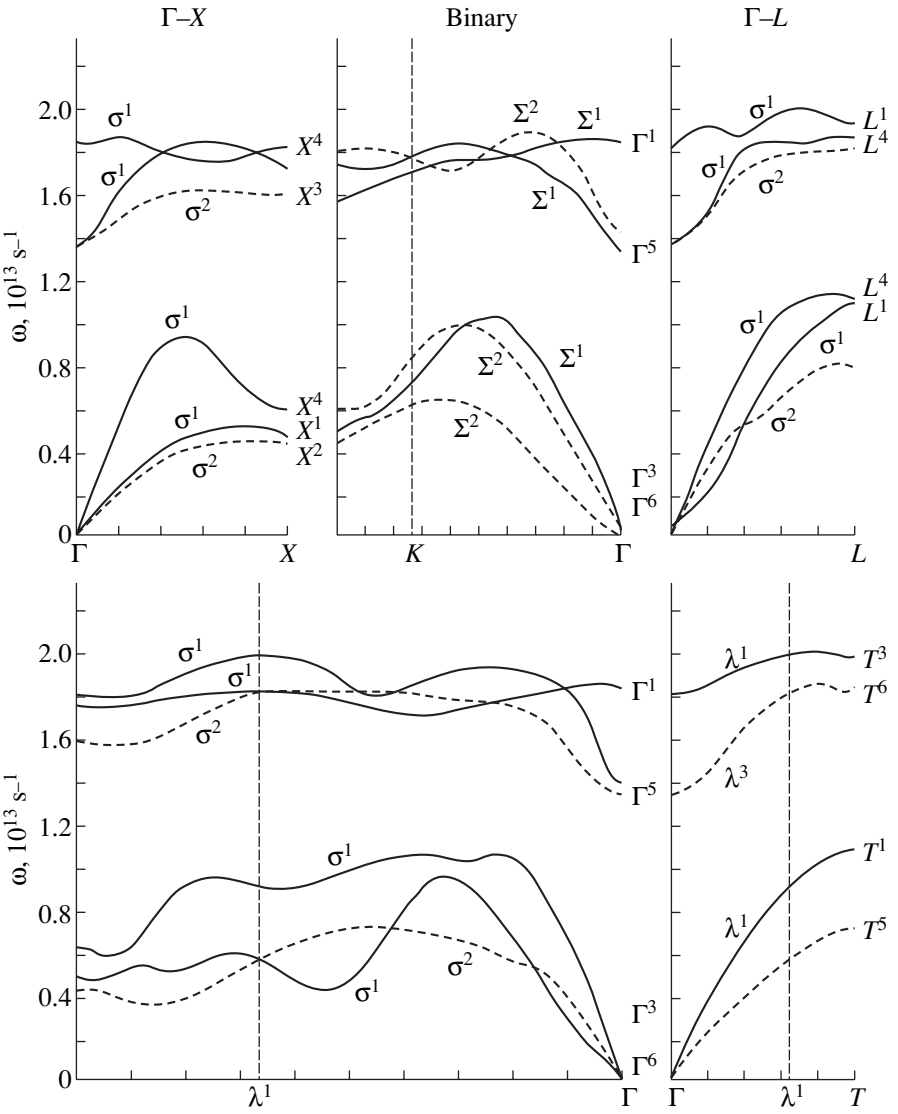

Fig. 1. Phonon spectrum of Bi crystals [8].

bismuth carried out in [8–10]. The phonon-energy spectrum was studied by neutron inelastic scattering measurements on Bi [8, 9] and $Bi_{0.95}Sb_{0.05}$ [10] single crystals. The most complete data, obtained in [8] for bismuth at $T = 78$ K, are shown in Fig. 1. According to the data of [10], the phonon spectrum of $Bi_{0.95}Sb_{0.05}$ single crystals differs from the phonon spectrum of bismuth by no more than 3%. The phonon spectra change only slightly in the temperature range 77–300 K [9, 10].

In general, optical (O) and acoustic (A) modes in crystals of bismuth type can be called neither purely longitudinal nor purely transverse, although they are similar to such modes along symmetry directions [8]. In this case, they can be considered quasi-longitudinal (LA, LO) or quasi-transverse (TA, TO) [9]. Along the trigonal direction, for which the symmetry conditions are simpler, one purely longitudinal mode (corresponding to the λ^1 representation) and two degenerate purely transverse modes (λ^3 representation) exist. It can be seen from Fig. 1 that the frequencies of longitudinal optical phonons ω_L along the trigonal direction are larger than the frequency of transverse phonons ω_T. According to the Lyddane–Sachs–Teller relation,

$$\frac{\varepsilon_s}{\varepsilon_\infty} = \frac{\omega_L^2}{\omega_T^2}, \tag{1}$$

which is indicative of the effect of polarization of valence electrons, leading to a reduction in the rigidity of the transverse mode and the enhancement of the rigidity of the longitudinal mode of lattice vibrations [3]. The higher the polarization of valence electrons, the larger the difference between ω_L and ω_T. The static value of the dielectric function ε_s can be represented in the form

$$\varepsilon_s = 1 + \chi_{\text{v.c.}} + \chi_{\text{ph}} = \varepsilon_\infty + \chi_{\text{ph}}. \tag{2}$$

When the condition $\omega_L/\omega_T > 1$ is satisfied, it follows from relations (1) and (2) that $\chi_{ph} > 0$. Positive values of χ_{ph} indicate the possibility of excitation of phonon–polaritons in bismuth.

In the course of systematic investigations of the reflectance of Bi crystals and Bi–Sb alloys doped with donor and acceptor impurities [4, 5, 7], it was found that the energy of plasma oscillations tends to the values corresponding to optical phonon frequencies, which is shown in Fig. 2. When the difference between the energies of elementary excitations in the electronic and ionic systems of a crystal is insignificant, the dielectric function can be written as

$$\varepsilon(\omega) = \varepsilon_{f.c.}(\omega) + \varepsilon_{v.c.}(\omega) + \varepsilon_{ph}(\omega), \qquad (3)$$

where $\varepsilon_{f.c.}(\omega)$ is the contribution of free charge carriers (intraband transitions), $\varepsilon_{v.c.}(\omega)$ is the contribution of bound carriers (interband transitions), and $\varepsilon_{ph}(\omega)$ is the contribution of the ion core.

The contribution of free charge carriers was taken into account in terms of the Drude model, where, when $\omega_p\tau \gg 1$, the real and imaginary parts of permittivity have the form

$$\varepsilon'_{f.c.}(\omega) = \varepsilon_\infty\left(1 - \frac{\omega_p^2}{\omega^2 - \tau_p^{-2}}\right), \quad \varepsilon''_{f.c.}(\omega) = \varepsilon_\infty\frac{\omega_p^2}{\omega^3\tau_p}, \qquad (4)$$

where ω_p and τ_p^{-1} are the frequency and decay rate of plasma oscillations, respectively.

At frequencies below the fundamental-absorption edge, the contribution $\varepsilon_{v.c.}(\omega)$ corresponds to the oscillations of shell valence electrons relative to the core under the action of light at the light wave frequency. As far as the effect of interband transitions is small, the quantities $\varepsilon_{v.c.}(\omega)$ and $\varepsilon_{ph}(\omega)$ can be combined and considered as the contribution to the dielectric function corresponding to the excitation of phonon–polaritons. Calculation of the spectral dependence of the phonon–polariton contribution can be performed within the model of a classical oscillator with dispersion:

$$\varepsilon'_{ph} = \varepsilon_\infty + \frac{(\varepsilon_s - \varepsilon_\infty)\left[1 - \left(\frac{\omega}{\omega_T}\right)^2\right]}{\left[1 - \left(\frac{\omega}{\omega_T}\right)^2\right]^2 + \left(\frac{\omega}{\omega_T}\right)^2\left(\frac{\tau_{ph}^{-1}}{\omega_T}\right)^2},$$

$$\varepsilon''_{ph} = \frac{(\varepsilon_s - \varepsilon_\infty)\left(\frac{\omega}{\omega_T}\right)\left(\frac{\tau_{ph}^{-1}}{\omega_T}\right)}{\left[1 - \left(\frac{\omega}{\omega_T}\right)^2\right]^2 + \left(\frac{\omega}{\omega_T}\right)^2\left(\frac{\tau_{ph}^{-1}}{\omega_T}\right)^2}, \qquad (5)$$

where τ_{ph}^{-1} is the decay rate of a phonon oscillator [3].

The results of calculation of the reflection coefficient in terms of the additive model (3) are shown in Fig. 3. As can be seen from Fig. 3, the additive model quite adequately describes the spectral behavior of the reflection coefficient in most of the frequency range under study.

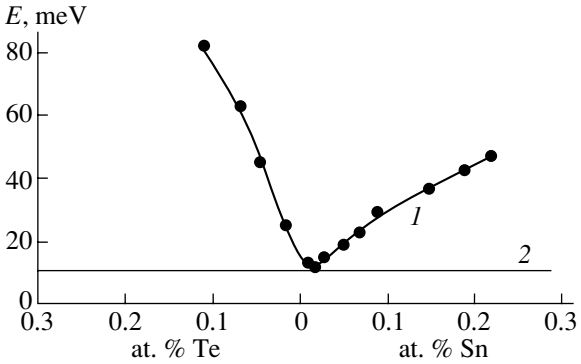

Fig. 2. (*1*) Energy of plasma oscillations in $Bi_{0.97}Sb_{0.03}$ single crystals ($\bar{K} \perp C_3$, $\bar{E} \parallel C_3$, $T = 80$ K) and (*2*) energy corresponding to the limiting frequency of longitudinal optical phonons in Bi, depending on the dopant concentration and type.

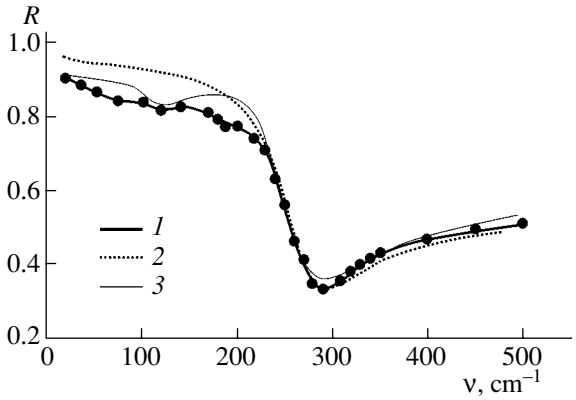

Fig. 3. Reflectance spectrum of a $Bi_{0.97}Sb_{0.03}$:Sn crystal with a content of Sn of 0.1 at. %: (1) experiment at $\bar{K} \perp C_3$, $\bar{E} \parallel C_3$, $T = 80$ K; (2) calculation in terms of the Drude model (see formulas (4)); and (3) calculation in terms of the additive model (3).

It is noteworthy that the dielectric function should be calculated with regard to the contribution of phonon–polaritons only in the case of $Bi_{0.97}Sb_{0.03}$ alloy crystals, which are characterized by anomalously small values of band gap width at the point *L* of the Brillouin zone (which, as was noted, leads to an increase in the polarizability of valence electrons). The decrease in the difference between the plasma resonance frequency of free charge carriers and the optical phonon frequency, which occurs when the above crystals are doped by acceptor impurities, leads to the formation of excitation known as the plasmon–phonon–polariton excitation. Here, the term *plasmon* means that free charge carriers

are involved in the formation of a polariton. The appearance of plasmon–phonon–polaritons in the case of similar energies of plasma oscillations and optical phonons is quite reasonable. This phenomenon is due to the fact that the energy accumulated by the electron gas in the form of longitudinal oscillations of charge density (plasma oscillations) is most likely dissipated into lattice vibrations via excitation of longitudinal optical phonons.

REFERENCES

1. E. Gerlah, P. Grosse, M. Rautenberg, and M. Senske, Phys. Status Solidi B **75**, 553 (1976).
2. W. S. Boyle and A. D. Brailsford, Phys. Rev. **120**, 1943 (1960).
3. P. Grosse, *Freie Elektronen in Festköpern* (Springer, Heidelberg, 1979; Mir, Moscow, 1982).
4. N. P. Stepanov and V. M. Grabov, Opt. Spektrosk. **84**, 581 (1998) [Opt. Spectrosc. **84**, 515 (1998)].
5. V. M. Grabov and N. P. Stepanov, Fiz. Tekh. Poluprovodn. (St. Petersburg) **35**, 155 (2001) [Semiconductors **35**, 149 (2001)].
6. T. M. Lifshits, A. B. Ormont, E. G. Chirkova, and A. Ya. Shul'man, Zh. Éksp. Teor. Fiz. **72**, 1130 (1977) [Sov. Phys. JETP **45**, 591 (1977)].
7. V. M. Grabov, V. V. Kudachin, A. S. Mal'tsev, and N. P. Stepanov, Izv. Vyssh. Uchebn. Zaved., Fiz., No. 3, 76 (1990).
8. F. E. Macfarlane, J. Phys. Chem. Solids **32**, 989 (1971).
9. I. L. Yarnell, I. L. Warren, R. G. Wenzel, and S. H. Koenig, IBM J. Res. Dev. **8**, 234 (1964).
10. J. Sosnowski, S. Bednarski, W. Buhrer, *et al.*, Phys. Status Solidi B **104**, 97 (1981).

Translated by Yu. Sin'kov

Semiconductors, Vol. 38, No. 5, 2004, pp. 537–542. Translated from Fizika i Tekhnika Poluprovodnikov, Vol. 38, No. 5, 2004, pp. 556–562.

ELECTRONIC AND OPTICAL PROPERTIES OF SEMICONDUCTORS

MOCVD Growth and Mg-Doping of InAs Layers

T. I. Voronina, T. S. Lagunova, S. S. Kizhayev*, S. S. Molchanov, B. V. Pushnyĭ, and Yu. P. Yakovlev

Ioffe Physicotechnical Institute, Russian Academy of Sciences, St. Petersburg, 194021 Russia

**e-mail: serguic@mail.ru*

Submitted October 27, 2003; accepted for publication November 4, 2003

Abstract—Epitaxial layers of Mg-doped InAs were grown by MOCVD, and electrical properties of these layers were studied. The doping with magnesium in the course of MOCVD growth allows one to obtain strongly compensated *p*-InAs with a high hole density ($p \approx 2 \times 10^{18}$ cm^{-3}) and a low carrier mobility ($\mu \approx 50$ cm^2/(V s)) at $T = 300$ K. When the samples are lightly doped with Mg, neutral impurities are bound with Mg, and *n*-type InAs layers with a carrier mobility exceeding that in undoped samples are formed. © *2004 MAIK "Nauka/Interperiodica".*

1. INTRODUCTION

Without intentional doping, InAs always has *n*-type conduction, regardless of the production method. In the Czochralski technique, crystallization proceeds from a near stoichiometric melt at a growth temperature of ~900°C. An *n*-type material is obtained, with a minimum electron density of $n \approx 10^{16}$ cm^{-3} and a mobility of $\mu \approx 5 \times 10^4$ cm^2/(V s) at $T = 77$ K, and $\mu \approx 2 \times 10^4$ cm^2/(V s) at $T = 300$ K. In this case, the conduction is controlled by shallow donor impurities S, Se, and Te with ionization energy $E_1 = 0.002$ eV, which are always present in the starting components.

In crystals synthesized at lower (500–650°C) temperatures by various epitaxial methods, studies of photoconductivity and temperature dependence of the Hall factor also reveal impurities with activation energy $E_2 =$ 0.02–0.03 eV, which are related to deviations from stoichiometry in the melt at the lower film growth temperature. According to the phase diagram, at these temperatures InAs crystallizes to form an As-deficient lattice. Consequently, there appears a donor-type structural defect, "As vacancy + impurity captured by this vacancy" (V_{As} + impurity), which raises the electron density in an epitaxial film. The ratio between the As and In content and, consequently, the number of structural defects and the electron density in a crystal depend on the growth temperature.

Materials of *p* type are most frequently obtained using zinc, which dissolves well in InAs and makes it possible to produce a material with the hole density $p > 1 \times 10^{18}$ cm^{-3}. However, the Zn impurity is characterized by a high diffusion rate, so it penetrates from epitaxial layers into the substrate, which may affect the properties of the material and their reproducibility. Also known is the use of Mn as an acceptor in InAs. In this case, the maximum carrier density is $p \approx (5–8) \times 10^{18}$ cm^{-3}. However, Mn produces deep levels in InAs, which reduces the efficiency of luminescence from the devices.

In this study, we investigated the doping of InAs with Mg. The diffusion coefficient of Mg is $D = 1.98 \times 10^{-6}$ cm^2/s, in contrast to Zn, for which $D = 3.11 \times 10^{-3}$ cm^2/s [1]. In all the III–V compounds produced by different methods, Mg replaces In atoms and behaves as an acceptor. Regarding the MOCVD technique, doping with Mg has been studied for GaAs layers [2], InP [3–5], GaInAsP and AlGaInP solid solutions [4, 6, 7], and InGaAs [4, 8], but the introduction of Mg into InAs layers has not been reported.

In this study, we made the first attempt to grow and study Mg-doped InAs layers using MOCVD. Our goal was to produce Mg-doped epitaxial InAs layers using MOCVD and to study their electrical properties. The conductivity, Hall factor *R*, mobility μ, and magnetoresistance $\Delta\rho/\rho$ were measured in samples with different levels of Mg doping in the temperature range $T = 77–300$ K. A comparison is made of results obtained for samples produced at the same substrate temperature and ratio of In and As components, but with different Mg concentrations.

2. EXPERIMENTAL RESULTS AND DISCUSSION

InAs layers were grown by MOCVD in a horizontal reactor at atmospheric pressure. The substrates were placed on a molybdenum holder with a resistance heater. Semi-insulating Cr-doped (111) GaAs or (100) InAs ($n \approx 2 \times 10^{16}$ cm^{-3}) were used as substrates. The total flow rate of hydrogen through the reactor was 16 l/min. Trimethylindium *TM*In and arsine AsH_3 diluted by hydrogen to 20% were used as precursors. To dope the epitaxial layers with Mg, we chose magnesium biscyclopentadienyl $(C_5H_5)_2Mg$. The photoluminescent properties of undoped InAs grown on InAs substrates were studied earlier in [9, 10], where the

Table 1. Parameters of undoped and Mg-doped InAs epitaxial layers

Sample no.	Amount of Mg introduced into the reactor, μmol min^{-1}	T = 300 K				T = 77 K			
		conduction type	carrier concentration, 10^{16} cm^{-3}	carrier mobility, cm^2/(V s)	$B_r^{\perp}$	conduction type	carrier concentration, 10^{16} cm^{-3}	carrier mobility, cm^2/(V s)	$B_r^{\perp}$
1	0	*n*	7.76	4450	0.55	*n*	7.7	4150	1.0
2	0.047	*n*	7.6	5220	1.1	*n*	6.4	7840	1.9
3	0.068	*n*	7.7	6430	0.6	*n*	6.35	11450	1.4
4	0.190	*n*	8.06	6320	0.95	*n*	1.4	9600	1.67
5	0.239	*n*	6.6	6130	1.1	*n*	5.8	9200	1.5
6	0.971	*n*	5.5	4250	0.83	*n*	1	4000	1.1
7	1.972	*n*				*n*			
8	3.223	*n*				*p*			
9	15.121	*n*				*p*			
*10**	15.121	*p*	180	50		*p*	125	40	

* Sample *10* was grown at 570°C; the growth temperature for other samples was 600°C.

optimal conditions for the layer growth were also determined: the ratio of components in the gas phase is V/III = 40; the growth temperature, 600°C; and the growth rate, 0.4 μm/h.

The basic parameters of the studied epitaxial layers, both Mg-doped and undoped, are listed in Table 1.

First, we will discuss the properties of samples not doped intentionally, which always had *n*-type conduction. Sample *1* is a typical representative of this kind of sample. In sample *1*, the electron density was $n_{77} = 7.8 \times 10^{16}$ cm^{-3} and $n_{300} = 8 \times 10^{16}$ cm^{-3}, and the electron mobility was $\mu_{77} = 4150$ cm^2/(V s) and $\mu_{300} = 4450$ cm^2/(V s). As can be seen, the electron mobility at this density is very low; it is defined not only by the scattering on lattice vibrations and impurity ions, but also by some additional factors. We will try to reveal their nature in our analysis of the temperature and field dependences of the Hall effect, mobility, and magnetoresistance in these samples.

We will now discuss the behavior of properties of InAs epitaxial layers as the amount of Mg introduced into the reactor is increased. When the amount of Mg dopant introduced is as low as 0.068 μmole/min, the electron density remains virtually unchanged, but the mobility increases by a factor of 2–3 (up to $\mu_{77} = 11450$ cm^2/(V s) in sample *3*). When the amount of Mg introduced into the reactor is raised to 0.19 μmole/min, the density of electrons in a layer and their mobility decrease. In sample *6*, $n_{77} = 5.2 \times 10^{16}$ cm^{-3}, $n_{300} = 5.5 \times 10^{16}$ cm^{-3}, $\mu_{77} = 4000$ cm^2/(V s), and $\mu_{300} = 4250$ cm^2/(V s). This indicates the beginning of compensation of impurities. As the amount of Mg introduced increases further, overcompensation of impurities takes place, starting from 3.223 μmole/min (sample *8*), and the InAs layers have *p*-type conduction (at T = 77 K) with a very low mobility ($\mu_{77} = 180$ cm^2/(V s)). At T = 300 K, the conduction is *n*-type. Similar behavior is observed when 15.121 μmole/min of Mg is introduced. We succeeded in obtaining *p*-type conduction at T = 300 and 77 K at the same Mg concentration, but with the growth temperature reduced to T = 570°C. In this case, the hole density in the layers was $p_{77} = 1.2 \times 10^{18}$ cm^{-3} and $p_{300} = 1.6 \times 10^{18}$ cm^{-3}, the mobility was low ($\mu_{77} = 40$ cm^2/(V s) and $\mu_{300} = 51$ cm^2/(V s)), and the layer morphology was very poor.

3. ANALYSIS OF RESULTS

We now turn to an analysis of the data obtained. First, we discuss the temperature dependence of the Hall factor R for all the samples under study. Figure 1 shows R as a function of the inverse temperature. It can be seen that the Hall factor remains virtually unchanged in the initial sample *1*, as well as in all the Mg-doped samples with the exception of sample *7*, which is indicative of the degeneracy of the electron gas. A small decrease in R can be seen only at high temperatures ($T > 210$ K), which can be attributed to the effect of deeper levels (not the hydrogen-like type) in the band gap ($E_D \approx 0.02$ eV). Anomalous behavior of $R(1/T)$ is observed in sample *7*. This can be attributed to a strong compensation of impurities, which leads to potential fluctuations and to the distortion of the conduction and valence band edges by the density-of-state "tails." In this case, according to the theory [11], the Hall factor does not reflect the carrier density of carriers, and the conduction occurs via the percolation level.

In *p*-type sample *10*, a maximum is observed in the temperature dependence of the Hall factor, which is an indication of impurity-band conduction ($p \approx 1.6 \times 10^{18}$ cm^{-3}) similar to Zn-doped InAs produced by the Czochralski method.

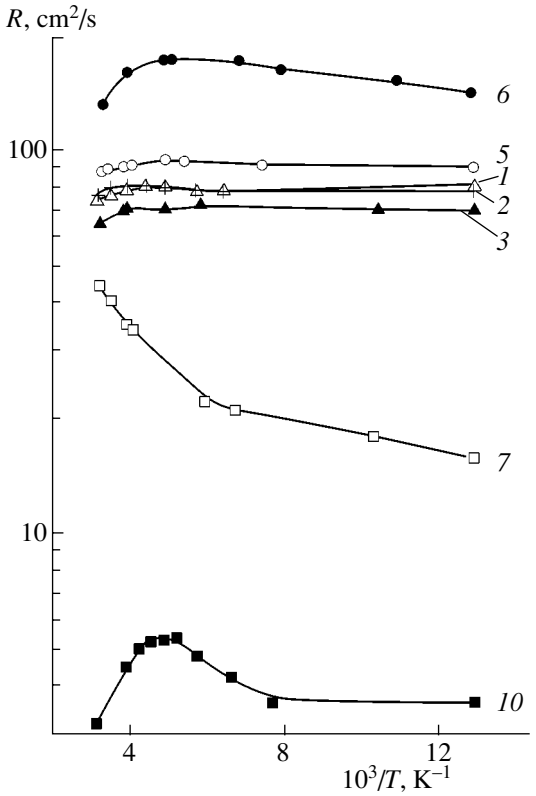

Fig. 1. The Hall constant vs. the inverse temperature. Curve numbers correspond to the sample numbers in Table 1.

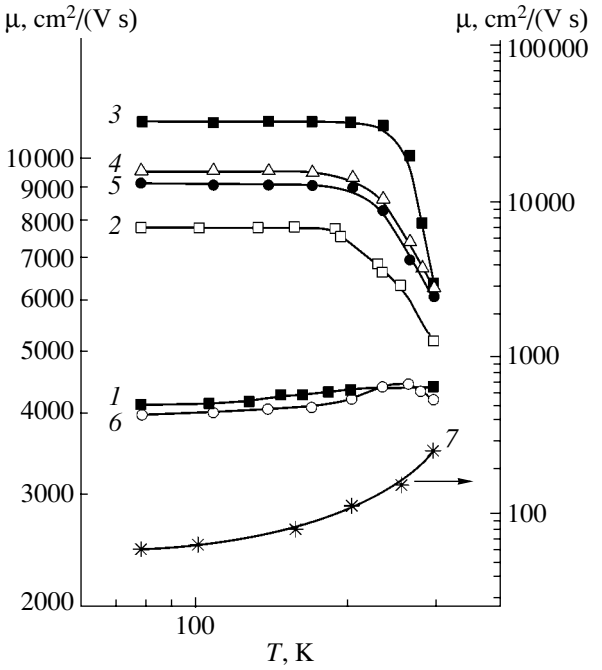

Fig. 2. Temperature dependences of mobility. Curve numbers correspond to the sample numbers in Table 1.

We will now analyze the mobility of carriers in the studied samples. It is well known that mobility, as well as magnetoresistance, are effects that are sensitive to the scattering mechanism and to the type of scattering centers. Figure 2 shows the temperature dependences of mobility. In all the samples, even in the initial undoped sample *1*, the mobility μ_e measured in the temperature range 77–300 K is very low. Normally, a low mobility may be related to the compensation of carriers. However, the form of the temperature dependence (a weak dependence at low temperatures) does not confirm this assumption but rather indicates the existence of some additional mechanisms of scattering (μ_{def}), which differ from the scattering on lattice vibrations (μ_{lat}) and ionized impurities (μ_{ion}). The experimental mobility is determined by the sum of these three components:

$$1/\mu_e = 1/\mu_{ion} + 1/\mu_{lat} + 1/\mu_{def}. \quad (1)$$

In turn, μ_{def} may be determined by several scattering mechanisms. First, this may be scattering on space charges, which reduces the room-temperature mobility to the greatest extent. The related mobility μ_s is temperature-dependent: $\mu_s \propto T^{-0.9}$ [12]. Second, there can exist large neutral clusters of impurities and defects, which distort the current-flow lines and reduce the mobility. In terms of the effective-medium theory [13], we can determine the mobility in the conducting matrix (μ_0) and the fraction of the volume occupied by a cluster. One other type of additional scattering is associated with neutral impurity atoms; in these cases, the mobility μ_N is temperature-independent and

$$\mu_N = 3.08 \times 10^{19}/N, \quad (2)$$

where N is the concentration of neutral impurities.

A complete pattern of the scattering mechanisms in the samples under study can be obtained from a combined analysis of the mobility and magnetoresistance, both transverse $(\Delta\rho/\rho)^{\perp}$ and longitudinal $(\Delta\rho/\rho)^{\parallel}$. The transverse magnetoresistance, i.e., the change in resistance in the magnetic field directed perpendicularly to the current-flow lines in the sample, is the sum of physical component $(\Delta\rho/\rho)_{phys}$, which is determined by the Lorentz mobility, and the component $(\Delta\rho/\rho)_{un\ hom}$, which is related to different inhomogeneities (clusters of defects, impurities, dislocations, etc.):

$$\Delta\rho/\rho = (\Delta\rho/\rho)_{phys} + (\Delta\rho/\rho)_{un\ hom}. \quad (3)$$

In a weak magnetic field (at $\mu H/c \le 1$), the physical magnetoresistance

$$\Delta\rho/\rho = B_r(\mu H/c)^2 \quad (4)$$

is proportional to H^2, and the coefficient B_r is determined by the mechanism of scattering and, according to the theory, cannot exceed 0.56. As can be seen in Table 1, $B_r > 0.56$ for all the samples studied, which indicates that the mobility is reduced and additional scattering mechanisms or inhomogeneities exist. Figure 3 shows $(\Delta\rho/\rho)^{\perp}$ as a function of H at $T = 77$ K. In

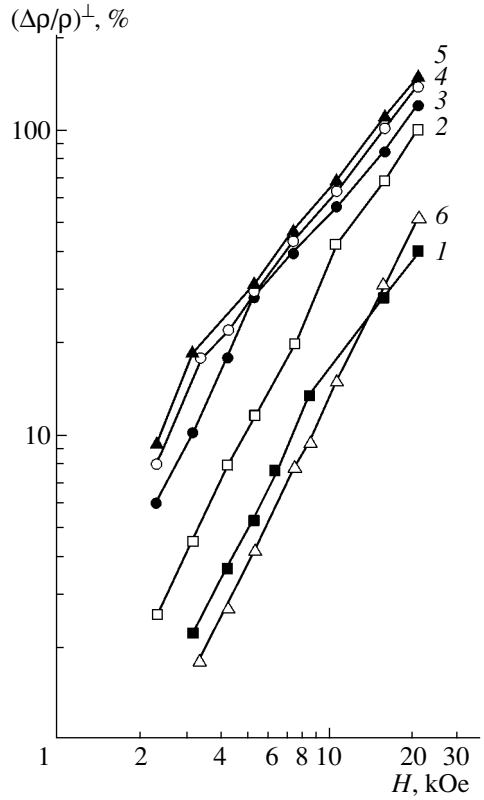

Fig. 3. Transverse magnetoresistance $(\Delta\rho/\rho)^{\perp}$ at $T = 77$ K vs. the magnetic field intensity at $T = 77$ K. Curve numbers correspond to the sample numbers in Table 1.

all the samples, $(\Delta\rho/\rho)^{\perp}$ increases in proportion to $\propto H^2$2 in a weak magnetic field (H < 4–5 kOe), and a deviation from quadratic behavior is observed in higher fields. It is noteworthy that the termination of the quadratic behavior depends on the carrier mobility in the samples, but it occurs at lower field values than would follow from the condition $\mu H/c = 1$, where μ is the mobility determined in the experiment. This fact indicates that the Lorentz mobility μ_{Lor}, related to scattering on impurity ions and lattice vibrations, is much higher than the Hall mobility measured in the experiment. The values of μ_{Lor}, calculated from the condition $\mu H/c = 1$, where H is the field at which the quadratic dependence terminates, are listed in Table 2. This mobility was used in the calculation of the donor and acceptor concentrations in the samples under study.

The principal indicator of the type of inhomogeneities in a sample is the longitudinal magnetoresistance, $(\Delta\rho/\rho)^{\parallel}$, i.e., the case when H and I vectors are in parallel.

In a homogeneous isotropic semiconductor, such as InAs, there should be no longitudinal magnetoresistance, i.e., $(\Delta\rho/\rho)^{\parallel} = 0$. If a sample is inhomogeneous, $(\Delta\rho/\rho)^{\parallel}$ may differ from zero. Two situations are possible: $(\Delta\rho/\rho)^{\parallel} > 0$ and $(\Delta\rho/\rho)^{\parallel} < 0$.

If $(\Delta\rho/\rho)^{\parallel}$ is positive, then that is an indication that large neutral clusters which distort the current-flow paths exist. In this case, kinetic effects are described in terms of the effective-medium theory as follows:

$$\sigma = \sigma_0(1 - 3/2\,f), \tag{5}$$

$$R = R_0/(1 - 3/4\,f), \tag{6}$$

$$\mu = \mu_0(1 - 3/2\,f)(1 - 3/4\,f), \tag{7}$$

$$(\Delta\rho/\rho)^{\parallel} = 0.3\,f(\mu_0 H/c)^2, \tag{8}$$

where σ_0, R_0, and μ_0 are the values of these parameters in the crystal matrix, and f is the fraction of the volume occupied by inhomogeneities.

Among the studied samples, only three (nos. *1*, *6*, and *7*) demonstrated positive longitudinal magnetoresistance. The values of μ_0 and f, determined from the measured $(\Delta\rho/\rho)^{\parallel}$, are listed in Table 2. For these samples, the mobility in the matrix, μ_0, was used as the experimental mobility in the calculation of N_A, N_D, and the compensation ratio

$$k = N_A/N_D. \tag{9}$$

We now turn to the case when $(\Delta\rho/\rho)^{\parallel} < 0$. This is possible in the case of random distribution of impurities in heavily doped and strongly compensated materials,

Table 2. Calculated values of N_A, N_D, N_N, and k

Sample no.	Amount of Mg introduced, μmol min^{-1}	μ_{Lor}, cm^2/(V s)	μ_0, cm^2/(V s)	f	μ_s^{300}, cm^2/(V s)	μ_s^{77}, cm^2/(V s)	μ_N^{77}, cm^2/(V s)	N_A, 10^{16} cm^{-3}	N_D, 10^{17} cm^{-3}	N_N, 10^{15} cm^{-3}	k
1	0	14300	5500	0.2	7600	28000	13400	6.2	1.4	23	0.44
2	0.047	22000	7840		7140	27800	21700	2.55	1.05	1.4	0.24
3	0.068	25000	11450		9500	37000	50000	2	1.05	0.6	0.2
4	0.190	25000	9800		9170	35700	25000	2	9.2	1.2	0.22
5	0.239	25000	9600		9260	36000	28000	1.9	1.07	1.1	0.18
6	0.971	8400	4200	0.06	5460	21300	13900	11	1.65	2.2	0.66
7	1.972		920	0.56							

when the impurity compensation ratio $k \approx 0.7$ and when potential fluctuations, distortions of the conduction band bottom, and density-of-state "tails" appear. Figure 4 shows $(\Delta\rho/\rho)^{\parallel}$ and $(\Delta\rho/\rho)^{\perp}$ as functions of the magnetic field H for samples *6* and *7* at $T = 77$ and 300 K.

As mentioned above, the decrease in mobility may be related to the existence of neutral impurities in crystals. We believe that these defects are present in those samples in which taking into account large defect clusters (in terms of the effective-medium model) and space charges, together with scattering on lattice vibrations and ionized impurities, fails to give the experimental mobility. It is necessary to add the scattering on neutral impurities. Thus,

$$1/\mu_e = 1/\mu_{\text{lat}} + 1/\mu_{\text{ion}} + 1/\mu_s + 1/\mu_N. \quad (10)$$

We will now trace the entire sequence of calculation of the sample parameters. At $T = 300$ K, we obtain μ_s from the relation

$$1/\mu_e = 1/\mu_{\text{lat}} + 1/\mu_{\text{ion}} + 1/\mu_s. \quad (11)$$

Since $\mu_{\text{ion}} \gg \mu_{\text{lat}}$ at $T = 300$ K, we obtain

$$1/\mu_s = 1/\mu_e - 1/\mu_{\text{lat}}, \quad (12)$$

$\mu_{\text{lat}} \approx 20000$ cm^2/(V s).

Taking into account the temperature dependence $\mu_s \propto T^{-0.9}$, we find μ_s at $T = 77$ K. Then at $T = 77$ K we have

$$1/\mu_0 = 1/\mu_{\text{lat}} + 1/\mu_{\text{ion}} + 1/\mu_s + 1/\mu_N, \quad (13)$$

since

$$1/\mu_{\text{Lor}} = 1/\mu_{\text{lat}} + 1/\mu_{\text{ion}}, \quad (14)$$

and then

$$1/\mu_N = 1/\mu_0 - 1/\mu_{\text{Lor}} - 1/\mu_s. \quad (15)$$

All the terms on the right are known, so we find μ_N and use relation (2) to obtain the concentration of neutral impurities, N (Table 2).

The concentrations of impurity ions N_{ion}, donors N_D, acceptors N_A, and the compensation ratio $k = N_A/N_D$ are determined from the comparison of the theoretical value of mobility, related to scattering on lattice vibrations and ionized impurities and calculated for the given carrier density, with the experimental values determined from the end of the range of a quadratic dependence of $(\Delta\rho/\rho)^{\perp}$ on H:

$$N_{\text{ion}} = (\mu_{\text{theor}}/\mu_{\text{Lor}_{77}})n_{77}, \quad (16)$$

$$N_A = (N_{\text{ion}} - n_{77})/2, \quad (17)$$

$$N_D = N_A + n_{300}, \quad (18)$$

$$k = N_A/N_D.$$

Calculated values of N_A, N_D, N_N, and k are listed in Table 2.

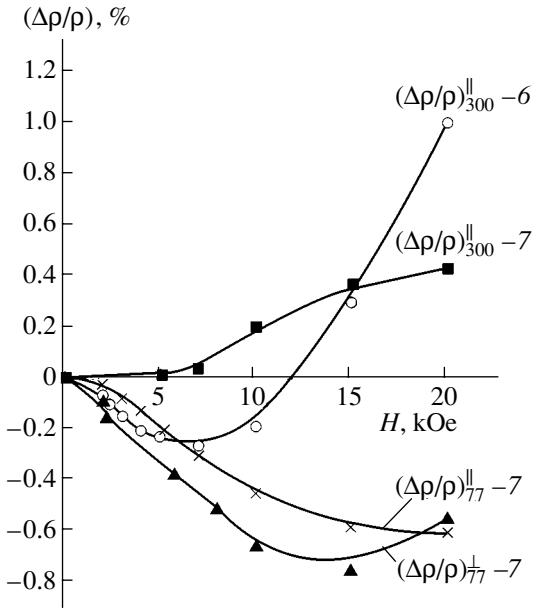

Fig. 4. Longitudinal and transverse magnetoresistance vs. the magnetic field intensity for samples *6* and *7* at $T = 77$ and 300 K. Curve numbers correspond to the sample numbers in Table 1.

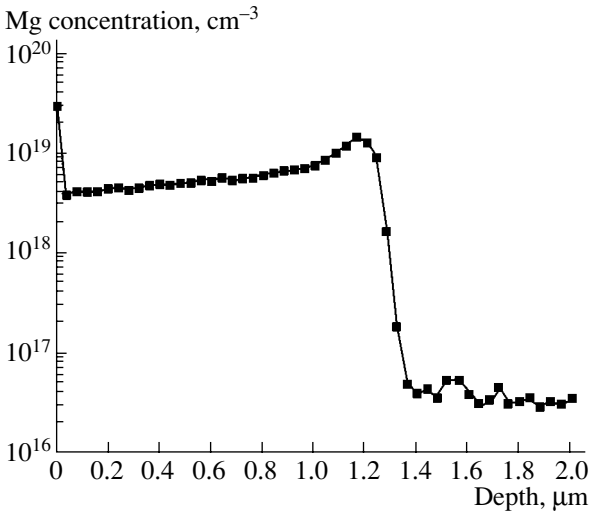

Fig. 5. The cross-sectional distribution of Mg atoms in sample *8*.

Figure 5 shows the Mg concentration profile in sample *8*, measured by SIMS. As can be seen in the figure, the concentration of Mg atoms in the layer is $3–5 \times 10^{18}$ cm^{-3}, and it changes stepwise across the interface between the InAs epitaxial layer and the substrate. The concentration of Mg atoms in the substrate lies at the sensitivity limit of the equipment, $\sim 5 \times 10^{16}$ cm^{-3}.

The reason why *p*-type conduction cannot be obtained at a growth temperature of 600°C remains unclear. It is possible that this case is similar to the sit-

uation observed with Mg doping of InP layers [4]. Starting from some definite concentration of Mg atoms in the layer, Mg is incorporated as a substituting acceptor and, simultaneously, as an interstitial donor, which results in the formation of the donor–acceptor pairs. When the temperature is reduced to 570°C, the Mg segregation coefficient increases, and the incorporation mechanisms are probably different.

During the doping of InAs epitaxial layers, Mg was deposited onto the reactor walls and within the gas system, which resulted in the background doping of InAs epitaxial layers with Mg. Thus, the "residual memory" effect was observed, which was earlier observed in Mg-doped epitaxial layers of GaAs, InP, and InGaAs solid solutions [2, 5, 7].

4. CONCLUSION

The undoped MOCVD-grown InAs epitaxial films studied always had *n*-type conduction ($n \approx 7 \times 10^{16}$ cm^{-3}) with a rather low mobility ($\mu_{77} \approx 4000$ cm^2/(V s)), which is related to the large number of defects and high concentration of shallow donors and acceptors ($N_A = 5.3 \times 10^{16}$ cm^{-3}, $N_D = 1.3 \times 10^{16}$ cm^{-3}, compensation ratio $k = 0.4$). The significant decrease in mobility is also related to the high concentration of neutral impurities ($N_N = 4.3 \times 10^{16}$ cm^{-3}), which are possibly un-ionized structural defects with the activation energy $E_D \approx 0.02$ eV (V_{As} + impurity).

In Mg-doping of the layers, the experimentally determined mobility at first sharply increases to $\mu_{77} = 7800$ cm^2/(V s) when a very small amount of Mg is introduced (0.047 μmole/min), while the electron density remains virtually unchanged. As can be seen in Table 2, the concentration of neutral impurities in this case decreases by a factor of 30 (from 4.3×10^{16} to 1.6×10^{15} cm^{-3}), and the mobility depression related to the distortion of current-flow paths disappears ($(\Delta\rho/\rho)^{\parallel}$ is zero). As the Mg concentration in epitaxial films is raised further (0.068 μmole/min), the electron mobility increases, but the electron density remains virtually unchanged. The compensation ratio in these samples is constant (0.2–0.24), and the concentration of donors and acceptors does not change. The concentration of neutral impurities decreases to an even greater extent (to ~6×10^{14} cm^{-3} in sample *3*). All these facts may indicate that, in the Mg-doped epitaxial films under study, residual impurity atoms can react with Mg, thus lowering the concentration of neutral centers.

Overcompensation in InAs:Mg films becomes noticeable when the amount of introduced Mg is 3.223 μmole/min (sample *6*): the electron density and mobility decrease, the acceptor concentration increases, and the compensation ratio becomes higher ($k = 0.66$). In these heavily doped and strongly compensated samples, negative transverse magnetoresistance $(\Delta\rho/\rho)^{\perp}$ is observed at $T = 77$ K, and at $T = 300$ K a small longitudinal magnetoresistance $(\Delta\rho/\rho)^{\parallel}$ arises. The observation of these two effects indicates that (i) these samples contain a small amount of large neutral clusters, which distort the current-flow lines (in accordance with the effective-medium theory, $f = 0.06$, $\mu_0 = 920$ cm^2/(V s)), and (ii) there exist potential fluctuations, which produce the density-of-states tails. When the amount of Mg exceeds 3.223 μmole/min, the compensation of carriers increases to an even greater extent (sample *7*), which is demonstrated by the anomalous temperature dependence of the Hall factor (Fig. 1). Negative magnetoresistance is observed at $T = 77$ K, and a positive longitudinal magnetoresistance at room temperature is indicative of the presence of large clusters (in terms of the effective-medium theory, the mobility in matrix $\mu_0 = 920$ cm^2/(V s) and the volume fraction occupied by inhomogeneities $f = 0.56$) (Fig. 4).

The type of conduction in epitaxial layers was changed at a Mg flow rate of 3.223 μmole/min. Conduction of *p*-type was observed at $T = 77$ K, while *n*-type conduction was at $T = 300$ K. Samples of *p*-type ($p = 10^{18}$ cm^{-3}) were reliably obtained only at a lower growth temperature (570°C), but the carrier mobility in these samples was very low.

Thus, Mg-doping of InAs in the course of MOCVD growth allowed us to produce strongly compensated *p*-InAs with the maximum hole density ($p \approx 2 \times 10^{18}$ cm^{-3}) and low carrier mobility ($\mu \approx 50$ cm^2/(V s) at $T = 300$ K). It is noteworthy that, at a low level of doping with Mg (0.068 μmole/min), the *n*-InAs layers crystallized had a higher mobility than that in undoped InAs samples because of the binding of neutral impurities by Mg.

REFERENCES

1. P. I. Baranskiĭ, V. P. Klochkov, and I. V. Potykevich, *Semiconductor Electronics* (Naukova Dumka, Kiev, 1975), p. 424.
2. M. Kondo, C. Anayama, H. Sekiguchi, and T. Tanahasni, J. Cryst. Growth **141**, 1 (1994).
3. A. W. Nelson and L. D. Westbrook, J. Cryst. Growth **68**, 102 (1984).
4. E. Veuhoff and H. Baumeister, J. Cryst. Growth **105**, 353 (1990).
5. E. Veuhoff, H. Baumeister, J. Rieger, *et al.*, J. Electron. Mater. **20**, 1037 (1991).
6. R. Winterhoff, P. Raisch, V. Frey, *et al.*, J. Cryst. Growth **195**, 132 (1998).
7. G. J. Bauhuis, P. R. Hageman, and P. K. Larsen, J. Cryst. Growth **191**, 313 (1998).
8. M. Ohkubo, J. Osabe, T. Shiojima, *et al.*, J. Cryst. Growth **170**, 177 (1997).
9. T. I. Voronina, N. V. Zotova, S. S. Kizhaev, *et al.*, Fiz. Tekh. Poluprovodn. (St. Petersburg) **33**, 1168 (1999) [Semiconductors **33**, 1062 (1999)].
10. S. S. Kizhayev, N. V. Zotova, S. S. Molchanov, and Y. P. Yakovlev, IEE Proc.: Optoelectron. **149**, 36 (2002).
11. A. Ya. Shik, Pis'ma Zh. Éksp. Teor. Fiz. **20**, 14 (1974) [JETP Lett. **20**, 5 (1974)].
12. L. R. Weisberg, J. Appl. Phys. **33**, 1817 (1962).
13. M. H. Cohen and J. Jorther, Phys. Rev. Lett. **30**, 696 (1973).

Translated by D. Mashovets

Semiconductors, Vol. 38, No. 5, 2004, pp. 543–545. Translated from Fizika i Tekhnika Poluprovodnikov, Vol. 38, No. 5, 2004, pp. 563–565.

ELECTRONIC AND OPTICAL PROPERTIES OF SEMICONDUCTORS

Coefficients of Capture of Free Excitons by Shallow Acceptors and Donors in Gallium Arsenide

K. D. Glinchuk*, N. M. Litovchenko, and O. N. Strilchuk**

Lashkarev Institute of Semiconductor Physics, National Academy of Sciences of Ukraine, Kiev, 03028 Ukraine

**e-mail: ria@isp.kiev.ua*

***e-mail: strilchuk@isp.kiev.ua*

Submitted August 5, 2003; accepted for publication September 25, 2003

Abstract—The excitonic luminescence spectra of semi-insulating GaAs crystals with various concentrations of shallow acceptors (C) and donors (Si) were measured at 4.2 K. An analysis of these spectra made it possible to determine the coefficients of capture of free excitons by shallow neutral acceptors [$b_{A^0X} = (4 \pm 2) \times 10^{-8}$ cm^3/s] and donors [$b_{D^0X} = (1.5 \pm 0.8) \times 10^{-7}$ cm^3/s] at liquid-helium temperature and also to estimate the coefficient of capture of free excitons by shallow ionized donors ($b_{D^+X} \gg b_{D^0X}$). © *2004 MAIK "Nauka/Interperiodica".*

1. INTRODUCTION

It is well known that the processes of binding of free excitons X by shallow neutral acceptors A^0 and also by ionized (D^+) and neutral (D^0) donors are active in semiconductors; henceforth, the concentrations of excitons, neutral acceptors, and ionized and neutral donors are denoted by n_X, N_{A^0}, N_{D^+}, and N_{D^0}, respectively. These processes give rise to exciton–impurity complexes; the latter include the complex A^0X, which consists of a neutral acceptor and an exciton; the complex D^+X, which consists of an ionized donor and an exciton; and the complex D^0X, which consists of a neutral donor and an exciton. Important characteristics of the rate of the processes under consideration are the coefficients of capture of free excitons by neutral acceptors (b_{A^0X}), ionized donors (b_{D^+X}), and neutral donors (b_{D^0X}). However, there are almost no published data on the aforementioned coefficients. Only Lipnik [1] considered theoretically the process of binding of free excitons by neutral impurities in semiconductors (unfortunately, an expression for b_{A^0X} was not derived in [1]). In addition, an attempt was made in [2, 3] to estimate the coefficient of capture of free excitons by shallow neutral and ionized traps in CdS: $b_{A^0X} = 3 \times 10^{-10}$ cm^3/s (or 3×10^{-7} cm^3/s if a different model is used), according to [2], and $b_{D^+X} = 6 \times 10^{-8}$ cm^3/s and $b_{D^0X} = 6 \times 10^{-9}$ cm^3/s, according to [3]. In this study, we measured the spectra of excitonic luminescence of semi-insulating GaAs crystals at $T = 4.2$ K (these crystals are photoconductors at low temperatures [4]) with various concentrations of shallow acceptors N_A and donors N_D. We analyzed these spectra and determined the coefficients b_{A^0X} and b_{D^0X} and estimated the coefficient b_{D^+X}.

2. A METHOD FOR DETERMINING THE COEFFICIENTS b_{A^0X}, b_{D^+X}, AND b_{D^0X}

Evidently, the conductivity of photoconductors is controlled by nonequilibrium electrons and holes. The concentrations of neutral and ionized impurity centers at $T = 4.2$ K are given by $N_{A^0} = N_{D^0} = 0$ and $N_{D^+} = N_D$ in the dark and $N_{A^0} \approx N_A$ and $N_{D^0} \approx N_D \gg N_{D^+}$ under illumination.[1] The intensities of luminescence bands caused by annihilation of exciton–impurity complexes A^0X (I_{A^0X}), D^+X (I_{D^+X}), and D^0X (I_{D^0X}) and also of free excitons X (I_X) are defined by the following expressions [4]:

$$I_{A^0X} = b_{A^0X} N_{A^0} n_X \approx b_{A^0X} N_A n_X, \quad (1)$$

$$I_{D^+X} = b_{D^+X} N_{D^+} n_X, \quad (2)$$

$$I_{D^0X} = b_{D^0X} N_{D^0} n_X \approx b_{D^0X} N_D n_X, \quad (3)$$

$$I_X = \alpha_X n_X. \quad (4)$$

Here, α_X is the probability of radiative annihilation of a free exciton; $\alpha_X = 2.5 \times 10^8$ s^{-1} at 4.2 K, as follows from the decay time of luminescence caused by annihilation

[1] The above expressions for N_{A^0}, N_{D^+}, and N_{D^0} in a photoconductor under illumination are valid for isolated acceptors and donors [4]. Free excitons are found to be bound mainly to these isolated impurities in semi-insulating GaAs [5].

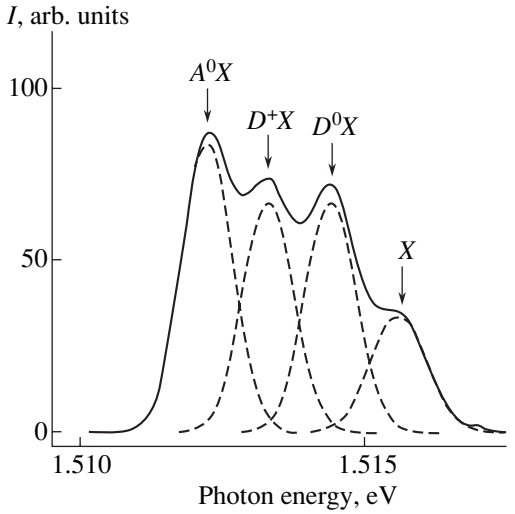

Fig. 1. Luminescence bands related to the bound (A^0X, D^+X, and D^0X) and free (X) excitons in semi-insulating gallium arsenide at $T = 4.2$ K.

of free excitons $\tau_X = 1/\alpha_X \approx 4$ ns at liquid-helium temperature [6].[2] When deriving formulas (1)–(4), we assumed that, first, the concentrations of donors and acceptors that bound the excitons are low and, second, the annihilation of free and bound excitons is mainly accompanied by the emission of photons. As can be seen from formulas (1)–(4), the quantities b_{A^0X}, b_{D^+X}, and b_{D^0X} can be expressed as

$$b_{A^0X} = \frac{I_{A^0X}}{I_X}\frac{\alpha_X}{N_A},\quad b_{D^+X} = \frac{I_{D^+X}}{I_X}\frac{\alpha_X}{N_{D^+}},$$
$$b_{D^0X} = \frac{I_{D^0X}}{I_X}\frac{\alpha_X}{N_D}, \tag{5}$$

if we use experimental relative intensities of excitonic-luminescence bands I_{A^0X}/I_X, I_{D^+X}/I_X, and I_{D^0X}/I_X, the concentrations of shallow acceptors and donors, and the known value of probability α_X.

3. EXPERIMENTAL

We used semi-insulating GaAs crystals in our experiments. The dark conductivity of these crystals was controlled by ionization of partially compensated deep donors (defects *EL*2). Their concentration $N_{EL2} \approx 2 \times 10^{16}$ cm$^{-3} > N_A - N_D > 0$. The resulting resistivity $\rho \simeq 4 \times 10^7$ Ω cm at $T = 300$ K. Under illumination (with intensity L) at $T = 4.2$ K, the conductivity was controlled by photoexcited electrons and holes [4]. We analyzed the spectra of excitonic luminescence of semi-insulating GaAs crystals with known (to within ±30%) concentrations of shallow acceptors (C) N_A and donors (Si) N_D; the spectra were measured at $T = 4.2$ K. When resolved (to within ±20%) into separate components, the spectra included the luminescence bands related to annihilation of bound excitons A^0X (the luminescence peak at $h\nu_m = 1.512$ eV), D^+X ($h\nu_m = 1.5133$ eV), and D^0X ($h\nu_m = 1.5141$ eV) and also of free excitons X ($h\nu_m = 1.5153$ eV) (see Fig. 1). The intensities I_{A^0X}, I_{D^+X}, I_{D^0X}, and I_X were determined for various concentrations of shallow acceptors and donors. For the excitation intensities L, the quantities I_{A^0X}, I_{D^+X}, I_{D^0X}, and I_X increased quadratically with L [4, 5]:

$$I_{A^0X}, I_{D^+X}, I_{D^0X}, I_X \propto L^2.$$

As expected [4], the normalized (caused by annihilation of bound excitons A^0X) intensity I_{A^0X}/I_X varied in proportion to N_A, whereas the normalized (caused by annihilation of bound excitons D^0X) intensity I_{D^0X}/I_X varied in proportion to N_D; i.e., $I_{A^0X}/I_X \propto N_A$ and $I_{D^0X}/I_X \propto N_D$ (see Fig. 2).

4. RESULTS AND DISCUSSION

We used formula (5) to determine the following values of coefficients of capture of free excitons by neutral acceptors and by ionized and neutral donors at $T = 4.2$ K:

$$b_{A^0X} = (4 \pm 2) \times 10^{-8}\ \text{cm}^3/\text{s},$$

$$b_{D^0X} = (1.5 \pm 0.8) \times 10^{-7}\ \text{cm}^3/\text{s},\quad b_{D^+X} \gg b_{D^0X}.$$

The value of b_{D^+X} was estimated from the experimentally observed relations $N_{D^+} \ll N_D$ and $I_{D^+X}/I_{D^0X} = b_{D^+X}N_{D^+}/b_{D^0X}N_{D^0} \leq 1$. Consequently, the coefficients b_{A^0X}, b_{D^+X}, and b_{D^0X} in gallium arsenide are related as $b_{A^0X} < b_{D^0X} \ll b_{D^+X}$.

These relations between the coefficients under consideration can be explained in the following way. The formation of the bound excitons A^0X, D^+X, and D^0X occurs as a result of attraction of free excitons to acceptors and donors. This attraction is caused by the dipole–dipole interaction (this corresponds to the formation of complexes A^0X and D^0X) and charge–dipole interaction (the formation of complexes D^+X). It is evident that the appearance of dipoles is related to the mutual polarization of free excitons and neutral acceptors and donors. Undoubtedly, the dipole moment of neutral acceptors is

[2] It is worth noting that, if free excitons have a Maxwell distribution at low temperatures, then theoretically $\alpha_X = 3 \times 10^9$ s^{-1} [7]. The difference between experimental and theoretical values of α_X indicates that free excitons do not have a Maxwell distribution at low temperatures.

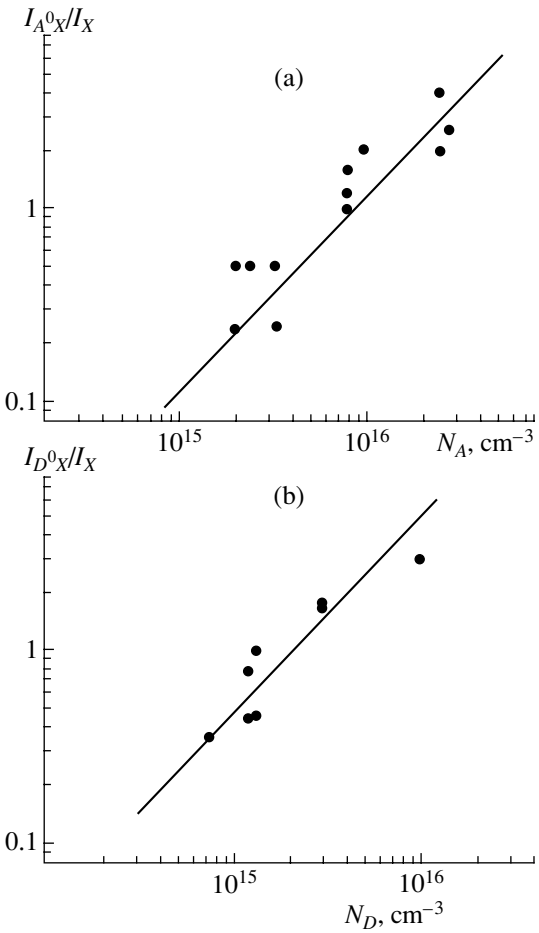

Fig. 2. Dependences (a) $I_{A^0X}/I_X = f(N_A)$ and (b) $I_{D^0X}/I_X = f(N_D)$ in semi-insulating gallium arsenide at T = 4.2 K. Straight lines correspond to the theoretical dependences [derived using formulas (1), (3), and (4)] (a) $I_{A^0X}/I_X = (b_{A^0X}/\alpha_X)N_A$ and (b) $I_{D^0X}/I_X = (b_{D^0X}/\alpha_X)N_D$, where $b_{A^0X} = 4 \times 10^{-8}$ cm^3/s, $b_{D^0X} = 1.5 \times 10^{-7}$ cm^3/s, and $\alpha_X = 3 \times 10^8$ s^{-1}. The mean deviation of experimental points from theoretical straight lines illustrates the accuracy of determination of coefficients b_{A^0X} and b_{D^0X}.

smaller than that of neutral donors. This inference follows from comparison of the Bohr radii of holes bound to acceptors with those of electrons bound to donors. The dipole moment of ionized donors is much larger than that of neutral donors.

The obtained values of the coefficients b_{A^0X}, b_{D^+X}, and b_{D^0X} in GaAs are fairly large. This fact is indicative of a very high efficiency of binding of free excitons by shallow acceptors and donors in gallium arsenide.

5. CONCLUSION

The obtained experimental values of the coefficients of capture of free excitons by neutral acceptors and by ionized and neutral donors in gallium arsenide are important for gaining insight into the mechanisms of formation of various exciton–impurity complexes in intermetallic semiconductors. These mechanisms are being actively investigated at present.

REFERENCES

1. A. A. Lipnik, Fiz. Tverd. Tela (Leningrad) **3**, 2322 (1961) [Sov. Phys. Solid State **3**, 1683 (1962)].
2. D. Magde and H. Mahr, Phys. Rev. B **2**, 4098 (1970).
3. V. L. Broude, I. I. Tartakovskiĭ, and V. B. Timofeev, Fiz. Tverd. Tela (Leningrad) **14**, 3531 (1972) [Sov. Phys. Solid State **14**, 2971 (1972)].
4. K. D. Glinchuk and A. V. Prokhorovich, Fiz. Tekh. Poluprovodn. (St. Petersburg) **36**, 519 (2002) [Semiconductors **36**, 487 (2002)].
5. K. D. Glinchuk and A. V. Prokhorovich, Semicond. Phys. Quantum Electron. Optoelectron. **5**, 353 (2002).
6. G. W. Hooft, W. A. Poel, L. W. Molenkamp, and C. T. Foxon, Phys. Rev. B **35**, 8281 (1987).
7. A. P. Levanyuk and V. V. Osipov, Usp. Fiz. Nauk **133**, 427 (1981) [Sov. Phys. Usp. **24**, 187 (1981)].

Translated by A. Spitsyn

Semiconductors, Vol. 38, No. 5, 2004, pp. 546–549. Translated from Fizika i Tekhnika Poluprovodnikov, Vol. 38, No. 5, 2004, pp. 566–569.

SEMICONDUCTOR STRUCTURES, INTERFACES, AND SURFACES

Variation in the Built-in Potential of a Photodiode Based on an *n*-InSe–*p*-GaSe Heterojunction in the Course of Aging

S. I. Drapak*, V. B. Orletskii, and Z. D. Kovalyuk

Frantsevich Institute for Problems in Materials Science (Chernovtsy Branch), National Academy of Sciences of Ukraine, ul. Zhovtneva 5, Chernovtsy, 58001 Ukraine

**e-mail: chimsp@unicom.cv.ua*

Submitted September 24, 2003; accepted for publication October 17, 2003

Abstract—Variations in the built-in potential of optical contact between *n*-InSe and *p*-GaSe in the course of long-term (over 10 years) storage under normal ambient conditions were investigated in the case of *n*-InSe–*p*-GaSe heterostructures. It was found that the above potential increases considerably with time. This increase is accounted for by the fact that the surfaces of InSe and GaSe become closer to each other as a result of the diffusive spread of oxygen originally adsorbed at the interface into the bulk of the contacting semiconductors. As a result, InSe/GaSe islands are formed and shunt the structure (regions of real close InSe/GaSe contact are formed). © *2004 MAIK "Nauka/Interperiodica".*

The *n*-InSe–*p*-GaSe heterojunction (HJ) is the first photosensitive structure formed by bringing the surfaces of two semiconductors into direct contact; these surfaces are obtained by cleaving in atmospheric air [1]. The results of studying the electrical, photoelectric, luminescent, and other properties of these structures were reported previously [1–4]. In a number of publications (see, e.g., [5]), it was suggested that this HJ be used as a photodiode that could replace traditional silicon-based analogues designed for operation under conditions of severe irradiation. In all the publications devoted to research on various properties of the aforementioned structure, the contact-potential difference (CPD) V_0 determined from both the capacitance–voltage and current–voltage characteristics was equal to ~0.5 V with a certain spread (up to 20%), depending on the ratio between the charge-carrier concentrations in the contacting semiconductors [1–5]. In this case, it is traditionally believed that, due to the natural anisotropy of chemical bonds in and between the layers, the surfaces obtained by cleaving in atmospheric air for these layered semiconductors are nearly ideal not only geometrically but also with respect to resistance to adsorption of extraneous gases from the atmosphere [1–7].

In this paper, we report the results of measuring the CPD for the *n*-InSe–*p*-GaSe HJs immediately after fabrication and after a lapse of 14 years. These results indicate that there is a substantial increase in the CPD in the course of aging of photosensitive structures.

In order to fabricate the HJ, we used the InSe and GaSe crystals with concentrations of electrons and holes of $n \approx 5 \times 10^{15}$ cm^{-3} and $p \approx 10^{16}$ cm^{-3}, respectively (at room temperature). The charge-carrier concentrations in both semiconductors were determined from the Hall effect measurements. The main difference between the structures we fabricated and those described in [1–5] was the fact that we used thicker GaSe wafers (~(100–200) μm instead of ~(10–40) μm in [1–5]), which made it possible to avoid plastic strain in the semiconductor wafers and, consequently, considerably reduce the level of leakage currents and improve the main characteristics of photoconversion. For example, the open-circuit voltage V_{oc} of the HJs immediately after fabrication was as high as 0.75–0.8 V when the HJs were exposed to natural radiation with a power density of 100 mW/cm^2; these data should be compared with the values V_{oc} = 0.3–0.65 V obtained previously [1–5, 8] under the same experimental conditions. The fact that we used thicker GaSe wafers allowed us to interpret the charge-transport mechanisms more correctly compared to [1–4]. The reason is that, in the forward-biased HJ with thicker wafers, an appreciable role in the charge transport is played by the currents described by the expression $J \propto \exp(eV/nkT)$, where e is the elementary charge, V is the voltage, T is the temperature, and k is the Boltzmann constant; the nonideality factor n remained virtually constant ($n \approx 1.2$) in the entire temperature range under consideration [9]. According to [1–4], tunneling processes play the most important role in forward-biased HJs.

The capacitance–voltage (C–V) characteristics $C(V)$ of our HJs depend on frequency, which is typical of structures with a high series resistance; therefore, the method suggested in [10] was used to determine the CPD. In Fig. 1a, we show the C–V characteristics plotted as C^{-2}–V at various frequencies ω. In this case, the value of V_0 was equal to 0.5 V, which is in good agreement with the results reported in [1–5]. The second measurement of the C–V characteristic of the same HJ kept in atmospheric air for 14 years indicated a significant increase in the CPD (to (1.65 ± 0.05) V; see

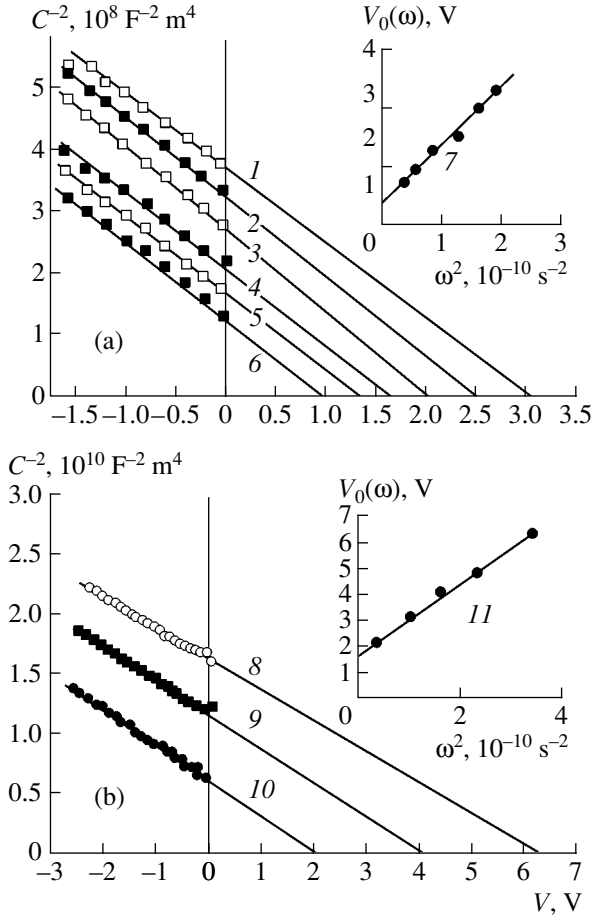

Fig. 1. Capacitance–voltage characteristics of (a) freshly fabricated and (b) aged *n*-InSe–*p*-GaSe heterojunctions at frequencies of (*1*) 22, (*2*, *9*) 20, (*3*) 18, (*4*) 15, (*5*) 12, (*6*, *10*) 10, and (*8*) 30 kHz. The frequency dependences of the capacitance cutoff voltage for the (*7*) freshly fabricated and (*11*) aged structures are shown in the insets. T = 295 K.

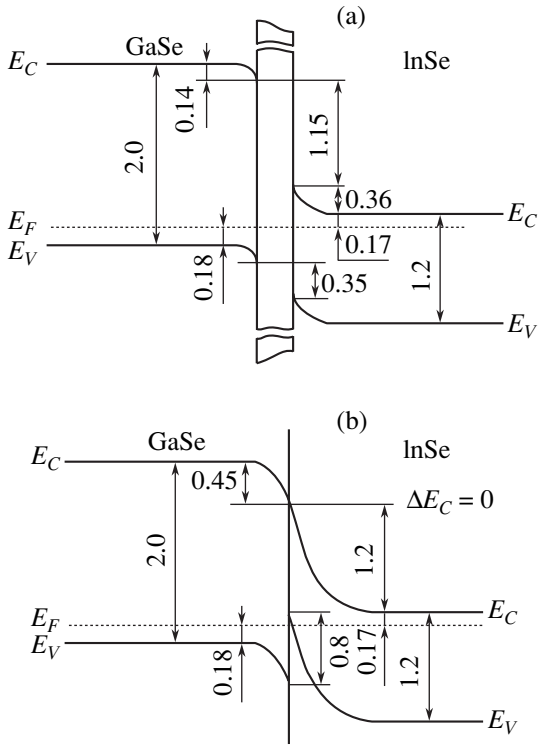

Fig. 2. The energy-band diagram for the (a) freshly fabricated and (b) aged *n*-InSe–*p*-GaSe heterojunctions under conditions of equilibrium. All the energies are expressed in electronvolts.

Fig. 1b, inset). In order to explain this experimental result, we use the energy-band diagram of an ideal heterojunction as suggested by Anderson. According to [11], the value of the CPD is given by

$$eV_0 = (\chi_p + E_{gp} - E_{F_p}) - (\chi_n + E_{F_n}), \qquad (1)$$

where χ_p and χ_n are the electron affinities for *p*- and *n*-type semiconductors, respectively; E_{gp} is the band gap of the *p*-type semiconductor; E_{F_p} is the energy spacing between the top of the valence band E_V and the Fermi level E_F in the *p*-type semiconductor; and E_{F_n} is the energy distance from the Fermi level to the bottom of the conduction band in the *n*-type semiconductor. The energy spacing between the Fermi level in *p*-GaSe and the top of the valence band was determined from the well-known formula [12] $E_{F_p} = kT\ln(N_V/p)$, in which all the designations are commonly accepted, and was found to be equal to 0.18 eV. The position of the Fermi level in *n*-InSe was determined similarly; we found that E_{F_n} = 0.17 eV. When using formula (1), we assumed that the electron affinity $\chi_n = \chi_p$ = 3.6 eV [13, 14]. According to (1), the value of CPD should be equal to 1.65 V in the ideal case, which is exactly what is observed experimentally for aged structures (Fig. 1b). In spite of the widespread opinion that the surfaces of layered semiconductors obtained by cleavage in atmospheric air are inert with respect to adsorption of atoms from the atmosphere, the initially formed structures most likely included a layer of adsorbed oxygen at the interface (an air interlayer), as illustrated in Fig. 2a. Indirect evidence that there is an air interlayer at the interface in the structures formed of layered semiconductors can be found in both earlier and recent publications (see [15, 16]). Nevertheless, as far as we know, the existence of this interlayer was not taken into account in any of the publications on the physical properties of *n*-InSe–*p*-GaSe HJs. Furthermore, if we treat the air gap in the initially fabricated *n*-InSe–*p*-GaSe structures as an insulating interlayer, we can understand why the open-circuit voltage far exceeds the CPD [17, 18].

It is worth noting that the capacitance of the HJ under investigation decreases in the course of aging (Figs. 1a, 1b). The charge-carrier concentration in the depletion region was determined from the slope of dependences $C^{-2} = f(V)$ and was found to be equal to

$\sim 1.2 \times 10^{15}$ and 3.8×10^{13} cm^{-3} for the freshly fabricated and aged samples, respectively. At the same time, the Hall measurements indicate that the charge-carrier concentration is the same in the initial and aged semiconductor wafers. Apparently, the decrease in the capacitance by a factor of $\sim(31 \times 3.3)^{1/2} = 10$ as a result of aging occurs due to a 31-fold decrease in the density of charged impurities at the interface (this decrease leads to an increase in the width of the space-charge region) and to an increase in the CPD by a factor of ~3.3. The decrease in the impurity concentration may be caused by diffusion of oxygen into the bulk of contacting semiconductors; oxygen is initially adsorbed at the interface and gives rise to a nonequilibrium state of the system with a long relaxation time. It is noteworthy that the diffusion of oxygen into the bulk of semiconductors (possibly accompanied by the formation of insulating GaO, Ga_2O, and Ga_2O_3 oxides on the GaSe side and similar oxides on the InSe side) occurs primarily in the regions where defects exist. For example, these defects may include selenium vacancies in the InSe and GaSe crystal lattices (the so-called "healing" of intrinsic defects in semiconductor crystals [19]). The disappearance of the oxygen layer at the interface gives rise to a closer contact between semiconductor wafers. In this case, the HJ interface consists of regions of real close contact InSe–GaSe (*p–n* junction) that alternate with regions with another chemical composition (regions with the possible formation of oxides). It is most likely that the close-contact regions "shunt" the entire structure and that it is precisely the properties of the InSe–GaSe *p–n* junction (an increase in the CPD and a decrease in the effective area of the structure) that govern the electrical properties of aged HJs. This assumption is also confirmed by the results of studying HJ electroluminescence at $T = 77$ K. The spectral distribution of emission is the same for the freshly fabricated and aged samples. However, the visual difference between these samples lies in the fact that alternating regions with different emission intensity are observed for aged samples (the emission intensity was distributed uniformly over the entire area in the case of freshly fabricated samples). As mentioned above, the effective area of aged HJ (the areas of formed regions of the *p–n* junction) amounts to ~10% of the area of the freshly fabricated structure (the semiconductor–(air gap)–semiconductor structure) according to tentative calculations based on the measurements of *C–V* characteristics. It is noteworthy that the calculated conversion efficiency of aged structures exposed to radiation with a power density of 75 mW/cm^2 is about 10% taking into account the effective area, which is ~4% greater than the highest efficiency attained for the structures based on *n*-InSe [13]. It should also be noted that the characteristics of the aged photodiodes are similar to a certain extent to those of charge-coupled devices; i.e., three portions with a negative differential conductivity appear in the *I–V* characteristics of the structures under consideration if a forward bias voltage in the range $V =$ 0–5.5 V is applied. These portions may be related to the formation of inclusions at the interface that differ from initial GaSe and InSe compounds and have a fairly small size (i.e., quantum-dimensional effects). Undoubtedly, this inference requires further careful study of the phenomena under consideration.

Thus, the HJ fabricated by bringing cleaved surfaces into direct optical contact is initially equivalent to a semiconductor–insulator–semiconductor structure where the layer formed as a result of adsorption of oxygen plays the role of insulator. The *n*-InSe and *p*-GaSe surfaces are brought closer together as a result of oxygen diffusion into the bulk of contacting semiconductors in the course of aging of the *n*-InSe–*p*-GaSe HJ. This closer contact of the InSe and GaSe surfaces leads to the formation of regions of the real *p–n* junction; as a result, the CPD of the structure increases by more than a factor of 3. Consequently, one should take into account the actual state of the transition layer when studying and designing photodetectors based on the direct optical contact of cleaved surfaces of layered semiconductors. In order to improve the main characteristics of photoconversion for both the *n*-InSe–*p*-GaSe HJ and other structures based on optical contact, it is necessary to develop the growth technology of these HJs and structures that would make it possible to use virtually the entire geometric area of the devices under consideration. It is also important to consider carefully the determination of the structure and the chemical composition of the regions where oxygen was introduced into semiconductor wafers the effect of these layers on the physical properties of device structures. In addition, it is important to study the feasibility of controlling the number and periodicity of the above regions at the surfaces of GaSe and InSe layers.

ACKNOWLEDGMENTS

We thank V.I. Litvinov of Waveband Corporation for his interest in this study and for helpful discussions.

REFERENCES

1. V. L. Bakumenko and V. F. Chishko, Fiz. Tekh. Poluprovodn. (Leningrad) **11**, 2000 (1977) [Sov. Phys. Semicond. **11**, 1171 (1977)].
2. V. L. Bakumenko, Z. D. Kovalyuk, L. N. Kurbatov, *et al.*, Fiz. Tekh. Poluprovodn. (Leningrad) **12**, 374 (1978) [Sov. Phys. Semicond. **12**, 216 (1978)].
3. T. V. Aver'yanova, V. L. Bakumenko, L. N. Kurbatov, *et al.*, Fiz. Tekh. Poluprovodn. (Leningrad) **14**, 1573 (1980) [Sov. Phys. Semicond. **14**, 932 (1980)].
4. V. N. Katerinchuk, Z. D. Kovalyuk, V. A. Manasson, and K. D. Tovstyuk, Fiz. Tekh. Poluprovodn. (Leningrad) **21**, 380 (1987).
5. É. G. Ashirov, V. L. Bakumenko, A. K. Bonakov, *et al.*, in *Abstracts of the All-Union Workshop on Radiation Effects in Semiconductors and Semiconductor Devices* (Azernesher, Baku, 1980), p. 91.

6. R. H. Williams and A. J. McEvoy, J. Vac. Sci. Technol. **9**, 867 (1972).
7. L. B. Anan'ina, V. L. Kurbatov, and V. F. Chishko, Fiz. Tekh. Poluprovodn. (Leningrad) **10**, 2373 (1976) [Sov. Phys. Semicond. **10**, 1405 (1976)].
8. Z. Kovalyuk, V. Makhniĭ, and O. Yanchuk, Vestn. L'vov. Univ., Ser. Fiz. **34**, 217 (2001).
9. V. N. Katerinchuk, *Photoelectric Properties of Semiconductor–Insulator–Semiconductor Structures Based on Gallium and Indium Monoselenides* (Chernov. Gos. Univ., Chernovtsy, 1989).
10. Yu. A. Gol'dberg, O. V. Ivanova, T. V. L'vova, and B. V. Tsarenkov, Fiz. Tekh. Poluprovodn. (Leningrad) **18**, 1472 (1984) [Sov. Phys. Semicond. **18**, 919 (1984)].
11. A. G. Milnes and D. L. Feucht, *Heterojunctions and Metal–Semiconductor Junctions* (Academic, New York, 1972; Mir, Moscow, 1975).
12. V. L. Bonch-Bruevich and S. G. Kalashnikov, *Physics of Semiconductors* (Nauka, Moscow, 1965), p. 363.
13. J. Martinez-Pastor, A. Segura, J. L. Valdes, and A. Chevy, J. Appl. Phys. **21**, 1477 (1987).
14. R. R. Daniels, G. Margaritondo, C. Quaresima, *et al.*, J. Vac. Sci. Technol. A **3**, 979 (1985).
15. A. G. Kyazym-zade and D. Kh. Dzhafarov, Dokl. Akad. Nauk AzSSR **36** (10), 7 (1980).
16. S. I. Drapak, V. A. Manasson, V. V. Netyaga, and Z. D. Kovalyuk, Fiz. Tekh. Poluprovodn. (St. Petersburg) **37**, 180 (2003) [Semiconductors **37**, 172 (2003)].
17. A. Ya. Vul' and A. V. Sachenko, Fiz. Tekh. Poluprovodn. (Leningrad) **17**, 1361 (1983) [Sov. Phys. Semicond. **17**, 865 (1983)].
18. S. I. Drapak, V. N. Katerinchuk, Z. D. Kovalyuk, and V. A. Manasson, Fiz. Tekh. Poluprovodn. (Leningrad) **23**, 1510 (1989) [Sov. Phys. Semicond. **23**, 937 (1989)].
19. K. D. Tovstyuk, *Semiconductor Materials Technology* (Naukova Dumka, Kiev, 1984).

Translated by A. Spitsyn

Semiconductors, Vol. 38, No. 5, 2004, pp. 550–553. Translated from Fizika i Tekhnika Poluprovodnikov, Vol. 38, No. 5, 2004, pp. 570–573.

SEMICONDUCTOR STRUCTURES, INTERFACES, AND SURFACES

On the Ultimate Quantum Efficiency of Band-Edge Electroluminescence in Silicon Barrier Structures

A. V. Sachenko, A. P. Gorban', and V. P. Kostylyov

Institute of Semiconductor Physics, National Academy of Sciences of Ukraine, Kiev, 03028 Ukraine

e-mail: sach@isp.kiev.ua

Submitted May 19, 2003; accepted for publication October 18, 2003

Abstract—The ultimate quantum efficiency of electroluminescence in silicon diodes and *p–i–n* structures at room temperature is calculated. It is shown that the internal quantum yield of electroluminescence is about 10% and is implemented at optimal doping levels for the *n*- and *p*-type regions of silicon diodes, ~10^{15} and 5×10^{16} cm^{-3}, respectively. With a decrease in the Shockley–Read–Hall lifetimes of electrons and holes, the internal quantum yield of electroluminescence in silicon barrier structures drops. The physical processes related to the effect of excitons in silicon has much in common with those in electroluminescence, photoluminescence, and photoconversion. It is shown that only electroluminescent *p–i–n* structures are promising for use in silicon integrated circuits. © *2004 MAIK "Nauka/Interperiodica".*

1. INTRODUCTION

In view of the possibility of fabricating large-scale silicon integrated circuits including optical transmission lines, much attention has been paid in recent years to electroluminescence in silicon barrier structures at room temperature (see, for example, [1–3]). Both device structures used for the photoelectric conversion of solar energy [1] and silicon diodes [2, 3] were studied. Specifically, an internal quantum yield of band-edge emission of ~1% was obtained in [1, 2]. It was shown in [3] that the band-edge electroluminescence (at least, at low temperatures) may be due to the annihilation of free excitons.

The influence of excitons on the effective lifetime of electron–hole pairs, band-edge photoluminescence, current–voltage characteristics, and the ultimate efficiency of photoelectric conversion in pure silicon and silicon device structures at room temperature was studied in [4–9]. When carrying out the analysis, we assumed that two interrelated subsystems (electron–hole and exciton) exist in a semiconductor and a quasi-equilibrium between these subsystems is maintained due to the coupling of electron–hole pairs into excitons and the decay of excitons into electron–hole pairs. In this approach, it was shown that the effective lifetime of electron–hole pairs in a number of practically important cases may be controlled by nonradiative exciton Auger recombination involving deep centers; the internal quantum yield of band-edge photoluminescence may be as high as 15% in this case. In this study, on the basis of the results of [4–6], we performed a detailed analysis of the conditions under which the highest quantum yield of band-edge electroluminescence can be obtained in Si *p–n* and *p–i–n* barrier structures. Specific quantitative estimations are made for the room temperature region.

2. BAND-EDGE ELECTROLUMINESCENCE IN FORWARD-BIASED SILICON DIODES

Let us consider the situation when the thicknesses of the *n*- and *p*-type regions of a diode exceed the diffusion lengths of electrons and holes in these regions. In this case, we can exclude the effect of surface recombination. We will also assume that the excitation is linear; i.e., the inequalities $n_n \gg p_n \exp(qV/kT)$ and $p_p \gg n_p \exp(qV/kT)$ are satisfied. Here, n_n and p_p are the concentrations of majority carriers in the *n*- and *p*-type regions, respectively; p_n and n_p are the concentrations of minority carriers in the *n*- and *p*-type regions, respectively; q is the elementary charge; k is the Boltzmann constant; T is temperature; and V is the applied bias voltage. The diffusion-current density in such a diode is given by the conventional expression

$$J = q\left(\frac{D_p p_n}{L_p} + \frac{D_n n_p}{L_n}\right)\exp(qV/kT), \qquad (1)$$

where L_p and L_n are the diffusion lengths of minority carriers in the *n*- and *p*-regions, respectively, and D_p and D_n are the diffusivities of minority carriers in the *n*- and *p*-regions, respectively. In the case of linear excitation, the expressions for L_p and L_n can be written as [4, 5]

$$L_p = \left\{D_p\left[\frac{1}{\tau_{rp}} + \left(A_i + \frac{1}{n^*\tau_x}\right)n_n + (C_n + C_p)n_n^2\right]^{-1}\right\}^{1/2}, \qquad (2)$$

$$L_n = \left\{ D_n \left[\frac{1}{\tau_{rn}} + \left(A_i + \frac{1}{n^*\tau_x} \right) p_p + (C_n + C_p) p_p^2 \right]^{-1} \right\}^{1/2}, \quad (3)$$

where τ_{rp} and τ_{rn} are the Shockley–Read–Hall lifetimes of holes and electrons in the *n*- and *p*-type regions, respectively; A_i is the constant of radiative electron–hole recombination; $n^* = (N_c N_v / N_x)\exp(-E_x/kT)$ (here, N_c, N_v, and N_x are the effective densities of states of electrons, holes, and excitons, respectively); E_x is the exciton binding energy; and $\tau_x = (1/\tau_x^r + 1/\tau_x^n)^{-1}$ (here, τ_x^r is the radiative lifetime of excitons and τ_x^n is the nonradiative lifetime of excitons, related to Auger recombination involving a deep volume level).

Generally, the internal quantum yield of electroluminescence of a diode with thick *n*- and *p*-type regions can be written as

$$\eta = \frac{J - J_0}{J + J_r}, \quad (4)$$

where J_0 can be derived from (1) (if we leave out the terms related to A_i and $1/n^*\tau_x^r$ in the expressions for L_p and L_n) and J_r is the recombination-current density in the space-charge region of the diode. Generally, the electroluminescence current density can be written as $J - J_0$. When the value of J_r can be neglected in comparison with J and the terms in parentheses in expressions (2) and (3), which are associated with the radiative recombination, are small in comparison with the term related to the nonradiative recombination, the expression for J_e acquires the form

$$J_e = \frac{q}{2} n_i^2 (L_{p0} + L_{n0}) \left[A_i + \frac{1}{n^*\tau_x^r} \right] \left[\exp\left(\frac{qV}{kT} \right) - 1 \right]. \quad (5)$$

The values of L_{p0} and L_{n0} can be determined from the expressions for L_p and L_n if we leave out the term related to radiative recombination.

We define the internal quantum efficiency of the electroluminescence in accordance with [3] for the case when J_r can be disregarded in comparison with J.

$$\eta = n_n p_p \frac{L_{p0} + L_{n0}}{D_p p_p / L_{p0} + D_n n_n / L_{n0}} \left(A_i + \frac{1}{n^*\tau_x^r} \right). \quad (6)$$

3. BAND-EDGE ELECTROLUMINESCENCE IN Si *p–i–n* STRUCTURES

We will derive the theoretical expression for the internal quantum yield of the band-edge electroluminescence of a silicon *p–i–n* structure on the assumption that the *i* region is only lightly doped and the excitation is nonlinear; thus, the criteria $p_n \exp(qV/kT) \gg n_n$ and $n_p \exp(qV/kT) \gg p_p$ are satisfied. In addition, we assume that the thickness of the *i* region d is smaller than the diffusion length of holes or electrons. Disregarding the recombination of electron–hole pairs on the surfaces of the p^+- and n^+-regions and the recombination current (in comparison with the diffusion current) in the space-charge region, we obtain, according to [7], the following expression for the internal quantum yield:

$$\eta = \left(A_i + \frac{1}{n^*\tau_x^r} \right) \Big/ \left[\frac{1}{\tau_r} n_i^{-1} \exp\left(-\frac{qV}{2kT} \right) + A_i + \frac{1}{n^*\tau_x} + (C_n + C_p) n_i \exp\left(\frac{qV}{2kT} \right) \right]. \quad (7)$$

In this case, the electroluminescence current density is

$$J_e = qd \left(A_i + \frac{1}{n^*\tau_x^r} \right) n_i^2 \exp\left(\frac{qV}{kT} \right), \quad (8)$$

where τ_r is the Shockley–Read–Hall lifetime at a high excitation level and n_i is the intrinsic carrier concentration in silicon.

It is noteworthy that in the case under consideration the excess concentration of electron–hole pairs Δp is determined by the relation

$$\Delta p = n_i \exp(qV/2kT). \quad (9)$$

4. RESULTS OF NUMERICAL CALCULATIONS AND DISCUSSION

A numerical estimation of the ultimate efficiency of band-edge electroluminescence in silicon barrier structures, with the parameters reported in [4], will be performed for the case of room temperature (T = 300K). In accordance with the results obtained from the analysis of the dependence of the effective lifetime of electron–hole pairs in Si on the excitation level, the sum of the probabilities of the edge interband and exciton recombinations in Si, $A_i + 1/n^*\tau_x^r$, is equal to 2.5×10^{15} cm^3 s^{-1} [4]. This value coincides with the value obtained in [10] using the principle of detailed balance between absorption and emission (the Roosbroeck–Shockley model) and is consistent with the experimental spectral dependence of the light absorption coefficient in Si near the intrinsic absorption edge measured in [11].

In the calculations, we used the maximum Shockley–Read–Hall lifetimes obtained for holes and electrons in *n*- and *p*-type silicon (4×10^{-2} and 7×10^{-3} s, respectively). The quantity $1/n^*\tau_x^n$, which characterizes the nonradiative exciton Auger recombination in *n*-Si, was assumed to be $2.7 \times 10^{16} \tau_{rp}^{-1}$; for *p*-silicon, the nonradiative exciton Auger recombination was assumed to be absent. For the coefficients of interband Auger recombination of electrons and holes in Si, we used the dependence $C_n = (2.8 \times 10^{-31} + 2.5 \times 10^{-22}/n_n^{1/2})$ cm^6 s^{-1}

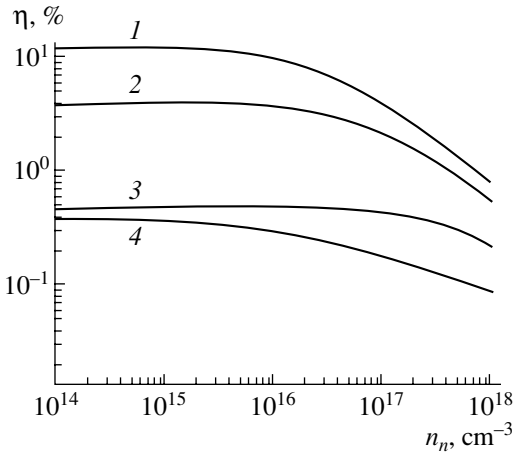

Fig. 1. Dependences of the internal quantum yield of electroluminescence of a thick diode on the level of doping of the *n*-type region for lifetimes τ_{rp} and τ_{rn} equal to (*1*) 4×10^{-2} and 7×10^{-3} s, (*2*) 10^{-2} and 10^{-3} s, (*3*) 10^{-3} and 10^{-4} s, and (*4*) 10^{-4} and 10^{-4} s. The hole concentration in the *p*-type region is 5×10^{16} cm^{-3}.

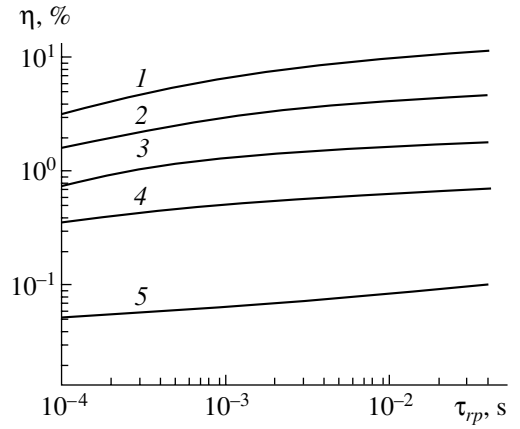

Fig. 2. Dependences of the internal quantum yield of electroluminescence of a thick diode on τ_{rp} for τ_{rn} = (*1*) 7×10^{-3}, (*2*) 10^{-3}, (*3*) 3×10^{-4}, (*4*) 10^{-4}, and (*5*) 10^{-5} s. $n_n = 10^{15}$ cm^{-3} and $p_p = 5 \times 10^{16}$ cm^{-3}.

and the value $C_p = 10^{-31}$ cm^6 s^{-1}. The diffusivities of holes and electrons were assumed to be $D_p = 10$ cm^2 s^{-1} and $D_n = 25$ cm^2 s^{-1}, respectively.

Figure 1 shows the dependences of the quantum efficiency of electroluminescence η in silicon diodes on the doping level of the *n*-type region for different electron concentrations in the *p*-type region. These dependences were calculated using expression (6) and the aforementioned parameters (the recombination in the space-charge region of the *p–n* junction was disregarded). As can be seen from Fig. 1, the maximum value of η is about 10%; it is attained at dopant concentrations of ~10^{15} cm^{-3} in the *n*-type region and 5×10^{16} cm^{-3} in the *p*-type region. Thus, the optimum doping levels for the *n*- and *p*-type regions in a silicon diode with maximum electroluminescence efficiency turn out to be similar to the optimum doping levels for the corresponding regions of silicon solar cells with the highest attainable photoconversion efficiency [6]. Interestingly, in this case, the net quantity $L_{p0} + L_{n0}$, with regard for the maximum values of the Shockley–Read–Hall lifetimes for holes in *n*-Si and for electrons in *p*-Si, is about 1 cm.

Figure 2 shows the dependences of η on the Shockley–Read–Hall lifetime τ_{rp} for holes in the *n*-type region for several fixed values of τ_{rn}. It can be seen that, with a decrease in τ_{rp} and τ_{rn}, the internal quantum yield of electroluminescence drops and, at $\tau_{rp} = \tau_{rn} = 10^{-5}$ s, turns out to be smaller than 0.1%. Therefore, a high efficiency of band-edge electroluminescence or photoluminescence cannot generally be attained in conventional silicon devices.

It is noteworthy that, in the case of high excitation levels, the results of the analysis require some corrections. For example, if the *i* region has *n*-type conductivity and the electron concentration in this region is equal to 10^{12} cm^{-3}, as calculations show, high excitation can be implemented at $V \gtrsim 0.25$ V. In this case, we assume the Shockley–Read–Hall lifetime to be 4×10^{-2} s and the quantity $1/n^*\tau_x^n$, which characterizes the exciton Auger recombination, to be $1.3 \times 10^{-16}\tau_r^{-1}$ [4]. The difference between the numerical value of the latter parameter and the previously used one is caused by the fact that the probability of an Auger process with ejection of a hole in Si, which controls the nonradiative exciton recombination at high excitation levels, is lower than the probability of an Auger process with ejection of an electron.

Figure 3 shows the dependences of the internal quantum yield of electroluminescence on applied voltage for thin (compared to the diffusion length) silicon *p–i–n* structures. As can be seen from this figure, the ultimate efficiency of electroluminescence in *p–i–n* structures (with the parameters used) can be as high as about 10%, i.e., comparable with the ultimate efficiency of photoluminescence [5], although it drops with decreasing τ_r, as in the case of linear excitation. In addition, the maximum of electroluminescence shifts to higher voltages with a decrease in τ_r.

Thus, the results of numerical estimations using the parameters reported in [4] showed that an ultimate internal quantum yield of electroluminescence of about 10% can be attained in silicon diode structures ≳1 cm thick. However, the conditions imposed on the diffusion lengths of holes and electrons at which a fairly high internal quantum yield can be attained practically exclude the possibility of using such structures in microelectronics. From the point of view of practical use in integrated circuits, *p–i–n* structures are more

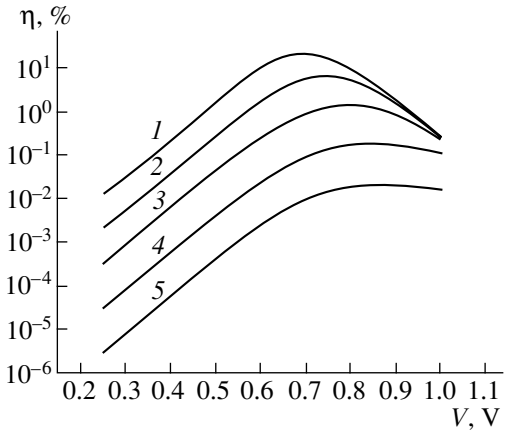

Fig. 3. Dependences of the internal quantum yield of electroluminescence of *p–i–n* structures on applied bias voltage V with lifetime τ_r in the *i*-region equal to (*1*) 4×10^{-2}, (*2*) 7×10^{-3}, (*3*) 10^{-3}, (*4*) 10^{-4}, and (*5*) 10^{-5} s.

promising since the internal quantum yield of electroluminescence in these structures is independent of the thickness of the *i* region.

REFERENCES

1. M. A. Green, J. Zhao, A. Wang, *et al.*, Nature **412**, 805 (2001).
2. W. L. Ng, M. A. Lourenco, R. M. Gwilliam, *et al.*, Nature **410**, 192 (2001).
3. M. S. Bresler, O. B. Gusev, B. P. Zakharchenya, and I. N. Yassievich, in *Proceedings of the Conference on Nanophotonics* (2003), Vol. 1, p. 59.
4. A. V. Sachenko, A. P. Gorban, and V. P. Kostylyov, Semicond. Phys. Quantum Electron. Optoelectron. **3**, 5 (2000).
5. A. V. Sachenko and Ju. V. Kryuchenko, Semicond. Phys. Quantum Electron. Optoelectron. **3**, 150 (2000).
6. A. P. Gorban, A. V. Sachenko, V. P. Kostylyov, and N. A. Prima, Semicond. Phys. Quantum Electron. Optoelectron. **3**, 322 (2000).
7. A. V. Sachenko, A. P. Gorban', and V. P. Kostylyov, Ukr. Fiz. Zh. **46**, 226 (2001).
8. A. V. Sachenko, N. A. Prima, A. P. Gorban, and A. A. Serba, in *Proceedings of 17th European Photovoltaic Solar Energy Conference* (Munich, 2001), Vol. 1, p. 230.
9. A. P. Gorban, V. P. Kostylyov, A. V. Sachenko, and V. V. Chernenko, in *Proceedings of 17th European Photovoltaic Solar Energy Conference* (Munich, 2001), Vol. 1, p. 234.
10. A. P. Gorban', V. A. Zuev, V. P. Kostylyov, *et al.*, Optoélektron. Poluprovodn. Tekh., No. 36, 161 (2001).
11. M. J. Keevers and M. A. Green, Appl. Phys. Lett. **66**, 174 (1995).

Translated by Yu. Sin'kov

Semiconductors, Vol. 38, No. 5, 2004, pp. 554–559. Translated from Fizika i Tekhnika Poluprovodnikov, Vol. 38, No. 5, 2004, pp. 574–579.

SEMICONDUCTOR STRUCTURES, INTERFACES, AND SURFACES

Theory of Tunneling Current in Metal–Semiconductor Contacts with Subsurface Isotype δ-Doping

V. I. Shashkin and A. V. Murel

Institute for Physics of Microstructures, Russian Academy of Sciences, Nizhni Novgorod, 603950 Russia

e-mail: sha@ipm.sci-nnov.ru

Submitted October 21, 2003; accepted for publication November 11, 2003

Abstract—The theory of tunneling current in metal–semiconductor contacts with subsurface isotype δ-doping is developed. Analytical expressions for current that take into account the decrease in the potential barrier height due to the image forces are obtained using the Murphy–Good approach. Characteristics of δ-doping that provide effective thermal field emission at the metal–semiconductor contact and a decrease in the effective barrier height from the original value to several *kT* are calculated. It is established that the main voltage dependence of the current in a contact with isotype δ-doping is exponential. It is shown that the nonideality factor can remain small ($n \le 1.07$) for all values of the barrier height. A dramatic increase in n to the values $n \ge 1.5$ is typical of contacts with a partially depleted layer. © *2004 MAIK "Nauka/Interperiodica".*

1. INTRODUCTION

The current in metal–semiconductor (MS) contacts depends on the doping level at the semiconductor surface. It is well known that tunneling processes begin to play an important role in field-enhanced thermal and autoelectronic emission as the doping level is increased [1, 2]. The theoretical description of current in MS contacts is based on the results of [3]. The most important theoretical studies of this problem were performed more than a quarter of century ago, and an overview of them can be found in [1, 4]. All the theoretical models of contacts were based on the common assumption that doping is homogeneous in the region near the surface. Somewhat later, with the development of epitaxial growth technologies, MS contacts with subsurface isotype δ-doping have appeared, where it is precisely the tunneling processes that lead to a decrease in the effective barrier height and the appearance of an ohmic nonfused MS contact in the limiting case of very heavy δ-doping [5–7].The resistivity for ohmic contacts was estimated using approximate formulas for the tunneling current [5], numerical quantum-mechanical calculations of transport processes in contacts with a lowered effective barrier height were performed, and good agreement with the experimental data [8] was obtained.

In this study, we derived and analyzed in detail expressions for the current–voltage characteristics of MS contacts with subsurface δ-doping, where the effects of field-enhanced thermal emission play a crucial role. The calculations took into account the image forces, and no restrictions were imposed on temperature and characteristics of δ-doping such as the surface density N_s and the distance from the δ-layer to the MS interface. We determined the tunneling transparency of the barrier by using the Miller–Good method [9], which ensured good accuracy in the theory of electron emission from metals to free space, insulators, and semiconductors [10, 11]. We calculated the effective barrier height and the nonideality factor for the current–voltage characteristic of an MS contact and compared the results with those for the case of heavy uniform doping [1–4]. By using the analytical expressions thus derived, one can optimize the parameters of current–voltage characteristics, which is necessary for various applications, for example, the development of detector diodes with a reduced effective barrier height [12, 13].

2. A MODEL OF POTENTIAL PROFILE: MOTT'S BARRIER WITH δ-DOPING

To be specific, we consider the problem for electrons. Figure 1 shows the profiles of the conduction band edge E_c along the x direction in a layered structure that consists of metal, an epitaxial layer, and a heavily doped n^+ substrate at some positive bias V. All the layer boundaries are assumed to be planar and parallel. The variation of E_c near the MS interface with allowance for the image forces can be written in the usual form [1–4] as

$$E_c(x) = \mu + \Phi\frac{e^2}{4\varepsilon x} + -eFx, \quad x < d, \qquad (1)$$

where μ is the Fermi level in the metal, Φ is the barrier height on the side of the metal, e is the elementary charge, ε is the relative permittivity of the semiconductor, and F is the electric-field strength. A δ layer of donor impurity atoms with surface density N_s is located in the $x = d$ plane. We disregard the broadening δx in impurity distribution along the x axis, assuming that $\delta x \ll d$. We also assume that the epitaxial layer is thin and the bulk doping is low, so that the screening of the

1063-7826/04/3805-0554$26.00

electric field is produced only by the δ layer. In what follows, we pay most attention to the MS contact, in which both the δ layer and the entire epitaxial layer up to the boundary $x = D$ with the n^+-substrate are fully depleted (Fig. 1a). According to [2], such a contact is Mott's barrier. In this contact an external applied voltage V creates an additional homogeneous electric field V/D which is added to the field of built-in charges at $V = 0$. It will be shown below that disregarding the bulk charge is not of fundamental importance for the calculations. Such an assumption only allows one to simplify the calculation of the potential in the contact and to establish the main features of the tunneling current. Using these assumptions, it is easy to calculate the potential profile in the contact at various levels of δ-doping and at different values of the applied dc bias (Fig. 1). Specifically, we can determine the position of the conduction-band edge Δ in the plane of the δ layer as a function of the applied voltage V:

$$\Delta(V) \equiv E_c(d) = \left(\Phi - \frac{4\pi e^2 N_s d}{\varepsilon}\right)\left(1 - \frac{d}{D}\right) + \frac{d}{D}eV. \quad (2)$$

It is easy to find the condition for full depletion of the δ layer:

$$\frac{4\pi e^2 N_s d}{\varepsilon} \le \Phi - eV. \quad (3)$$

At a high doping level N_s or at a large forward bias, the δ layer is not fully depleted and the relation (2) does not hold. In that case, the variation of the potential with a characteristic potential well filled by electrons is illustrated in Fig. 1b.

3. EXPRESSIONS FOR THE TUNNELING TRANSMISSION FACTOR AND CURRENT DENSITY

The triangular barrier at the top of the potential profile shown in Fig. 1 can be transparent for tunneling at small d. The current–voltage characteristics of such contacts were numerically calculated and measured in [8]. To obtain analytical expressions for the current and for the tunneling transmittance through the barrier (1) taking the image forces into account, we use the approach developed in [10]. Disregarding the effects of nonparabolicity and nonsphericity of the semiconductor energy-band spectrum and denoting by E_x the energy for the electron motion along the x direction, we can write the following expression for the current density $j(V)$ in the MS contact:

$$j(V) = \frac{A^*T}{k}\int\limits_{\mu+\Delta(V)}^{\infty} \exp[-Q(E_x)] \times \ln\left\{\frac{\exp(eV/kT) + \exp[(E_x-\mu)/kT]}{1 + \exp[(E_x-\mu)/kT]}\right\}dE_x, \quad (4)$$

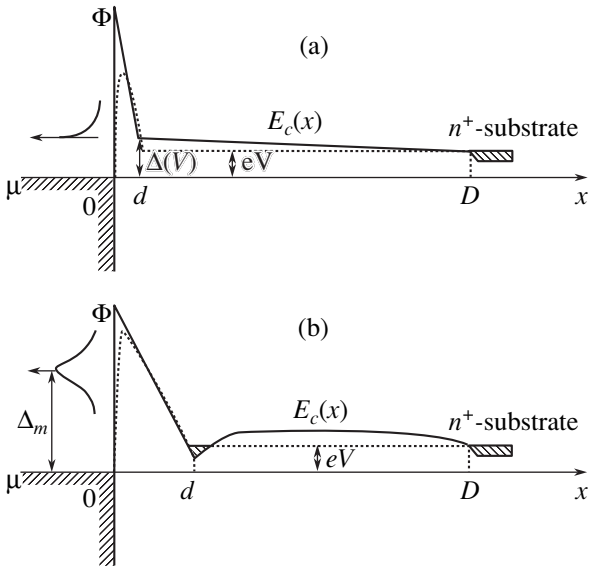

Fig. 1. Profile of the conduction-band edge $E_c(x)$ in an MS structure with δ-doping in the plane $x = d$ for a (a) complete and (b) partial depletion. The voltage V is applied in the forward direction. The dashed line shows the lowering of the potential barrier due to image forces. On the left, the arrows indicate tunneling electrons and the solid lines show the conditional electron energy distribution.

where

$$Q(E_x) = \frac{4\sqrt{2}}{3}\frac{\sqrt{m}}{e\hbar F}(\mu + \Phi - E_x)^{3/2} v(y), \quad (5)$$

$$y \equiv \frac{1}{\sqrt{\varepsilon}}\frac{\sqrt{e^3F}}{|\mu + \Phi - E_x|}, \quad (6)$$

$v(y)$ is the Nordheim function tabulated in [14], m is the electron effective mass, k is the Boltzmann constant, and $A^* = 4\pi emk^2/(2\pi\hbar)^3$ is Richardson's constant. In writing expression (4), we assumed that $Q(E_x) \gg 1$ and the transparency of the tunnel barrier vanishes for $E_x < \mu + \Delta(V)$. The difference between the above and the classical results for electron emission from metals to free space [10, 14] is that expression (6) for y contains a factor that depends on ε. As a result, the relative role of the image forces decreases. It should be noted that the tunneling transmission factor and the electron energy distribution function can vary over a very wide range, but their magnitude is bounded from above. Therefore, the integrand necessarily has a maximum at some energy Δ_m, which we measure from the Fermi level in the metal (see Fig. 1). Depending on the parameters of the tunnel barrier and temperature, the maximum can be found outside or inside the integration domain. Provided that the quantity $[\max(\Delta, \Delta_m) - eV]$ is

several times greater than the thermal energy kT, we can eliminate the logarithm in the integral (4):

$$j(V) = \frac{A^*T}{k}\left[\exp\left(\frac{eV}{kT}\right)-1\right] \times \int\limits_{\mu+\Delta(V)}^{\infty} \exp\left[-Q(E_x)-\frac{E_x-\mu}{kT}\right]dE_x. \quad (7)$$

An approximate method of integration using the power expansion of $Q(E_x)$ near an arbitrary energy Δ_0 was suggested in [10]. To within the second power in energy E_x, we have

$$Q(E_x) \approx b - c(E_x - \mu - \Delta_0) + f(E_x - \mu - \Delta_0)^2. \quad (8)$$

The coefficients in (8) coincide with those calculated previously [10, 11, 14]:

$$b = \frac{4\sqrt{2}}{3}\frac{d\sqrt{m}}{\hbar(\Phi-\Delta)}(\Phi-\Delta_0)^{3/2}v(y_0), \quad (9)$$

$$c = \frac{2d\sqrt{2m}}{\hbar(\Phi-\Delta)}(\Phi-\Delta_0)^{1/2}t(y_0), \quad (10)$$

$$f = \frac{d\sqrt{2m}}{2\hbar(\Phi-\Delta)}(\Phi-\Delta_0)^{-1/2}\frac{v(y_0)}{1-y_0^2}, \quad (11)$$

$$y_0 = \frac{e}{\sqrt{\varepsilon d}}\frac{(\Phi-\Delta)^{1/2}}{\Phi-\Delta_0}. \quad (12)$$

Here we introduced the function $t(y) \equiv v(y) - (2/3)yv'(y)$, which varies relatively little near unity [10, 14]. Using these relations, we can obtain analytical expressions for the current, which have different forms depending on the tunneling transparency of the barrier (or on temperature).

We can expand $Q(E_x)$ near the maximum of the integrand in (7) at $\Delta_0 = \Delta_m$. The position of the maximum is determined from the condition that, in the exponential in (7), the coefficient of the term linear in energy vanishes. This condition has the form $c_m \equiv c(\Delta_m) = 1/kT$ or

$$c_m \equiv \frac{2d\sqrt{2m}}{\hbar(\Phi-\Delta)}(\Phi-\Delta_m)^{1/2}t(y_m) = \frac{1}{kT}, \quad (13)$$

$$y_m = \frac{e}{\sqrt{\varepsilon d}}\frac{(\Phi-\Delta)^{1/2}}{\Phi-\Delta_m}. \quad (14)$$

Since the dependence $t(y)$ is weak, Δ_m can be determined with the required accuracy by several iterations from the equations

$$\Delta_m = \Phi - \frac{(\Phi-\Delta)^2\hbar^2}{8(kT)^2md^2t^2(y_m)} \quad (15)$$

and (14), setting $t(y_m) = 1$ at the first step.

4. THIN TUNNEL BARRIERS (LOW TEMPERATURES)

We call the tunnel barrier thin if $\Delta_m < \Delta$. Note that such a characterization of tunnel barriers is justified at a fixed temperature, since the value Δ_m is a function of T. In some cases, it is more convenient to introduce a restriction on temperature. Setting $t(y_m) = 1$, we find from (15) the following inequalities for d or T:

$$d < \frac{\hbar}{2kT}\sqrt{\frac{\Phi-\Delta}{2m}}, \quad (16a)$$

$$T < \frac{\hbar}{2kd}\sqrt{\frac{\Phi-\Delta}{2m}}. \quad (16b)$$

For $\Phi - \Delta = 0.5$ eV and $m = 0.067m_0$ (the case of gallium arsenide), we obtain from the above formulas $d <$ 10 nm at $T = 300$ K or $T < 300$ K at $d = 10$ nm.

To find the current in the case of a thin tunnel barrier, i.e., for $\Delta_m < \Delta$, we expand $Q(E_x)$ in the neighborhood of $\Delta_0 = \Delta$ and use (7) to obtain the following expression:

$$j(V) = \frac{A^*T}{2k}\sqrt{\frac{\pi}{f_\Delta}}\exp\left[-b_\Delta - \frac{\Delta}{kT} + \frac{(1-kTc_\Delta)^2}{4(kT)^2f_\Delta}\right] \times \left[\exp\left(\frac{eV}{kT}\right)-1\right]\left[1-\operatorname{erf}\left(\frac{1-kTc_\Delta}{2kT\sqrt{f_\Delta}}\right)\right]. \quad (17)$$

Here, $\operatorname{erf}(z) \equiv (2/\sqrt{\pi})\int_0^z \exp(-t^2)dt$ is the probability integral [15] and the coefficients $b\Delta$, $c\Delta$, $f\Delta$, and $y\Delta$ are determined from formulas (9)–(12) with Δ_0 replaced by Δ.

For barriers with high tunneling transparency for which the condition $1 - kTc_\Delta \gg kT\sqrt{2f_\Delta}$ is satisfied, the expression for the current density can be substantially simplified using the asymptotic representation of the probability integral:

$$j(V) = A^*T\frac{\exp(-b_\Delta)}{1-kTc_\Delta}\exp\left(-\frac{\Delta}{kT}\right)\left[\exp\left(\frac{eV}{kT}\right)-1\right]. \quad (18)$$

This fairly simple expression has been previously derived for Schottky diodes with subsurface δ-doping [12]. Indeed, if we retain only two terms in expansion (8), the integral (4) is reduced to tabulated form [15]:

$$j(V) = A^*T^2\exp(-b_\Delta) \times \sum_{m=0}^{\infty}\frac{(-1)^m\exp[-(m+1)\Delta/kT]\exp[(m+1)eV/kT-1]}{(m+1)(m+1-kTc_\Delta)}. \quad (19)$$

For $\Delta > 2kT$, the series is approximated with good accuracy by the first term (18). Specifically, it follows from (18) that the current is determined by thermal emission over the barrier of height Δ, and the voltage dependence of the forward current is close to exponential with the argument eV/nkT. The nonideality factor n only slightly

exceeds unity, since the ratio d/D is small and, according to (2), Δ weakly depends on V. The second reason for exponential dependence of current is that, under condition (16), the coefficient $b\Delta$ itself weakly depends on Δ. The main conclusion that follows from expression (18) is that, for heavy δ-doping several nanometers from the MS interface, the decrease in the effective Schottky barrier height can be as large as several kT. At the same time, the current–voltage characteristic remains almost exponential with the nonideality factor $n \approx 1$. One difference between this and the usual formulas for the current in Schottky barriers is that an additional factor appears, which is equivalent to a strong decrease in Richardson's constant and the weak dependence of this constant on temperature and bias voltage.

For greater d and a smaller tunneling-barrier transparency corresponding to the condition $1 - c_\Delta kT \ll \pi kT\sqrt{f_\Delta}$, expression (17) can also be simplified:

$$j(V) = \frac{A^*T}{2k}\sqrt{\frac{\pi}{f_\Delta}}\exp\left(-b_\Delta - \frac{\Delta}{kT}\right)\left[\exp\left(\frac{eV}{kT}\right) - 1\right]. \quad (20)$$

In this case, Δ_m approaches the lower integration limit Δ. We see that the exponential variation of the current differs from that in expression (18). However, the temperature dependence of the preexponential factor becomes linear, which is typical of MS contacts, in which tunneling processes become important [1–4].

5. WIDE TUNNELING BARRIERS (HIGH TEMPERATURES)

If condition (16) is no longer valid, the maximum of the energy distribution of tunneling electrons lies above the lower integration limit Δ, as shown in Fig. 1b. As in [10], in this case we expand $Q(E_x)$ near the energy $\Delta_0 = \Delta_m$. The position of Δ_m is determined by condition (13); we determined the quantity Δ_m by joint solution of Eqs. (14) and (15). The integral for the current density (7) is reduced to the following expression:

$$j(V) = \frac{A^*T}{2k}\sqrt{\frac{\pi}{f_m}}\exp\left(-b_m - \frac{\Delta_m}{kT}\right)\left[\exp\left(\frac{eV}{kT}\right) - 1\right] \times \{1 + \mathrm{erf}[\sqrt{f_m}(\Delta_m - \Delta)]\}. \quad (21)$$

While retaining some formal similarity with (17), formula (21) has essential differences. The effective barrier height for thermal emission is Δ_m rather than Δ, and all the expansion coefficients acquire the index m, which indicates that b_m, c_m, and f_m are determined by relations (9)–(12) with $\Delta_0 = \Delta_m$. In the case of $\Delta_m = \Delta$, expression (21) coincides with the above solution (20). If $\Phi - \Delta_m \gg kT$, we can estimate the coefficients b_m and f_m. At $T = 300$ K, $\Phi - \Delta = 0.5$ eV, and $\Phi - \Delta_m = 0.4$ eV, we obtain $b_m \approx 10$ and $\sqrt{f_m} \approx 5$ eV^{-1}. For wide tunneling barriers and $2\sqrt{f_m}(\Delta_m - \Delta) \geq \sqrt{\pi}$, the probability function in (21) can be set equal to unity, which slightly increases the absolute value of the current but practically does not affect the form of the current–voltage characteristic, which, after a series of transformations, assumes the following form:

$$j(V) \approx j_0\exp\left[-\frac{\Phi}{kT} + \frac{3t(y_m) - 2v(y_m)}{24t^3(y_m)}\frac{(\Phi - \Delta)^2\hbar^2}{(kT)^3 d^2 m}\right] \times \left[\exp\left(\frac{eV}{kT}\right) - 1\right], \quad (22)$$

$$j_0 = A^*k^{-3/2}\sqrt{T}\sqrt{\frac{\pi(1 - y_m^2)}{2v(y_m)t(y_m)}}\frac{(\Phi - \Delta)\hbar}{d\sqrt{m}}. \quad (23)$$

The analysis of the exponential functions in (22) shows that the nonideality factor n can substantially exceed unity and the temperature dependence of the current can be strongly perturbed because of the presence of the term $\propto T^{-3}$ in the argument of the exponential function. It follows from the above expressions that the effective barrier height tends to Φ with increasing d or T, as one would expect because of the increasing contribution of the thermal component of the emission to the current. Nevertheless, the accuracy of calculations based on expressions (22) and (23) decreases as Δ_m approaches Φ; this is related to the chosen approximation for the tunneling transparency (8), which fails near the top of the barrier. For this reason, in (23) we cannot pass to the limit corresponding to the classical expression for the preexponential factor in thermal emission. For a more adequate representation of the current in this range of parameters, we can divide the interval of energy integration in (4) into two parts [10, 16] and set the tunneling transparency for thermal emission above the barrier top equal to unity.

It should be noted that, if $\Delta_m - eV \gg kT$, the requirement for complete depletion of the δ layer is not necessary and the current–voltage characteristic can be calculated approximately. If the maximum of the distribution of electrons tunneling through a triangular barrier is high in energy as shown in Fig. 1b, the form of the lower part of the tunnel barrier and the energy spectrum of electrons in the potential well of the δ layer are not important. For partial depletion of the δ layer, i.e., for $\Delta(V) < eV$ in expression (2), the distribution of the electric field in the MS contact changes. Provided that the characteristic localization scale for electrons in the potential well of the δ layer is much smaller than d and the difference between the Fermi energy and $E_c(d)$ can be disregarded, we may assume that all the applied voltage falls within the interval from 0 to d. The electric field is easily estimated, $F \approx (\Phi - eV)/ed$. To find the current, we can use expressions (22) and (23) and set $\Delta \equiv eV$. This result corresponds in essence to the current–voltage characteristic of the contact between a metal and an undoped semiconductor of thickness d if we disregard the screening length of the field in a

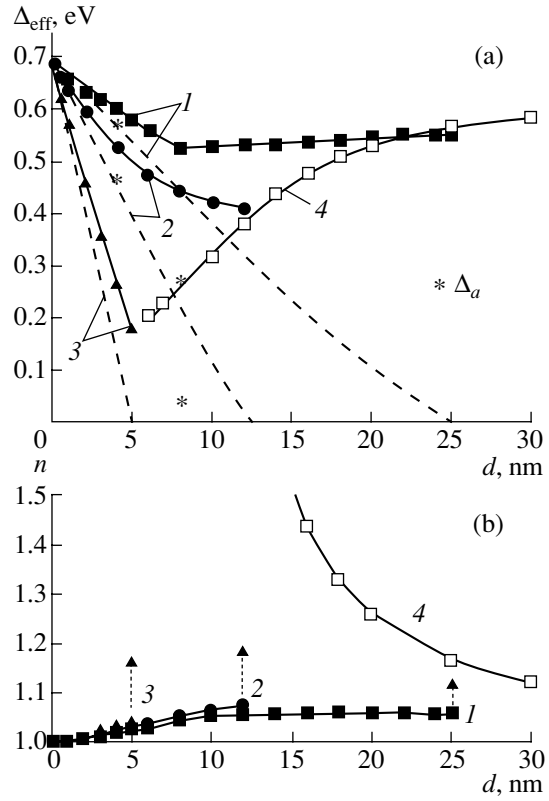

Fig. 2. (a) Effective barrier height Δ_{eff} and (b) the nonideality factor n as functions of the distance d for the Al–n-GaAs contact at T = 300 K at different levels of surface δ-doping density: N_s = (*1*) 2×10^{12}, (*2*) 4×10^{12}, and (*3*) 1×10^{13} cm^{-2}. (a) Dashed lines show the dependence of Δ on d for the corresponding values of N_s; the values of Δ_a are indicated. (*4*) The results of the calculation for partially depleted δ layers. (b) The arrows indicate jumps in n as the δ layer is filled with electrons.

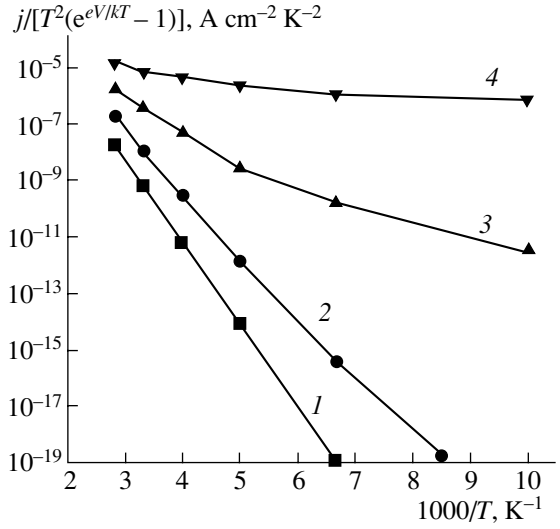

Fig. 3. Temperature dependences of the current in thin MS tunneling contacts for four alternatives modes of δ-doping: (*1*, *2*) d = 4 nm, (*1*) $N_s = 2 \times 10^{12}$ and (*2*) 4×10^{12} cm^{-2}; (*3*, *4*) d = 8 nm, (*3*) $N_s = 4 \times 10^{12}$ and (*4*) 8×10^{12} cm^{-2}.

degenerate semiconductor compared to d. This case is characterized by greater n and still greater deviations of the temperature dependence from that for thermal emission.

6. DISCUSSION

Using the above expressions, we can illustrate the form of current–voltage characteristics of MS contacts with subsurface δ-doping. To this end, we approximate the current calculated using the above formulas at some fixed temperature by the expression for the current of thermal emission over the effective barrier Δ_{eff}:

$$j(V) = A^* T^2 \exp\left(-\frac{\Delta_{eff}}{kT}\right)\left[\exp\left(\frac{eV}{nkT}\right) - 1\right]. \qquad (24)$$

This expression does not take into account the modification of Richardson's constant but provides an opportunity to estimate the "apparent" effective barrier height Δ_{eff} and the nonideality factor n. In Fig. 2, these parameters are plotted as functions of the distance d to the Al–n-GaAs contact at T = 300 K for different levels of surface doping N_s. In the range of parameters corresponding to nondepleted layers, all the d-dependences of Δ_{eff} and n at different N_s are the same (Fig. 2, curves *4*). It can be seen that, both for small and large values of d, the effective barrier height increases and the magnitude of the nonideality factor $n \approx 1$. The minimum values of the effective barrier heights are attained at d = 5–10 nm. A steep variation in n occurs as the δ layer is filled with electrons. Dashed lines show the values of Δ determined from formula (2) at V = 0. Introducing the parameters Δ_{eff} and n by expression (24), we can compare the results with the experimental data and with numerical calculations [8] and verify that there is good agreement between the data.

For a better representation of the temperature dependence of the current and more detailed analysis of the current in MS contacts, in Fig. 3 we plotted $\ln\{j/[T^2(\exp(eV/kT) - 1)]\}$ as a function of $1/T$. The chosen parameters corresponded to thin tunnel contacts with very different barrier heights. In the region of high temperatures, curves *1*, *2*, and *3* are well approximated by straight lines; thus, we can determine the activation energy Δ_a and the effective Richardson's constant A^{**} in the standard way [1, 2]. We obtain (*1*) Δ_a = 0.58 eV, A^{**} = 2.74 A cm^{-2} K^{-2}; (*2*) Δ_a = 0.47 eV, A^{**} = 0.76 A cm^{-2} K^{-2}; and (*3*) Δ_a = 0.27 eV, A^{**} = 0.012 A cm^{-2} K^{-2}. For curve *4*, we can obtain a rough estimate $\Delta_a \le 0.05$ eV. All the values of Δ_a are indicated in Fig. 2a. We can see that these values are close to those calculated by formula (2), and Δ_{eff} is always greater than Δ, since we have overestimated A^* in (24).

Therefore, processing the experimental data for diodes with a reduced barrier height [12, 13], one can obtain reliable information about the variation in the conduction-band edge near the contact only on the basis of an analysis of the measured temperature dependence using the above expressions for the current.

7. CONCLUSION

We obtained analytical expressions for the current of field-enhanced thermal emission in MS contacts with subsurface isotype δ-doping. Tunneling was described in the context of the Murphy–Good approach, and the decrease in barrier height due to the image forces was taken into account. We showed that subsurface isotype δ-doping can give rise to a decrease in the effective barrier height from the original values to several kT. Thus the voltage dependence of the current can remain exponential with a relatively small increase in the nonideality factor ($n \le 1.07$); i.e., the characteristic voltage at which the current–voltage characteristic of such a contact deviates from linearity is comparable to kT/e. At the same time, a drastic increase in the nonideality factor (up to $n \ge 1.5$) is predicted for contacts with a partially depleted δ layer. The expressions for the current–voltage characteristic differ substantially from the classical results on field-enhanced thermal emission for contacts between a metal and a heavily doped semiconductor obtained in [3] (see also [1, 2, 4]). For this reason, attempts [16] to use the formulas of [3] to process the experimental data for MS tunneling contacts with δ-doping were unproductive. On the contrary, the above expressions provide good agreement with numerical calculations and with experiment [8] and ensure effective diagnostics of the contacts by using temperature measurements of current–voltage characteristics.

ACKNOWLEDGMENTS

This study was supported by the Russian Foundation for Basic Research (project no. 01-02-16451) and by the program "Physics of Solid-State Nanostructures" of the Ministry of Science, Technology, and Industry.

REFERENCES

1. E. H. Rhoderick and R. H. Williams, *Metal–Semiconductor Contacts*, 2nd ed. (Claredon Press, Oxford, 1988).
2. S. M. Sze, *Physics of Semiconductor Devices*, 2nd ed. (Wiley, New York, 1981; Mir, Moscow, 1984).
3. F. A. Radovani and R. Stratton, Solid-State Electron. **9**, 695 (1966).
4. *Tunneling Phenomena in Solids*, Ed. by E. Burstein and S. Lundqvist (Plenum, New York, 1969; Mir, Moscow, 1973).
5. E. F. Schubert, J. E. Cunningham, W. T. Tsang, and T. H. Chiu, Appl. Phys. Lett. **49**, 292 (1986).
6. M. Missous and T. Taskin, Semicond. Sci. Technol. **8**, 1848 (1993).
7. V. I. Shashkin, A. V. Murel', Yu. N. Drozdov, *et al.*, Mikroélektronika **26**, 57 (1997).
8. V. I. Shashkin, A. V. Murel', V. M. Danil'tsev, and O. I. Khrykin, Fiz. Tekh. Poluprovodn. (St. Petersburg) **36**, 537 (2002) [Semiconductors **36**, 505 (2002)].
9. S. G. Miller and R. H. Good, Phys. Rev. **91**, 174 (1953).
10. E. L. Murphy and R. H. Good, Phys. Rev. **102**, 1464 (1956).
11. S. G. Christov, Surf. Sci. **70**, 32 (1978).
12. V. I. Shashkin, V. M. Daniltsev, O. I. Khrykin, *et al.*, in *Proceedings of International Semiconductor Device Research Symposium (ISDRS 1997)* (Charlottseville, USA, 1997), p. 147.
13. V. Shashkin, Yu. Chechenin, V. Danil'tsev, *et al.*, in *Proceedings of 23rd International Conference on Microelectronics (MIEL 2002)* (Nis, Yugoslavia, 2002), p. 335.
14. A. Modinos, *Field, Thermionic and Secondary Electron Emission Spectroscopy* (Plenum, New York, 1984; Nauka, Moscow, 1990).
15. A. P. Prudnikov, Yu. A. Brychkov, and O. I. Marichev, *Integrals and Series* (Nauka, Moscow, 1981; Gordon and Breach, New York, 1986).
16. J. M. Geraldo, W. N. Rodrigues, G. Medeiros-Ribeiro, and A. G. de Oliveira, J. Appl. Phys. **73**, 820 (1993).

Translated by I. Zvyagin

Semiconductors, Vol. 38, No. 5, 2004, pp. 560–564. Translated from Fizika i Tekhnika Poluprovodnikov, Vol. 38, No. 5, 2004, pp. 580–584.

LOW-DIMENSIONAL SYSTEMS

Geometric Structure and Spectral Characteristics of Electronic States in Silicon Nanoparticles

S. I. Kurganskiĭ* and N. A. Borsch

Voronezh State University, Voronezh, 394006 Russia

**e-mail: phssd18@main.vsu.ru*

Submitted September 8, 2003; accepted for publication September 11, 2003

Abstract—The results of optimization of the geometric structure and calculations of the electronic structure of silicon anionic Si_{12}^-–Si_{16}^- clusters are reported. The semiempirical PM3 method was used in the calculations. States of different multiplicities ($2S + 1 = 2$, 4, and 6) were considered. Comparison of the results of the calculations with experimental photoelectron spectra shows that, for Si_{12}^-–Si_{14}^- clusters, there is good agreement for states of multiplicity 2. For Si_{15}^- and Si_{16}^- clusters, the spectra for states of multiplicities 4 and 2, respectively, agree with experiment. © *2004 MAIK "Nauka/Interperiodica".*

1. INTRODUCTION

Over the last decade, silicon clusters have become an object of intensive studies, both experimental and theoretical. This is related to the possibility of their application in optoelectronics [1] and the need to search for qualitatively new materials that can accelerate the transition from microelectronics to nanoelectronics. Clusters may become a basis for such materials due to their unique properties, such as the strong dependence of the electronic structure on size and geometry, which allow one to model the required characteristics of a device. Silicon is a basic material of the modern semiconductor industry, and, therefore, silicon clusters are the most interesting objects to be studied.

Experimental studies of the geometric structure of nanoparticles are rather difficult, since the production and separation of clusters containing a given number of atoms is a complicated problem. Theoretical simulation of cluster geometry is therefore of special interest. There are numerous studies in which the structure of silicon clusters was simulated by different methods (see, for example, [2–4]). At the same time, there are only a few studies in which the structure of a cluster was obtained by optimizing the geometry using semiempirical methods. Moreover, the dependence of a cluster's structure on state multiplicity was not considered. In addition, in none of the studies was even an indirect comparison of model calculations with experimental data made.

We discuss the results of semiempirical calculations of the geometric and electronic structure of anionic silicon clusters that have a unit charge and contain from 12 to 16 silicon atoms. We calculated geometric structures of Si_{12}^-–Si_{16}^- clusters for states of different multiplicities ($2S + 1 = 2$, 4, and 6). The electronic structure was calculated for each geometric configuration. On the basis of such calculations, densities of electronic states were determined and compared to the experimental photoelectron spectra [5]. The agreement of the theory with experiment makes it possible to identify the structure of the clusters that were experimentally produced. Moreover, we optimized the cluster geometry and performed ab initio calculations of the electronic structure of the Si_{12}^- cluster. Therefore, we were able to compare the adequacy of semiempirical and nonempirical methods. It will be shown below that the use of the semiempirical PM3 method for studying the electronic structure of the clusters considered is more efficient, as it allows one to obtain the desired results in much shorter calculation times.

We chose anionic clusters as objects of our study because it is precisely Si_n^- clusters that are detected in the experiments on the production of the clusters [6] and, especially, in the study of the electronic structure by photoelectron spectroscopy [5].

2. METHOD OF CALCULATION

We performed the calculations by the semiempirical PM3 method [7, 8]. This method is based on the approximation that neglects diatomic differential overlap (NDDO) [9]. The PM3 method takes into account much more experimental data than other semiempirical methods, thus yielding better results [7, 8]. The basis 6-21G was used for nonempirical calculations.

We calculated the energy eigenvalues for each molecular orbital, i.e., the energy spectrum in which each molecular orbital was represented by a level. We

1063-7826/04/3805-0560$26.00 © 2004 MAIK "Nauka/Interperiodica"

obtained the theoretical spectra after replacing each energy level with a Gaussian distribution with a half-width of 0.2 eV and summing the intensities of all distributions at each energy. We constructed partial contributions of Si*s* and Si*p* states in a similar way, taking into account that the intensity of each line corresponding to a molecular orbital was equal to the sum of the squares of the coefficients in the expression for the molecular orbital written out as a linear combination of atomic orbitals. The calculated and experimental spectra were matched on the energy axis using the position of the principal maximum.

3. GEOMETRIC STRUCTURE

In Fig. 1, the geometric structures of the Si_{12}^- and Si_{14}^- clusters for the states of multiplicity 6 and of the Si_{16}^- cluster for the state of multiplicity 2 are shown; these structures were optimized according to the principle described above. As will be shown below, the best agreement between the theoretical and experimental spectra is obtained for these structures. The structures corresponding to the other multiplet states of these clusters, as well as the structures of the Si_{13}^- and Si_{15}^- clusters, are considered below in detail. In Table 1, we give the symmetry types for each structure, as well as the bonding energies per atom.

3.1. The Si_{12}^- *Cluster*

All three structures of the Si_{12}^- cluster of different multiplicities belong to the C_s symmetry group. Each of these structures can be described as a hexagonal bipyramid with four additional atoms. The structure corresponding to the state of multiplicity 2 is most stable. The bonding energy per atom for this cluster is greater than for the clusters with the multiplet states 4 and 6. The distances between the nearest neighbor atoms at the base of the bipyramid are different. The distance between the atoms near the vertex atoms is 2.48 Å, whereas the other distances in this ring are equal to only 2.23 Å. The cluster structure calculated by the nonempirical method is identical to the optimized structure obtained by the semiempirical method. On average, the interatomic distances differ by 10%.

3.2. The Si_{13}^- *Cluster*

The structure of the anionic Si_{13}^- cluster in states of multiplicities 2 and 4 is similar to that of the Si_{12}^- cluster. This structure also corresponds to a hexagonal bipyramid but with 5 additional atoms. The distances between the nearest neighbor atoms at the base of this bipyramid decrease as the distance from the group of additional atoms increases. Thus, we note that the dis-

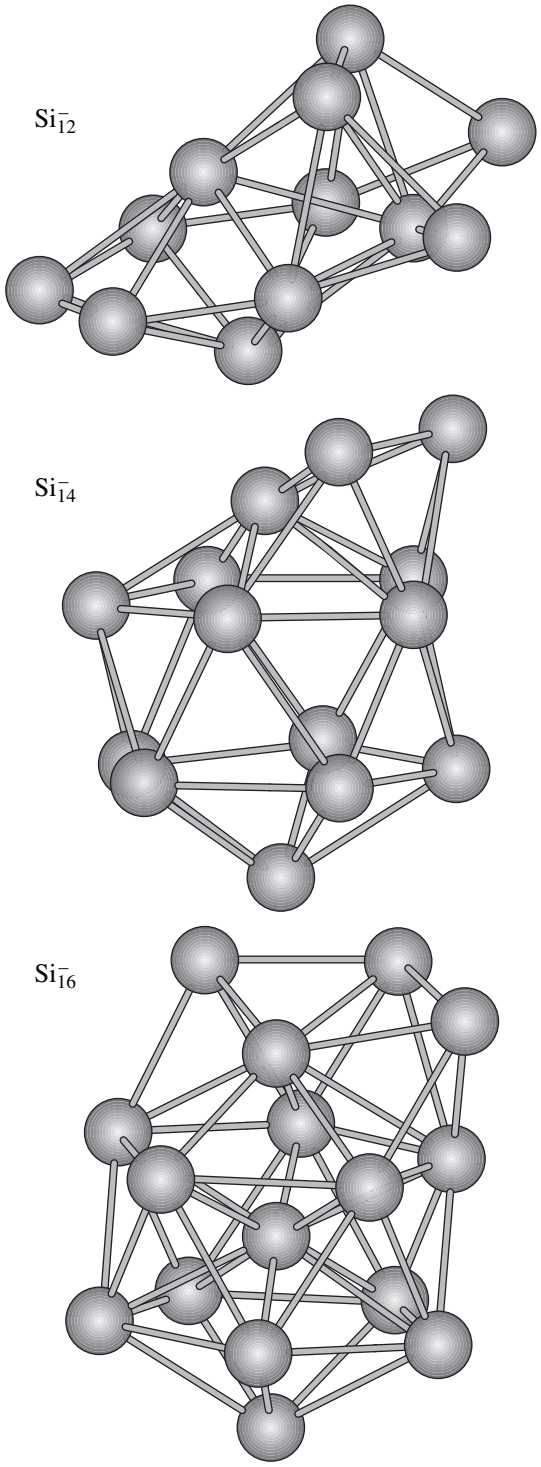

Fig. 1. Optimized geometric structure of the Si_{12}^- and Si_{14}^- clusters for the states of multiplicity 6 and of the Si_{16}^- cluster for the state of multiplicity 2.

Table 1. Parameters of the geometric structure and bonding energies in the Si_{12}^-–Si_{16}^- – clusters

Cluster	Symmetry			Bonding energy, eV/atom		
	$2S+1=2$	$2S+1=4$	$2S+1=6$	$2S+1=2$	$2S+1=4$	$2S+1=6$
Si_{12}^-	C_s	C_s	C_s	4.59	4.53	4.55
Si_{13}^-	C_s	C_s	C_1	4.72	4.69	4.68
Si_{14}^-	C_{2v}	C_{2v}	C_s	4.77	4.74	4.68
Si_{15}^-	C_{2v}	C_{2v}	C_s	4.97	4.91	4.88
Si_{16}^-	C_1	C_1	C_s	4.94	4.93	4.91

Table 2. Energy positions of the main features in the spectra of the Si_{12}^- clusters

Experiment [5]	PM3 calculations	Ab initio calculations
0.0	0.2	–
0.6	0.6	0.6
1.0	1.0	1.1
1.8	1.5	1.6
2.5	2.2	2.6

Note: The energies are measured from the highest occupied orbital (in eV).

tances between the nearest neighbor atoms decrease with the number of neighboring atoms. The Si_{13}^- cluster in the state of multiplicity $2S + 1 = 6$ has a somewhat different structure. It consists of two pentagonal bipyramids that share a face with one additional atom per bipyramid. The greatest bonding energy per atom corresponds to the Si_{13}^- cluster in the state of multiplicity 2.

3.3. The Si_{14}^- *Cluster*

The structure of the Si_{14}^- cluster is an icosahedron with two additional atoms. Clusters with multiplicities 2 and 4 have a structure of symmetry C_{2v}. The cluster in the multiplet state $2S + 1 = 6$ has a structure of lower symmetry, C_s. The greatest bonding energy per atom corresponds to the cluster in the state of multiplicity 2.

3.4. The Si_{15}^- *and* Si_{16}^- *Clusters*

The Si_{15}^- and Si_{16}^- clusters have similar structures, which can be obtained by centering a 12-atom icosahedron and adding two and three vertex atoms, respectively. The most stable configuration of 15 silicon atoms corresponds to the state of multiplicity 4, and the Si_{16}^- cluster is most stable in the state of multiplicity 2.

4. ELECTRONIC STRUCTURE

The calculated density of states and the experimental photoelectron spectra [5] are shown in Fig. 2. The position of the highest occupied orbital is chosen as the energy zero. Comparison of the theoretical and experimental data shows that, for the Si_{16}^- cluster only, the best agreement between the calculations and the experiment corresponds to the most stable configuration (i.e., to that of multiplicity 2). For clusters with a different number of atoms, agreement between the experiment and the calculated spectra is attained for the structures that do not have a maximum bonding energy per atom. Thus, for Si_{12}^-–Si_{14}^- clusters, the agreement of the calculated spectra with experiment is obtained for states of multiplicity 6, and for the Si_{15}^- cluster, for the state of multiplicity 2. The agreement of the experimental spectrum with the spectrum obtained for the Si_{12}^- cluster by ab initio calculations is much worse than the agreement with the spectrum obtained by semiempirical calculations. Although the energy positions of the main features of the nonempirical spectrum practically coincide with the positions of the peaks in the experimental spectrum (Table 2), the shapes of the spectra are appreciably different (Fig. 2a). The semiempirical calculations yield a spectrum whose shape and energy positions of the main peaks agree with the experiment.

Analyzing the spectra, we can make the following remark: the contribution of Si*p* states is predominant in all clusters at the top of the valence band. For the Si_{12}^- cluster, the Si*s* states are located in the region where the intensity of the spectrum of Si*p* states decreases. For the Si_{13}^- cluster, partial contributions of Si*s* and Si*p* states are more diffuse and the features of the spectra of Si*s* and Si*p* states coincide in the interval (–1)–(–3) eV. For the spectra of the Si_{14}^-–Si_{16}^- clusters, the maximum of Si*s* states shifts to the top of the valence band and coincides in energy with the principal maximum of the spectrum of Si*p* states. The predominant contribution of Si*p* states in the region near 0 eV is preserved.

We also calculated such characteristics of the electronic structure as the width of the cluster valence band and the gap between the highest occupied and the lowest unoccupied orbitals (HOMO–LUMO gap). These values are listed in Table 3.

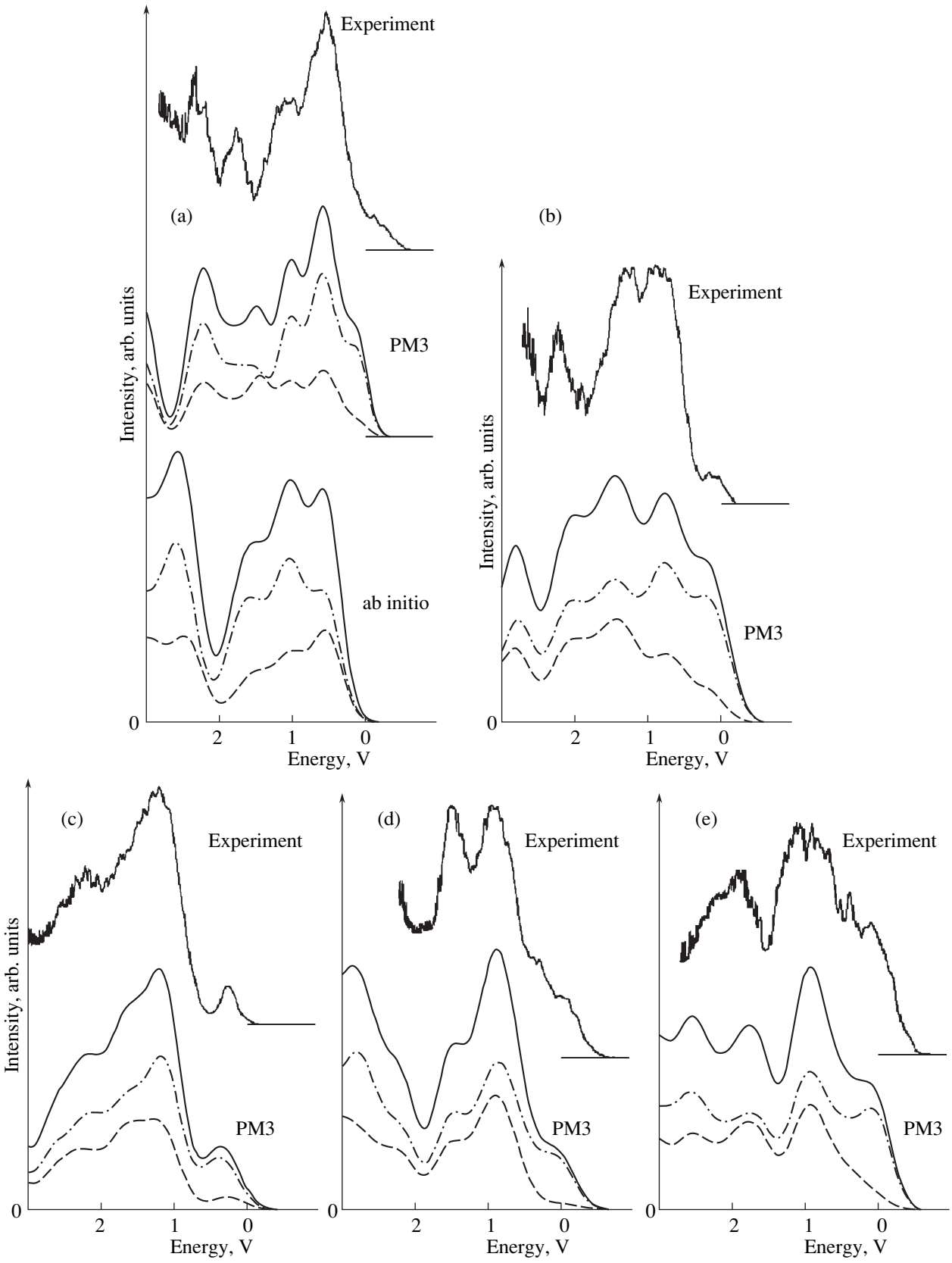

Fig. 2. Experimental [5] and theoretical photoelectron spectra for the (a) Si_{12}^-, (b) Si_{13}^-, (c) Si_{14}^-, (d) Si_{15}^-, and (e) Si_{16}^- clusters (solid lines). Dashed curves correspond to the contributions of the Si*s* states and dash-dotted lines, to the contributions of Si*p* states.

Table 3. Main characteristics of the electronic structure of the Si_{12}^-–Si_{16}^- – clusters

Cluster	Multiplicity	E_v, eV			$E_{HOMO–LUMO}$, eV		
		spin up	spin down	total energy	spin up	spin down	total energy
Si_{12}^-	$2S + 1 = 2$	13.51	13.12	13.50	4.34	3.97	3.97
	$2S + 1 = 4$	14.08	13.52	14.08	3.18	3.47	3.06
	$2S + 1 = 6$	13.60	12.80	13.60	3.90	4.20	3.65
Si_{13}^-	$2S + 1 = 2$	13.98	13.51	13.98	4.13	3.87	3.68
	$2S + 1 = 4$	14.03	13.37	14.03	3.90	4.11	3.57
	$2S + 1 = 6$	14.28	13.55	14.28	3.83	3.97	3.61
Si_{14}^-	$2S + 1 = 2$	13.47	13.53	13.63	3.59	4.08	3.75
	$2S + 1 = 4$	13.99	13.05	13.99	3.94	3.63	3.17
	$2S + 1 = 6$	14.23	12.93	14.23	3.82	3.29	2.82
Si_{15}^-	$2S + 1 = 2$	15.12	14.84	15.12	4.07	3.88	3.92
	$2S + 1 = 4$	15.30	14.55	15.30	3.81	3.88	3.25
	$2S + 1 = 6$	15.38	14.35	15.38	3.97	3.73	3.34
Si_{16}^-	$2S + 1 = 2$	15.22	15.14	15.24	3.68	3.70	3.70
	$2S + 1 = 4$	15.46	14.96	15.46	3.77	3.55	3.48
	$2S + 1 = 6$	15.45	14.59	15.45	3.71	3.70	3.14

Note: E_v is the width of the valence band, $E_{HOMO–LUMO}$ is the HOMO–LUMO gap.

5. CONCLUSIONS

We can draw the following conclusions from our study.

(i) The geometric structure of the Si_{12}^- and Si_{13}^- clusters can be conceived as a hexagonal bipyramid with additional atoms. The exception is the structure of the Si_{13}^- cluster in the state of multiplicity 6.

(ii) The structures of the Si_{14}^-–Si_{16}^- clusters can be represented as regular icosahedrons with additional atoms; the icosahedrons are centered in the case of Si_{15}^- and Si_{16}^- clusters.

(iii) For the Si_{12}^-–Si_{14}^- clusters, the calculated photoelectron spectra agree with the experimental spectra for the state of multiplicity 6; for the Si_{15}^- and Si_{16}^- clusters, the spectra agree in the case of multiplicities 4 and 2, respectively. For the Si_{12}^- cluster, the spectrum obtained by the semiempirical method agrees with the experimental one much better than the spectrum obtained by nonempirical calculations.

(iv) For all clusters, the contribution of the Si*p* states at the top of the valence band is predominant. For the Si_{14}^-–Si_{16}^- clusters, the maximum of the spectrum of Si*s* states lies much closer to the top of the valence band than in the spectra of Si*s* states in the Si_{12}^- and Si_{13}^- clusters.

REFERENCES

1. L. Pavesi, L. Dal Negro, C. Mazzoleni, *et al.*, Nature **408**, 440 (2000).
2. B. K. Panda, S. Mukherjee, and S. N. Behera, Phys. Rev. B **63**, 45404 (2001).
3. D. K. Yu, R. Q. Zhang, and S. T. Lee, Phys. Rev. B **65**, 245417 (2002).
4. K. M. Ho, A. A. Shvartsburg, B. Pan, *et al.*, Nature **392**, 582 (1998).
5. M. Astruc Hoffmann, G. Wriggle, B. Issendorff, *et al.*, Eur. Phys. J. D **16**, 9 (2001).
6. H. Hiura, T. Miyazaki, and T. Kanayama, Phys. Rev. Lett. **86**, 1733 (2001).
7. J. J. P. Stewart, J. Comput. Chem. **10**, 209 (1989).
8. J. J. P. Stewart, J. Comput. Chem. **10**, 221 (1989).
9. *Semiempirical Methods of Electronic Structure Calculation*, Ed. by G. Segal (Plenum, New York, 1977; Mir, Moscow, 1980), Vol. 1.

Translated by I. Zvyagin

Semiconductors, Vol. 38, No. 5, 2004, pp. 565–571. Translated from Fizika i Tekhnika Poluprovodnikov, Vol. 38, No. 5, 2004, pp. 585–592.

LOW-DIMENSIONAL SYSTEMS

Luminescence of Stepped Quantum Wells in GaAs/GaAlAs and InGaAs/GaAs/GaAlAs Structures

V. F. Agekyan[1], Yu. A. Stepanov[1], I. Akai[2], T. Karasava[2], L. E. Vorob'ev[3], D. A. Firsov[3], A. E. Zhukov[4], V. M. Ustinov[4], A. Zeilmeyer[5], S. Shmidt[5], S. Hanna[5], and E. Zibik[5]

[1]*St. Petersburg State University, St. Petersburg, 198504 Russia*
[2]*Osaka City University, Sugimoto, Osaka 558, Japan*
[3]*St. Petersburg State Polytechnical University, St. Petersburg, 195251 Russia*
[4]*Ioffe Physicotechnical Institute, Russian Academy of Sciences, St. Petersburg, 194021 Russia*
[5]*Institute of Physics, University of Bayreuth, Bayreuth 95440, Germany*

Submitted October 15, 2003; accepted for publication October 17, 2003

Abstract—Luminescence spectra of doped and undoped GaAs/GaAlAs and InGaAs/GaAs/GaAlAs structures containing several tens of stepped quantum wells (QW) are investigated. The emission bands related to free and bound excitons and impurity states are observed in QW spectra. The luminescence excitation spectra indicate that the relaxation of free excitons to the *e*1*hh*1 state proceeds via the exciton mechanism, whereas an independent relaxation of electrons and holes is specific to bound excitons and impurity states. The energy levels for electrons and holes in stepped QWs, calculated in terms of Kane's model, are compared with the data obtained from the luminescence excitation spectra. The analysis of the relative intensities of emission bands related to *e*1*hh*1 excitons and exciton states of higher energy shows that, as the optical excitation intensity increases, the *e*1*hh*1 transition is more readily saturated at higher temperature, because the lifetime of excitons increases. Under stronger excitation, the emission band of electron–hole plasma arises and increases in intensity superlinearly. At an excitation level of ~10^5 W/cm^2, excitons are screened and the plasma emission band dominates in the QW emission. Nonequilibrium luminescence spectra obtained in a picosecond excitation and recording mode show that the *e*1*hh*1 and *e*2*hh*2 radiative transitions are 100% polarized in the plane of QWs.

1. INTRODUCTION

Optical spectra of quasi-2D III–V semiconductor structures have been actively investigated over the last three decades: the objects of study were different undoped and doped structures with different types of heterointerfaces. Recently, particular attention was drawn to optical spectra of structures containing $In_xGa_{1-x}As$ solid solutions in the form of quasi-2D quantum wells (QW), quantum wires, and quantum dots, which were fabricated either specially for scientific research or for commercial applications in transistor and laser structures [1–9]. Structures with a simple QW profile have been thoroughly studied, so now attention has turned to structures containing QWs with a complicated profile, in particular, stepped QWs [10]. In this study, we discuss optical properties of $GaAs/Ga_{1-x}Al_xAs$ and $In_{1-x}Ga_xAs/GaAs/Ga_{1-x}Al_xAs$ structures containing wide QWs, with narrow QWs built in their bottom. The main goals of this study were (i) to compare the energies of electron and hole levels, as determined from the photoluminescence (PL) excitation spectra, with those calculated taking into account the band nonparabolicity; (ii) to determine the types of radiative recombination in doped and undoped structures; and (iii) to study the emission spectra under weak and strong optical excitation at different temperatures and modes of recording.

2. SAMPLES AND EXPERIMENT

$GaAs/Ga_{1-x}Al_xAs$ structures containing several tens of stepped QWs were grown by MBE on semi-insulating ⟨100⟩ GaAs substrates. We studied the undoped structure 4-447 and the structures 4-443 and 4-445 with doped narrow QW regions, in which the Si concentration was 2.6×10^{17} and 7.9×10^{17} cm^{-3}. Structures 4-447, 4-443, and 4-445 contained, respectively, 35, 60, and 40 stepped QWs (Fig. 1a shows the potential profile in structure 4-447). The undoped $In_{0.24}Ga_{0.76}As/GaAs/Ga_{1-x}Al_xAs$ structure 4-189 contains 20 undoped stepped QWs that are separated from the substrate and the capping layer by short-period $Ga_{0.65}Al_{0.35}As$ superlattices (Fig. 1b).

Luminescence was excited with a CW Ar laser and pulsed lasers: a nitrogen laser with a photon energy of 3.68 eV, a pulse width of 5 ns, and a pulse repetition rate of 100 Hz; a parametric system based on a Nd:YAG laser (10 ns, 10 Hz); and the second harmonic of a Nd:YAG laser, with a pulse width of several picoseconds. A parametric system that allows smooth tuning of the photon energy of laser light was used in the study of

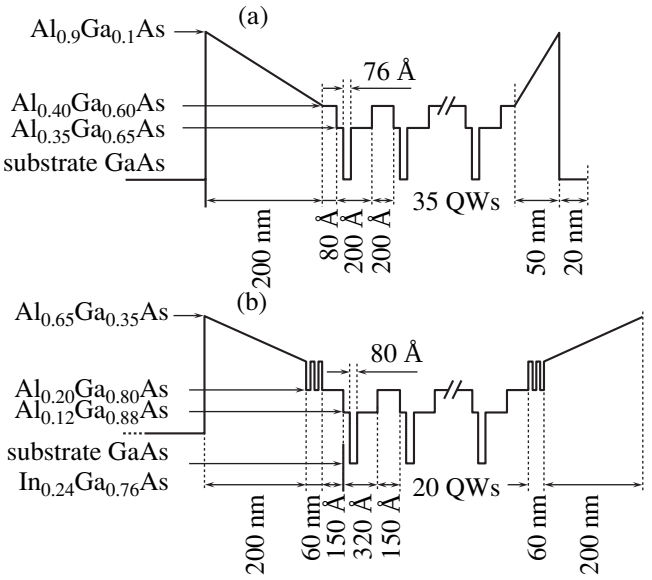

Fig. 1. Potential profile in QW structures. (a) GaAs/GaAlAs structure 4-447 with 35 undoped QWs; 20-nm-thick capping layer is doped with Si to 3×10^{17} cm^{-3}. (b) InGaAs/GaAlAs structure 4-189 with 20 undoped QWs; the QW region is confined by $[Al_{0.35}Ga_{0.65}As(20\ Å)/Al_{0.2}Ga_{0.8}As(10\ Å)] \times 50$ superlattices.

the PL excitation spectra of QWs. Picosecond pulses of the second harmonic of the Nd:YAG laser were used in the study of fast kinetics of the QW luminescence and in the recording of nonequilibrium spectra of the QW emission. The transmission spectra in the range of inter-subband transitions were recorded in a multiple-pass configuration.

3. RESULTS AND DISCUSSION

3.1. Luminescence Spectra

The shape of the luminescence spectrum of undoped structure 4-447 at $T = 3$ K heavily depends on the optical excitation mode (Fig. 2a). When the above-barrier excitation is strong enough, the spectrum consists of three narrow bands. In the case of a selective subbarrier excitation of *e*2*hh*2 exciton transition (see the PL excitation spectrum, Fig. 3a), only one band appears in the QW luminescence, and two bands of lower energy are observed under weak above-barrier excitation. The high-energy band corresponds to *e*1*hh*1 free excitons, and the energy spacings between this and the two other bands are 4 and 8 meV, which corresponds to typical energies of exciton localization on single-layer QW width fluctuations of different lateral sizes in $GaAs/Ga_{1-x}Al_xAs$ systems [11]. We explain the strong dependence of the structure of the luminescence spectrum on the energy of exciting photons as follows: under resonant excitation of a *e*2*hh*2 exciton, the relaxation of an exciton as a single whole occurs; in this case, it is not localized during the radiative lifetime. In

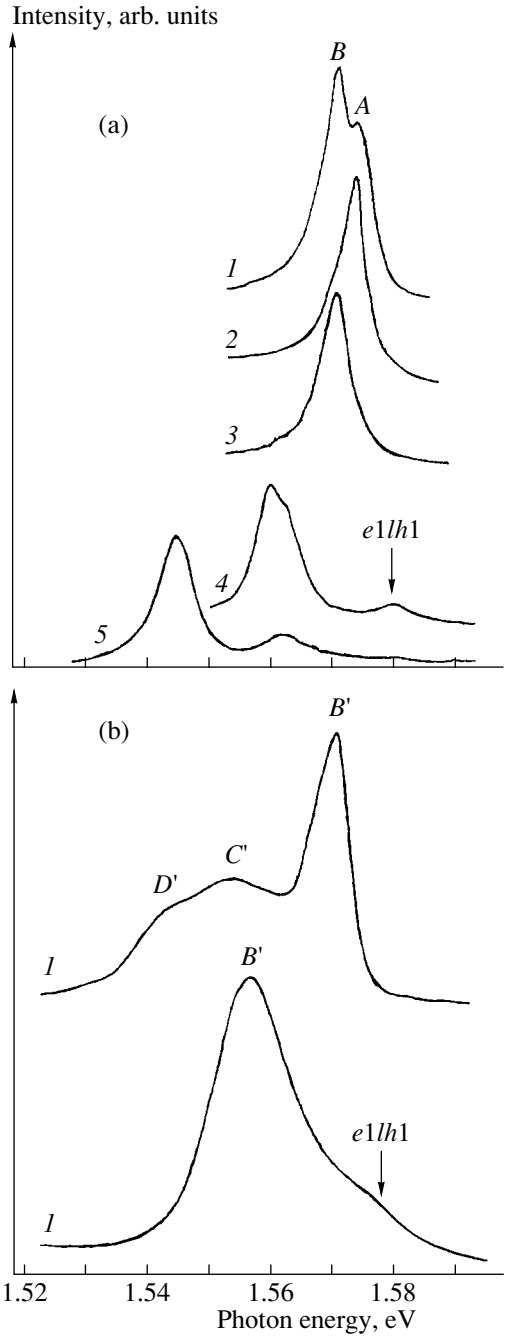

Fig. 2. Luminescence spectra of undoped and doped GaAs/GaAlAs structures. (a) Undoped structure 4-447: (*1*, *4*, *5*) strong above-barrier excitation, (*2*) selective excitation at the peak of the PL excitation spectrum at 1.7395 eV (see Fig. 3a), (*3*) weak above-barrier excitation; temperature T = (*1*–*3*) 3, (*4*) 100, and (*5*) 200 K; (*A*) free exciton *e*1*hh*1, (*B*) exciton localized at the interface. (b) Doped structure 4-445, above-barrier excitation: T = (*1*) 3.4 and (*2*) 100 K; (*B*') localized excitons *e*1*hh*1, (*C*', *D*') impurity states, (*e*1*lh*1) exciton transition involving a light hole.

the case of above-barrier excitation, the relaxation of an electron and hole proceeds independently. They form a localized exciton in the following manner: first, a hole is trapped by a QW width fluctuation; then, a localized

hole captures an electron in its Coulomb field. When the above-barrier excitation is strong enough, the states of localized excitons are completely filled, and free excitons are formed from electrons and holes under these conditions. When a sample is heated above 130 K, the luminescence spectrum is narrowed because of the delocalization of excitons, and, in addition, an emission band related to the $e1lh1$ exciton transition involving light holes appears. The nature of emission from GaAs QWs was recently studied using the time-resolved luminescence and pump-probe techniques [12]. The authors of [12] came to the conclusion that the spectra obtained under resonant and nonresonant excitation are fundamentally different, which agrees with our data.

The emission spectra of Si-doped structures 4-443 and 4-445 contain a strong band of localized excitons and two weaker bands that are spaced 20–30 meV from the main one (Fig. 2b) and are presumably caused by impurities. At $T > 50$ K, the impurity bands disappear successively, and $e1lh1$ excitons are delocalized.

The study of kinetics of luminescence at $T = 3.4$ K has shown that the rise time of the exciton emission is several tens of picoseconds. The intensity then decreases fast over a period of 250 ps, and its further decay is described well by the dependence $\exp(-t/t_0)$ with $t_0 \approx 1$ ns; t_0 varies only slightly when the excitation intensity is raised by up to two orders of magnitude. The intensity of impurity-related emission in doped structures varies only slightly during the time of full decay of the exciton luminescence.

In the range $T = 3$–300 K, the temperature variation of the energy of the $e1hh1$ exciton peak is well described by the Varshni relation [13]: $\Delta E = aT^2/(T + b)$, $a = 0.5405 \times 10^{-3}$, $b = 204.0$.

As the temperature is raised from 80 to 200 K, the quantum yield of the QW luminescence in the structures under study decreases by a factor of 4–6, depending on the excitation level and structure type. As the excitation level increases, the integral intensity of the QW luminescence in InGaAs/GaAs grows faster at 100 K than at 1.4 K.

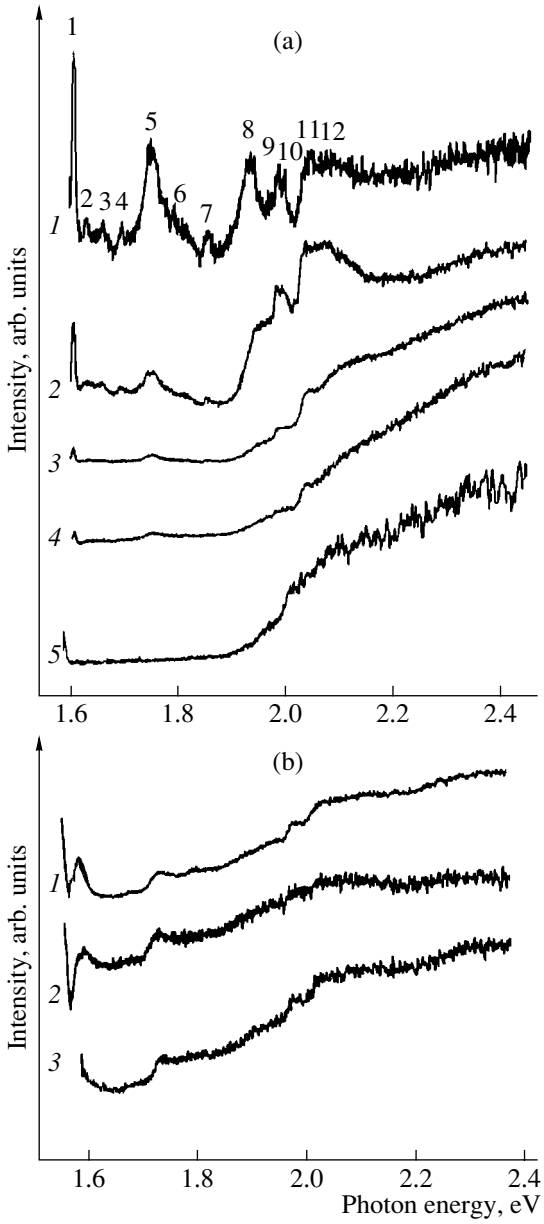

Fig. 3. PL excitation spectra of GaAs/GaAlAs structures at $T = 3.4$ K. (a) Undoped structure 4-447; recorded at (*1*) the blue shoulder of luminescence band *A*, (*2*) the peak of *A* band, (*3*) the peak of luminescence band *B*, and (*4*, *5*) the red tail of *B* band (see Fig. 2a); peak numbers in spectrum *1* correspond to notations in Table 2. (b) Doped structure 4-445; recorded at the peaks of luminescence bands (*1*) *B*', (*2*) *C*', and (*3*) *D*' (see Fig. 2b).

3.2. Luminescence Excitation Spectra

In undoped structure 4-447, the shape of the PL excitation spectrum at low temperature strongly depends on the photon energy at which the spectrum is recorded (Fig. 3a). At $T = 3.4$ K, the excitation spectrum of PL of free excitons (the high-energy edge of the QW emission spectrum) exhibits a series of sharp peaks, both strong and weak, and a sharp short-wavelength step at about 2.03 eV. When the recording energy is shifted to the range of emission of localized states, the PL excitation spectra become smoother, and there remain only weak features corresponding to strong peaks and steps in the excitation spectrum of the PL of free excitons. At $T = 100$ K, the PL excitation spectrum has a weak structure throughout the entire luminescence spectrum. In the case of doped structures 4-443 and 4-445, the PL excitation spectrum exhibits no sharp features and only weakly depends on temperature and photon energy (Fig. 3b). These results show that the resonant excitation of excitons corresponding to upper ($e2hh2$, etc.) electron and hole subbands in QW strongly enhances the quantum yield of luminescence only for free excitons. The lack of a similar effect in the excitation spectrum of PL of localized excitons con-

Table 1. Energies of quantum-well levels in structure 4-447

Principal quantum number	Electrons	Heavy holes	Light holes
1	47.5	12.8	34.5
2	171.3	50.7	132.8
3	284.8	111.6	217.0
4		187.3	–
5		209.6	–

Note: Energies (meV) are reckoned from the bottom of the related QWs.

Table 2. Comparison of experimental and calculated transition energies

Number of peak in the PL excitation spectrum and the transition type		Energy spacing from the *e1hh1* transition, meV	
		experiment (3.4 K)	calculation
1	*e*1*lh*1	17	21.7
2	*e*1*lh*2	41.5	38
3	?	72	
4	*e*1*lh*3	108	100
	(*e*1*lh*1)		(120)
5	*e*2*hh*2	164	162
6	*e*1*hh*3	210	204
7	*e*3*lh*1	270	259
8	*e*3*hh*3	348	336
	(*e*3*lh*2)		(357)
9	*e*3*hh*4	404	412
10	*e*3*hh*4	409	412
11	*e*3*lh*3	450	441
	(*e*3*hh*5)		(434)
12	(step) interband transition in $Al_{0.4}Ga_{0.6}As$ barrier	500	500

firms that they are formed mainly via successive localization of a hole and an electron in a broadened region of QW, not via the capture of free excitons in this region.

The sharp structure of the excitation spectrum of PL of free excitons makes it possible to compare the peak positions in this spectrum with the energies of electron levels in stepped QWs of structure 4-447, calculated for a nonparabolic electron band. The calculation was done in terms of Kane's model, using the transfer-matrix method. The positions of hole levels were determined in the approximation of a constant effective mass. Calculated energies of quantum-well levels for electrons and holes, reckoned from the bottom of corresponding QWs, are listed in Table 1.

Calculated values of the energy differences between the *e*1*hh*1 transition and transitions corresponding to higher quantum-well levels for electrons and holes are listed in Table 2. These data are compared with the energy spacing between the peaks in the PL excitation spectrum and the *e*1*hh*1 peak of the free exciton emission at 1.5757 eV at $T = 3.4$ K for structure 4-447. These results allowed us to identify the peaks in the PL excitation spectrum and to estimate the degree of coincidence between the calculation and experiment for stepped QWs.

3.3. Inter-Subband Transitions

The absorption spectrum related to inter-subband transitions was studied for doped structure 4-445 in the temperature range $T = 20$–300 K (Fig. 4). The spectrum contains an absorption band whose energy (0.118 eV at $T = 20$ K) coincides with the energy spacing between *e*1 and *e*2 levels, calculated and found from the PL excitation spectrum. When the temperature is raised to room temperature, the peak is shifted to 0.115 eV; this characterizes the temperature dependence of the energy spacing between the two lowest electron levels in a stepped QW. This dependence is defined mainly by the temperature-related variation of the barrier height in the structures under study.

3.4. Luminescence under Strong Excitation

Now we discuss how the luminescence spectra recorded in the CW mode change when the intensity of pulsed excitation is raised. In the spectrum of the undoped 4-447 structure recorded at $T = 3$ K, the *e*1*hh*1 exciton band becomes wider when the above-barrier pulsed pumping is increased. At pumping level $I \approx 5 \times 10^3$ W/cm^2, a new band appears. When the pumping level is raised further, this band increases in intensity superlinearly and shifts to lower energies, whereas the exciton band is depressed and vanishes at $I = 3 \times 10^4$ W/cm^2 (Fig. 5a). This new band can be attributed to the emission of the electron–hole plasma, and the strong shift with the increase in I is related to the renormalization of the electron and hole energies in a QW at high density of photocarriers. The excitation level $I = 3 \times 10^4$ W/cm^2 corresponds to a photon flux density of 10^{16} cm^{-2} in a 10-ns laser pulse, i.e., more than 10^{14} cm^{-2} per QW. If the exciton radius in a QW $a_{ex} = 10$ nm, then $(\pi a_{ex}^2)^{-1} = 3 \times 10^{11}$ cm^{-2}. If the exciton lifetime is ~1 ns, the excitation at this level should cause a complete screening of the Coulomb interaction, which is observed in the experiment.

A similar transformation of the emission spectrum with a rise in I is observed at 100 K; the difference is that the blue tail of the exciton luminescence is enhanced to a much greater extent, and the exciton and plasma emission bands overlap. The strong narrowing of the spectrum at $I > 10^4$ W/cm^2 indicates that the exci-

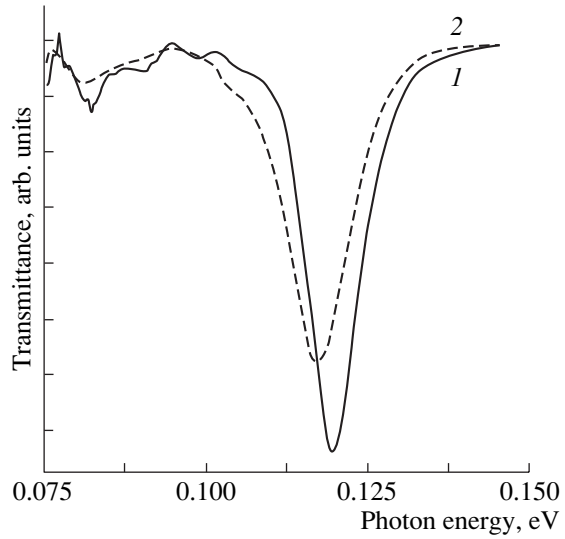

Fig. 4. Transmission spectra of doped structure 4-445 in the range of inter-subband transitions at $T = (1)$ 20 and (2) 300 K. The absorption band corresponds to electron transition $e1e2$.

ton effect is completely screened; in this case, all the QW luminescence is related to plasma emission (Fig. 5b). The appearance and superlinear enhancement of the new band cannot be attributed to the formation of charged exciton complexes, because this band is observed at high temperatures.

Now we consider in some detail how the luminescence spectra of stepped QWs change when the intensity of pulsed optical excitation with a nitrogen laser is raised, and when temperature increases from 4 K to room temperature. Under weak excitation, a slight blue tail appears in the emission spectrum with increasing temperature as a result of thermal population of the excited states. When the pulsed optical excitation is enhanced, the relative intensity of transitions from higher states increases. At low temperatures, the energies of two sharp short-wavelength peaks are in satisfactory agreement with the expected energies of radiative exciton transitions $e1hh3$ and $e2hh2$ (Fig. 6).

A specific feature of the luminescence of the QWs under study is as follows: the higher the temperature, the larger the relative intensity of emission from excited states at an elevated level of excitation. The stronger contribution of higher states can be accounted for by the saturation of the ground-state transition $e1hh1$; i.e., the higher temperature makes saturation easier. This is equivalent to the increase in the $e1hh1$ exciton lifetime, τ_{ex}, as temperature rises, which correlates well with the data of [14–16]. In [14], the relation between τ_{ex} and the temperature-dependent spectral width of the exciton line in a QW was obtained, and it was shown that, by virtue of the momentum conservation law, the number of excitons involved in the radiative recombination decreases as temperature increases. A linear increase in τ_{ex} with temperature in 2D structures was experimentally observed in [15, 16]; in QWs 6–10 nm in width, τ_{ex} increased from 150 to 1500 ps when temperature was raised from 10 to 100 K [16]. Recently [17] it was shown that the temperature behavior of τ_{ex} in InGaAs QWs depends strongly on the orientation of the GaAs substrate, and a considerable rise in τ_{ex} is observed for the $\langle 001 \rangle$ orientation as the sample is heated.

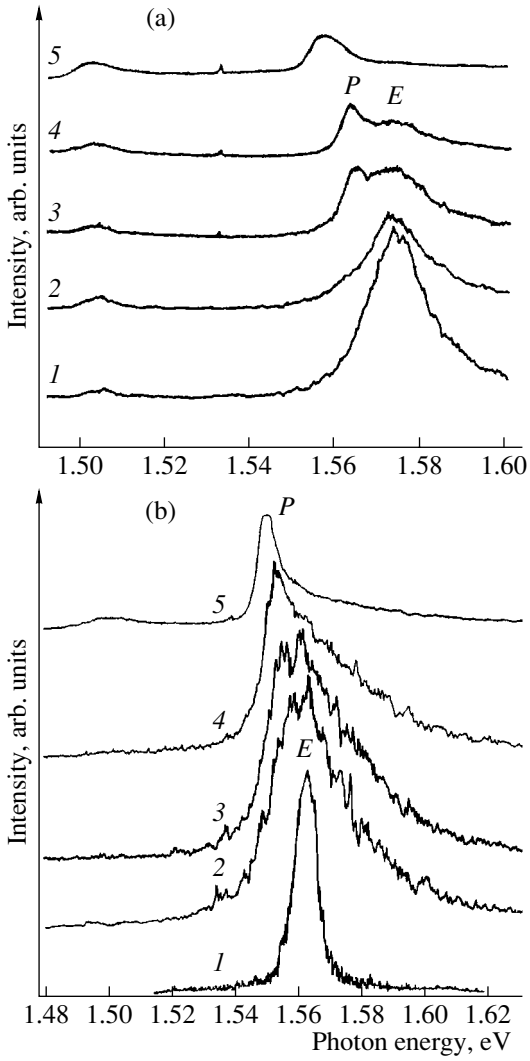

Fig. 5. Luminescence spectra of undoped GaAs/GaAlAs structure 4-447 at different temperatures and excitation levels *I*. *E* and *P* are the emission bands of excitons and electron–hole plasma. (a) $T = 3$ K: $I = (1)$ 0.2, (2) 0.4, (3) 0.6, (4) 1.3, and (5) 8.7×10^4 W cm^{-2}. (b) $T = 100$ K: $I = (1)$ 1×10^2, (2) 1.5×10^3, (3) 3×10^3, (4) 6×10^3, and (5) 4×10^4 W cm^{-2}.

The strongest transformation of the emission of $In_{0.24}Ga_{0.76}As$ QWs (structure 4-189) was observed at high temperatures when the excitation power was raised to 10^4 W/cm^2 or more. Figure 7 shows luminescence spectra at high and low excitation level in the temperature range $T = 4$–300 K. Under strong excitation, we observe a $e2hh2$ exciton and a new band that appears as a shoulder on the $e1hh1$ exciton emission

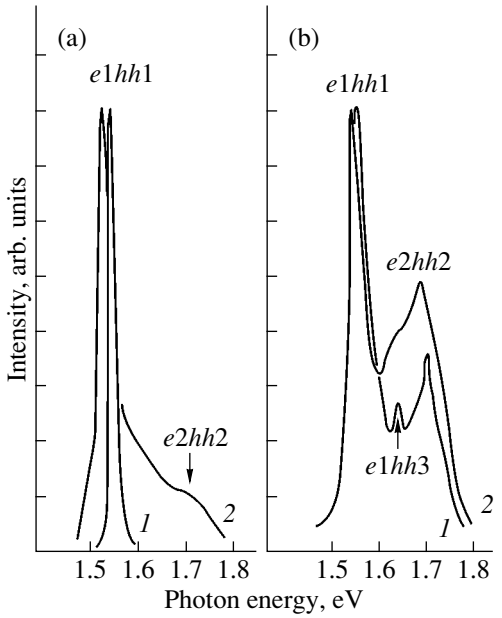

Fig. 6. Luminescence spectra of GaAs/GaAlAs structure 4-445 at (a) $T = 77$ and (b) 160 K, at excitation levels $I =$ (*1*) 10^2 and (*2*) 10^4 W/cm^2. The spectra are normalized to maximum intensity.

band at 4 K. As temperature increases, this band is strongly enhanced and is predominant in the emission at $T = 270$ K; in this case, *e*1*hh*1 and *e*2*hh*2 exciton transitions are observed as weak features on both sides of its profile. Presumably, this band can be attributed to the emission of the electron–hole plasma, by analogy to the emission of an undoped structure 4-447 with GaAs QWs under strong excitation (Fig. 5). It is noteworthy that in stepped $In_{0.24}Ga_{0.76}As$ QWs the peak of the plasma-related band, which dominates under strong excitation, lies on the high-energy side of the *e*1*hh*1 exciton transition.

The behavior of the luminescence spectra of doped structures 4-443 and 4-445 is dependent on the temperature and excitation level like the spectra in the undoped structure 4-447, but the domination of plasma emission is not reached at the same excitation level in these structures.

Figure 8 shows spectra of polarized luminescence from structure 4-447 excited with laser pulses (2.33 eV, ~300 W, ~4 ps) and the absorption spectrum of this structure. The exciting light was focused onto a spot 300 μm in diameter on the structure surface at the end of the sample, and luminescence from the edge facet was detected. At this excitation level, the surface density of nonequilibrium carriers is 10^{13}–10^{14} cm^{-2}, so the

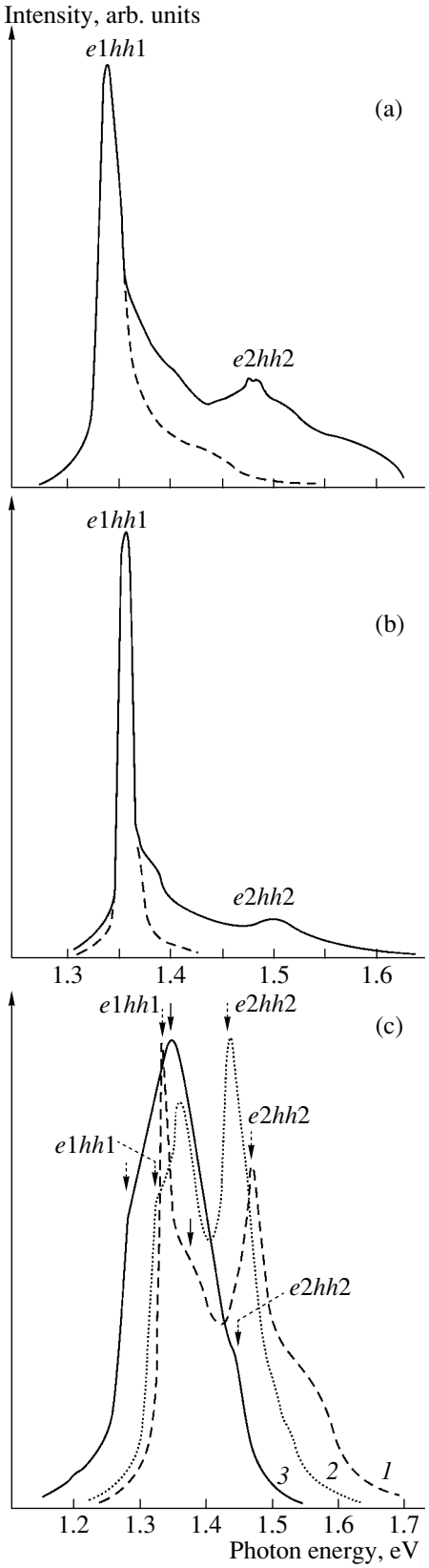

Fig. 7. Luminescence spectra of InGaAs/GaAs/GaAlAs structure 4-189 at different temperatures and optical excitation levels. (a) $T = 77$, $I = 10$ and 10^3 W/cm^2 (solid and dashed lines, respectively). (b) $T = 4$ K, $I = 10$ and 10^3 W/cm^2 (solid and dashed lines). (c) Strong excitation, $I > 10^4$ W/cm^2, $T =$ (*1*) 130, (*2*) 185, and (*3*) 300 K; dashed arrows indicate exciton transitions, solid arrows indicate the emission band of electron–hole plasma.

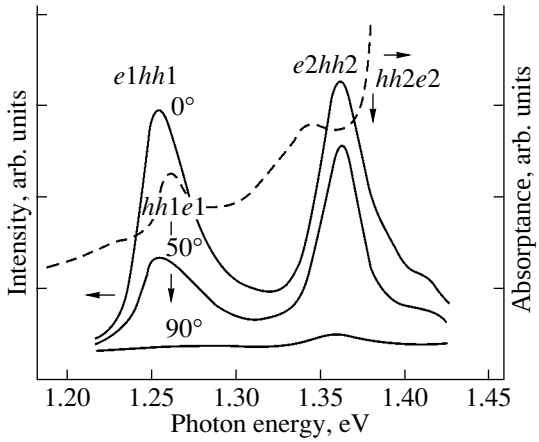

Fig. 8. Spectra of InGaAs/GaAs/GaAlAs structure 4-189 at $T = 300$ K. PL spectra at different polarizations (solid lines); interband absorption spectrum (dashed line). The angle between the plane of polarization of light and the QW plane is indicated.

upper subbands are filled with carriers, not only the ground ones. The emission related to electron transitions to heavy-hole levels must be polarized in the plane of a structure [18], as is observed in the experiment. Since in this experiment luminescence is excited with picosecond pulses and recorded for only a few picoseconds after the excitation is terminated, nonequilibrium spectra are observed. These spectra exhibit a strong band related to transitions between excited electron and heavy-hole subbands, and the above-described emission of electron–hole plasma is not observed, because its formation is relatively slow.

4. CONCLUSION

In undoped GaAs/GaAlAs structures with stepped QWs, excitation spectra of PL of $e1hh1$ free excitons, recorded at $T \approx 3$ K, demonstrate sharp peaks corresponding to the excitation of excitons related to higher electron and hole subbands. At the same time, these peaks are weak or not observed at all in the excitation spectra of PL of localized excitons and impurity states in undoped and doped structures. In the first case, an exciton relaxes as a whole, whereas localized and impurity states are formed from electrons and holes that relax independently. When GaAs/GaAlAs and InGaAs/GaAs/GaAlAs structures are subjected to strong optical excitation, the lowest radiative transition $e1hh1$ is saturated more easily at elevated temperatures, which indicates that the lifetime of the $e1hh1$ exciton increases at higher temperatures. The emission band of electron–hole plasma appears at an excitation level of 5×10^3 W/cm^2 and increases in intensity superlinearly with rising excitation intensity, whereas the exciton emission disappears owing to the screening of the Coulomb interaction. Radiative transitions $e1hh1$ and $e2hh2$ observed in the picosecond mode of excitation and recording are polarized in the plane of a QW, which agrees with theory.

ACKNOWLEDGMENTS

This study was supported in part by the Ministry of Education of the Russian Federation (grant no. E02-3.4-426).

REFERENCES

1. H. Q. Hou, W. Staguhn, S. Takeyama, *et al.*, Phys. Rev. B **43**, 4152 (1991).
2. R. Cingolani, R. Rinaldi, H. Lipsanen, *et al.*, Phys. Status Solidi A **178**, 263 (2000).
3. S. Martini, A. A. Quivy, A. Tabata, and J. R. Leite, J. Appl. Phys. **90**, 2280 (2001).
4. G. Bacquet, F. Hassen, N. Lauret, *et al.*, Superlattices Microstruct. **14**, 117 (1993).
5. J. Martinez-Pastor *et al.*, Superlattices Microstruct. **14**, 39 (1993).
6. C. Lopez, R. Mayoral, F. Meseguer, *et al.*, J. Appl. Phys. **81**, 3281 (1997).
7. Q. Zhou, M. O. Manasreh, B. D. Weaver, and M. Missous, Appl. Phys. Lett. **81**, 3374 (2002).
8. H. Weman, L. Sirigu, K. F. Karisson, *et al.*, Appl. Phys. Lett. **81**, 2839 (2002).
9. C. Constantin, E. Martinet, M.-A. Dupertius, *et al.*, Phys. Rev. B **61**, 4488 (2000).
10. V. Ya. Aleshkin, D. M. Gaponova, D. G. Revin, *et al.*, Izv. Ross. Akad. Nauk, Ser. Fiz. **67** (2), 196 (2003).
11. U. Jahn and H. T. Grahn, Phys. Status Solidi B **234**, 443 (2002).
12. G. R. Hayes and B. Deveaux, Phys. Status Solidi A **190**, 637 (2002).
13. Y. P. Varshni, Physica (Amsterdam) **34**, 149 (1967).
14. J. Feldman, G. Peter, E. O. Gobel, *et al.*, Phys. Rev. Lett. **59**, 2337 (1987).
15. L. C. Andreani, F. Tassone, and F. Bassani, Solid State Commun. **77**, 641 (1991).
16. H. Jeong, I.-J. Lee, J.-C. Seo, *et al.*, Solid State Commun. **85**, 111 (1993).
17. B. L. Liu, B. Liu, Z. Y. Xu, and W. K. Ge, J. Appl. Phys. **90**, 5111 (2001).
18. *Quantum Well Lasers*, Ed. by P. S. Zory, Jr. (Academic, Boston, 1993).

Translated by D. Mashovets

Semiconductors, Vol. 38, No. 5, 2004, pp. 572–575. Translated from Fizika i Tekhnika Poluprovodnikov, Vol. 38, No. 5, 2004, pp. 593–597.

LOW-DIMENSIONAL SYSTEMS

Properties of Self-Organized SiGe Nanostructures Formed by Ion Implantation

Yu. N. Parkhomenko*, A. I. Belogorokhov^, N. N. Gerasimenko***, A. V. Irzhak*, and M. G. Lisachenko******

**Moscow Institute of Steel and Alloys (Technological University), Leninskiĭ pr. 4, Moscow, 119936 Russia*
***State Research Institute for the Rare-Metals Industry, Moscow, 119017 Russia*
^e-mail: belog@mig.phys.msu.su
****Moscow State Institute of Electronic Engineering (Technical University), Zelenograd, Moscow oblast, 103498 Russia*
*****Moscow State University (Faculty of Physics), Vorob'evy gory, Moscow, 119892 Russia*
Submitted October 29, 2003; accepted for publication November 4, 2003

Abstract—Properties of self-organized SiGe quantum dots formed for the first time by ion implantation of Ge ions into Si are studied using Auger electron spectroscopy, atomic-force microscopy, and scanning electron microscopy. It is found that a spatially correlated distribution of Ge atoms is observed in Si layers implanted with Ge ions after subsequent annealing of these layers. As a result, nanometer-sized regions enriched with germanium are formed; germanium concentration in these regions is 10–12% higher than that in the surrounding matrix of the SiGe solid solution. Optical properties of the layers with SiGe quantum dots were studied using Raman scattering and photoluminescence. An intense photoluminescence peak is observed in the wavelength region of 1.54–1.58 μm at room temperature. © *2004 MAIK "Nauka/Interperiodica".*

1. INTRODUCTION

Recently, considerable attention has been given to the problem of searching for new methods for the generation, modulation, and detection of electromagnetic radiation in the infrared and microwave spectral regions. Nanometer-sized semiconductor structures can be used to fabricate next-generation optoelectronic devices that can operate in the aforementioned spectral regions and have properties that cannot be obtained using traditional materials. In this context, it is necessary to develop new types of semiconductor nanostructures and carry out studies aimed at clarifying the special features of interparticle interactions and collective phenomena in low-dimensional systems. Among these systems, SiGe nanostructures occupy a prominent place because of their potential application in devices and integration based on silicon technology.

Progress in the formation of structures with quantum dots (QDs) was achieved owing to the self-organized growth of QDs in the Stranski–Krastanov mode using molecular-beam epitaxy. At the same time, there are other promising methods for the synthesis of ordered nanostructures. One of these methods is ion implantation.

In this paper, we report the results of studying the properties of self-organized $Si_{1-x}Ge_x$ QDs ($x = 0.3$) that were formed for the first time using ion implantation.

2. EXPERIMENTAL

Germanium ions $^{74}Ge^+$ were implanted into the wafers of crystalline *p*-Si with a (111) orientation using a SCI-218 BALZERS high-current accelerator. The implantation doses were $D = 5 \times 10^{16}$ or 1×10^{17} cm^{-2}, and the ion energy was $E = 50$ keV. In order to eliminate the channeling effect, the beam of ions incident on the silicon wafer was deflected by 7° from the normal incidence. After implantation, the samples were subjected to photonic pulsed annealing for 3 s at a temperature of 900°C in a nitrogen atmosphere. Using the above treatment, we managed to form regions with an increased concentration of Ge in a thin layer of SiGe solid solution. The lateral size of these regions was several tens of nanometers and the height could be as large as 10 nm (nanosized structures).

We used a PHI-680 (Physical Electronics, USA) Auger spectrometer to study the local elemental composition of the structures and also to estimate the geometric parameters and spatial distribution of QDs in the surface region. The energy and current of primary electrons were equal to 10 keV and 10 nA, respectively; the diameter of the primary beam was ~15 nm, and the depth of the analysis was no larger than 50 Å. The surface topography was studied using a Solver P47 (NT-MDT Co.) atomic-force microscope (AFM). In order to study the shape of the nanosized structures and their elemental composition, we treated the surface of the samples in a KOH solution (33%) for 25 s at 100°C,

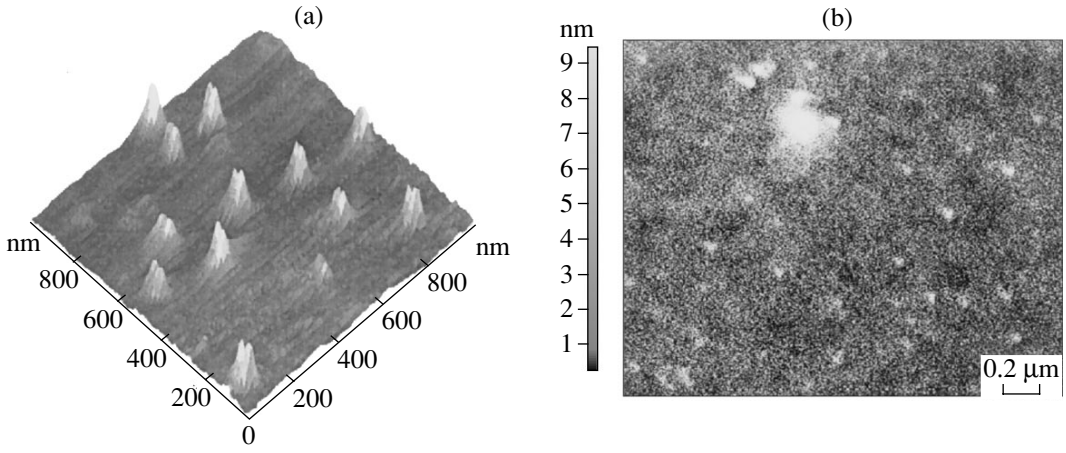

Fig. 1. Images of the regions enriched with germanium in a SiGe sample; the images were obtained using (a) atomic-force microscopy and (b) scanning electron microscopy. The dose of implanted Ge ions $D = 5 \times 10^{16}$ cm^{-2}.

which made it possible to reveal the regions with the highest germanium concentration.

Raman spectra were obtained in the backscattering geometry (in which case the planes of polarization of the incident and scattered light are perpendicular to each other) using the 457.9-nm line of an Ar^+ laser for pumping. In order to avoid irreversible thermal effects on the sample or its degradation, we set the pumping power at 30 mW. The setup included a Jobin-Yvon T64000 double monochromator and a GaAs photomultiplier cooled to 78 K.

Photoluminescence (PL) was excited by radiation from a He–Ne laser (wavelength, 632.8 nm; power, 20 mW). The excitation intensity was varied from 10 to 20 mW/cm^2. The PL spectra were recorded using an InGaAs photodiode (with an operating wavelength range from 700 to 1800 nm) and synchronous detection. To this end, the laser radiation was modulated using a chopper with a frequency of 400 Hz. The samples were mounted in an optical cryostat at an angle of 45° to the optical beam, whose diameter was 0.3 mm. The PL spectra were measured in the temperature range 11–300 K.

3. RESULTS AND DISCUSSION

Chemical etching of the surface of the samples under investigation made it possible to reveal a structure that was ordered in size. The profile of this structure was caused by the different etching rates for silicon and germanium (the etching rate for germanium is lower under the conditions specified above). The structure revealed using the AFM consists of regions whose lateral sizes are (50 ± 10) nm and height varies from 5 to 10 nm (Fig. 1a). An analysis of the surface image obtained in secondary electrons using a scanning electron microscope confirmed the presence of regions with a different contrast related to the nonuniformity of germanium distribution (Fig. 1b); these regions are 30–50 nm in size.

Using Auger spectroscopy with a high spatial resolution, we determined the elemental composition of the regions under consideration (Fig. 2). We found that the concentration of Ge atoms in these regions was 10–12% higher than in the surrounding $Si_{1-x}Ge_x$ solid solution (outside of these regions) and amounted to $x \approx 0.3$.

The Raman spectra of the samples are shown in Fig. 3. After the structures under investigation were annealed, the peaks that are located at 270 cm^{-1} (Ge–Ge, TO), 370 cm^{-1} (Si–Ge, TO), 480 cm^{-1} (Si–Si, LO) and correspond to the scattering of photons by the transverse (TO) and longitudinal (LO) optical phonons in the SiGe amorphous material [1] disappeared from the spectra; this observation indicates that there is no amorphous phase in the annealed samples (unlike the unannealed samples). Peaks at 316 cm^{-1} (related to optical phonons in stressed germanium [2]) and at 500–515 cm^{-1} (related to optical phonons in stressed silicon [3]) were also not observed in the spectra. This fact suggests that the layer of the SiGe solid solution is not stressed and, consequently, the appearance of regions enriched with germanium is caused by the relaxation of elastic stresses.

The presence of additional peaks at 502.7 and 250 cm^{-1} (related to vibrations of the Si–Si and Ge–Ge bonds in SiGe, respectively) in the Raman spectra, along with the peaks inherent in the $Si_{0.8}Ge_{0.2}$ solid solution (518.6, 403.3 cm^{-1} (vibrations of Si–Ge bonds), and 285.7 cm^{-1} [4]), indicates that $Si_{0.7}Ge_{0.3}$ regions are present in SiGe. In the latter case ($Si_{0.7}Ge_{0.3}$), the aforementioned wave numbers should be equal to 517.9, 404.8, and 287.3 cm^{-1} [4]. A shift of the peaks to lower frequencies for $x \approx 0.3$ is related to the spatial confinement of the main modes of optical phonons, which is characteristic of the vibrations in SiGe QDs [3, 5].

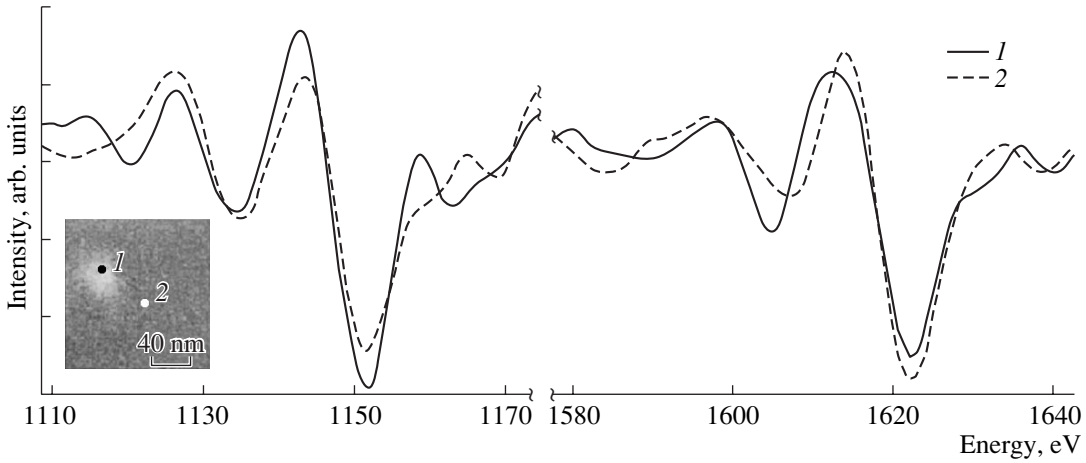

Fig. 2. Auger spectra of a SiGe sample (*1*) in the region enriched with Ge and (*2*) in the surrounding SiGe matrix. The dose of implanted Ge ions $D = 5 \times 10^{16}$ cm^{-2}.

Two main peaks are observed in the PL spectra measured at various temperatures *T*: a peak at a wavelength λ = 1124 nm (1.1 eV, *T* = 11–30 K) and a peak at λ = 1530–1540 nm (0.794–0.805 eV, *T* = 11–300 K). The former peak corresponds to the zero-phonon line in silicon emission (the phonon replica peaked at 1.04 eV is also observed in the spectrum measured at *T* = 11 K; this line is spaced ~60 meV from the main line, which corresponds to the energy of a TO phonon in Si). The latter peak corresponds to the emission from Si_xGe_{1-x} QDs. The inference that the PL peak in the region of 1540 nm is caused by emission from ordered $Si_{0.7}Ge_{0.3}$ QDs is supported by the fact that this peak should be located at wavelengths λ = 1.252–1310 nm for the $Si_{1-x}Ge_x$ solid solution with *x* = 0.2–0.3. Furthermore, the intensity of emission in the region of 0.8 eV is much higher than that in the region of 1.1 eV and is detected even at temperatures higher than 295 K in the samples implanted with a dose of Ge ions of $D = 5 \times 10^{16}$ cm^{-2}; the half-width of the PL peak under consideration is ~61 meV. Most likely, the relaxation of elastic stresses in the SiGe layer in the course of heat treatment led to the ordering of the regions with an increased concentration of Ge atoms, i.e., to the formation of QDs, which caused the observed intensity of the PL signal. Emission from dislocations in silicon may be another cause of the PL signal at an energy of ~800 meV. In that case, two characteristic lines peaked at 810 and 870 meV should be observed in the PL spectrum; the width of these lines should be ~10 meV, and their intensity should decrease severalfold as the sample temperature increases from 11 to 77 K [2]. An analysis of variations in the PL spectra with temperature (Fig. 4) shows that the contribution of emission from dislocations in Si is insignificant in the case under consideration.

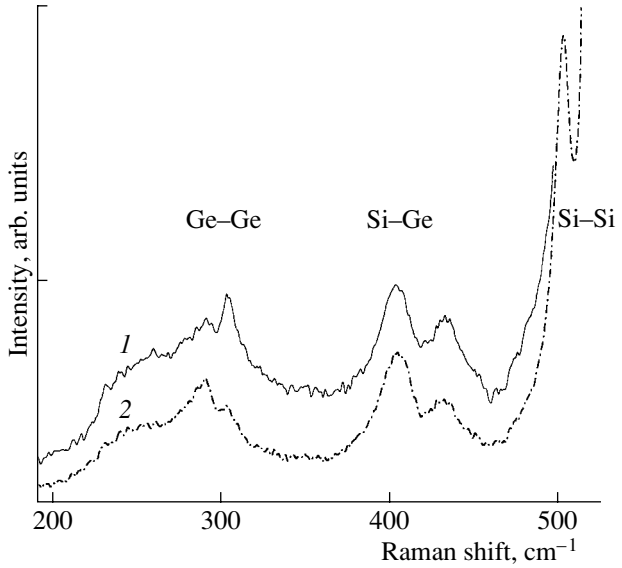

Fig. 3. Raman spectra of a SiGe sample. The dose of implanted Ge ions D = (*1*) 5×10^{16} and (*2*) 1×10^{17} cm^{-2}.

We can use a model based on the effective-mass approximation [6] to estimate the average size of QDs. In Fig. 5, we show the calculated energies of band-to-band transitions in SiGe QDs in relation to the QD height at *T* = 11 and 77.3 K. Horizontal lines correspond to the transition energies determined from the PL spectra (taking into account the measurement accuracy) at the temperatures under consideration. Comparison of the experimental data with the results of calculations made it possible to estimate the average QD height, which was found to be equal to ~(7.2–7.3) nm, which was in satisfactory agreement with the AFM data.

The origination of ordered regions with increased content of germanium can be explained in the following way. A mismatch between the lattice constants of Si and Ge amounts to ~4% and gives rise to appreciable elastic stresses in the SiGe structure. Under certain conditions related to the thickness of the Si–Ge layer and the specific features of the layer formation, these stresses relax; as a result, dislocations are generated.

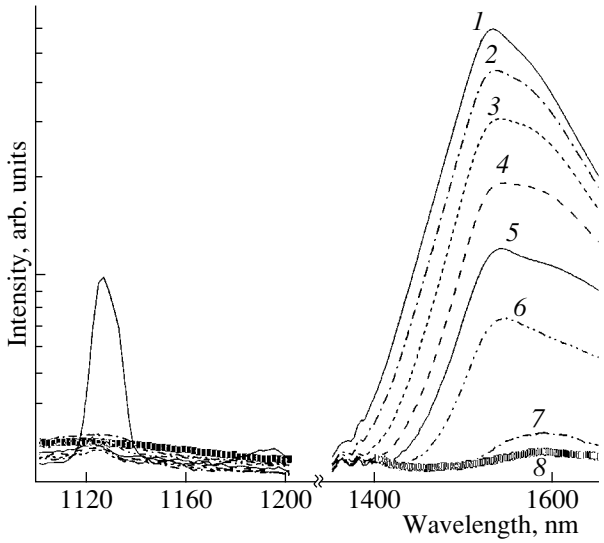

Fig. 4. Photoluminescence spectra of a SiGe sample at temperatures T = (*1*) 11, (*2*) 30, (*3*) 45, (*4*) 60, (*5*) 75, (*6*) 100, (*7*) 150, and (*8*) 300 K. The dose of implanted Ge ions $D = 5 \times 10^{16}$ cm^{-2}.

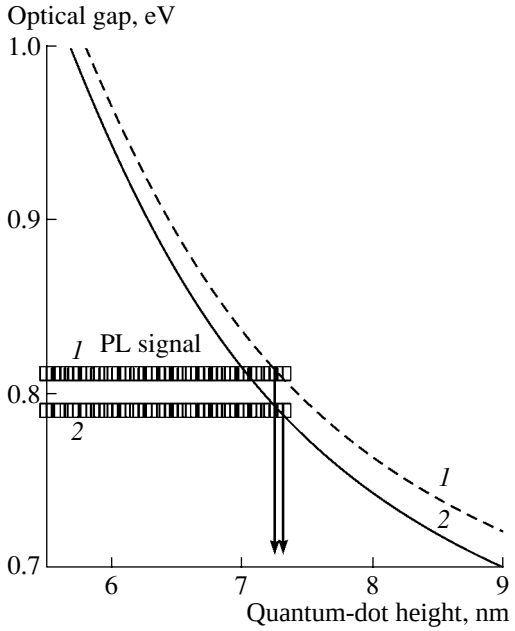

Fig. 5. Calculated energies of band-to-band transitions for a SiGe quantum dot in relation to the quantum-dot height at temperatures T = (*1*) 11 and (*2*) 77.3 K. Horizontal lines represent the transition energies determined from the photoluminescence (PL) spectra.

The elastic-stress fields arising around misfit dislocations and the interaction of these fields lead to the redistribution and spatial ordering of dislocations. The spatially ordered dislocations act as gettering centers for germanium, which, in turn, leads to a periodic distribution of the regions with an increased content of germanium, i.e., to the formation of QDs. According to Burbaev *et al.* [2], the dislocation density in a completely relaxed $Si_{0.7}Ge_{0.3}$ epitaxial film with a thickness of 100 Å is equal to 10^{10}–10^{11} cm^{-2}. The QD density in the structure we obtained ($D = 5 \times 10^{16}$ cm^{-2}) is equal to ~10^{10} cm^{-2}. Thus, the assumption that dislocations are trapping centers for germanium is confirmed.

4. CONCLUSION

We note that ion implantation was used for the first time to form an array of self-organized ordered SiGe quantum dots. The reported results of experiments on the detection of clusterization of germanium atoms introduced into silicon by ion implantation open up new possibilities for forming nanosized structures in a germanium–silicon system.

The observation of intense photoluminescence in the SiGe quantum dots at room temperature in the wavelength range 1.54–1.58 μm is reason to hope that these structures will find practical application in optoelectronic devices and fiber-optic information links.

ACKNOWLEDGMENTS

This study was carried out in the context of the program “Integration” (code I-0964) and was supported by the Russian Foundation for Basic Research (project no. 03-02-16938).

REFERENCES

1. Sunil Kumar and H. J. Trodahi, J. Appl. Phys. **70**, 3088 (1991).
2. T. M. Burbaev, T. N. Zavaritskaya, V. A. Kurbatov, *et al.*, Fiz. Tekh. Poluprovodn. (St. Petersburg) **35**, 979 (2001) [Semiconductors **35**, 941 (2001)].
3. K. Sawano, Y. Hirose, S. Koh, *et al.*, J. Cryst. Growth **251**, 685 (2003).
4. J. C. Tsang, P. M. Mooney, F. Dacol, and J. O. Chu, J. Appl. Phys. **75**, 8098 (1994).
5. N. N. Gerasimenko, V. Yu. Troitskiĭ, M. N. Pavlyuchenko, *et al.*, Perspekt. Mater., No. 5, 26 (2002).
6. L. E. Brus, J. Chem. Phys. **80**, 4403 (1984).

Translated by A. Spitsyn

Semiconductors, Vol. 38, No. 5, 2004, pp. 576–580. Translated from Fizika i Tekhnika Poluprovodnikov, Vol. 38, No. 5, 2004, pp. 598–602.

LOW-DIMENSIONAL SYSTEMS

Vertical Transport of Hot Electrons in GaAs/AlAs Superlattices

D. N. Mirlin, V. F. Sapega*, and V. M. Ustinov

Ioffe Physicotechnical Institute, Russian Academy of Sciences, ul. Politekhnicheskaya 26, St. Petersburg, 194021 Russia

**e-mail: sapega@dnm.ioffe.rssi.ru*

Submitted November 11, 2003; accepted for publication November 12, 2003

Abstract—Ballistic transport of hot photoexcited electrons injected from a superlattice into an enlarged quantum well is studied using the polarized hot photoluminescence technique. It is established that most photoexcited electrons thermalize before they are captured by the enlarged QW; however, a minor fraction of them reach the enlarged quantum well ballistically, keeping their momentum-distribution anisotropy or spin orientation arising due to the absorption of linearly or circularly polarized light in the superlattice. © *2004 MAIK "Nauka/Interperiodica".*

1. INTRODUCTION

When the width of a barrier separating two neighboring quantum wells (QWs) in a superlattice (SL) is decreased, the overlap between the electron states in the neighboring QWs increases. Such a coupling between the neighboring QWs results in a significant modification of the energy spectrum of the SL, which consists in the formation of minibands separated by forbidden bands in the charge-carrier spectrum. In turn, the formation of minibands in the charge-carrier spectrum has a considerable effect on the transport properties of the SL. In particular, the motion of charge carriers along the SL growth direction (so-called vertical transport) becomes possible. Interest in the vertical transport in SLs has arisen since the existence of negative differential resistance [1] and Bloch oscillations [2] in these structures was predicted. In addition, this is a kind of system where localization effects originating from the fluctuations of the structural parameters of SLs can be investigated.

Vertical transport and localization effects were studied by optical techniques, which offer higher spectral and temporal resolution in comparison to conventional methods based on electrical measurements. To make use of optical techniques for transport studies, an enlarged QW is introduced in the structure; this QW serves as a detector of electrons injected from the SL. This method was used mainly for studies of the behavior of thermalized charge carriers or excitons, whose transport is affected significantly by the localization effects in SLs. At the same time, there are specific difficulties in investigating the transport of hot charge carriers in SLs as compared to bulk semiconductors, because the application of external electric or magnetic fields leads to a considerable modification of the electron spectrum of SLs. The results reported in this paper, as well as in our previous publications, were obtained by the method of enlarged QW. However, in contrast to our previous studies, we analyzed here the spectrum of charge carriers injected from the SL. For this purpose, we examined the spectrum of hot electrons excited high in the conduction band by photons with an energy that considerably exceeds the SL band gap. We had previously shown [5–7] that hot photoexcited electrons in an SL are characterized by a strongly anisotropic quasi-momentum distribution function, in which the degree of anisotropy is strongly dependent on the excitation photon energy. One would expect this anisotropy to show up in the dependence of the number of electrons injected into the QW on the excitation photon energy.

In this study, we examined the intensity and polarization of the photoluminescence (PL) of electrons injected into an enlarged QW from an SL. It is found that the momentum distribution of injected electrons differs significantly from the distribution initially formed in the SL after photoexcitation. It is shown that electrons mostly become thermalized before they reach the enlarged QW. However, a minor fraction of the electrons are injected into the QW through a ballistic vertical-transport process. These electrons partially retain the momentum-alignment anisotropy or spin orientation that is initially formed in the SL upon absorption of linearly or circularly polarized light. The electrons that become bound with holes into excitons are apparently localized mainly within the SL at structural imperfections.

2. EXPERIMENTAL

Experiments were performed on a heterostructure containing an undoped GaAs/AlAs SL and an enlarged QW. The undoped SL was grown on a (100)-oriented substrate. The SL had 60 periods; the widths of the wells and the barriers were fixed and equal to $L_w = 40$ Å and $L_b = 6$ Å, respectively. The Be-doped ($\sim 10^{18}$ cm^{-3}) enlarged (100 Å) GaAs QW was grown on top of the SL

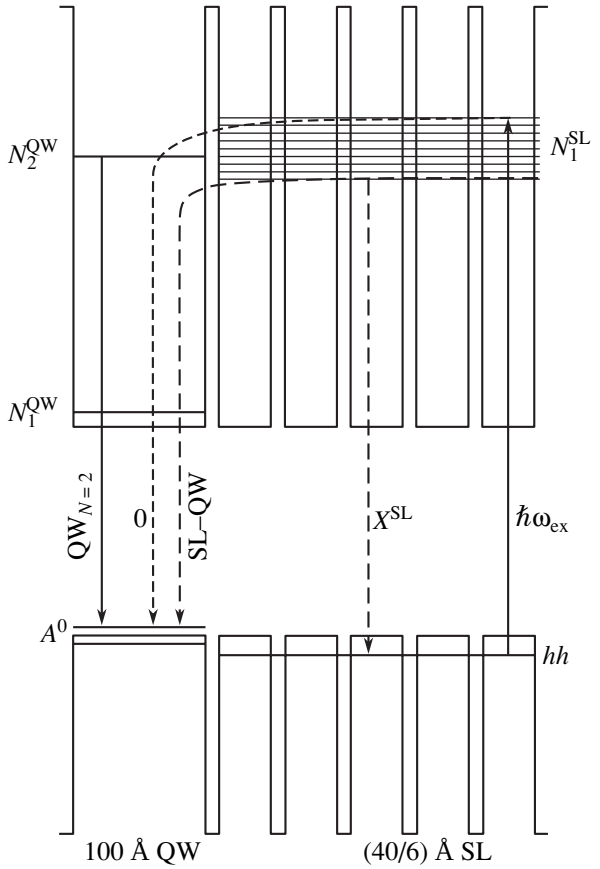

Fig. 1. Schematic layout of the structure SL + QW [(40/6) + 100] Å and the optical transitions observed in the PL spectra (see Fig. 2). The labeling used here corresponds to that in Fig. 2. N_1^{QW} and N_2^{QW} denote the quantum-confinement levels in the enlarged QW, and N_1^{SL} denotes the first miniband in the SL.

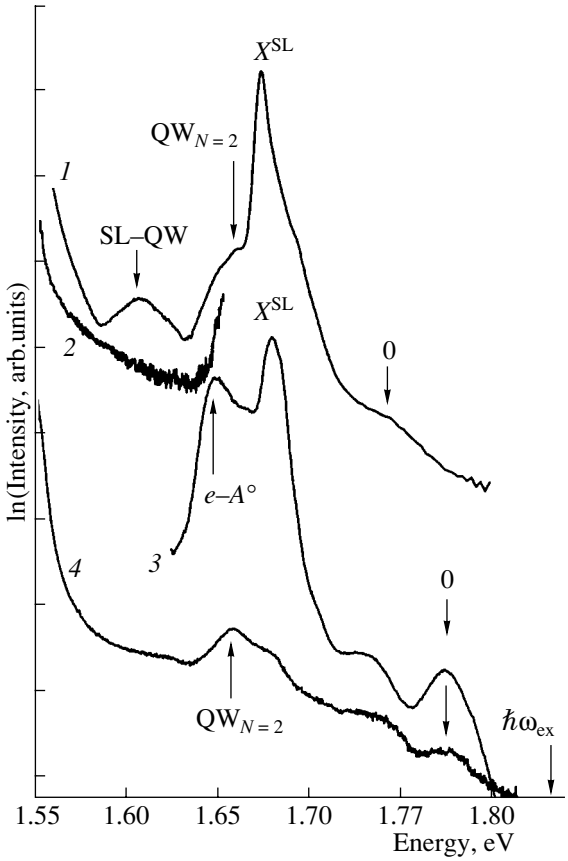

Fig. 2. PL spectra of the structure SL + QW [(40/6) + 100] Å for the excitation photon energy $\hbar\omega_{ex}$ = (*1*) 1.833 and (*2*) 1.664 eV. The spectra of the test (*3*) SL and (*4*) QW structures were measured with $\hbar\omega_{ex}$ = 1.833 eV at temperature T = 4 K. The labeling of the spectral features is explained in the text and in Fig. 1.

(see Fig. 1). In addition, two test structures were grown: one of them was a Be-doped 40/6 Å SL, and the other was a structure with a Be-doped 100/100 Å QW. The test SL and QW structures were used to interpret the spectra of the SL + QW structure.

The hot PL (HPL) of the samples was excited by a tunable Ti:sapphire laser pumped by an Ar^+-ion laser. The PL spectra were recorded using a DFS-24 double grating monochromator equipped with a photomultiplier and a photon-counting system. Experiments on the HPL depolarization were carried out in magnetic fields of up to 7 T in the Voigt configuration (in which the magnetic field is perpendicular to the photon wave vector and lies in the plane of the SL layers) or in the Faraday configuration (the magnetic field is collinear with the SL growth direction and with the photon wave vector). The degree of linear polarization of the HPL was measured on the high-frequency wing of the spectrum; its magnitude was determined from the conventional expression

$$\rho_l = \frac{I_\parallel - I_\perp}{I_\parallel + I_\perp},$$

where $I_\parallel$ and $I_\perp$ stand for the intensities of the luminescence polarized parallel ($\mathbf{e}_{lum} \parallel \mathbf{e}_{ex}$) or perpendicular ($\mathbf{e}_{lum} \perp \mathbf{e}_{ex}$) to the polarization of the excitation photons.

3. RESULTS AND DISCUSSION

Figure 2 shows the PL spectra of the SL + QW structure for two values of excitation photon energy: $\hbar\omega_{ex}$ = (*1*) 1.833 eV and (*2*) 1.664 eV. The most intense band, labeled X^{SL} in spectrum *1*, is due to the recombination of excitons in the SL (the corresponding optical transitions are shown in Fig. 1). The weak shoulder ($QW_{N=2}$) is apparently related to the recombination of electrons from the second quantum-confinement level in the enlarged QW through the acceptor level. The weak line (denoted as SL–QW) is present in the spectrum only when the excitation photon energy exceeds the band

Linear and circular polarization of the HPL measured in the 40/6 Å SL, the 100 Å QW, and the structure SL + QW [(40/6) + 100] Å

Polarization	SL (40/6) Å	QW 100 Å	SL + QW [(40/6) + 100] Å
ρ_t	0.08	0.27	0.16
ρ_c	0.69	0.18	0.3

gap of the SL; this is demonstrated by the shape of spectrum *2*, corresponding to the excitation photon energy $\hbar\omega_{ex}$ = 1.664 eV (which is lower in energy than the SL exciton band X^{SL}). Finally, on the high-energy wing of the spectrum, there is also a step denoted as 0. Its position depends on the excitation photon energy: it shifts to higher energies as $\hbar\omega_{ex}$ increases. However, when the excitation photon energy is lower than the SL band gap, this step is absent (compare spectra *1* and *2*). In contrast to the other features in the PL spectrum, step 0 is linearly polarized under excitation with linearly polarized light. If the excitation is circularly polarized, step 0 and the SL–QW band are circularly polarized as well, but the degree of polarization of step 0 exceeds that of the SL–QW band by a factor of 2. The degrees of linear and circular polarizations ρ_l and ρ_c, measured on the high-energy wing of the HPL spectrum (point 0), are listed in the table.

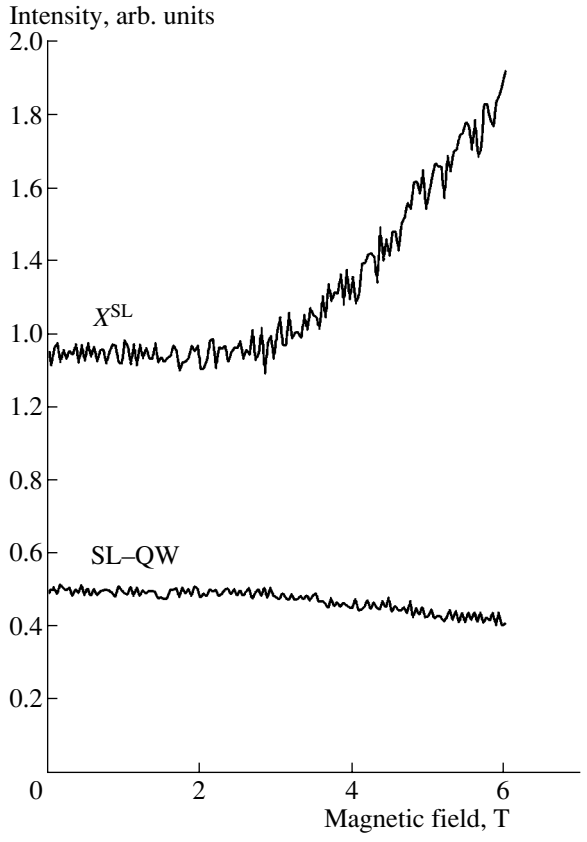

Fig. 3. Dependences of the intensities of the X^{SL} and SL–QW bands on the magnetic field applied perpendicularly to the SL growth direction (the Voigt geometry). The measurement temperature T = 4 K.

For comparison, we also show in Fig. 2 the PL spectra of the test SL and QW structures (curves *3* and *4*, respectively) obtained for the excitation photon energy $\hbar\omega_{ex}$ = 1.833 eV. The band e–A^0, appearing in the spectrum of the test SL (curve *3*) in addition to the exciton band X^{SL}, originates from the recombination of thermalized electrons with holes bound to acceptors (note that the test SL is doped with acceptors, in contrast to the SL in the SL + QW structure). Arrows marked with 0 in curves *3* and *4* indicate the points where the linear and circular polarizations of the PL of the test structures were measured; the corresponding degrees of polarization are listed in the table.

Figure 3 shows the dependences of the intensities of the X^{SL} and SL–QW bands on the strength of the external magnetic field applied in the Voigt geometry (i.e., with the field oriented in the plane of the QW layers). The intensity of the X^{SL} band grows noticeably (by a factor of ~1.5) as the field is increased from 3 to 6 T. In contrast, the intensity of the SL–QW band decreases slightly (by ~10%) as the field varies in the same range. The intensities of the e–A^0 and $QW_{N=2}$ PL bands are almost independent of the magnetic field.

Let us discuss the origin of the SL–QW band and the step 0. The linearly polarized step 0 and the nonpolarized SL–QW band are present in the PL spectrum only when the excitation photon energy exceeds the SL band gap. Thus, we believe that these spectral features are due to the recombination, through the acceptor states localized in the enlarged QW, of electrons injected from the SL. We suggest that the step 0 originates from the recombination of electrons that are excited in the SL and reach the enlarged QW ballistically (i.e., without energy and momentum relaxation). An indication of the ballistic nature of the transport process is the significant linear and circular polarization of the HPL of electrons injected from the SL.

Indeed, the absorption of linearly or circularly polarized light in an SL results in the momentum alignment or spin orientation of the photoexcited electrons [5–7], which are partially retained in the process of ballistic motion from the SL to the enlarged QW. Thus, linearly or circularly polarized photons are emitted in the process of recombination of these momentum-aligned or spin-oriented electrons with equilibrium holes bound to acceptors. Since only the enlarged QW is doped with acceptors, linearly or circularly polarized emission can only originate from the recombination of electrons that were excited in the SL and reached the enlarged QW ballistically. Polarized HPL could be related to electron–hole recombination directly in the SL; however, we rule out this possibility, because the SL is not doped with acceptors. At the same time, electrons excited in the QW itself upon absorption of linearly or circularly

polarized light also recombine with acceptor-bound holes, emitting polarized photons. However, the number of such electrons is apparently small because of the small size of the QW in comparison to the whole SL. This is corroborated by the shape of the HPL spectrum obtained upon excitation by photons with energies lower than the SL band gap, i.e., when the electrons are generated only in the QW. In this case, step 0 is not observed in the luminescence spectrum of the QW (compare curves *1* and *2* in Fig. 2).

Let us compare polarization HPL characteristics measured in the zero-phonon peaks 0 of the SL and QW structures with those of the step 0. The degree of linear polarization of the step 0 was measured as 16% (see table). This value considerably exceeds the degree of polarization for the zero-phonon peak of the test SL with the same parameters as the SL in the SL + QW structure. In the test SL under similar excitation conditions (the kinetic energy of photoexcited electrons is comparable to the SL miniband width), the degree of HPL polarization does not exceed $\rho_l \approx 0.08$. On the other hand, the linear polarization of the 0 band is considerably smaller than the polarization of the zero-phonon peak recorded at the same energy in the spectrum of the test QW, which is similar to the QW in the SL + QW structure. This means that electrons injected from the SL into the QW partially retain the momentum alignment formed in the SL upon absorption of linearly polarized light. Furthermore, this means that electrons reach the enlarged QW through the ballistic-transport mechanism. Let us discuss the factors that cause a reduction in the linear polarization of the HPL of electrons injected into the QW from the SL, as compared to the HPL polarization in the test SL structure.

In semiconductor SLs, the absorption of linearly or circularly polarized light leads to the momentum alignment or spin orientation of photoexcited charge carriers, with the degree of electron momentum alignment or spin orientation dependent on the relationship between the kinetic energy of the motion of electrons in the plane of the SL layers and the energy of their motion along the SL growth direction (the *z* axis) [6]. Accordingly, the degree of linear or circular polarization of the HPL in the SL depends on the energy of recombining electrons. This is related to the fact that, for a given total kinetic energy of photoexcited electrons, various energies of miniband motion and in-plane (lateral) motion are possible. Electrons excited in states with the *z* component of the wave vector $Q_z \approx 0$ have the largest lateral quasi-momentum and, thus, they recombine, emitting photons with the highest linear or lowest circular polarization [6]. In contrast, electrons whose kinetic energy is equal to that of the miniband motion have the smallest lateral quasi-momenta ($k \approx 0$), and therefore they recombine, emitting photons with the highest circular and nearly zero linear polarization. It is evident that, among all the electrons photoexcited in the SL, there are two groups with the lowest probability of reaching the enlarged QW: electrons with the wave vector $Q \approx \pi/(L\omega + L_b)$ (which suffer Bragg reflections at the SL Brillouin minizone boundaries) and electrons with the wave vector $Q \approx 0$. The probability that these electrons will be injected into the QW and contribute to the corresponding HPL emission is the lowest. Thus, the linear and circular HPL polarizations are determined by the electrons ballistically injected into the QW with nonzero lateral and nonextremum miniband quasi-momentum ($0 < Q < \pi/(L_w + L_b)$). The recombination radiation of these electrons in the enlarged QW turns out to be partially polarized (linearly or circularly). It should be noted that the degree of momentum alignment or spin orientation of electrons may change during their capture in the QW. However, the existence of appreciable linear and circular polarization of the HPL indicates that the momentum alignment and spin orientation do not relax completely upon capture.

We believe that the nonpolarized SL–QW band is due to the recombination of electrons (injected from the SL) via the acceptor states in the QW. However, the energy position of this band and the fact that it is not linearly polarized indicate that recombining electrons are injected into the QW from the bottom of the SL miniband. Evidently, the quasi-momentum distribution function of electrons reaching the bottom of the SL miniband is isotropic, and their recombination radiation is not linearly polarized. Such an interpretation of the nature of this band implies that its energy position is determined by the energy of the miniband bottom and, thus, should be independent of the excitation photon energy (unlike the position of the step 0). Obviously, the intensity ratio of the step 0 and the SL–QW band corresponds to the ratio of probabilities of an electron reaching the enlarged QW in the processes of ballistic and nonballistic vertical transport. The experimentally measured ratio is equal to $I_{(0)}/I_{(SL-QW)} \approx 0.07$, which means that the majority of electrons become thermalized before they are captured by the enlarged QW.

In a magnetic field applied in the Voigt configuration, the intensity of the SL–QW band slightly decreases (see Fig. 3), as one would expect. This is caused by the localization of the thermalized electrons in the SL under the influence of the magnetic field. On the other hand, this localization favors the binding of thermalized electrons with holes and, thus, the formation of excitons in the SL. This effect manifests itself in a noticeable (by a factor of 1.5) increase in the SL exciton luminescence intensity (the X^{SL} band), in agreement with the conclusions of [8].

4. CONCLUSION

We investigated the vertical transport of hot momentum-aligned or spin-oriented electrons from a GaAs/AlAs SL to an enlarged QW. It is shown that, during the ballistic transport, hot electrons partially retain the anisotropy of the quasi-momentum distribution function or spin orientation that builds up under

excitation with linearly or circularly polarized light, respectively. Only 7% of photoexcited electrons reach the enlarged QW ballistically. Most of the photoexcited electrons are thermalized in the SL before they are captured by the QW. Application of a magnetic field perpendicular to the SL growth direction leads to the localization of electrons in the SL and, thus, to a reduction in the electron flow from the SL to the QW.

ACKNOWLEDGMENTS

We are deeply grateful to Prof. V.I. Perel' for useful discussions.

This study was supported by the Russian Foundation for Basic Research, project no. 02-02-17673; the Ministry of Industry, Science, and Technology of the Russian Federation; and the Spintronics program of the Russian Academy of Sciences.

REFERENCES

1. L. Esaki and R. Tsu, IBM J. Res. Dev. **14**, 61 (1970).
2. C. Zener, Proc. R. Soc. London, Ser. A **145**, 523 (1934).
3. Yu. A. Pusep, A. J. Chiquito, S. Mergulha, and J. C. Galzerani, Phys. Rev. B **56**, 3892 (1997).
4. T. Amand, J. Barrau, X. Marie, *et al.*, Phys. Rev. B **47**, 7155 (1993).
5. V. F. Sapega, V. I. Perel', A. Yu. Dobin, *et al.*, Pis'ma Zh. Éksp. Teor. Fiz. **63**, 305 (1996) [JETP Lett. **63**, 305 (1996)].
6. V. F. Sapega, V. I. Perel', A. Yu. Dobin, *et al.*, Phys. Rev. B **56**, 6871 (1997).
7. V. F. Sapega, V. I. Perel', A. Yu. Dobin, *et al.*, Phys. Status Solidi B **204**, 141 (1997).
8. V. F. Aguekian, B. S. Monozon, C. A. Bates, *et al.*, Phys. Rev. B **56**, 1479 (1997).

Translated by M. Skorikov

Semiconductors, Vol. 38, No. 5, 2004, pp. 581–587. Translated from Fizika i Tekhnika Poluprovodnikov, Vol. 38, No. 5, 2004, pp. 603–609.

AMORPHOUS, VITREOUS, AND POROUS SEMICONDUCTORS

Interaction of Infrared Radiation with Free Carriers in Mesoporous Silicon

L. A. Osminkina, E. V. Kurepina, A. V. Pavlikov, V. Yu. Timoshenko, and P. K. Kashkarov

Faculty of Physics, Moscow State University, Vorob'evy gory, Moscow, 119899 Russia

e-mail: osminkina@vega.phys.msu.ru

Submitted July 8, 2003; accepted for publication July 9, 2003

Abstract—Features of absorption and reflection of infrared radiation in the range 500–6000 cm^{-1} are investigated; these features are associated with free carriers in the layers of mesoporous Si (porosity, 60–70%) formed in single-crystal p-Si(100) wafers with a hole concentration of $N_p \approx 10^{20}$ cm^{-3}. It is found that the contribution of free holes to the optical parameters of the samples decreases as the porosity of the material increases and further falls when the samples are naturally oxidized in air. The experimental results are explained in the context of a model based on the Bruggeman effective medium approximation and the Drude classical theory with a correction for additional carrier scattering in silicon residues (nanocrystals). A comparison between the calculated and experimental dependences yields a hole concentration in nanocrystals of $N_p \approx 10^{19}$ cm^{-3} for as-prepared layers and shows a reduction of N_p when they are naturally oxidized. © *2004 MAIK "Nauka/Interperiodica".*

1. INTRODUCTION

At present, porous Si (*por*-Si) formed by electrochemical etching of crystalline Si is an object of great interest (see, for example, reviews [1, 2]). For fairly high porosity (≥50%), this material consists of a system of associated Si nanocrystals with an open surface [2]. This circumstance determines the diversity of the physical properties of *por*-Si and, as a consequence, new areas of possible optical [3, 4], energy [5], and medical and biological [6] applications.

In most previous studies, as a rule, the properties of *por*-Si that were not associated with the presence of nonequilibrium carriers in it were used. Moreover, until recently, it was considered that virtually complete depletion of equilibrium carriers occurs in this material for various reasons (see, for example, [7, 8]). Such a depletion is easy to explain for so-called microporous Si that is obtained on lightly doped substrates and has a pore size and Si nanocrystal size on the order of a few nanometers [1]. In this case, the electronic spectrum of carriers undergoes considerable variations due to the quantum-dimensional effect [1]. However, in mesoporous Si (*mesopor*-Si) obtained from heavily doped *p*-Si wafers, the minimal crystallite size can exceed 10 nm [2], and consequently the quantum-dimensional effect is negligible [1]. Moreover, the concentration of the doping impurity in *mesopor*-Si layers can attain a level comparable with the level of substrate doping [8]. It has been recently found that the concentration of equilibrium free carriers (holes) in *mesopor*-Si can be rather high (10^{16}–10^{18} cm^{-3}) and sensitive to the dielectric surrounding and surface state of Si residues (nanocrystals) [9, 10]. The above hole concentrations were estimated from the IR absorption spectra of *mesopor*-Si layers, which were analyzed in terms of the Drude classical theory for the same scattering constants as for the initial single-crystal substrate. However, one would expect the size of Si nanocrystals and their large specific surface to have an effect on the concentration and characteristic scattering times of free carriers in *mesopor*-Si. Both parameters noted can be obtained by the simultaneous analysis of the absorption and reflection spectra of free charge carriers [11].

In this study, the transmission and reflection spectra of *mesopor*-Si layers with various values of porosity are investigated experimentally and analyzed theoretically. This approach makes it possible to determine the concentrations and scattering times of equilibrium holes in Si nanocrystals that form *mesopor*-Si.

2. EXPERIMENTAL

The *mesopor*-Si layers were formed on single-crystal *p*-Si(100) wafers (resistivity $\rho \approx 1.5$ mΩ cm) using the standard method of electrochemical etching (anodization) [1] in an HF (48%) : C_2H_5OH solution in a ratio of 1 : 1 at various current densities *j* (see table). The etching time was chosen as 20, 30, and 60 min for the layers formed at $j = 75$, 50, and 25 mA/cm^2, respectively. The thicknesses of porous layers subsequently measured using an optical microscope over the cleaved surfaces of the samples were $d = (40 \pm 1)$ μm. After the process of anodization had finished, the *mesopor*-Si layers were separated from the substrate by increasing the current density to 500 mA/cm^2 for a short time. Free-standing films of *meso*-PS were rinsed in deionized water for 1–2 s and dried in air for several hours. The porosity of the samples determined by gravimetry was in the range

Table

Current density j, mA/cm^2	Porosity p, %	Refractive index n	Concentration of free carriers N_p, cm^{-3}	
			as-prepared samples	samples aged in air
25	62	1.76	1.1×10^{19}	1.4×10^{18}
50	68	1.60	1.3×10^{19}	1.02×10^{18}
75	71	1.52	1.5×10^{19}	1.23×10^{18}

60–70% (see table). Both the as-prepared layers and the same samples kept in air (naturally oxidized) for 1 month were used.

The IR transmission and reflection spectra were measured using a Perkin-Elmer RX I Fourier spectrometer in the frequency range ν = 500–6000 cm^{-1} with a resolution of 2 cm^{-1}. The spectra were recorded with a normal incidence of IR radiation on the sample. The experiments were carried out at room temperature in air.

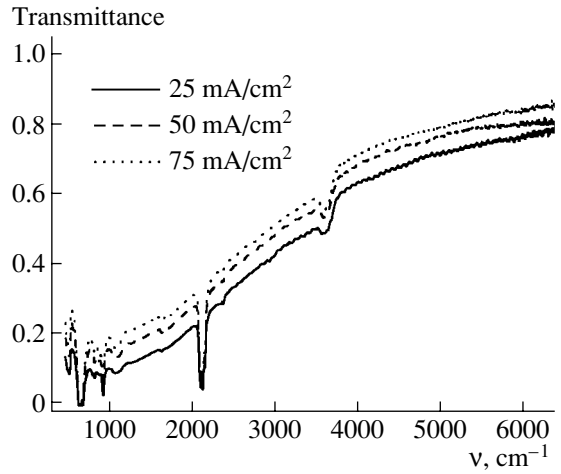

Fig. 1. Transmission spectra of as-prepared *mesopor*-Si layers for various current densities of anodization.

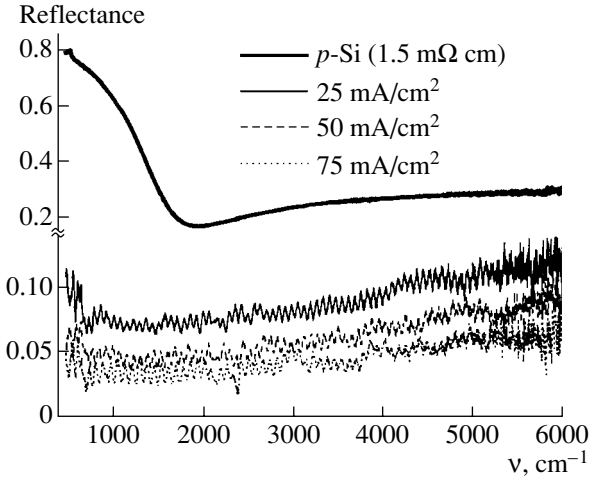

Fig. 2. Reflection spectra of as-prepared *mesopor*-Si layers formed at various current densities of anodization and of single-crystal Si wafers used for the fabrication of *mesopor*-Si.

3. RESULTS

Figure 1 shows the IR transmission spectra for the layers of as-prepared *mesopor*-Si. The spectra include the absorption bands that correspond to various local surface vibrations. Among them, the following are most noticeable: the stretching modes Si–H_x (x = 1, 2, 3) at frequencies 2070–2170 cm^{-1}, the scissors mode Si–H_2 at a frequency of 910 cm^{-1}, and the bending vibrations Si–H_x with a band peaked at 660 cm^{-1}. In addition, a weaker band of stretching vibrations Si–O–Si (1050–1100 cm^{-1}) and a band in the range 3000–3800 cm^{-1} associated with the absorption at vibrations of O–H bonds in water molecules adsorbed at the surface of pores of *mesopor*-Si were noticeable. These two bands are apparently caused by rinsing the samples in water with subsequent exposure to air. Note that during subsequent exposure of *mesopor*-Si to air, the intensities of the two aforementioned bands increase steadily.

In addition to the bands of local surface vibrations, absorption associated with the presence of free carriers (the monotonic spectral component in Fig. 1) is observed in the spectrum of as-prepared *mesopor*-Si. The transmittance of porous layers decreases as the current density j decreases; i.e., the porosity p decreases (see table). This can be caused, for example, by an increase in the amount of the substance in the porous layer and/or by a change in the contribution of free carriers. To clarify the causes of the dependence observed, the reflection spectra of *mesopor*-Si should be analyzed.

Figure 2 shows the reflection spectra of the layers under study as well as (for comparison) those of the wafers of single-crystal Si used to prepare *mesopor*-Si. For silicon wafers, a nonmonotonic dependence of the reflectance with a clearly pronounced plasma minimum is observed. Such a dependence is characteristic of heavily doped semiconductors and is caused by the contribution of free carriers [12]. Reflectance R of the *mesopor*-Si layers is several times less and has a less pronounced minimum than the substrate. The absolute values of R decrease as the layer porosity increases.

The spectral dependence $R(\nu)$ for the *mesopor*-Si layers includes oscillations caused by the interference of beams reflected from the surface of the *mesopor*-Si film (see Fig. 2). An analysis of the interference period yields the refractive indices n of the samples under investigation (see table). The refractive indices can be determined correctly from the interference period only in the region of weak dispersion, i.e., weak absorption in our case. Therefore, we will find n only for frequencies $\nu > 3000$ cm^{-1}. It can be seen (see table) that values of n decrease as j decreases, which agree well with the

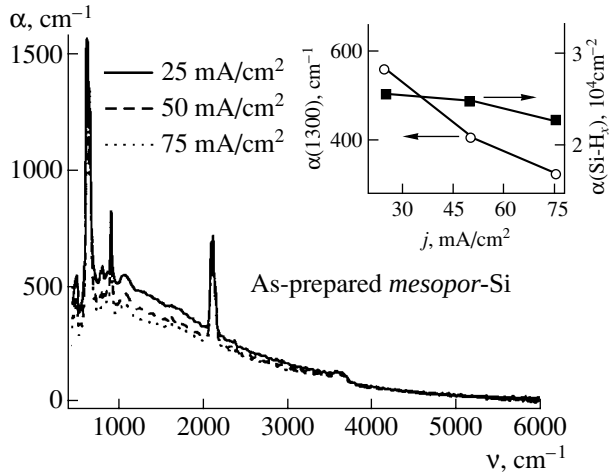

Fig. 3. Spectra of the absorption coefficient for as-prepared *mesopor*-Si layers formed at various current densities of anodizing. The dependence of the absorption factor at free carriers at a frequency of 1300 cm^{-1}, α(1300), and integrated absorption at the surface vibrations $Si–H_x$ ($x = 1, 2, 3$), α($Si–H_x$), versus current density j of formation of the samples are shown in the inset.

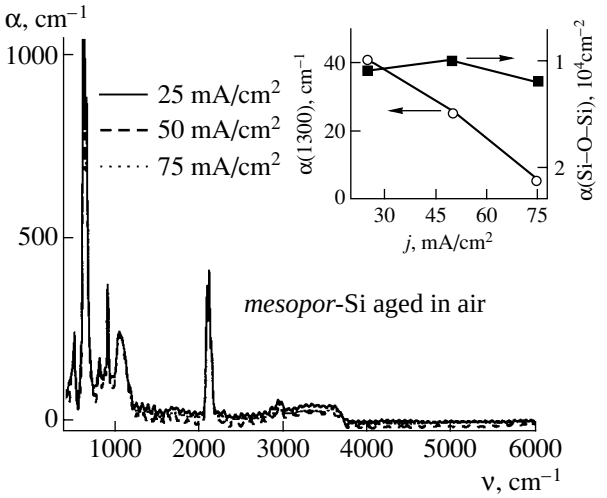

Fig. 4. Spectra of the absorption coefficient for *mesopor*-Si layers formed at various current densities of anodization and then oxidized in air for 1 month. The dependence of the coefficient of absorption at free carriers at a frequency of 1300 cm^{-1}, α(1300), and integrated absorption at the Si–O–Si surface vibrations, α(Si–O–Si), versus current density j of formation of the samples are shown in the inset.

decrease in the amount of the substance in the layers with higher porosity.

Comparing the position of the plasma minimum in the $R(\nu)$ spectra for the Si substrate and the *mesopor*-Si layers, which are shown in Fig. 2, we may conclude that the concentration of free carriers in porous layers is lower than in the substrate. However, to obtain quantitative information on the concentration and scattering times of free carriers in the layers with different porosity, a more detailed analysis is required, which will be carried out below. As the first stage of such an analysis, let us consider the spectral dependences of the absorption coefficient obtained from the experimental data on the transmission and reflection.

Figure 3 shows the spectra of the absorption coefficient of as-prepared *mesopor*-Si layers calculated by the formula $\alpha = -[\ln(T/(1-R)^2]/d$, where T is the transmittance (the $T(\nu)$ dependences are shown in Fig. 1) and d is the layer thickness. One can see that, along with the lines of absorption at local bonds listed above, absorption at free carriers, which depends nonlinearly on the frequency of the IR radiation, is observed. The contribution of free carriers to α decreases with increasing j, as shown in Fig. 3 (inset). This circumstance can be caused both by an increase in the amount of the substance and by a decrease in the concentration of free holes as the surface area of Si residues (nanocrystals) varies with decreasing nanocrystal sizes as the layer porosity increases.

Since the area of the internal surface of *mesopor*-Si is apparently directly proportional to the number of surface atoms, we can consider the absorption at local vibrations caused by the presence of foreign atoms at the surface as its quantitative measure. The inset to Fig. 3 shows the total absorption at the $Si–H_x$ ($x = 1, 2, 3$) valence bonds integrated over the spectrum in the range 2070–2170 cm^{-1} minus the contribution of free carriers as a function of the anodizing current density. The decrease in this parameter with increasing j indicates that the area of the internal surface of *mesopor*-Si decreases, which is quite understandable if one takes into account the rather high porosity of the layers under study.

Spectral dependences α(ν) for the *mesopor*-Si samples aged for a long time in air were calculated and analyzed in a similar way. These dependences are shown in Fig. 4. First of all, it can be seen that the contribution of free carriers is much smaller than that in as-prepared layers (see Fig. 3). Simultaneously, the amplitude of absorption at the Si–O–Si stretching modes and O–H bonds in water molecules adsorbed at the surface of pores noticeably increases in the absorption spectrum of the layers aged in air. This is indicative of the natural oxidation of the surface of Si nanocrystals in *mesopor*-Si. It seems likely that the decrease in the concentration of free holes in the samples is associated with these processes.

Note that the absorption caused by free carriers in naturally oxidized layers depends on j much more than in as-prepared layers (Figs. 3, 4, insets). The simultaneous absorption at the Si–O–Si surface bonds integrated in the range 1050–1100 cm^{-1} depends very slightly on j and, consequently, on the layer porosity. A decrease in the number of free holes can be attributed to their trapping at the surface states generated under the natural oxidation of the surface of Si nanocrystals in *meso*-PS. These states can be initiated by breaking the

Si–Si surface bonds, i.e., by the formation of the so-called dangling Si bonds in the inverse (to O–Si) bond or the P_b centers [11, 13]. In addition, holes can be trapped at the donor states associated with water adsorbed at the surface of pores [13].

4. MODEL AND COMPARISON WITH EXPERIMENT

To describe quantitatively the IR absorption and reflection spectra of the *mesopor*-Si layers, it is necessary to take into account that such layers are a heterosystem that consists of Si residues (nanocrystals) and separating voids (pores). It should be taken into account that the transverse (i.e., in the layer plane) sizes of nanocrystals and voids in the layers are in the range 10–50 nm [3, 11]. This is much smaller than the wavelength of the IR radiation used. Therefore, *mesopor*-Si may be considered an effective isotropic (in the layer plane) medium with a certain complex permittivity ε_{eff}. To describe the magnitude ε_{eff}, various models are used, of which the so-called Bruggeman model, or the effective-medium approximation, seems to be most adequate [11]. In this approach, the phases constituting the system are equitable and form an effective medium with permittivity ε_{eff}, which is described by the Bruggeman formula [14]

$$\left(\frac{\varepsilon_1 - \varepsilon_{\text{eff}}}{\varepsilon_1 + 2\varepsilon_{\text{eff}}}\right) f_1 + \left(\frac{\varepsilon_2 - \varepsilon_{\text{eff}}}{\varepsilon_2 + 2\varepsilon_{\text{eff}}}\right) f_2 = 0, \qquad (1)$$

where ε_1, ε_2 and f_1, f_2 are the permittivities and the filling factors for corresponding phases.

Using formula (1) for the description of the results obtained, it should be taken into account that the voids are filled with air. Consequently, $\varepsilon_1 = 1$ and $f_1 = p$. For Si nanocrystals, the filling factor $f_2 = 1 - p$ and permittivity depends on the frequency due to the contribution of free carriers. This contribution in *p*-Si in the mid-IR range is described well by the classical Drude model, and permittivity can be expressed as

$$\varepsilon_2(\omega) = \varepsilon_\infty - \frac{\omega_p^2}{\omega^2 + i\omega g}, \qquad (2)$$

where ε_∞ is the high-frequency (optical) permittivity of the semiconductor ($\varepsilon_\infty = 11.7$ for *c*-Si), ω_p is the plasma frequency of vibrations, and g is the damping constant ($g = \tau^{-1}$, τ is the relaxation time of quasi-momentum of free carriers [11]). The plasma frequency in the International System of Units is given by the expression

$$\omega_p^2 = \frac{N_p e^2}{m_p^* \varepsilon_0}, \qquad (3)$$

where N_p is the concentration of free holes, m_p^* is the effective mass (for free holes in *c*-Si, $m_p^* = 0.37m_0$), $m_0 = 9.1 \times 10^{-31}$ kg, and $\varepsilon_0 = 8.85 \times 10^{-12}$ F/m.

It should be noted that the experimental absorption and transmission spectra are obtained using spectroscopy units ν ($\nu = \omega/2\pi c$). It is also convenient to express the damping constants in such units: $g^* = g/2\pi c$.

Note that formulas (2) and (3) describe well the dependence $R(\nu)$ for a single-crystal substrate, as shown in Fig. 2 for $\nu_p = \omega_p/2\pi c = 5500$ cm^{-1} and $g^* = 740$ cm^{-1}. Specifically, the position of the reflection minimum $\nu_{\min}$ in the $R(\nu)$ dependence is consistent with the known approximate relationship: $\nu_{\min} \approx \nu_p(\varepsilon_\infty - 1)^{-1/2}$ [12]. The found value of ν_p corresponds to the free hole concentration $N_p = 1.2 \times 10^{20}$ cm^{-3}, which agrees well with the doping level of the substrates used.

In the *mesopor*-Si layers, the holes are located within Si nanocrystals with transverse sizes $d = 10$–50 nm. Therefore, additional scattering of their quasi-momentum should be expected for the interaction with the surface of nanocrystals, for example, for the reflection from the surface. Such scattering should manifest itself especially noticeably at the times $t \gtrsim dV^{-1}$, where V is the thermal velocity of carrier motion, i.e., in the case where the amplitude of hole oscillations (L) in the electric field of the IR radiation is comparable with nanocrystal sizes or exceeds them: $L = VT \gtrsim d$, where $T = 2\pi/\omega$ is the period of the electromagnetic wave [9, 10]. An exact mathematical description of such a dependence would certainly require the development of a corresponding microscopic theory. However, as a first approximation an analogy with the description of the carrier lifetime in diffusion-thin semiconductor layers in relation to the layer thickness and surface recombination rate can be used [15]. This allows us to write the following expression for the scattering time of quasi-momentum of holes in nanocrystals:

$$\tau^{-1} = \tau_0^{-1} + \frac{sL}{d}. \qquad (4)$$

Here, τ_0 is the scattering time independent of the nanocrystal size ("bulk" scattering time), and s is the dimensionless constant that determines the efficiency of surface scattering. This constant depends on the nanocrystal shape and on the state of its surface coverage. Since $L = VT = V \cdot 2\pi\omega^{-1}$, the scattering time depends on the frequency of the IR radiation. The expression for the damping constant, which enters formula (2), can then be written as

$$g = g_0\left(1 + \frac{g_1}{\omega}\right), \qquad (5)$$

where $g_0 = \tau_0^{-1}$ and $g_1 = 2\pi sV(g_0 d)^{-1}$. Let us introduce the notation $g_0^* = g_0/2\pi c$ and $g_1^* = g_1/2\pi c$.

The absorption coefficient for *mesopor*-Si can be expressed in terms of the imaginary part κ of the com-

plex refractive index with the use of the known relationship [12]

$$\alpha = 4\pi\nu\kappa, \quad (6)$$

where $\kappa = \mathrm{Im}\tilde{n}$ and $\tilde{n} = \sqrt{\varepsilon_{\mathrm{eff}}}$.

To simulate the reflectance of the *mesopor*-Si layer, the possibility of Fabry–Perot interference in the layer should be taken into account, which can be clearly seen from the experimental data (see Fig. 2). To take into account the contribution of interference to the $R(\nu)$ spectrum, let us use the expression for intensity of reflected light in the presence of multilayer interference and absorption [16]

$$R = R_0\left[1 + \frac{(1-R_0)^2\exp(-2\alpha d)}{1-R_0^2\exp(-2\alpha d)}\right], \quad (7)$$

where α is given by expression (6), and R_0 is the reflectance for the normal incidence of light with no allowance made for interference, which is given by the well-known formula

$$R_0 = \frac{(n-1)^2+\kappa^2}{(n+1)^2+\kappa^2}. \quad (8)$$

Figure 5 shows certain $\alpha(\nu)$ and $R(\nu)$ dependences calculated by formulas (6) and (7) with allowance made for relationships (1)–(5) and (8) for $p = 0.65$ and $\nu_p = 1200$ cm^{-1}. One can see from Fig. 5a that, for $\nu > g^*$, the dependence $\alpha(\nu) \propto \nu^{-2}$ is observed. This dependence is consistent with the well-known high-frequency asymptotic behavior for absorption at free carriers in homogeneous bulk semiconductors [13, 15]. In the frequency region $\nu > g^*$, the run of calculated absorption and reflection curves substantially depends on the features of damping. In the limiting case of the absence of hole scattering at the surface of Si nanocrystals ($s = g_1^* = 0$), the damping is frequency-independent, and α depends on ν only slightly. The existence of a frequency-dependent component of damping causes a sharper fall in the $\alpha(\nu)$ dependence with frequency and simultaneously a smoother run of $R(\nu)$ in the vicinity of the plasma minimum (see Fig. 5b). Such characteristics of the absorption and reflection spectra agree well with the experimental curves (see Figs. 2, 3), which confirms the validity of the chosen model of decay. It is also noteworthy that it is necessary to take into account simultaneously the multilayer interference and the absorption in the *mesopor*-Si layer in order to describe the reflectance of this layer correctly (see Figs. 2, 5b).

Figure 6 shows the spectra of absorption and reflection for one of the as-prepared samples. These spectra were measured and calculated by the approximation of experimental curves. For the approximation, the parameters ν_p, g^*, and g_1^* were varied. It was established above (see Fig. 5) that g_1^* affects $\alpha(\nu)$ and $R(\nu)$ only in the low-frequency region. Therefore, the choice of values of ν_p and g^* for the description of the experimental results is rather strict. The good agreement obtained between the calculated and experimental dependences makes it possible to determine the parameters of the model.

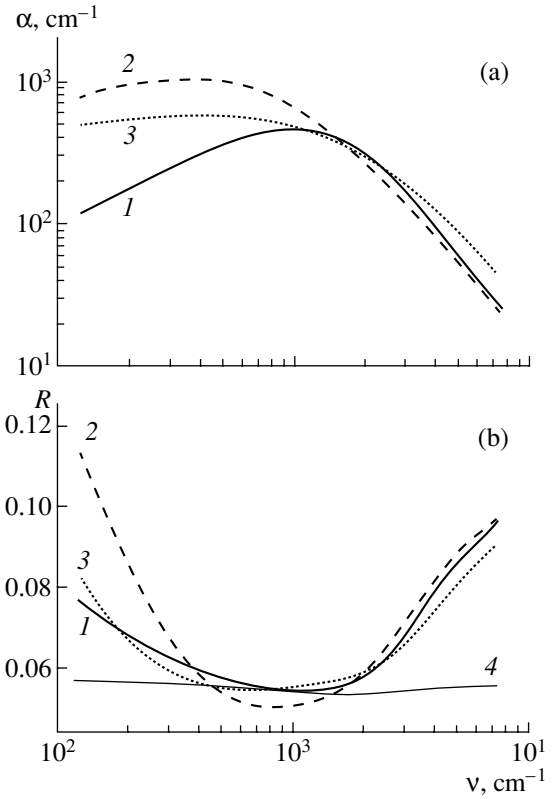

Fig. 5. Calculated spectra of (a) absorption factors and (b) reflectances related to free carriers for $p = 0.65$ and $\nu_p = 1200$ cm^{-1}. The damping constants: (*1*) $g_0^* = 1100$ cm^{-1}, $g_1^* = 1000$ cm^{-1}; (*2*) $g_0^* = 1100$ cm^{-1}, $g_1^* = 0$; (*3*) $g_0^* = 2100$ cm^{-1}, $g_1^* = 0$; and (*4*) $g_0^* = 1100$ cm^{-1}, $g_1^* = 1000$ cm^{-1}. The calculations were performed disregarding the multilayer interference.

The experimental spectra were approximated by the calculated spectra; as a result, we obtained $g^* = 1100$, 1100, and 1150 cm^{-1} and $\nu_p = 1780$, 1640, and 1900 cm^{-1} for the layers of as-prepared *mesopor*-Si with $j = 25$, 50, and 75 mA/cm^2, respectively. For all the samples, the approximately constant value of g_1^* was ~10^3 cm^{-1}. A similar analysis was also carried out for the layers aged in air and prepared with the same values of j. The found values of ν_p yield, according to formula (3), the concentrations of free holes listed in the table. One can see that, for as-prepared *mesopor*-Si, $N_p = (1.1\text{–}1.5) \times 10^{19}$ cm^{-3}, while for naturally oxidized samples this concentration decreases to $N_p = (1.0\text{–}1.4) \times$

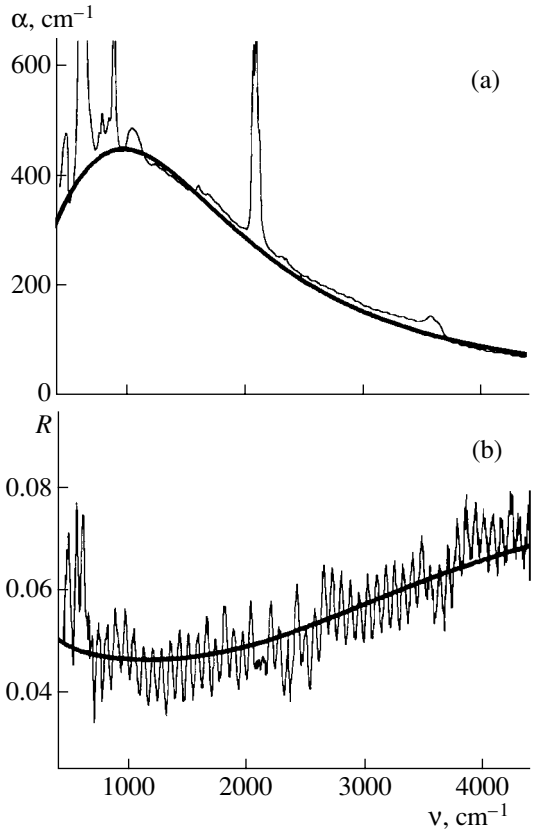

Fig. 6. Measured (thin line) and calculated approximation (thick line) spectra of (a) absorption coefficients and (b) reflectances for *mesopor*-Si prepared at $j = 50$ mA/cm^2.

10^{18} cm^{-3}. This result is in good agreement with the experimentally measured decrease in the absorption factor at free carriers (see Figs. 3, 4).

At first glance, the absence of a decrease in N_p and even its certain increase with increasing layer porosity is somewhat unexpected, since the measured coefficient of absorption at free carriers decreases in this case (see Fig. 3). However, it is noteworthy that the found values of N_p, according to the model, characterize the concentration of free carriers inside the nanocrystals, i.e., with no allowance made for the space occupied by voids. An increase in the value of N_p for the samples with higher porosity can be attributed to an increase in the relative concentration of the doping impurity (boron). Indeed, as was established experimentally in [8], the ratio between the concentrations of B and Si in *mesopor*-Si increases with increasing porosity. This fact is associated with the preferential removal of Si atoms during electrochemical etching in a hydrofluoric acid solution. Our values of N_p are consistent with an increase in relative B concentrations and at the same time indicate that only a small fraction (<10%) of the retained impurity is active and produces free holes in *mesopor*-Si. The incomplete activation may be caused by an increase in the binding energy of acceptors in Si nanocrystals surrounded by an insulator medium with lower permittivity ("dielectric confinement" [9]). In addition, equilibrium holes can be captured at the surface by the traps associated with dangling Si bonds and adsorption complexes with the involvement of water molecules, as our results for *meso*-PS samples aged in air indicate.

5. CONCLUSION

Thus, we investigated the IR absorption and reflection spectra of *mesopor*-Si layers formed on heavily doped Si substrates. The experimental results indicate that free holes make a noticeable contribution to the optical characteristics of as-prepared layers and that this contribution decreases during natural oxidation of the samples. The measured absorption and reflection spectra are explained well in the context of the suggested model based on the Bruggeman effective medium approximation and the Drude classical model with a correction for the additional surface scattering of carriers. For as-prepared *mesopor*-Si layers, the concentrations of free holes in Si nanocrystals found by fitting to the experimental data are equal to $N_p = (1.1–1.5) \times 10^{19}$ cm^{-3}. This value is an order of magnitude smaller than N_p for the single-crystal substrate. For the *mesopor*-Si samples aged in air, an additional decrease in N_p is observed and is attributed to hole trapping at the surface states that arise. The dependence of N_p and scattering parameters of holes in Si nanocrystals on the degree of porosity of the layers is investigated. It is concluded that N_p may increase in high-porosity samples of as-prepared *mesopor*-Si. The results obtained show that high concentrations of equilibrium carriers in *mesopor*-Si are attainable and that it is possible to control this concentration by varying the conditions of formation and storage of the samples.

ACKNOWLEDGMENTS

This study was supported by CRDF (grant no. RE2-2369), the Russian Foundation for Basic Research (project nos. 02-02-17259 and 03-02-16647), and by programs of the Ministry of Industry and Science of the Russian Federation.

REFERENCES

1. A. G. Cullis, L. T. Canham, and P. D. J. Calcott, J. Appl. Phys. **82**, 909 (1997).
2. O. Bisi, S. Ossicini, and L. Pavesi, Surf. Sci. Rep. **38**, 1 (2000).
3. N. Künzner, D. Kovalev, J. Diener, *et al.*, Opt. Lett. **26**, 1265 (2001).
4. L. A. Golovan, V. Yu. Timoshenko, A. B. Fedotov, *et al.*, Appl. Phys. B **73**, 31 (2001).

5. D. Kovalev, V. Yu. Timoshenko, E. Gross, *et al.*, Phys. Rev. Lett. **87**, 068301 (2001).
6. D. Kovalev, E. Gross, N. Künzner, *et al.*, Phys. Rev. Lett. **89**, 137401 (2002).
7. V. Lehmann, F. Hofmann, F. Möller, and U. Grüning, Thin Solid Films **255**, 20 (1995).
8. G. Polisski, D. Kovalev, G. G. Dollinger, *et al.*, Physica B (Amsterdam) **273–274**, 951 (1999).
9. V. Yu. Timoshenko, Th. Dittrich, V. Lysenko, *et al.*, Phys. Rev. B **64**, 085314 (2001).
10. V. Yu. Timoshenko, L. A. Osminkina, A. I. Efimova, *et al.*, Phys. Rev. B **67**, 113405 (2003).
11. W. Theiß, Surf. Sci. Rep. **29**, 91 (1997).
12. Yu. I. Ukhanov, *Optical Properties of Semiconductors* (Nauka, Moscow, 1977).
13. P. K. Kashkarov, E. A. Konstantinova, and V. Yu. Timoshenko, Fiz. Tekh. Poluprovodn. (St. Petersburg) **30**, 1479 (1996) [Semiconductors **30**, 778 (1996)].
14. D. A. G. Bruggeman, Ann. Phys. (Leipzig) **24**, 636 (1935).
15. K. V. Shalimova, *Physics of Semiconductors* (Énergoatomizdat, Moscow, 1985).
16. M. Born and E. Wolf, *Principles of Optics*, 4th ed. (Pergamon Press, Oxford, 1969; Nauka, Moscow, 1970).

Translated by N. Korovin

Semiconductors, Vol. 38, No. 5, 2004, pp. 588–593. Translated from Fizika i Tekhnika Poluprovodnikov, Vol. 38, No. 5, 2004, pp. 610–615.

AMORPHOUS, VITREOUS, AND POROUS SEMICONDUCTORS

Photoconductivity of Polymer Compositions with a High Content of Organic Dyes

N. A. Davidenko*, A. A. Ishchenko, L. I. Kostenko, N. G. Kuvshinsky, D. D. Mysyk, and R. D. Mysyk

Shevchenko National University, Vladimirskaya ul. 64, Kiev, 01033 Ukraine

**e-mail: daviden@ukrpack.net*

Submitted June 9, 2003; accepted for publication September 9, 2003

Abstract—The photoconductivity of films of an amorphous molecular semiconductor based on poly-*N*-epoxypropylcarbazole with high contents of organic dye molecules and films of a polymer composition with organic dye aggregates is studied. It is found that the dependence of the photoconductivity activation energy on the external electric field disappears as one passes from polymer compositions of the former type to those of the latter. The experimental results are explained by assuming that carrier photogeneration and transport in polymer compositions with regions of quasi-ordered dye molecules, in contrast to amorphous molecular semiconductors, take place within such regions. © *2004 MAIK "Nauka/Interperiodica".*

1. INTRODUCTION

Materials based on functional polymers and polymer compositions with organic dyes and related compounds that exhibit photoconductivity in the visible and near infrared (IR) regions are used as media for recording and displaying optical information, solar energy conversion, and light emission control [1–3]. Such materials often feature the absence of translation symmetry in the molecule distribution; from the viewpoint of the disorder and structure model, they are solid solutions [4–6]. In general, this is a true solution of three types of materials in a neutral film-forming binder. Molecules of two materials in the solid solution are responsible for electron and hole transport, and molecules of the third material play the role of carrier-photogeneration and/or carrier-recombination centers. In this case, the transport of electrons proceeds via molecules that have acceptor properties and are spaced at a distance of $R_n = N_a^{-1/3}$ from each other (N_a is the concentration of these molecules in polymer composition). The transport of holes proceeds via molecules that have donor properties and are spaced at a distance of $R_p = N_d^{-1/3}$ from each other (N_d is the concentration of these molecules in polymer composition). Due to the isotropic arrangement and steric factors, the electronic levels of molecules are not split and remain local. The localization radii of electron wave functions at acceptor molecules (α_n) and holes at donor molecules (α_p) can differ. The transport of carriers proceeds due to tunneling transitions between local levels of molecules: electrons between the lowest unoccupied molecular orbitals (LUMOs) of neighboring acceptor molecules and holes between the highest occupied molecular orbitals (HOMOs) of donor molecules. Most of the practically useful polymer compositions are characterized by the empirically established dependence of the electron and hole drift mobility (μ_n and μ_p) on the external electric field E and temperature T (see [1, 4]):

$$\mu_n \propto R_n^2 \exp(-2R_n/a_n) \times \exp[-(W_{0n} - \beta E^{1/2})(1/T - 1/T_0)/k_B], \quad (1)$$

$$\mu_p \propto R_p^2 \exp(-2R_p/a_p) \times \exp[-(W_{0p} - \beta E^{1/2})(1/T - 1/T_0/k_B)], \quad (2)$$

where W_{0n} and W_{0p} are the activation energies of electron and hole mobility at $E = 0$; k_B is the Boltzmann constant; T_0 is the temperature at which the experimental dependences $\log(\mu_n)(1/T)$ and $\log(\mu_p)(1/T)$ measured at various E and extrapolated to the region of high T intersect; β is the coefficient numerically identical with the Pool–Frenkel constant,

$$\beta = (q^3/\pi\varepsilon\varepsilon_0)^{1/2}; \quad (3)$$

q is the elementary charge; ε_0 is the permittivity of free space; and ε is the relative permittivity. We note that the first cofactors in Eqs. (1) and (2) are similar to the expression for the probability of a carrier tunneling transition between localized states [7]. The second cofactors are similar to the expression for the probability that a carrier will overcome the potential barrier caused by an oppositely charged center, when a carrier moves in the external electric field [8]. Therefore, the carrier transport can be conceived as involving diffusion within molecules and carrier hops (tunneling) between these molecules [1–4].

As a photon is absorbed by a photogeneration center, an electron and hole become separated and can leave the center and transfer to the LUMO of an acceptor molecule and the HOMO of a donor molecule, respectively. Thus, a Coulomb-bound (geminate) electron–hole pair (EHP) is formed with the initial distance r_0 between charges in it. The quantum yield Φ_0 of the EHP formation is controlled by intramolecular conversion and interconversion of a molecule of the photogeneration center, by the ratio of the HOMO and LUMO energies of this center and the energies of corresponding molecular orbitals of donor and acceptor molecules, and by steric factors and spin conversion in the EHP. EHP carriers can then either become widely separated, thus forming the free nonequilibrium carriers that are responsible for photoconductivity, or recombine at the photogeneration center. For most practically useful polymer compositions, the photocurrent density j_{ph} and the quantum yield of free carrier photogeneration η can be expressed by the empirical dependence [4]

$$j_{ph} \propto \eta \propto \Phi_0 R_n R_p \exp(-R_n/\alpha_n - R_p/\alpha_p) \times \exp[-(W_{0ph} - \beta E^{1/2})(1/T - 1/T_0)/k_B], \quad (4)$$

where W_{0ph} is the activation energy of free carrier photogeneration at $E = 0$ and T_0 is the temperature at which the experimental dependences $\log(\eta)$ on $1/T$, measured at various E and extrapolated to the region of high T, intersect. We note that, within the model of two-stage carrier photogeneration via the EHP formation and dissociation, the quantity W_{0ph} can be identified with the energy of the Coulomb interaction between an electron and hole in the EHP:

$$W_{0ph} = q^2/4\pi\varepsilon_0\varepsilon r_0, \quad (5)$$

where r_0 is the distance between opposite-sign carriers in the EHP.

Although the above scheme of carrier photogeneration and transport in polymer compositions corresponds very approximately to reality, this scheme can be used to detect significant differences between crystalline and amorphous vitreous semiconductors [9]. We note in particular the heavy dependence of the mobility and efficiency of carrier photogeneration on the activation energy of these parameters in a zero electric field. This factor is limiting for polymer-composition applications in recording media and photoelectric converters, where high EHP dissociation rates are required [10] along with high photogeneration efficiency. Apparently, this circumstance has recently stimulated interest in compositions containing both nanoparticles of inorganic semiconductor materials [11, 12] and organic dye aggregates [13, 14]. It is assumed that the mobility of nonequilibrium carriers in such materials can be significantly increased if the carrier transport proceeds in ordered fragments of polymers; the band mechanism of transport takes place in these fragments. However, the photoconductivity can be limited in these cases due to potential barriers and traps for carriers in the regions of aggregate–polymer–aggregate heterojunctions. Moreover, the problem of changes in the carrier photogeneration mechanism in going from polymer compositions with isotropic spatial distribution of molecules to polymer compositions with a high dye content has so far been inadequately studied. The aim of this study is to compare features of the photoconductivity of polymer composition films with various contents of dyes susceptible to and incapable of aggregation, as well as to clarify the carrier photogeneration mechanism at a high dye content.

2. EXPERIMENTAL

To achieve the above goal, we studied the special features of optical absorption, photoluminescence (PL), and photoconductivity of polymer composition films based on the photoconductive oligomer, poly-*N*-epoxypropylcarbazole (PEPC) (I) (see [15])

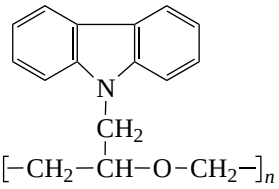

I

with additives of dyed boron–fluoride (BF) complexes (II) [16] and compounds with intramolecular charge transport (CICT) (III) [17].

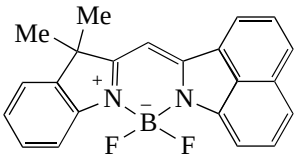

II

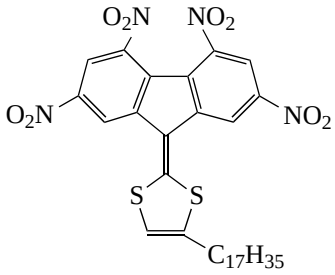

III

Samples were prepared as structures with a free surface (glass substrate)–(PEPC+BF or PEPC + CICT polymer composition film) and as sandwich structures (glass substrate)–(conducting SnO_2:In_2O_3 layer)–(PEPC + BF or PEPC + CICT polymer composition film)–Al. The BF and CICT content N was varied from

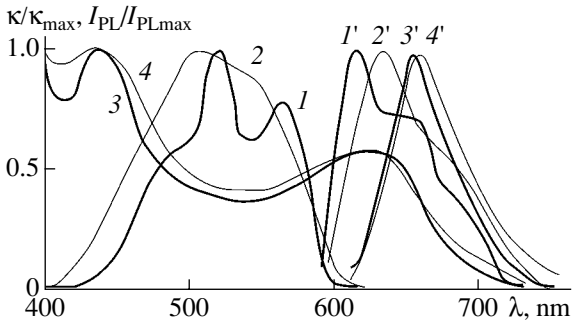

Fig. 1. (*1*–*4*) Optical absorption spectra κ/κ_{max} and (*1*'–*4*') photoluminescence intensities $I_{PL}/I_{PL\,max}$ (normalized to maximum values) of (*1*, *1*') PEPC + 1% BF, (*2*, *2*') PEPC + 50% BF, (*3*, *3*') PEPC + 1% CICT, and (*4*, *4*') PEPC + 50% CICT films at $T = 293$ K. The photoluminescence excitation wavelength is λ = (*1*', *2*') 585 and (*3*', *4*') 620 nm.

0 to 70%.[1] The PEPC + BF and PEPC + CICT films were prepared by applying a corresponding amount of PEPC and BF or CICT solution in tetrahydrofurane onto glass substrates with or without a conducting layer and with subsequent drying for 4 h in an oven at a temperature of 80°C. The thickness L of these films (0.5–5 μm) was measured using an MII-4 interference microscope. Aluminum contacts were deposited onto the polymer film surface by thermal evaporation in a vacuum chamber of a VUP-4M setup at a residual gas pressure of $(2–5) \times 10^{-5}$ Torr. These contacts were no thinner than 500 Å. The sandwich structure area was 25 mm^2. The spectra of the absorptivity κ and the PL intensity (I_{PL}) of PEPC + BF and PEPC + CICT films in the samples with a free surface were measured in the wavelength range λ = 400–1000 nm using a KSVIP-23 computerized spectrometric system. The sandwich structure samples were used to measure the photocurrent density (j_{ph}) when the side of the SnO_2:In_2O_3 electrode is exposed to monochromatic light. As a light source, an incandescent lamp with a set of light filters or a He–Ne laser with the wavelength λ = 633 nm were used. The light intensity I in the range of 0.2–10 W/m^2 was varied using neutral light filters. The electric field E in polymer films (as an electric voltage was applied to the electric contacts) was varied in the range $(1–20) \times 10^7$ V/m. The current kinetics during and after exposure to light was measured using a storage oscilloscope. To measure the dependences of j_{ph} on E and T, the samples were placed in a thermostat with an optical window; the temperature could be varied from 290 to 360 K. The temperature dependences of j_{ph} were used to determine W_{0ph}.

3. RESULTS AND DISCUSSION

The PEPC films without specially introduced additives do not absorb light, and the samples with a sandwich structure with such films do not exhibit a photoconductivity effect in the visible region of the spectrum. Absorption and photoconductivity is observed in this wavelength region when BF and CICT additives are introduced into PEPC.

Figure 1 shows the normalized dependences of κ and I_{PL} on λ for films of polymer composition with various BF and CICT contents. As the BF content increases, the vibrational structure of the absorption and luminescence spectra in the PEPC films becomes significantly smoothed beginning from $N > 1\%$, and the band broadens and shifts to longer wavelengths. This observation indicates that intermolecular interactions in the dye–dye system set in; ultimately, these interactions lead to aggregation [16]. Hence, at a high BF content in films of polymer composition, regions of sandwich-structure aggregates are formed, which are characterized by an inhomogeneous broadening of allowed electronic states. The affinity of BF to form aggregates is caused by the intraionic structure of molecules and the absence of steric hindrances. In contrast to BF, the absorption and luminescence spectra do not exhibit appreciable changes as the CICT content increases in PEPC films (Fig. 1). This means that there are no strong interactions between molecules in PEPC films even at high CICT content, and electronic states remain degenerate. The latter is caused by the following. First, the fluorene base of the CICT molecule contains four nitro groups; as shown by quantum chemical calculations [18], two central groups emerge from the molecule plane and prevent the formation of sandwich-structure aggregates. Second, the long flexible $–C_{17}H_{35}$ chain is a hindrance for neighboring CICT molecules to approach each other.

In the sandwich-structure samples with PEPC + BF and PEPC + CICT films, photoconductivity was detected in the dye absorption region. After the samples with low dye content and with an applied voltage have begun to be exposed to light, the electric current flowing through the polymer composition film increases and reaches its quasi-steady value j_{ph}, which varies only slightly during further irradiation. The current decreases after the exposure to light; the kinetics of the photocurrent rise and relaxation is symmetric. At fixed E, j_{ph} increases with I, and the dependence of j_{ph} on I can be analytically expressed as

$$j_{ph} \propto I^m, \tag{6}$$

where the exponent $m = (0.95 \pm 0.05)$. The photocurrent increases with temperature. Figure 2 shows the results of j_{ph} measurements in the samples with PEPC + 1% BF and PEPC + 1% CICT films, exposed to light with a 0–0 transition wavelength $\lambda_{0–0}$. This quantity was estimated using the value of λ at the intersection point of the normalized dependences of the absorptivity and PL intensity of films of polymer composition (Fig. 1). The dependences of j_{ph} on E and T can be approximated by straight lines in the $\log j_{ph}$–$E^{1/2}$ and $\log j_{ph}$–$1/T$ coordinates, respectively, and can be analytically described by

[1] Hereinafter, this refers to the mass fraction.

an expression similar to formula (4). We note that, in the case of the samples with PEPC + 1% BF and PEPC + 1% CICT films, the dependences $\log j_{ph}(1/T)$ extrapolated to high T and measured at various $E < 1.2 \times 10^8$ V/m intersect near the temperatures $T_0 = (490 \pm 15)$ K (Fig. 2). The activation energies W_{ph} of the photocurrent, which are determined from the slopes of the dependences $\log j_{ph}$ on $1/T$ for various $E < 1.2 \times 10^8$ V/m, decrease as E increases. The dependences of W_{ph} on E are linear in the coordinates $W_{ph} - E^{1/2}$ (Fig. 3, curves *1*, *2*); the slope yields $(4.6 \pm 0.3) \times 10^{-5}$ eV $(V/m)^{-1/2}$, which is close to the Pool–Frenkel constant (see formula (3)) for $\varepsilon = 3$. The straight lines extrapolated to the point $E = 0$ intersect with the vertical axis, which allows one to determine the corresponding photogeneration activation energies W_{0ph} in the zero field. The results show that the photoconductivity of polymer composition films at low dye content is caused by carrier photogeneration from dye molecules; hence, the model concepts of photogeneration and transport previously developed for amorphous molecular semiconductors [4] are applicable in this case.

However, the differences in the photoconductivity features of films of polymer composition with BF and CICT begin to manifest themselves as N increases. For example, the sandwich-structure samples with PEPC + 50% CICT films, in comparison with PEPC + 1% CICT films, exhibit the following features:

(i) the kinetics of the photocurrent rise and relaxation remains symmetric;

(ii) the exponent m in the dependence (6) decreases to $m = (0.65 \pm 0.1)$;

(iii) the dependences $\log j_{ph}$ on $E^{1/2}$ remain linear, and the slope decreases only slightly;

(iv) the regions of the dependences $\log j_{ph}(1/T)$ extrapolated to high T and measured for various $E < 1.2 \times 10^8$ V/m intersect but near a higher temperature, $T_0 = (510 \pm 15)$ K (Fig. 2); and

(v) the dependences W_{ph} on E are also linear in the coordinates W_{ph} and $E^{1/2}$; however, the slope slightly decreases and the photogeneration activation energy W_{0ph} in the zero field decreases (Fig. 3).

The results obtained indicate that the basic features of carrier photogeneration are unchanged as the CICT content increases; however, the probability of EHP dissociation increases (W_{0ph} decreases). The W_{0ph} decrease can be explained by the fact that the average distance between CICT molecules decreases as N increases. After photon absorption, an EHP can be formed not only due to a positive charge (hole) release from an excited CICT molecule to a PEPC carbazole fragment, but also due to electron transfer from an excited CICT molecule to an unexcited CICT molecule. In this case, r_0 in formula (5) increases. An additional factor affect-

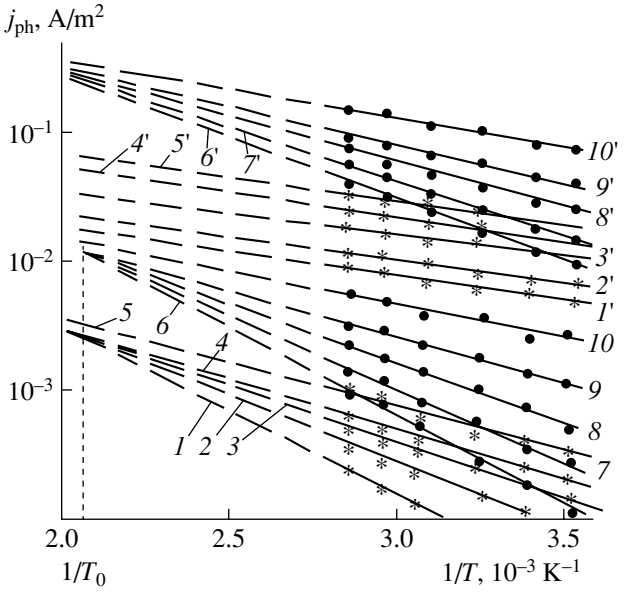

Fig. 2. Temperature dependences of the photocurrent in the sandwich-structure samples with (*1–5*) PEPC + 1% BF, (*1'–5'*) PEPC + 50% BF, (*6–10*) PEPC + 1% CICT, and (*6'–10'*) PEPC + 50% CICT films with a positive voltage at the Al electrode for $E = (1, 1', 6, 6') 4 \times 10^7$, $(2, 2', 7, 7') 5 \times 10^7$, $(3, 3', 8, 8') 7 \times 10^7$, $(4, 4', 9, 9') 8 \times 10^7$, and $(5, 5', 10, 10') 11 \times 10^7$ V/m. The excitation light wavelength is $\lambda = (1–5, 1'–5')$ 585 nm and $(6–10, 6'–10')$ 633 nm; the intensity is $I = 2$ W/m^2. The polymer film thickness is $L = 2$ μm.

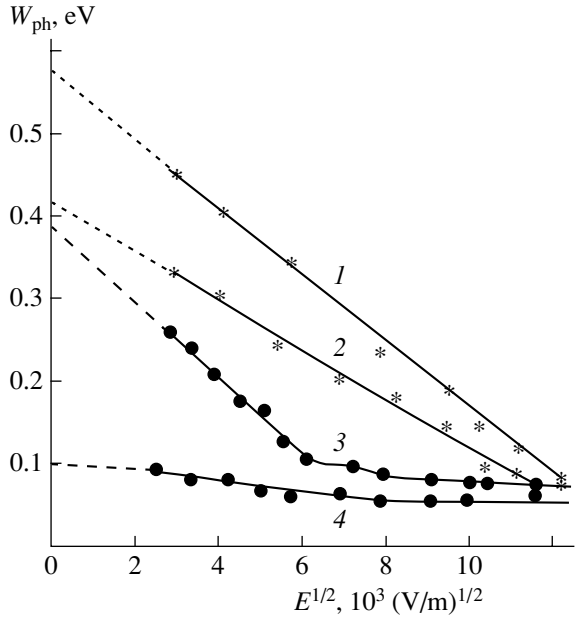

Fig. 3. Dependence of the photoconductivity activation energy on the electric field in sandwich-structure samples with (*1*) PEPC + 1% CICT, (*2*) PEPC + 50% CICT, (*3*) PEPC + 1% BF, and (*4*) PEPC + 50% BF films with a positive voltage at the Al electrode, excitation light wavelength $\lambda = (1, 2)$ 633 and $(3, 4)$ 585 nm, and excitation light intensity $I = 2$ W/m^2. The polymer film thickness is $L = 2$ μm.

ing the decrease in W_{0ph} may be an increase in ε in Eq. (5) as the content of CICTs increases. These compounds have a larger intrinsic dipole moment in comparison with that of PEPC carbazole fragments. The above inference is confirmed by a decrease in the slope of the dependences W_{ph} on $E^{1/2}$ (Fig. 3) and the previously obtained data [19, 20] on the features of carrier photogeneration and recombination in PEPC films containing compounds with intramolecular charge transport and various dipole moments of molecules.

The sandwich-structure samples with PEPC + 50% BF films, in comparison with the PEPC + 1% BF films, exhibit the following features:

(i) the kinetics of photocurrent rise and relaxation becomes asymmetric; after the end of exposure to light, a slow (a few seconds) component arises in the kinetics of photocurrent relaxation;

(ii) the exponent m in dependence (6) decreases to $m = (0.65 \pm 0.1)$;

(iii) the dependences $\log j_{ph}$ on $E^{1/2}$ at $E < 1.2 \times 10^8$ V/m remain linear and the slope of these plots decreases only slightly;

(iv) the portions of the dependences of $\log j_{ph}(1/T)$ extrapolated to high T and measured for various $E < 1.2 \times 10^8$ V/m become parallel (see Fig. 2);

(v) the value of W_{ph} is almost independent of E, and the photogeneration activation energy W_{0ph} in the zero field is close to (0.1 ± 0.05) eV (Fig. 3).

The results obtained indicate that, as the BF content increases, carriers are photogenerated not only in individual BF molecules, but also in their aggregates. In the latter case, transitions occur between interacting BF molecules, whose electronic levels cannot be considered as degenerate. As nonequilibrium carriers are generated, the main hindrance for their drift in an external electric field is potential barriers for the transitions from molecule to molecule, especially at the aggregate–PEPC–aggregate interfaces. The activation energy of these transitions is close to the activation energy of carrier release from localized states, whose density is higher between regions of clustered aggregates, i.e., in the polymeric binder. Therefore, the activation energy W_{0ph} of the photocurrent is close to 0.1 eV (Fig. 3) and corresponds to the activation energy of the hole transitions between PEPC carbazole fragments [21]. An external electric field increases the transparency of potential barriers of intermolecular electron transitions, which manifests itself in the linearity of the dependence of $\log j_{ph}$ on $E^{1/2}$. The asymmetric kinetic curves (photocurrent rise at the beginning of exposure to light and its slow decrease after exposure), as well as the sublinear current–illuminance characteristic, show the effect of trapping nonequilibrium carriers and their volume recombination [22]. The latter effect seems to be caused by different energies of localized states at the aggregate–PEPC interfaces, where traps can be efficiently generated. Such traps with captured carriers are also recombination centers [23].

4. CONCLUSION

The main result of this study is as follows. It was detected that the dependence of the photoconductivity activation energy on the external electric field changes as one passes from polymeric compositions that correspond to the model concepts of amorphous molecular semiconductors to those containing regions of clustered quasi-ordered structures of organic molecules. As the dye molecule content increases, the photoconductivity activation energy decreases and the characteristic temperature T_0 in relation (4) increases. In polymer compositions with regions of dye quasi-ordered molecules, in contrast to amorphous molecular semiconductors, carrier photogeneration and transport take place both between these regions and within them. In the film volume near heterojunctions, localized states can be formed; the trapping of excess carriers by these states enhances volume recombination. The results obtained can be used to refine the physical models of carrier photogeneration in materials with organic semiconductor nanoparticles and, specifically, to develop new media with a high efficiency of volume radiative recombination [24].

REFERENCES

1. P. M. Borsenberger and D. S. Weiss, *Photoreceptors for Xerography* (Marcel Dekker, New York, 1998).
2. J.-M. Nunzi, C. R. Phys. **3**, 1 (2002).
3. E. I. Mal'tsev, D. A. Lypenko, B. I. Shapiro, and A. V. Vannikov, Zh. Nauchn. Prikl. Fotogr. **46** (1), 13 (2001).
4. N. G. Kuvshinsky, N. A. Davidenko, and V. M. Komko, *Physics of Amorphous Molecular Semiconductors* (Lybid', Kiev, 1994).
5. D. Hertel, H. Bassler, U. Scherf, and H. Horhold, J. Chem. Phys. **110**, 9214 (1999).
6. M. Pope and C. E. Swenberg, *Electronic Processes in Organic Crystals* (Clarendon Press, Oxford, 1982).
7. O. Madelung, *Introduction to Solid-State Theory* (Springer, Berlin, 1978; Nauka, Moscow, 1985).
8. P. T. Oreshkin, *Physics of Semiconductors and Insulators* (Vysshaya Shkola, Moscow, 1977).
9. N. F. Mott and E. A. Davis, *Electronic Processes in Non-Crystalline Materials* (Clarendon Press, Oxford, 1971; Mir, Moscow, 1974).
10. E. L. Frankevich, A. N. Chaban, and D. I. Kadyrov, Khim. Fiz. **21** (4), 103 (2002).
11. A. Henglein, Ber. Bunsenges. Phys. Chem. **101**, 1562 (1997).
12. R. F. Khaĭrutdinov, Usp. Khim. **67** (2), 125 (1998).

13. J. J. M. Halls, C. A. Walsh, N. C. Greenham, and E. A. Marseglia, Nature **376**, 498 (1995).
14. S. A. Carter, J. C. Scott, and P. J. Brock, Appl. Phys. Lett. **71**, 1145 (1997).
15. V. D. Filimonov and E. E. Sirotkina, *Chemistry of Monomers Based on Carbazole* (Nauka, Novosibirsk, 1995).
16. A. A. Ishchenko, *Structure and Spectral-Luminescent Properties of Polymethine Dyes* (Naukova Dumka, Kiev, 1994).
17. N. Davidenko, N. Kuvshinsky, L. Kostenko, and D. Misik, Mol. Cryst. Liq. Cryst. **324**, 71 (1998).
18. N. G. Kuvshinsky, N. A. Davidenko, V. V. Reshetnyak, *et al.*, Chem. Phys. Lett. **165**, 323 (1990).
19. N. A. Davidenko, A. K. Kadashchuk, N. G. Kuvshinsky, *et al.*, J. Inf. Recording **24**, 327 (1996).
20. A. K. Kadashchuk, N. I. Ostapenko, N. A. Davidenko, *et al.*, Fiz. Tverd. Tela (St. Petersburg) **39**, 1183 (1997) [Phys. Solid State **39**, 1047 (1997)].
21. H. Bassler, Phys. Status Solidi B **107**, 9 (1981).
22. S. M. Ryvkin, *Photoelectric Effects in Semiconductors* (Fizmatgiz, Leningrad, 1963; Consultants Bureau, New York, 1964).
23. N. A. Davidenko, S. L. Studzinskiĭ, N. A. Derevyanko, *et al.*, Fiz. Tekh. Poluprovodn. (St. Petersburg) **36**, 1248 (2002) [Semiconductors **36**, 1169 (2002)].
24. N. A. Davidenko and A. A. Ishchenko, Pis'ma Zh. Tekh. Fiz. **28** (11), 84 (2002) [Tech. Phys. Lett. **28**, 483 (2002)].

Translated by A. Kazantsev

Semiconductors, Vol. 38, No. 5, 2004, pp. 594–597. Translated from Fizika i Tekhnika Poluprovodnikov, Vol. 38, No. 5, 2004, pp. 616–620.

AMORPHOUS, VITREOUS, AND POROUS SEMICONDUCTORS

Tensoresistive Effect in Porous Silicon Layers with Different Morphology

S. P. Zimin and A. N. Bragin

Demidov State University, ul. Sovetskaya 14, Yaroslavl, 150000 Russia

e-mail: zimin@univ.uniyar.ac.ru

Submitted July 22, 2003; accepted for publication September 25, 2003

Abstract—The effect of elastic flexural strain on electrical conductivity of porous silicon with different pore morphology and different properties of depletion regions around the pores is studied. Porous layers are formed using anodic electrochemical etching of the *p*- and *n*-Si wafers and have a porosity of 5–68%. It is shown that specific features of variations in electrical conductivity of porous silicon under the effect of deformation depend on the structural characteristics of the porous material. In order to explain the results obtained, various physical models of the charge-carrier transport in porous silicon are used. © *2004 MAIK "Nauka/Interperiodica".*

1. INTRODUCTION

Porous silicon (*por*-Si) is one of the promising materials in modern electronics and can be used as a buffer in heteroepitaxy, in active elements of semiconductor devices, components of ultrasonic-electronics devices, and so on. All these potential applications require a detailed study of the mechanical properties of porous layers. Information about the mechanical characteristics of *por*-Si in scientific publications is very scanty, and there is no published research on the tensoresistive effect in *por*-Si. In this paper, we report the results of a comprehensive study of the tensoresistive effect in *por*-Si layers with differing morphology and porosity.

It is well known that *por*-Si can have porosity in the range 3–95%. The complexity of any studies involving *por*-Si consists in the fact that it is necessary to constantly take into account the structural parameters of the porous material. It was shown previously [1] that electrical properties of *por*-Si can be classed into four groups, depending on porosity, morphology of pores, and special features of the formation of depletion regions around the pores. It is important, that, in each of the four groups (*por*-Si1–*por*-Si4), there exists a specific mechanism of drift of charge carriers, which governs not only the electrical conductivity of the material but also the characteristics of variations in conductivity with variations in temperature, illumination intensity, and so on. Low porosity and the absence of depletion in charge carriers are characteristic of *por*-Si of the first group (*por*-Si1). In this material, drift of charge carriers occurs over the single-crystal matrix and is described in the context of the effective-medium theory in the model of "silicon + pores." Low porosity and the presence of depletion regions around pores are characteristic of *por*-Si of the second group (*por*-Si2). In this case, the charge-carrier transport proceeds over nondepleted regions of the silicon matrix, according to the effective-medium theory in a system that consists of silicon, pores, and depletion regions. Charge-carrier transport proceeds over the depleted silicon matrix in *por*-Si of the third group (*por*-Si3), where porosity does not exceed 50% and the processes of depletion encompass the entire interpore space. The above transport is described by the theory of heavily compensated disordered semiconductors with small-scale fluctuations. The *por*-Si material of the fourth group (*por*-Si4) has high porosity and includes the products of electrochemical reactions in the bulk, which envelop the silicon nanocrystals. The composition of this envelope can depend on the conditions of anodization and can range from amorphous hydrogenated silicon *a*-Si:H to oxide phases SiO_x. In these cases, the drift of charge carriers can proceed either over the low-resistivity *a*-Si:H envelope or by hops between nanocrystallites through oxide interlayers.

According to the data of Zimin *et al*. [2–5], porous Si layers of different groups react specifically to external effects such as heat treatment at 450–550°C in an inert medium or irradiation with 2-MeV electrons. We attempted to solve two main problems in the course of carrying out this study. First, it was necessary to describe the quantitative characteristics of the tensoresistive effect in *por*-Si layers that belonged to each of the four groups (*por*-Si1–*por*-Si4). Second, it was of interest to analyze how the phenomena under study in porous layers with different morphology can be interpreted in terms of the physical models suggested previously [1] for charge-carrier transport. In this context, it became necessary to measure additionally the tensoresistive effect in the samples of initial crystalline silicon (*c*-Si) that were obtained with the corresponding crystallographic orientations.

1063-7826/04/3805-0594$26.00

Table 1. Conditions of production and parameters of porous layers

por-Si type	Substrate	Conditions of production	*P*, %	d_p, μm
por-Si1	n^+-Si:Sb, (111)	j = 10 mA/cm^2	23	48
		t = 40 min, an aqueous HF solution (48%)		
por-Si2	*n*-Si:P, (100)	j = 10 mA/cm^2	5	100
		t = 50 min, an aqueous HF solution (48%)		
por-Si3	p^+-Si:B, (111)	j = 10 mA/cm^2	20	42
		t = 30 min, an aqueous HF solution (48%)		
por-Si4	n^+-Si:Sb, (111)	j = 50 mA/cm^2, t = 10–60 min	48–60	72–121
	p^+-Si:B, (111)	Aqueous solution of HF (48%) : $(CH_3)_2CHOH$		

2. EXPERIMENTAL

Porous layers were formed using anodic electrochemical etching of silicon wafers by the Unno–Imai liquid-contact method [6]. By varying the type of doping impurity, the electrolyte composition, and the conditions of anodization, we managed to form porous structures that had porosity *P* in the range 5–68% and belonged to one of the four groups, according to the classification suggested in [1]. The anodization-current densities *j* and the electrochemical-treatment times *t* are listed in Table 1. The silicon resistivity was chosen as 0.01, 4.5, 0.03, and 0.01 or 0.03 Ω cm in order to obtain *por*-Si1, *por*-Si2, *por*-Si3, and *por*-Si4, respectively. The amorphized film was removed from the *por*-Si surface using plasmochemical etching. The porosity of the samples was determined gravimetrically. The thickness of the *por*-Si layers d_p ranged from 40 to 120 μm. X-ray diffractometry showed that the phase of the products of electrochemical reactions was similar to that of amorphous silicon in the *por*-Si4 samples.

The samples of two-layer *por*-Si/*c*-Si structures under study, as well as the reference samples of initial *c*-Si, were cut into strips with an area of 20×5 mm^2. The long side of the strips was parallel to the primary flat of the silicon wafer. Aluminum electric contacts were formed on the *por*-Si and *c*-Si surfaces using thermal evaporation with subsequent fusing for 10 min at 300°C. The test structures were glued to a cantilever that had a constant cross section and was made of elastic steel. One end of the cantilever was rigidly fixed, while the other end was subjected to flexure that gave rise to the elastic tensile or compressive strain in the sample. The long side of the samples was oriented along the cantilever axis.

The value of strain ε was determined from the expression

$$\varepsilon = \frac{3}{2}\frac{ah}{L^3}c, \quad (1)$$

where *a* is the distance from the sample center to the free end of the cantilever, *h* is the cantilever thickness, *L* is the cantilever length, and *c* is the flexure in the vertical direction. The flexural deformation with tension or compression of the *por*-Si layer corresponded to the conditions $\varepsilon > 0$ and $\varepsilon < 0$, respectively. It is well known [7] that, in the case of a slight homogeneous flexure (elastic deformation), each volume element in the sample under study is deformed in the same way as under simple uniaxial loading. Deformation is effected along the axis that corresponds to the crystallographic direction of the primary flat of the silicon wafer for all the samples under investigation.

The values of strains ε in our experiments were in the range $\pm 1 \times 10^{-3}$. These values exceed the intrinsic strains in *por*-Si by an order of magnitude [8], which makes it possible to ignore the latter strains when analyzing the experimental data. The electrical conductivity of the test structures was measured both in the dark and with additional illumination in the visible region of the spectrum. After removing the deforming force, we observed a recovery of the conductivity to the initial values, which indicated that the conditions for elastic deformation were satisfied. If the measurements were repeated for the *por*-Si samples of all groups, we observed good reproducibility of the results, which could be related to the structural stability of the material in the strain range under consideration. In order to characterize quantitatively the tensoresistive effect, we used the values of relative variation in the resistance $\Delta R/R_0$ and the tensosensitivity coefficient for the material $K_T = \Delta R/(R_0\varepsilon)$, where R_0 is the resistance of the sample in the initial state and ΔR is the variation in the sample's resistance as a result of deformation.

Taking into account that *por*-Si resistivity is quite specific for each of the four *por*-Si groups [1], we used different methods of electrical measurements that made it possible to determine directly the resistance of the *por*-Si layer [3].

3. RESULTS

Measurements of the tensoresistive effect in the single-crystal *n*-Si samples showed that the electrical resistance of the test structures decreased as a result of flexural deformation with tension and increased as a result of flexural deformation with compression. For *p*-Si single crystals, the situation was opposite. This

Table 2. Effect of strain on relative variation in the resistance of porous layers of different groups and the corresponding initial single-crystal silicon (*n*- or *p*-Si)

Material	Strain $\varepsilon = 10^{-3}$			
	in the dark		with illumination	
	$\Delta R/R_0$ (compression)	$\Delta R/R_0$ (tension)	$\Delta R/R_0$ (compression)	$\Delta R/R_0$ (tension)
por-Si1	0.050	−0.012	0.051	−0.011
n^+-Si:B, (111)	0.046	−0.007	0.044	−0.008
por-Si2	0.098	−0.019	0.082	−0.025
n-Si:P, (100)	0.076	−0.019	0.079	−0.017
por-Si3	0.048	−0.010	−0.035	0.120
p^+-Si:B, (111)	−0.032	0.100	−0.030	0.100
por-Si4	The tensoresistive effect is not observed			

fact is well known for silicon strain sensors [9] and corresponds to the cases of negative and positive values of the tensosensitivity coefficient for *n*- and *p*-Si, respectively. The values of relative variation in the resistance of *c*-Si and *por*-Si/*c*-Si structures for the largest magnitude of the strain are listed in Table 2. It follows from an analysis of the data in Table 2 that the situation for *por*-Si is not as predictable as for *c*-Si. Irrespective of the type of doping impurity in initial silicon, the resistance of all *por*-Si1–*por*-Si4 samples increases as a result of flexural deformation with compression of the porous layer and decreases if this layer is tensile-stressed. It is worth noting that the tensoresistive effect was not observed in *por*-Si4 layers to within the experimental accuracy. The K_T coefficient in the *por*-Si1–*por*-Si4 layers under study was negative when measured without illumination and depended on the value of ε. Dependences of the tensosensitivity coefficient on strain for the *por*-Si1, *por*-Si2, and *por*-Si3 samples subjected or not subjected to illumination are shown in Figs. 1, 2, and 3, respectively. The results for the reference samples of original *c*-Si are also shown for comparison.

4. DISCUSSION

The relative variation in electrical resistance of *por*-Si1 as a result of deformation did not exceed 5% (Table 2) and almost coincided with the corresponding parameter for starting silicon. Additional illumination did not affect the magnitude of the tensoresistive effect. The similarity between the tensoresistive properties of *por*-Si1 and those of initial silicon doped heavily with antimony (Fig. 1) is related to the absence of depletion regions in *por*-Si1. In this case, the resistivity of the porous material, according to the effective-medium theory [10], is described by the formula

$$\rho_p = \rho_s \frac{1+P}{1-P}, \qquad (2)$$

where ρ_s and ρ_p are the resistivities of initial silicon and the porous layer, respectively. According to formula (2), the variations in electrical properties of *por*-Si1 as a result of deformation should be identical to those of initial silicon since the elastic strain does not affect the porosity *P* in the porous material.

Without additional illumination, *por*-Si2 featured a higher tensosensitivity compared to that in initial single-crystalline Si (Fig. 2, straight lines *3*, *1*). However, under conditions of additional illumination, the tensosensitivity coefficient of *por*-Si2 was smaller and nearly coincided with the values for initial silicon. At the same time, we observed no significant effect of illumination on tensoresistive properties of single-crystalline silicon. The above experimental facts are attributed to the existence of high-resistivity depletion regions around

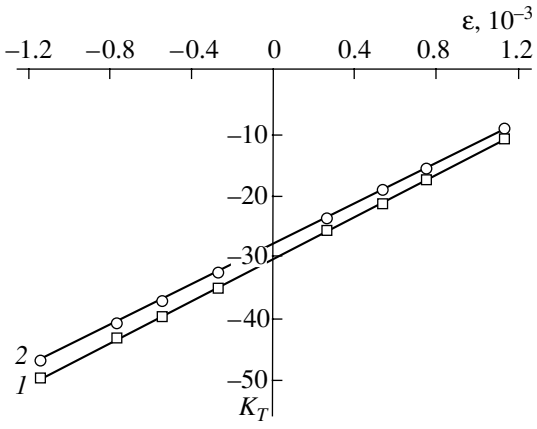

Fig. 1. Dependences of the tensosensitivity coefficient K_T on strain ε for *por*-Si1 and initial silicon n^+-Si:Sb: (*1*) for porous Si and (*2*) for single-crystal Si.

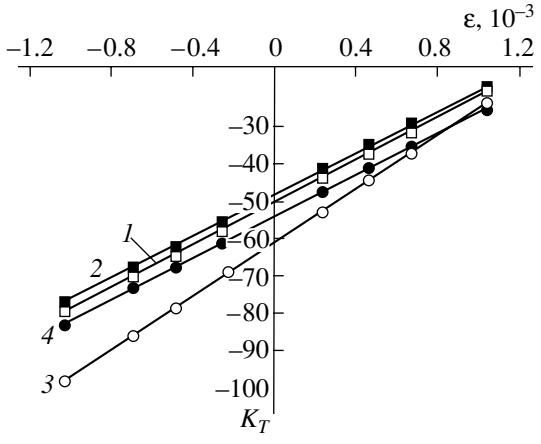

Fig. 2. Dependences of the tensosensitivity coefficient K_T on strain ε for (*3*, *4*) *por*-Si layer and (*1*, *2*) initial single-crystal silicon (*1*, *3*) in the dark and (*2*, *4*) with additional illumination.

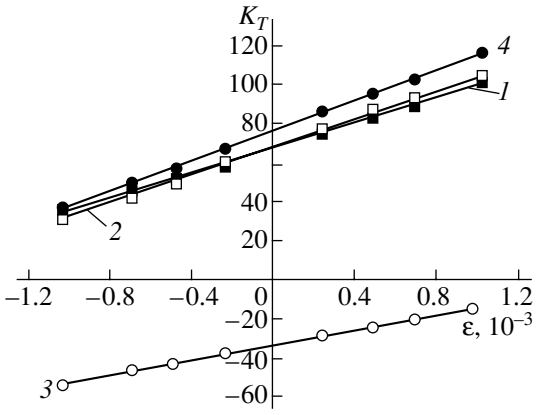

Fig. 3. Dependences of the tensosensitivity coefficient K_T on strain ε for (*3*, *4*) *por*-Si sample and (*1*, *2*) corresponding initial single-crystal silicon (*1*, *3*) in the dark and (*2*, *4*) with additional illumination.

the pores. If the depletion regions are taken into account, the resistivity of porous material can be expressed by the following formula in the context of the effective-medium theory:

$$\rho_p = \rho_s \frac{1 + P^*}{1 - P^*}. \quad (3)$$

Here, P^* is the effective porosity that involves not only the volume of the porous space but also the volume occupied by depletion regions. An increase in the tensosensitivity coefficient for *por*-Si2 in comparison with initial silicon is related to the contribution of depletion regions. A decrease in K_T in *por*-Si2 exposed to illumination is caused by an increase in the charge-carrier concentration in depletion regions; as a result, the resistivity of *por*-Si2 approaches that of initial *c*-Si owing to a decrease in the effective porosity.

The change of sign of the tensosensitivity coefficient from negative to positive was observed in the *por*-Si3 samples as a result of additional illumination (Fig. 3). In addition, the values of K_T in *por*-Si3 under illumination became close to those in initial *c*-Si. This unusual behavior can be explained in the following way. It is known [1] that effective *n*-type conductivity is observed in low-porosity silicon layers formed in p^+-Si:B. This fact is related to the appreciable decrease in the hole concentration in the single-crystal *por*-Si3 matrix; as a result, the conductivity of the material approaches that of intrinsic silicon. This circumstance accounts for the negative sign of the tensosensitivity coefficient in the samples that are not exposed to additional illumination. A drastic increase in the hole concentration is observed in *por*-Si3 as a result of illumination. Consequently, the material acquires *p*-type conductivity, which is confirmed by measurements of thermoelectric power. As a result, the sign of K_T becomes positive, which is characteristic of silicon piezoresistors with *p*-type conductivity.

Studies of the *por*-Si4 layers made it possible to ascertain that the *por*-Si4 material did not feature tensoresistive properties (to within experimental accuracy) even at the largest strains. This fact is consistent with the model of the charge-carrier transport in *por*-Si4 over the sheath of amorphous silicon that envelops silicon crystallites [1, 3]. As shown by Gleskova *et al.* [11], the tensoresistive effect is not observed in amorphous hydrogenated silicon *a*-Si:H at a strain of 2%; the latter exceeds the strains used in this study by an order of magnitude.

5. CONCLUSION

The results of our studies of the effect of elastic deformation on electrical conductivity of porous silicon (*por*-Si) with varying morphology indicate that deformation specifically affects the properties of porous layers of different types (*por*-Si1–*por*-Si4). It is worth noting that the results obtained for *por*-Si of all four groups are consistent with the suggested corresponding models of the charge-carrier transport. In our future research we plan to analyze the dependence of tensoresistive properties on porosity for each of the *por*-Si groups and evaluate the thermal stability of the tensosensitivity coefficient.

ACKNOWLEDGMENTS

This study was supported by the Ministry of Education of the Russian Federation, grant no. E02-3.4-423.

REFERENCES

1. S. P. Zimin, Fiz. Tekh. Poluprovodn. (St. Petersburg) **34**, 359 (2000) [Semiconductors **34**, 353 (2000)].
2. S. P. Zimin and A. N. Bragin, Fiz. Tekh. Poluprovodn. (St. Petersburg) **33**, 476 (1999) [Semiconductors **33**, 457 (1999)].
3. S. P. Zimin, D. S. Zimin, Yu. V. Ryabkin, and A. N. Bragin, Phys. Status Solidi A **182**, 221 (2000).
4. S. P. Zimin and E. P. Komarov, Pis'ma Zh. Tekh. Fiz. **24** (6), 45 (1998) [Tech. Phys. Lett. **24**, 226 (1998)].
5. S. P. Zimin, A. N. Bragin, and Yu. V. Ryabkin, in *Abstracts of All-Russian Scientific Conference on Physics of Semiconductors and Semimetals* (St. Petersburg, Russia, 2002), p. 59.
6. K. Imai and H. Unno, IEEE Trans. Electron Devices **31**, 297 (1984).
7. S. A. Antipov, I. A. Bataronov, A. I. Drozhzhin, and A. M. Roshchupkin, Fiz. Tekh. Poluprovodn. (St. Petersburg) **27**, 937 (1993) [Semiconductors **27**, 508 (1993)].
8. G. Dolino and D. Bellet, in *Properties of Porous Silicon*, Ed. by L. Canham (DERA, Malvern, UK, 1997), p. 118.
9. L. S. Il'inskaya and A. N. Podmar'kov, *Semiconductor Tensometers* (Énergiya, Moscow, 1966), p. 119.
10. E. V. Kuchis, *Galvanomagnetic Effects and Methods for Studying Them* (Radio i Svyaz', Moscow, 1990).
11. H. Gleskova, S. Wagner, and Z. Suo, J. Non-Cryst. Solids **266–269**, 1320 (2000).

Translated by A. Spitsyn

Semiconductors, Vol. 38, No. 5, 2004, pp. 598–602. Translated from Fizika i Tekhnika Poluprovodnikov, Vol. 38, No. 5, 2004, pp. 621–625.

AMORPHOUS, VITREOUS, AND POROUS SEMICONDUCTORS

ESR Studies of Nanocrystalline Silicon Films Obtained by Pulsed Laser Ablation of Silicon Targets

V. Ya. Bratus*, S. M. Okulov, É. B. Kaganovich, I. M. Kizyak, and É. G. Manoilov

Lashkarev Institute of Semiconductor Physics, National Academy of Sciences of Ukraine, Kiev, 03028 Ukraine

**e-mail: dept_5@isp.kiev.ua*

Submitted September 11, 2003; accepted for publication October 17, 2003

Abstract—Nanocrystalline silicon films formed using laser ablation of silicon targets were studied using electron spin resonance. The measurements were performed in the *X* band with modulation of the magnetic field at a frequency of ~100 kHz at temperatures of 300 and 77 K. Two types of spectra were observed. The first type of spectra is related to the high concentration of dangling silicon bonds in Si nanocrystals and SiO_x sheaths of nanocrystals and are inherent in nanocrystalline silicon (*nc*-Si) films that do not exhibit photoluminescence in the visible region of the spectrum. The second type of spectra is related to the presence of *E*' centers, nonbridging oxygen hole centers (NBOHC), and peroxide radicals and is characteristic of films with photoluminescence in the visible region of the spectrum, which indicates that high-barrier SiO_2 layers exist in these films. An increase in the photoluminescence intensity and a decrease in the signal of electron spin resonance were observed in porous *nc*-Si films exposed to atmospheric air for a long time. *© 2004 MAIK "Nauka/Interperiodica".*

1. INTRODUCTION

After reports on the observation of intense photoluminescence (PL) in the visible region of the spectrum at room temperature in porous silicon (*por*-Si) obtained by anodization [1, 2], a large number of publications concerned with both the clarification of the emission mechanism and the search for new methods for producing PL-active nanostructures based on silicon have appeared. Among these materials is nanocrystalline silicon (*nc*-Si), which is a nanocomposite (a nanoheterostructure) in which the Si nanocrystals are embedded in the SiO_x matrix ($1 < x \leq 2$). The *nc*-Si films can be obtained by various methods; among them, the well-developed method based on laser ablation of silicon targets has distinct advantages when composite structures are formed. This method features a high vacuum purity; in addition, the composition and structure of the films can be controlled by varying the laser-radiation parameters, the composition and pressure of the reactive or inert gas in the chamber, the target composition, and other parameters [3–5]. The following has been established: the origin of visible PL in the materials under consideration is related to the quantum-confinement effect and the effect of dielectric enhancement; recombination of charge carriers is controlled by annihilation of electron–hole excitations in quantum dots (QDs) and by kinetically coupled subsystems of excitons and electron–hole pairs in quantum wires; and the PL intensity is governed to a great extent by the degree of suppression of the nonradiative-recombination channel. It is well known that the main channel for nonradiative recombination is related to the presence of dangling silicon bonds at the surface of Si nanocrystals. There is no definitive conception of specific mechanisms of radiative recombination (for example, for quantum wires, the mechanisms related to the annihilation of free excitons, self-localized excitons, or those localized at the Si–O bonds), the mechanisms of Auger recombination with the involvement of local states, and other processes in relation to the production conditions and structure of the films. Nanocrystals are difficult to study because their dimensions are 1–5 nm, the area of internal Si/SiO_x surface is large, and the defects both in the interface region and in the SiO_x shell of a nanocrystal are diverse. In this context, it is very important to ascertain the spectrum of defect-related states in photoluminescent *nc*-Si films and the relationship between this spectrum and the conditions of formation of the film in order to gain insight into both the recombination mechanisms in these films and the mechanisms of formation of the films under consideration.

Electron spin resonance (ESR) makes it possible to determine the defect types in single-crystal Si (*c*-Si), amorphous Si (*a*-Si), SiO_x films, and interfaces. A brief review of ESR studies of nanosized Si/SiO_2 heterostructures that exhibit PL in the visible region of the spectrum can be found in [6]. The complex structure of ESR spectra in *por*-Si and the difficulties in identifying the P_b centers at Si/SiO_2 nanocrystal boundaries due to the random orientation of Si nanocrystals in *nc*-Si films were mentioned [6]. Nevertheless, an anticorrelation between the P_b-center concentration in *por*-Si and the PL intensity was observed. There are a number of publications concerned with measurements of ESR spectra in *por*-Si obtained by anodization (see, for example, [7]) and by staining chemical etching [8], as well as in *nc*-Si films with Si and Ge QDs obtained by implantation of Si and Ge ions in SiO_2 [9, 10]. However, as far as we

know, there have been no publications on ESR studies of *nc*-Si films obtained using the laser ablation of Si targets.

The aim of this study was to identify the main types of paramagnetic defects and gain insight into their evolution in *nc*-Si films whose conditions of formation and luminescent properties have been investigated previously (see, for example, [5, 11–14]).

2. EXPERIMENTAL

The films with Si nanocrystals in a SiO_x matrix were obtained by pulsed laser deposition using ablation of an *c*-Si target exposed to the radiation of a YAG:Nd^{3+} laser with a wavelength of 1.06 μm. The laser operated in the *Q*-switched mode; the energy in a pulse was ~0.2 J, the pulse width was 10 ns, and the pulse-repetition rate was 25 Hz [5, 11–14]. Films of type I were deposited from the direct high-energy flux of particles of the erosion plume onto a substrate that was 15–30 mm from the target along the normal. We used argon as the buffer gas and oxygen as the reactive gas; the gas pressure was varied from 0.039 to 32 Pa. Films of type II were deposited from the inverse flow of low-energy particles onto the substrate positioned in the target planet. The deposition was carried out in an Ar atmosphere at a pressure of ~13 Pa, which was optimal for producing films with intense PL. Pyroceram and mica platelets with an area of 15×15 mm^2 were used as substrates. We also formed *nc*-Si films of both types by using an Si target with an ~80-nm-thick Au film deposited on the target surface. The thickness of the *nc*-Si films was ~0.9 μm. In order to increase the ESR signal intensity, we cut the sample into four strips with an area of 3.75×15 mm^2; these strips were then glued to each other.

We studied the ESR in the *X* band at temperatures $T = 300$ and 77 K; the magnetic field B was modulated at the frequency $\nu_H = 100$ kHz. We determined the number of paramagnetic defects and the value of the *g*-factor from comparison with the ESR of a standard MgO:Mn^{2+} sample with a known number of spins; this sample was placed in the cavity along with the sample under investigation. The error in determining the number of defects in these measurements was ~40%; the relative error in comparing the ESR signals from different samples was no larger than ~15%.

3. RESULTS AND DISCUSSION

It was ascertained from the measurements that the intensity and shape of ESR spectra depend on the conditions of deposition of *nc*-Si films (Fig. 1). For the type-I films deposited in an oxygen atmosphere under its residual or higher (~15 Pa) pressure, a symmetric line with a Gaussian shape is dominant in the spectrum; the value of the *g*-factor for this line varies from 2.0029 to 2.0055 at the point of intersection with the base line, while the linewidth varies from 1.3 to 0.6 mT (Fig. 1, curves *1* and *2*, respectively) (the spectrum of the first type). A completely different shape of ESR spectrum

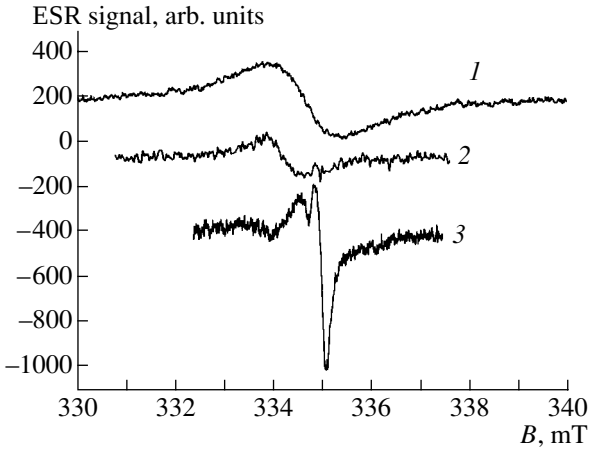

Fig. 1. ESR spectra of *nc*-Si films: (*1*, *2*) type-I films obtained at an oxygen pressure of (*1*) 0.039 and (*2*) 15 Pa and (*3*) type-II films. The spectra were measured at $\nu_H = 9.379$ GHz, $P_{mw} = 0.8$ mW, and $T = 300$ K. The ESR intensities are normalized to the unit volume of the sample.

(the spectrum of the second type) is observed for the type-I *nc*-Si films deposited at an oxygen pressure of ~6.5 Pa, which is optimal for attaining efficient PL. This spectrum is similar in shape to that of the type-II films and is a superposition of several lines (Fig. 1, curve *3*). The number of paramagnetic centers determined from comparison of integrated intensities of ESR lines for the sample under investigation and the standard sample was on the order of 10^{15} for as-prepared films. On the assumption that the defects are uniformly distributed over the film thickness, their concentration varies in the range $(1–6) \times 10^{18}$ cm^{-3}. We did not detect any difference between the ESR spectra of films doped with Au and those of undoped films deposited under identical conditions.

Measurements carried out at a microwave power of $P_{mw} > 1$ mW and at temperatures $T = 300$ and 77 K made it possible to identify the defects. The parameters of the broad ESR lines observed for the type-I films (Fig. 1, curves *1*, *2*) remain unchanged as temperature decreases. The intensities of these lines do not level off as the power P_{mw} increases to 50 mW. This behavior is characteristic of the ESR lines of dangling silicon bonds that are observed in crystalline and amorphous Si, where $g = 2.0055$ [15], and in amorphous SiO_x layers, where the *g*-factor varies from 2.0055 to 2.0006 as *x* increases from 0 to 2 [16]. The defects under consideration can be represented as $Si_3{\equiv}Si–$ (in Si) and $Si_2O{\equiv}Si–$ and $SiO_2{\equiv}Si–$ (in SiO_x).

An appreciable narrowing of the lines and the appearance of a number of pronounced features in the low-field portion of the spectrum are observed for the type-II films at $T = 77$ K (Fig. 2). As in the case of room temperature, a narrow line that is observed in the spectra of powders and may be associated with the values $g_{\|} = (2.0017 \pm 0.0001)$ and $g_{\perp} = (2.0000 \pm 0.0001)$ sat-

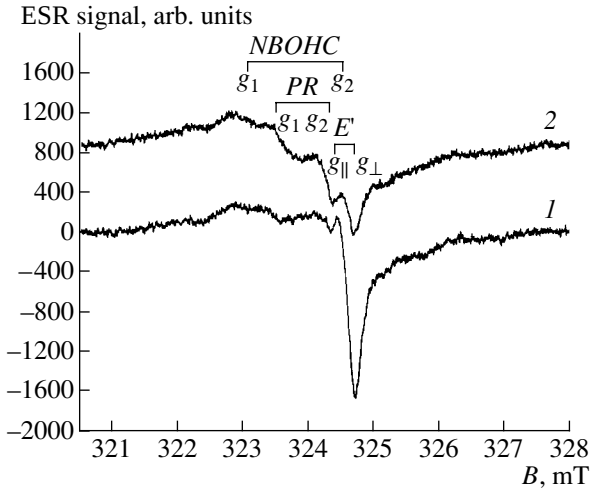

Fig. 2. ESR spectra of type-II *nc*-Si films measured at P_{mw} = (*1*) 0.8 and (*2*) 10 mW, ν_H = 9.089 GHz, and T = 77 K. Special features: $g_\parallel$ = 2.0017 and $g_\perp$ = 2.0000 (*E*' center, O_3≡Si–); g_1 = 2.0019 and g_2 = 2.0072 (*PR*, Si_3≡Si–O–O–); and g_1 = 2.0100 and g_2 = 2.0010 (*NBOHC*, O_3≡Si–O–).

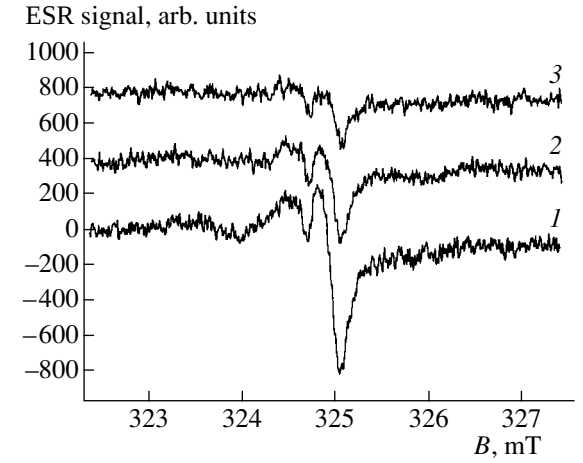

Fig. 3. ESR spectra of type-II *nc*-Si films (*1*) immediately after deposition and (*2*, *3*) after exposure to air for (*2*) 20 and (*3*) 90 h. The spectra were measured at ν_H = 9.379 GHz, P_{mw} = 0.8 mW, and T = 300 K.

urates easily with increasing P_{mw} (Fig. 2, curve *2*). This behavior and the parameters of the spectra are typical of *E*' centers [17], which are the dangling Si bonds in SiO_2 and have the configuration O_3≡Si–.

Other lines in the spectra (Fig. 2) increase in amplitude as the microwave power increases, which makes it possible to determine their positions accurately. The values of the *g*-factor (g_1 = 2.0019 ± 0.0002 and g_2 = 2.0072 ± 0.0002) determined for the spectrum designated as *PR* in Fig. 2 coincide to within the measurement accuracy with the corresponding principal values of the *g* tensor for peroxide radicals in SiO_2 [18, 19]. Due to the relatively low intensity of spectrum *PR*, we failed to detect the ESR signal in the region of magnetic fields that corresponded to $g_3 \approx 2.067$. Apparently, as in the case of fused-quartz glass irradiated with gamma-ray photons [18, 19], this portion of the *PR* spectrum has an amplitude that is lower by an order of magnitude owing to the appreciable broadening caused by the spread in the values of g_3. A peroxide radical is an O_2^- molecular ion connected to a single Si atom in the SiO_2 matrix; i.e., this radical has the configuration Si_3≡Si–O–O–.

The line detected with confidence at g_1 = 2.0100 ± 0.0002 and denoted as *NBOHC* in Fig. 2 can be assigned to the nonbridging oxygen hole centers and has the configuration O_3≡Si–O– [20]. Thus, depending on the deposition conditions, the defects are related both to the dangling bonds of Si atoms (*E*' centers) and to the dangling bonds of oxygen atoms (the *NBOHC* and *PR* centers).

It was found that the intensity of ESR spectra decreased by no more than 35% as a result of keeping the type-I samples for half a year in atmospheric air at room temperature. The ESR intensity decreases substantially for type-II *nc*-Si films under the same conditions of oxidation. As can be seen from Fig. 3, this behavior is mainly characteristic of the *E*' defects, whose ESR signal cannot be detected after exposure to air for a month. At the same time, the lines in the *PR* spectrum whose intensity is decreased severalfold can be detected even after a exposure to air for half a year. The intensity of ESR spectra for the *nc*-Si films of type II do not change if the samples are kept in liquid nitrogen.

Let us compare the results of studying the PL spectra [5, 11–14] with those of studying the ESR spectra reported here using the same *nc*-Si films. First of all, it is noteworthy that the ESR spectra for the films that exhibit PL and those that do not exhibit PL differ substantially. As shown by Kaganovich *et al.* [5], the type-I films whose ESR spectra are shown in Fig. 1 (curves *1*, *2*) do not exhibit PL. The absence of PL was attributed [5] to specific features of the type-I films grown in a vacuum chamber under a low residual pressure of oxygen. First, these films contain mostly large Si nanocrystals in which there is no quantum confinement of charge carriers and excitons. Second, the shells of such Si nanocrystals have the composition of low-barrier phase SiO_x with x = 1. The concentration of Si nanocrystals is negligible in the type-I films obtained under a high oxygen pressure; these films are amorphized SiO_x structures ($1 < x < 2$).

The ESR studies of these type-I films obtained under the aforementioned conditions are also indicative of both the presence of the SiO_x phase and the absence of the high-barrier SiO_2 phase. Moreover, a high concentration of dangling Si bonds was deduced from the ESR spectra. Therefore, the conditions for efficient radiative recombination are not satisfied even if a small number of Si nanocrystals are present in the film.

The ESR spectra of the second type (Fig. 1, curve *3*) were observed for the films that exhibited PL. These were the type-I films obtained under optimal oxygen pressure and the type-II films. According to data reported previously [5, 11–14], the PL excited by the radiation of a nitrogen laser is easily detected in the energy range 1.55–3.2 eV; the PL decay times are shorter than 50 ns.

The PL parameters of photoluminescent type-I films changed only slightly (if at all) as a result of exposure to air, whereas both the PL intensity and the PL decay time increased as a result of this exposure for photoluminescent type-II films. The different behavior of these two types of films was attributed to the fact that the porosity of type-I and type-II films differs considerably. According to ellipsometric data, the porosity amounts to several percent for type-I films and 20–40% for type-II films. The role of oxygen as a passivator of nonradiative-recombination centers and as an oxidizer of SiO_x shells ($x \le 2$) to phases with higher barriers due to the porosity of type-II films manifested itself when these films were exposed to air for some time. The results of ESR studies are consistent with the measurements of PL in the two types of films under consideration from the standpoint of the evolution of defects. The composition of defects in type-I films is stable, whereas the concentration of defects (especially, the *E*' defects, i.e., the dangling Si bonds in SiO_2) decreases sharply as a result of exposure to air. An increase in the PL intensity and a correlated decrease in the concentration of nonradiative-recombination centers are observed after *nc*-Si was exposed to air for some time.

According to the studies of PL in the *nc*-Si films of type II [11–14], doping these films with Au resulted in an increase in the PL intensity and stability and in an increase in the PL decay time by more than three orders of magnitude (to tens of microseconds). This phenomenon was attributed to the catalytic effect of the electropositive metal (gold) when the Si nanocrystals were oxidized and to passivation of dangling Si bonds in the course of the formation of the film.

According to the ESR spectra, there is no difference between undoped films and films doped with Au, neither in the defect composition nor in the number of defects in the form of dangling bonds. In order to explain this fact, we may assume that dopant Au atoms (similarly to O atoms) saturate the paramagnetic dangling Si bonds and transform them into diamagnetic bonds, although this explanation needs verification. Indeed, neutral centers containing electrons and acting as nonradiative-recombination centers interact with nonsaturated dangling Si bonds. An O (Au) atom captures this electron and saturates the dangling Si bond; as a result, a positively charged center of radiative recombination comes into existence. When the material is doped with Au, the number of *E*' centers can remain almost unchanged owing to an increase in the volume of oxide phase as a result of the catalytic effect of Au in the course of oxidation. The absence of differences in the defect composition between undoped films and the films doped with Au can also be caused by the structure of doped films. For example, the distribution of grains in sizes is more uniform in undoped *nc*-Si films than doped films, according to the data of atomic-force microscopy that are plotted in the form of a bar chart of probabilities for grains that have specific diameters. Only a single characteristic grain size is observed in undoped films, whereas there are several additional pronounced characteristic sizes with larger values in doped films. The appearance of the larger grain sizes is a result of the activation effect of Au on the crystallization process. The larger nonuniformity of the grain-size distribution in doped films indicates that the structure of these films is farther from equilibrium and, consequently, is more imperfect. The increased number of defects detected by ESR compensates for the decrease in the number of defects, which is conducive to an improvement in the photoluminescent characteristics of the films. It is noteworthy that the change in photoluminescent characteristics is also related to the effect of Au not only on the nonradiative component of recombination, but also on radiative recombination. As a result, we have a large variation in PL and an insignificant variation in the concentration of defects related to dangling Si bonds according to ESR spectra. Neither the origin of PL nor its mechanism change as a result of doping. Emission occurs as a result of the annihilation of electron–hole excitations in Si nanocrystals (zero-dimensional objects) [11–14]. It is worth noting that the *NBOHC* radiative-recombination centers are of no importance here.

4. CONCLUSIONS

(i) Two types of ESR spectra are observed for *nc*-Si films obtained using laser ablation of Si targets. The first type of spectra is observed for films that do not exhibit PL in the visible spectral region and indicates that there is a high concentration of dangling bonds in Si nanocrystals and the composition of the nanocrystal shell corresponds to SiO_x. The second type of spectra is observed only for films that exhibit PL in the visible spectral region. In these films, the *E*' centers, peroxide radicals, and nonbridging oxygen hole centers are detected, which indicates that Si nanocrystals are surrounded by SiO_2 high-barrier phase.

(ii) When type-I films deposited from direct flux of an erosion plume are aged in air, the defect spectrum remains unchanged according to the ESR data; the PL intensity does not increase. The same treatment of type-II films deposited from the inverse flow of erosion particles leads to both a decrease in the concentration of *E*' defects in the SiO_2 shell and a correlated increase in the PL intensity. This result is related to the high porosity of type-II films.

REFERENCES

1. V. Lehmann and U. Gösele, Appl. Phys. Lett. **58**, 1046 (1991).
2. L. T. Canham, Appl. Phys. Lett. **57**, 1046 (1990).
3. D. H. Lowndes, D. B. Geohegan, A. A. Puretzky, *et al.*, Science **273**, 898 (1996).
4. L. Patrone, D. Nelson, V. I. Safarov, *et al.*, J. Appl. Phys. **87**, 3829 (2000).
5. E. B. Kaganovich, A. A. Kudryavtsev, E. G. Manoĭlov, *et al.*, Thin Solid Films **349**, 298 (1999).
6. E. S. Demidov, V. V. Karzinov, and N. E. Demidova, in *Proceedings of the Conference on Nanophotonics* (Nizhni Novgorod, 2003), p. 48.
7. P. K. Kashkarov, E. A. Konstantinova, and V. Yu. Timoshenko, Fiz. Tekh. Poluprovodn. (St. Petersburg) **30**, 1479 (1996) [Semiconductors **30**, 778 (1996)].
8. M. Schoisswohl, J. L. Cantin, H. J. von Bardeleben, and J. Amato, Appl. Phys. Lett. **66**, 3660 (1995).
9. V. Ya. Bratus, M. Ya. Valakh, I. P. Vorona, *et al.*, J. Lumin. **80**, 269 (1999).
10. B. Garrido Fernandez, M. Lopez, C. Garcia, *et al.*, J. Appl. Phys. **91**, 798 (2002).
11. A. V. Sachenko, É. B. Kaganovich, É. G. Manoĭlov, and S. V. Svechnikov, Fiz. Tekh. Poluprovodn. (St. Petersburg) **35**, 1445 (2001) [Semiconductors **35**, 1383 (2001)].
12. É. B. Kaganovich, É. G. Manoĭlov, and S. V. Svechnikov, Ukr. Fiz. Zh. **46**, 1196 (2001).
13. É. B. Kaganovich, É. G. Manoĭlov, I. R. Bazylyuk, and S. V. Svechnikov, Fiz. Tekh. Poluprovodn. (St. Petersburg) **37**, 353 (2003) [Semiconductors **37**, 336 (2003)].
14. É. B. Kaganovich, I. M. Kizyak, S. I. Kirillova, *et al.*, Fiz. Tekh. Poluprovodn. (St. Petersburg) **36**, 1105 (2002) [Semiconductors **36**, 1027 (2002)].
15. M. H. Brodsky and R. S. Title, Phys. Rev. Lett. **23**, 581 (1969).
16. E. Holzenkampfer, F.-W. Richter, J. Stuke, and U. Voget-Grote, J. Non-Cryst. Solids **32**, 327 (1979).
17. W. L. Warren, E. H. Poindexter, M. Offenberg, and W. Muller-Warmuth, J. Electrochem. Soc. **139**, 872 (1992).
18. M. Stapelbroek, D. L. Griscom, E. J. Friebele, and G. H. Sigel, Jr., J. Non-Cryst. Solids **32**, 313 (1979).
19. R. A. Weeks, R. H. Magruder III, and P. W. Wang, J. Non-Cryst. Solids **149**, 122 (1992).
20. D. L. Griscom and E. J. Frieble, Phys. Rev. B **24**, 4896 (1981).

Translated by A. Spitsyn

Semiconductors, Vol. 38, No. 5, 2004, pp. 603–606. Translated from Fizika i Tekhnika Poluprovodnikov, Vol. 38, No. 5, 2004, pp. 626–629.

AMORPHOUS, VITREOUS, AND POROUS SEMICONDUCTORS

Specific Features of Electrical Transport in Anisotropically Nanostructured Silicon

P. A. Forsh, L. A. Osminkina, V. Yu. Timoshenko, and P. K. Kashkarov

Moscow State University, Moscow, 119992 Russia

Submitted October 27, 2003; accepted for publication November 4, 2003

Abstract—Electrical transport in layers of porous silicon obtained by electrochemical etching of (110)-oriented single-crystal silicon wafers of *p* type was studied. It was found that the lateral conductivity and photoconductivity of the layers along the $[1\bar{1}0]$ crystallographic axis substantially exceed those along the [001] axis. The results obtained are explained in terms of the effective-medium model, which takes into account the presence of potential barriers at boundaries of anisotropically shaped silicon nanocrystals. The exponential dependence of the conductivity of porous silicon on the square root of the applied voltage is interpreted in terms of the Poole–Frenkel effect. © *2004 MAIK "Nauka/Interperiodica".*

1. INTRODUCTION

Recently, porous silicon (*por*-Si) has attracted greater attention from researchers because of the prospects for using it in the development of optoelectronic devices, such as photoresistors, solar cells, light-emitting diodes, etc. Not long ago, it was discovered that *por*-Si exhibits a noticeable anisotropy [1–4]. For example, *por*-Si samples prepared on low-symmetry substrates, e.g., (110)-oriented wafers, show birefringence at normal incidence of light [2, 3, 5]. Until now, researchers have focused their attention mainly on the optical properties of systems of this kind. At the same time, in order to develop devices with optimal parameters on the basis of anisotropic *por*-Si, it is worthwhile analyzing the specific features of carrier transport in this material. In this study, the conductivity and photoconductivity along the $[1\bar{1}0]$ and [001] crystallographic directions of anisotropically nanostructured *por*-Si with a (110) surface orientation were examined. To analyze the influence exerted by the ambient conditions on the conductivity of *por*-Si, IR transmittance spectra were recorded together with electrical measurements.

2. EXPERIMENTAL PROCEDURE

The *por*-Si layers studied were obtained by electrochemical etching of (110)-oriented single-crystal p^{++}-Si:B wafers (ρ = 1.5 mΩ cm) in a 1 : 1 solution of HF (48%) with ethanol. The etching current density was 40 mA/cm^2, which corresponds to a 60% porosity of the sample. The resulting film was detached from the substrate by sharply raising the current density to 500 mA/cm^2 in the course of several seconds. The thickness of the detached porous silicon layers was approximately 50 μm. *por*-Si obtained by this method is composed of silicon nanocrystals about 10 nm in size, which are elongated along the $[1\bar{1}0]$ crystallographic axis [6].

For photoelectric measurements, aluminum contacts were deposited by vacuum evaporation onto the surface of the samples in two different configurations: in parallel with the $[1\bar{1}0]$ crystallographic axis (along which the nanocrystals are elongated) and perpendicularly to it (i.e., in parallel with the axis [001]). The interelectrode spacing was 0.1 mm. The temperature dependences of conductivity and photoconductivity were studied in the temperature range T = 120–410 K at a voltage of 5 V across the contacts of a sample. The photoconductivity was measured with a sample exposed to monochromatic light with photon energy $h\nu$ = 1.4 eV and intensity $I = 4 \times 10^{16}$ cm^{-2} s^{-1}. Transmittance spectra were recorded with a Perkin Elmer Spectrum RXI FT-IR Fourier spectrometer in the spectral range 500–4000 cm^{-1} with a resolution of 4 cm^{-1} at normal incidence of light.

3. EXPERIMENTAL RESULTS

Figure 1 shows transmittance spectra of *por*-Si with a (110) surface orientation, measured using unpolarized IR light. The transmittance spectra were recorded at room temperature in air (curve *1*), in a vacuum with a residual pressure $P = 10^{-3}$ Pa (curve *2*), and in a vacuum with a residual pressure $P = 10^{-3}$ Pa after annealing the sample at T = 135°C for 1 h (curve *3*). It can be seen that a noticeable difference between the transmittance spectra of *por*-Si samples obtained in different conditions is observed only in the spectral ranges 3300–3500 and 1600–1650 cm^{-1}, which correspond to absorption by O–H bonds in H_2O molecules. It follows from the figure that, when the residual vapor pressure in the mea-

1063-7826/04/3805-0603$26.00 © 2004 MAIK "Nauka/Interperiodica"

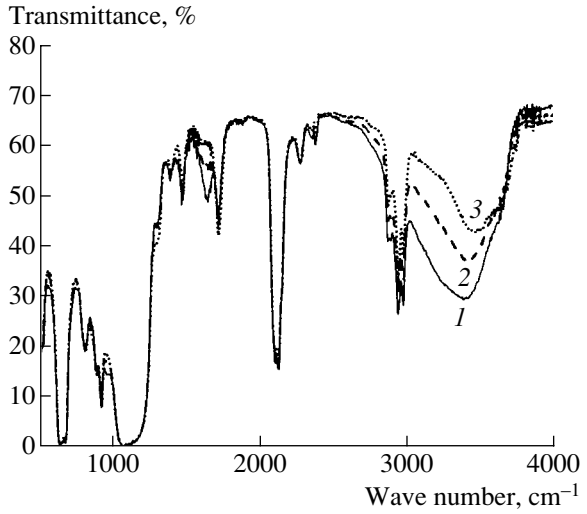

Fig. 1. IR transmittance spectra of *por*-Si measured at room temperature (*1*) in air, (*2*) in a vacuum at residual pressure $P = 10^{-3}$ Pa, and (*3*) in a vacuum at residual pressure $P = 10^{-3}$ Pa after annealing a sample at $T = 135$°C for 1 h.

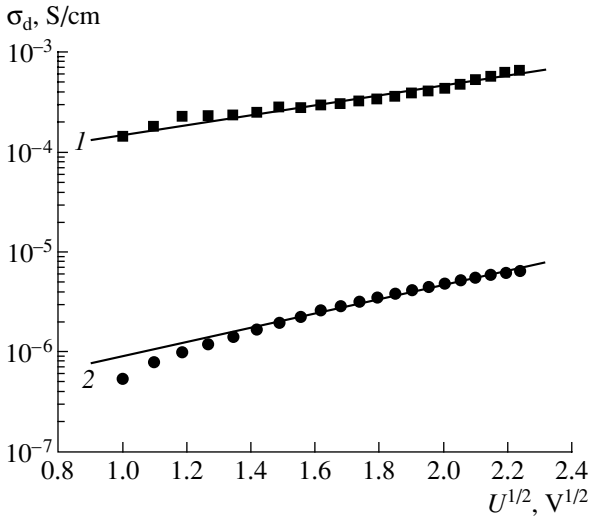

Fig. 2. (*1*) Longitudinal (along the $[1\bar{1}0]$ crystallographic axis) and (*2*) transverse (along the [100] crystallographic axis) conductivities of *por*-Si at room temperature vs. the square root of the applied voltage.

suring cell is lowered or a sample is thermally annealed in a vacuum, water molecules are desorbed from the surface of *por*-Si.

It was found that the dark conductivity σ_d, as well as the activation energy (E_A) of the temperature dependence of the conductivity of the *por*-Si samples under study (in both the direction $[1\bar{1}0]$ and the [001] directions), strongly depends on measurement conditions. As the residual vapor pressure is lowered, σ_d increases and its activation energy decreases. A further increase in the conductivity and a decrease in E_A occur when *por*-Si samples are annealed in a vacuum. The electrical properties of *por*-Si are stabilized on annealing the samples in a vacuum with a residual pressure $P = 10^{-3}$ Pa at $T = 135$°C for 1 h. Therefore, detailed studies of the dark conductivity and photoconductivity were carried out under precisely these conditions.

The measurements performed indicate that the conductivity of *por*-Si with a (110) surface orientation exhibits a nonlinear dependence on the voltage applied to a sample. Figure 2 shows how the dark conductivity measured along the $[1\bar{1}0]$ (longitudinal conductivity) and [001] (transverse conductivity) crystallographic directions depends on the square root of the applied voltage, $U^{1/2}$. It can be seen that the dark conductivity of *por*-Si exponentially depends on $U^{1/2}$ and that the longitudinal conductivity of *por*-Si substantially exceeds the transverse conductivity at any of the bias voltages used in the study.

The temperature dependences of the longitudinal and transverse conductivity of *por*-Si are shown in Fig. 3. It can be seen that the dependences $\sigma_d(T)$ are thermally activated in the entire range of temperatures studied, i.e., $\sigma_d(T) = \sigma_0 \exp(-E_A/kT)$, where σ_0 is the preexponential factor and k is the Boltzmann constant. The value of E_A for the longitudinal conductivity is 0.06 eV, which is substantially lower than the activation energy of the transverse conductivity (0.22 eV). The preexponential factor for the longitudinal conductivity is 0.006 Ω^{-1} cm^{-1}, which is nearly an order of magnitude lower than the value $\sigma_0 = 0.05$ Ω^{-1} cm^{-1} for the transverse conductivity. The fact that σ_0 increases as the activation energy becomes higher is in qualitative agreement with the Meyer–Neldel rule, which is in par-

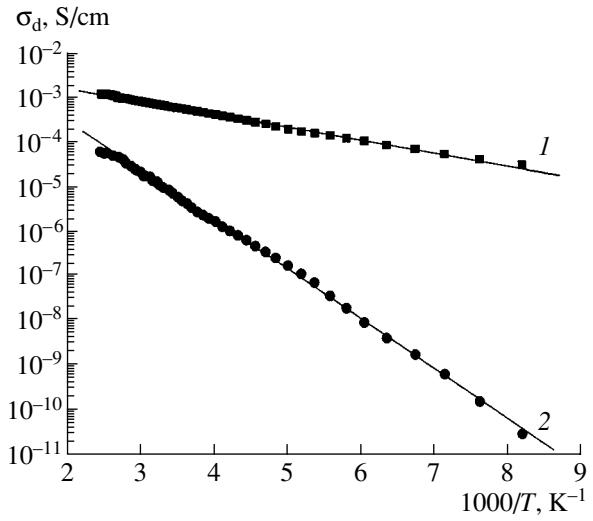

Fig. 3. Temperature dependences of (*1*) the longitudinal (along the $[1\bar{1}0]$ crystallographic axis) and (*2*) transverse (along the [100] crystallographic axis) conductivities of *por*-Si.

ticular characteristic of amorphous hydrogenated silicon, in which σ_0 exponentially grows with E_A [7]. It should be noted that the relative difference between the longitudinal and transverse conductivities is smaller at higher temperatures (Fig. 3).

We also studied the influence exerted by the anisotropy of the structure of *por*-Si on the photoconductivity σ_{ph}. Figure 4 shows temperature dependences of the longitudinal (along the $[1\bar{1}0]$ axis) and transverse (along the [001] axis) photoconductivity. It can be seen that the longitudinal photoconductivity exceeds the transverse photoconductivity in the entire range of temperatures studied. The relative difference between the longitudinal and transverse conductivities, as well as that between the longitudinal and transverse photoconductivities σ_{ph}, decreases as the temperature increases. It is also noteworthy that the difference between the longitudinal and transverse photoconductivities is smaller than that for the dark conductivity.

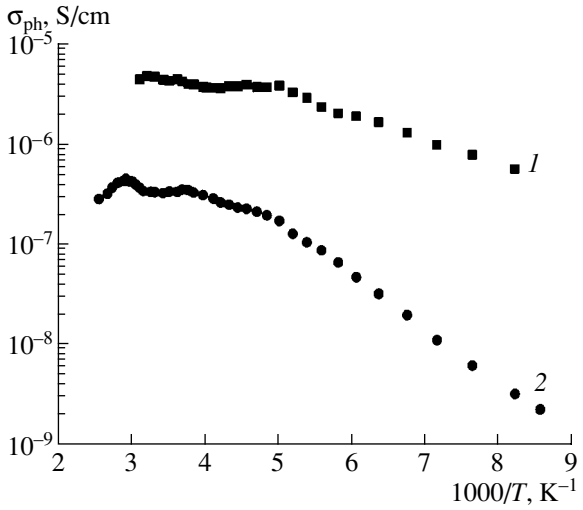

Fig. 4. Temperature dependences of (*1*) the longitudinal (along the $[1\bar{1}0]$ crystallographic axis) and (*2*) transverse (along the [100] crystallographic axis) photoconductivities of *por*-Si. The photoconductivity was measured with a sample exposed to light with photon energy $h\nu = 1.4$ eV and intensity $I = 4 \times 10^{16}$ cm^{-2} s^{-1}.

4. DISCUSSION

The exponential dependence of the dark conductivity on $U^{1/2}$ is characteristic of the Poole–Frenkel mechanism [8]. It is well known that the Poole–Frenkel effect consists in the fact that the probability of thermal ionization of Coulomb centers in solids increases under the action of an external electric field [8, 9]. In the case in question, the electric field may enhance the thermal ionization of impurity atoms and reduce fluctuations of the potential profile (barriers at boundaries of nanocrystals). This circumstance may lead to an increase in thermal emission of carriers across the potential barriers at the boundaries of nanocrystals. Previously, the Poole–Frenkel mechanism of conduction was observed in *por*-Si samples (in "sandwich" configuration) prepared from (100)-oriented *p*-type single-crystal silicon wafers [10]. It is noteworthy that, in the case of lateral contacts used in the present study, it is difficult to determine the parameters of the Poole–Frenkel mechanism because of the more complex geometric pattern of current transport in a sample.

The activation energy of the temperature dependence of the conductivity of the samples studied may be determined by the position of the Fermi level with respect to the top of the valence band and by the height of potential barriers that exist at the boundaries of nanocrystals and give rise to the thermally activated behavior of the mobility. The increase in σ_d on lowering the residual pressure in the cell or annealing the samples in a vacuum may be accounted for by desorption of water molecules from the internal surface of *por*-Si, as follows from the transmittance spectra in Fig. 1. As water molecules on the silicon surface exhibit donor properties [11], the desorption of water from the boundaries of nanocrystals leads to an increase in the density of free holes in the material. As a result, the conductivity increases and its activation energy decreases.

It is known that the anisotropy of optical properties of *por*-Si can be successfully accounted for in terms of the effective-medium model [4, 5]. Note that the effective-medium model can also be used to describe conduction in disordered systems [12]. However, correct use of this model for describing the conduction in *por*-Si requires that the presence of potential barriers at the boundaries of nanocrystals be taken into account. Apparently, the material has a certain distribution of potential barriers by height. As the length of the percolation path (constituted by silicon nanocrystals) in the $[1\bar{1}0]$ direction is shorter than that in the [001] direction owing to the shape anisotropy of nanocrystals, the average height of potential barriers in the $[1\bar{1}0]$ direction will also be lower than that in the [001] direction. This will lead to higher values of longitudinal conductivity and lower values of its activation energy compared to transverse conductivity.

The anisotropy of photoconductivity in *por*-Si observed in this study can be accounted for in a similar way. However, the density of free carriers in a sample exposed to light increases, and the height of potential barriers at the boundaries of nanocrystals decreases as a result of screening. Therefore, the difference between the longitudinal and transverse photoconductivities should be less pronounced than that between the longitudinal and transverse conductivities, and this is the case in the experiment (Figs. 3, 4).

5. CONCLUSION

Thus, it was demonstrated that the conductivities and photoconductivities of *por*-Si with a (110) surface orientation are different for the $[1\bar{1}0]$ and [001] directions. In the authors' opinion, this fact can be accounted for in terms of the effective-medium model if barriers at boundaries of nanocrystals, which give rise to the thermally activated behavior of the mobility, are considered. The dependence of the conductivity on the electric field produced by external voltage indicates that the Poole–Frenkel effect is observed in the *por*-Si samples studied.

ACKNOWLEDGMENTS

This study was financially supported by programs of the Ministry of Industry, Science, and Technology of the Russian Federation and by CRDF (U.S. Civilian Research and Development Foundation), project RT-2-2369-MO-02.

REFERENCES

1. M. E. Kompan, Ya. Salonen, and I. Yu. Shabanov, Zh. Éksp. Teor. Fiz. **117**, 368 (2000) [JETP **90**, 324 (2000)].
2. O. G. Sarbeĭ, E. K. Frolova, R. D. Fedorovich, and D. B. Dan'ko, Fiz. Tverd. Tela (St. Petersburg) **42**, 1205 (2000) [Phys. Solid State **42**, 1240 (2000)].
3. D. Kovalev, G. Polisski, J. Diener, *et al.*, Appl. Phys. Lett. **78**, 916 (2001).
4. V. Yu. Timoshenko, L. A. Osminkina, A. I. Efimova, *et al.*, Phys. Rev. B **67**, 113405 (2003).
5. L. P. Kuznetsova, A. I. Efimova, L. A. Osminkina, *et al.*, Fiz. Tverd. Tela (St. Petersburg) **44**, 780 (2002) [Phys. Solid State **44**, 811 (2002)].
6. N. Kunzner, D. Kovalev, J. Diener, *et al.*, Opt. Lett. **26**, 1265 (2001).
7. C. Popescu and T. Stoica, Phys. Rev. B **46**, 15063 (1992).
8. J. Frenkel, Phys. Rev. **54**, 647 (1938).
9. V. N. Abakumov, V. I. Perel', and I. N. Yassievich, *Nonradiative Recombination in Semiconductors* (Peterb. Inst. Yad. Fiz., Ross. Akad. Nauk, St. Petersburg, 1997).
10. M. Ben-Chorin, F. Moller, and F. Koch, Phys. Rev. B **49**, 2981 (1994).
11. V. F. Kiselev and O. V. Krylov, *Electronic Phenomena in Adsorption and Cathalists on Semiconductors and Dielectrics* (Nauka, Moscow, 1979; Springer, Berlin, 1987).
12. D. Stroud, Phys. Rev. B **12**, 3368 (1975).

Translated by M. Tagirdzhanov

Semiconductors, Vol. 38, No. 5, 2004, pp. 607–609. Translated from Fizika i Tekhnika Poluprovodnikov, Vol. 38, No. 5, 2004, pp. 630–633.

PHYSICS OF SEMICONDUCTOR DEVICES

Low-Threshold 1.3-μm Injection Lasers Based on Single InGaAsN Quantum Wells

V. A. Odnoblyudov, A. Yu. Egorov, M. M. Kulagina, N. A. Maleev, Yu. M. Shernyakov, E. V. Nikitina, and V. M. Ustinov

Ioffe Physicotechnical Institute, Russian Academy of Sciences, St. Petersburg, 194021 Russia

Submitted October 20, 2003; accepted for publication October 21, 2003

Abstract—The design of the active region in InGaAsN quantum well (QW) injection lasers is investigated. Long-wavelength (1.27–1.3 mm), low-threshold (<400 A/cm^2), and high-efficiency (>50%) lasing is obtained at room temperature from structures based on single InGaAsN QWs in GaAs or InGaAsN barrier layers. The principal parameters (threshold, temperature, power) of these lasers have been studied in the wide-stripe configuration. The characteristics of injection lasers with different designs of the active region are compared.

1. INTRODUCTION

The development of GaAs-based injection lasers for the 1.3-μm wavelength is a scientific and technological problem of current practical interest. These systems offer an alternative to InGaAsP/InP lasers. It is expected that they will serve as inexpensive elements for telecommunication systems and allow wide use of fiber-optic communication in local computer networks. The fundamental advantage of GaAs-based structures over InP structures is the possibility of epitaxial growing of vertical-cavity surface-emitting lasers (VCSELs) in a single growth cycle.

InGaAsN/GaAs quantum-well (QW) and InAs/InGaAs quantum-dot (QD) heterostructures are the main candidates to be used as an active region of GaAs-based injection lasers operating in the 1.3-μm range. Injection lasers, both those with Fabry–Perot resonators [1, 2] and VCSELs with distributed Bragg reflectors [3], with a lasing wavelength in the 1.3-μm range were successfully fabricated from both types of heterostructures.

Technological difficulties encountered in the growth of the quaternary compound InGaAsN have drawn attention to the study of different designs of the active region of QW InGaAsN lasers. These investigations are necessary in order to develop lasers that meet the requirements imposed on light emitters for fiber-optic communication lines.

There exist two principal designs of InGaAsN QW heterostructures emitting at 1.3 μm. The main difference is as follows. In the first case, a narrow-gap InGaAsN layer is inserted between GaAs layers, so that the band gap in the barrier layers corresponds to the GaAs band gap. In the other case, the barrier layers are produced from InGaAsN of another elemental composition, with a band gap that is narrower than in GaAs but wider than in the material of the QW. The insertion of InGaAsN QW between (In)GaAsN layers lattice-matched with GaAs allows one to vary the parameters (thickness and composition) of InGaAsN QWs, while the emission wavelength remains unchanged.

In course of our study, we thoroughly analyzed and optimized the parameters of MBE growth and tested various designs of the active region of injection lasers based on InGaAsN QWs in GaAs and InGaAsN matrices. A comparative analysis of the performance characteristics of these lasers has revealed a significant advantage of the approach based on the use of lattice-matched InGaAsN layers as the barriers for InGaAsN QWs. The lowest threshold current density of 390 A/cm^2 was achieved in the wide-stripe configuration with the cavity length of 2000 μm. The lowest transparency current for this structure was 190 A/cm^2. The external differential quantum efficiency for a device of this configuration (with a cavity length of 2000 μm) in pulsed mode was 50%. Furthermore, CW lasing with an efficiency of 48% was obtained. The temperature stability of the threshold current density and lasing wavelength was studied for both types of lasers.

2. EXPERIMENT

The structures were grown in an EP-1203 MBE machine equipped with an Epi Unibulb RF Plasma Source of nitrogen and a solid-state As source. The active region was grown at 400°C. A laser structure included a 1.5-μm-thick $Al_{0.35}Ga_{0.65}As$ emitter and a 0.5-μm-thick GaAs waveguide. InGaAsN QWs in GaAs (structure no. 1) or InGaAsN (structure no. 2) barrier layers served as the active region. The growth process was monitored by means of the high-energy electron diffraction (HEED).

The laser structures were used to fabricate stripe devices with a stripe width of 100 μm and various cav-

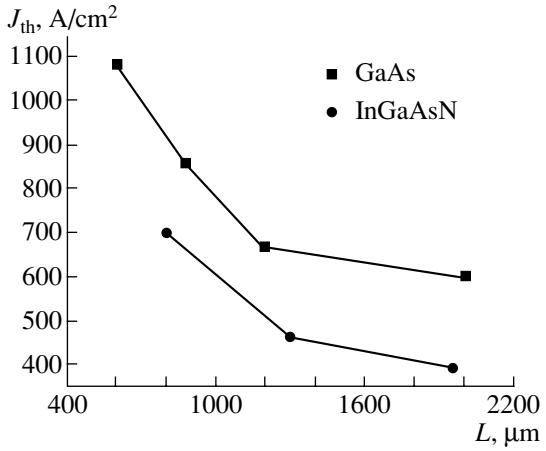

Fig. 1. Threshold current density J_{th} vs. the cavity length L for lasers produced from structure no. 1 (GaAs barriers) and no. 2 (InGaAsN barriers).

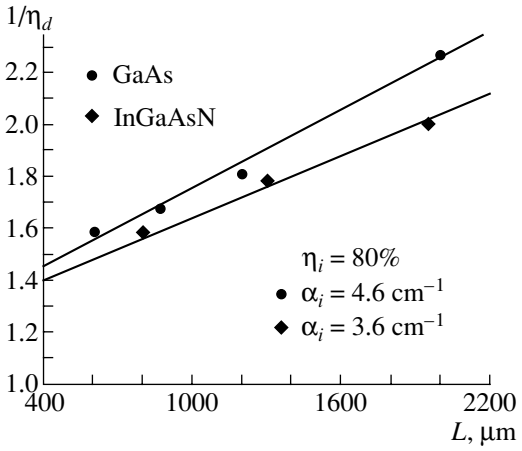

Fig. 2. Inverse differential quantum efficiency $1/\eta_d$ vs. the cavity length L for lasers produced from structure nos. 1 and 2. Points represent experimental data; lines, approximation.

ity lengths (L = 600–2000 μm). The characteristics of stripe lasers were measured with pulsed injection pumping with a pulse width of 0.2 μs and a 1-kHz repetition rate. CW lasing was obtained with a stabilized heat-sink temperature.

3. RESULTS AND DISCUSSION

Figure 1 shows experimental dependences of the threshold current density J_{th} on the cavity length L for lasers based on InGaAsN QWs in GaAs and InGaAsN barrier layers. As can be seen in the figure, the threshold current density in lasers produced from structure no. 2 is lower than in those from structure no. 1 in all the range of cavity lengths. The lowest threshold current density of 390 A/cm^2 was achieved in a laser with a cavity length of 1950 μm. This value ranks among the best reported data on the threshold current density for InGaAsN QW lasers operating at wavelengths of about 1.3 μm. A threshold current density of 600 A/cm^2 was obtained in a device with the same cavity length of 1950 μm produced from structure no. 1.

Figure 2 shows experimental dependences of the inverse differential quantum efficiency $1/\eta_d$ as functions of the cavity length L for lasers produced from structures nos. 1 and 2. For all the cavity lengths, the external differential quantum efficiency of the devices produced from structure no. 2 is higher. For a 1950-μm cavity, η_d was 50%. The maximum $1/\eta_d$ = 64% was obtained in a 800-μm cavity. Internal loss α_i in lasers produced from structures nos. 1 and 2 was calculated from the experimental dependences of η_d on the cavity length. With InGaAsN QWs in GaAs barriers used as the active region, the internal loss was α_i = 4.6 cm^{-1}. The use of InGaAsN barriers lattice-matched with GaAs reduced the internal loss to α_i = 3.6 cm^{-1}. The internal differential efficiency was the same in both types of structures, η_i = 80%.

Thus, the use of InGaAsN barriers allowed us to significantly reduce the threshold current density, raise the external differential quantum efficiency, and reduce the internal loss.

CW lasing in both types of structures was demonstrated at a heat-sink temperature stabilized at 15°C. Figure 3 shows experimental dependences of the total output optical power as functions of the driving current for lasers with a 2000-μm cavity. A threshold current density of 420 A/cm^2 and an efficiency of 0.47 W/A were obtained in a laser produced from structure no. 2. The corresponding data for a laser produced from structure no. 1 were 550 A/cm^2 and 0.39 W/A.

In lasers produced from structures no. 1 and 2, we also studied the temperature stability of the threshold current density and lasing wavelength. Figure 4 shows these experimental dependences for lasers with a 2000-μm cavity. The characteristic temperature T_0 for

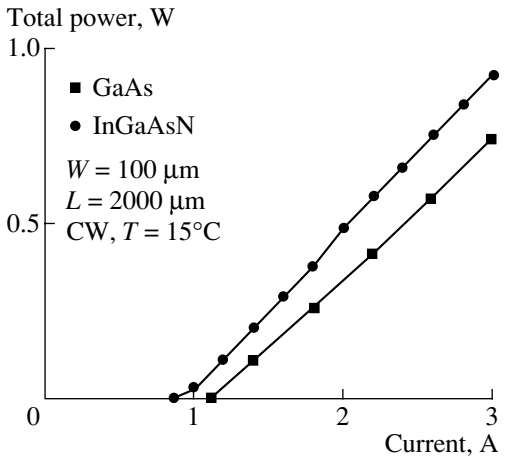

Fig. 3. Total output optical power in the CW mode vs. the driving current in lasers produced from structure nos. 1 and 2.

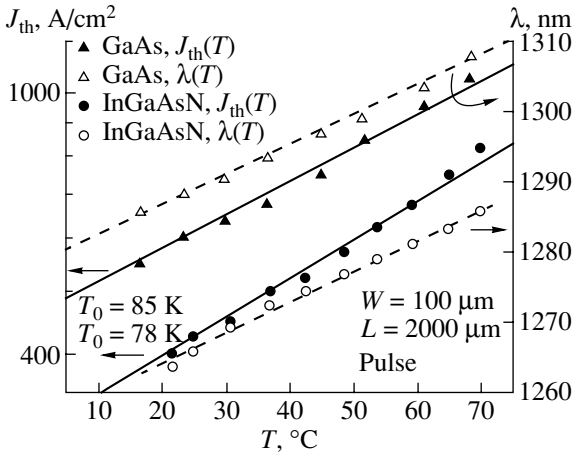

Fig. 4. Temperature dependences of the threshold current density J_{th} and lasing wavelength λ in lasers produced from structure nos. 1 and 2. Full symbols stand for experimental data for $J_{th}(T)$; open symbols, for λ(T). Lines represent approximation.

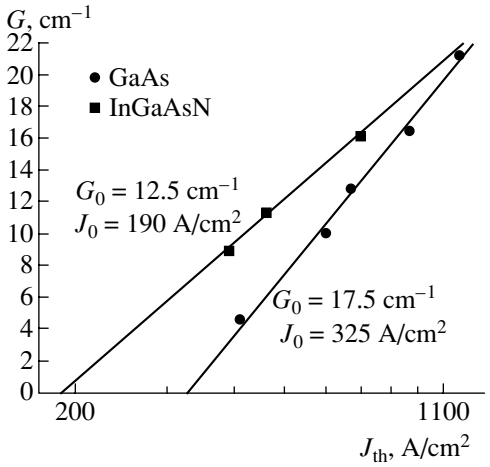

Fig. 5. Gain G vs. the threshold current density J_{th} for lasers produced from structure nos. 1 and 2. Points represent experimental data; lines, approximation.

lasers based on InGaAsN QWs in GaAs and InGaAsN barriers was 85 and 78 K, respectively. Changing the barrier material from GaAs to InGaAsN resulted in a small decrease in the characteristic temperature. However, the temperature dependence of the lasing wavelength for both types of lasers is the same, with the coefficient $\Delta\lambda/\Delta T$ = 0.43 nm/K.

Based on the measured dependences of the differential efficiency and threshold current density on the cavity length, we calculated the dependences of gain G on J_{th} for lasers produced from structures no. 1 and 2; $G(J_{th})$ are presented in Fig. 5. We calculated the gain G_0 and the transparency current density J_0 from $G(J_{th})$. These values were, for lasers based on structures no. 1, G_0 = 17.5 cm^{-1} and J_0 = 325 A/cm^2; for no. 2, 12.5 cm^{-1} and 190 A/cm^2, respectively. The use of InGaAsN barrier layers lattice-matched with GaAs led to a significant reduction in the transparency current density compared to the case of GaAs barrier layers but resulted in the depression of the gain. The minimal value achieved (J_0 = 190 A/cm^2) ranks among the best data reported.

4. CONCLUSION

The characteristics of injection lasers based on InGaAsN QWs inserted between GaAs or InGaAsN barrier layers were studied. Pulsed and CW lasing was obtained in devices produced from both types of structures. The use of InGaAsN barriers in the active region of a laser reduces the threshold current density and the transparency current density by a factor of ~1.5 and raises the external differential efficiency. These trends are accompanied by a slight decrease (by ~5–7 K) in the characteristic temperature T_0 of lasers based on structure no. 2 and a decrease in gain G_0.

ACKNOWLEDGMENTS

This study was supported by the "Physics of Solid-State Nanostructures" program of the Ministry of Industry, Science, and Technology of the Russian Federation, the Russian Foundation for Basic Research, and the NATO Science for Peace Program (SfP).

V.M. Ustinov acknowledges the support of the Russian Science Welfare Social Fund.

REFERENCES

1. V. M. Ustinov and A. E. Zhukov, Semicond. Sci. Technol. **15**, R41 (2000).
2. A. Yu. Egorov, D. Bernklaua, B. Borchert, *et al.*, J. Cryst. Growth **227–228**, 545 (2001).
3. N. A. Maleev, A. Yu. Egorov, A. E. Zhukov, *et al.*, Fiz. Tekh. Poluprovodn. (St. Petersburg) **35**, 881 (2001) [Semiconductors **35**, 847 (2001)].

Translated by D. Mashovets

Semiconductors, Vol. 38, No. 5, 2004, pp. 610–614. Translated from Fizika i Tekhnika Poluprovodnikov, Vol. 38, No. 5, 2004, pp. 634–638.

PHYSICS OF SEMICONDUCTOR DEVICES

Kinetics of Electroluminescence in an Efficient Silicon Light-Emitting Diode with Thermally Stable Spectral Characteristics

A. M. Emel'yanov*, Yu. A. Nikolaev*, N. A. Sobolev*^, and T. M. Mel'nikova**

**Ioffe Physicotechnical Institute, Russian Academy of Sciences, Politekhnicheskaya ul. 26, St. Petersburg, 194021 Russia*

^e-mail: nick.sobolev@mail.ioffe.ru

***NPO Orion, Moscow, 111123 Russia*

Submitted July 4, 2003; accepted for publication November 4, 2003

Abstract—The kinetics of the rise and decay of electroluminescence in an efficient silicon light-emitting diode that is formed by diffusion and features a high thermal stability of spectral parameters of electroluminescence in the region of band-to-band transitions is studied for various injection currents. The parameters of the electroluminescence kinetics are compared with effective lifetimes of minority charge carriers and characteristics of the current kinetics. It is found that the onset of a sharp rise in the electroluminescence intensity is delayed with respect to the instant when the voltage is applied to the diode; the results of measuring the emission distribution over the diode area are reported. © *2004 MAIK "Nauka/Interperiodica".*

1. INTRODUCTION

The growing interest in the electroluminescence (EL) of indirect-gap semiconductors is caused by recent reports [1, 2] on the fabrication of silicon light-emitting diodes (LEDs) in which the quantum efficiency of the band-to-band EL at room temperature was almost as high as that for LEDs based on direct-gap semiconductors. Since it was previously believed that a high quantum efficiency is unattainable for single-crystal silicon, the effects of various technological factors and operation conditions for silicon LEDs in the region of band-to-band recombination have not been studied in detail. Such studies are important not only for designing efficient silicon LEDs with emission in the band-to-band region but also for improving the efficiency of silicon-based LEDs and studying the mechanisms of excitation–deexcitation of these LEDs where the emission occurs with photon energies that are smaller than the band gap. Specifically, the latter silicon LEDs include those in which the EL is caused by excitation of impurity centers (for example, Er^{3+} or Ho^{3+} ions [3–5]), centers related to extended defects (dislocations and oxygen precipitates [6–9]), and nanostructures [10]. The data on band-to-band EL in silicon at room temperature published so far (in addition to [1, 2], see also [11–19]) do not give a complete and clear conception of the aforementioned phenomenon, mainly because a comprehensive approach to research on these LEDs, in particular, to studies of the EL parameters and various electrical and structural characteristics of the LEDs, is lacking. For example, Green *et al.* [1] did not study the EL kinetics, the current dependence of the lifetime (τ_p) of minority charge carriers in the LED, and the structural defects in the optically active region of the diode. It is also worth noting the research in [2], where dislocation loops were observed in the active region of a Si LED. A high attained quantum yield was related to these dislocations [2]; however, the lifetime τ_p and the kinetics of the EL rise and decay at different currents were not measured. The kinetics of the band-to-band EL for a commercial silicon diode was studied recently in considerable detail [11]. However, not only complete data on the technology and structural defects in the studied devices were lacking, but also the results of measurements of the lifetime of the minority charge carriers for various currents were not reported [11].

In [20] we began to describe the results of comprehensive research into an efficient silicon LED (the internal quantum efficiency was no lower than 0.1% at room temperature) for which an unprecedentedly high thermal stability of both the band-to-band EL intensity at the maximum of distribution over the wavelengths and the position of this maximum was observed [20]. In this paper, we continue to report the results of further studies in this field and concentrate on gaining insight into the EL kinetics and related electrical parameters of the diode.

2. EXPERIMENTAL

The diodes under investigation were produced using planar technology on the basis of a ~350-μm-thick wafer of *n*-Si with a dopant concentration of $\sim 6 \times 10^{13}$ cm^{-3}. After final rinsing in an ammonium–peroxide solution, the wafer was oxidized in the atmosphere of wet oxygen for 2 h at a temperature of 1150°C. The *p–n* junctions were formed by boron diffusion through 2×2 mm^2 windows in the oxide film. Two stages of diffusion were used: predeposition diffusion for 1 h at

1063-7826/04/3805-0610$26.00 © 2004 MAIK "Nauka/Interperiodica"

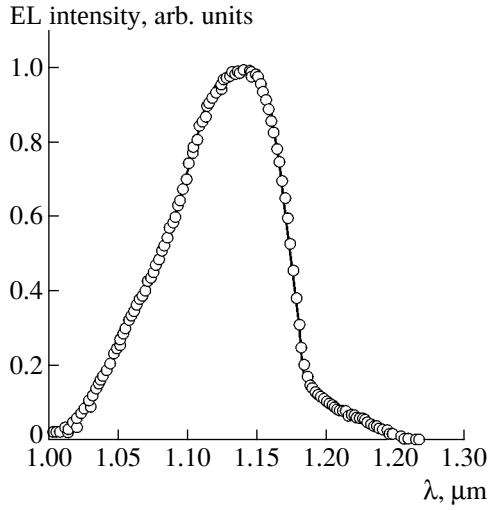

Fig. 1. Electroluminescence (EL) spectrum of a Si light-emitting diode at a temperature of 300 K and a current of 100 mA.

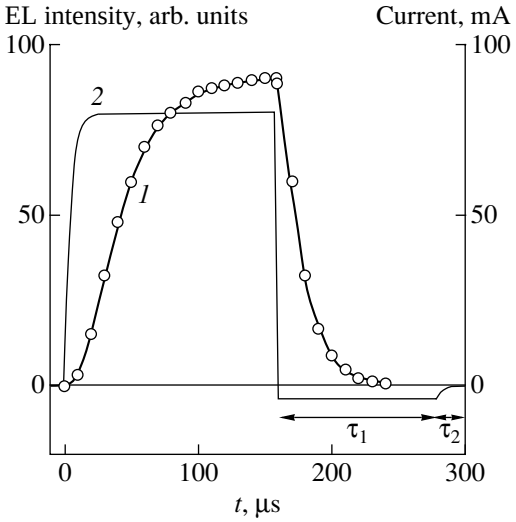

Fig. 2. (*1*) Kinetics of electroluminescence (EL) and (*2*) the corresponding current pulse at 300 K and a current-pulse amplitude of 80 mA.

950°C from boron nitride and drive-in diffusion for 2 h at 1150°C in an atmosphere of dry oxygen. The layer of borosilicate glass was removed using a special etchant before drive-in diffusion of boron. After the oxide film was removed from the rear side of the wafer and after final rinsing, the wafer was additionally doped with phosphorus from PCl_3 for 1 h at 1000°C in a nitrogen atmosphere. Ohmic contacts were formed by sputtering of Al in vacuum without additional fusing. A continuous Al layer was deposited onto the rear side of the wafer; the contact on the front side was formed using photolithography and had the form of a thin strip along the perimeter of the *p–n* junction area. Emission from the central part (unshielded by metal) of the *p–n* junction was focused using a lens system either onto the entrance slit of an MDR-23 monochromator (when the EL was measured) or onto the entrance window of an FD-10 AG germanium photodiode (when the quantum efficiency or the EL kinetics were measured). The radiation outgoing from monochromator was detected using an uncooled InGaAs photodiode and a selective nanovoltmeter. In order to excite the EL in the forward-current mode, we used a pulsed voltage with pulse rise and fall times shorter than 0.5 μs and a pulse-repetition rate of 32 Hz. The time constant of the detection system was equal to 2.7 μs in measurements of the EL rise and decay times.

The lifetimes of charge carriers were determined using the method suggested by Lax and Neustadter [21]. Provided the condition $0.1 < J_1/J_0 < 1$ is satisfied, the value of τ_p is calculated with the following simplified formula [22]:

$$\tau_p \approx t_1 J_1 / 0.2 J_0. \quad (1)$$

Here, J_0 is the amplitude of the forward-current pulse, J_1 is the amplitude of the part of the reverse-current pulse that corresponds to a high reverse conductance of the diode, and t_1 is the duration of this part of the pulse. It is also worth noting that, according to [23], the effect of the electric field on the results of measuring τ_p by the employed method [21] at a high injection level can be disregarded owing to the low concentration of doping impurity in the *n*-type region. This field arises as a result of gradual variation in the impurity concentration in a diffused *p–n* junction.

3. RESULTS AND DISCUSSION

The EL spectrum measured at $T = 300$ K is shown in Fig. 1. The resolution of the monochromator amounted to 3 nm. The spectrum was corrected for spectral characteristics of both the photodetector and the entire optical system; the shape of the spectrum is characteristic of indirect (with involvement of phonons) band-to-band transitions in single-crystal silicon. Microscopy studies of angle laps of the samples using selective etching showed that there were no dislocations and nor any other extended defects in the base. As a result, dislocation-related lines in the wavelength range $\lambda = 1.0$–1.6 μm were not observed in the EL spectra. The position of the peak in the EL spectrum of the sample under investigation (at $\lambda = 1.136$ μm) was independent of current in the entire range of currents under consideration (20–500 mA).

The EL kinetics at 300 K for the current pulse with an amplitude of 80 mA is illustrated in Fig. 2; the time dependence of the current is also shown. The point in time $t = 0$ corresponds to the onset of the voltage pulse. It can be seen that there is a time lag in the onset of the sharp increase in EL with respect to $t = 0$; as a result, the kinetics of the rise in EL is significantly nonexponential. In Fig. 3, we show the EL time dependences

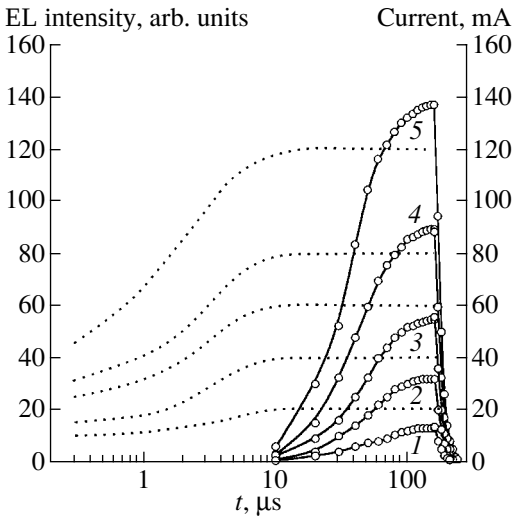

Fig. 3. Electroluminescence (EL) kinetics of a Si light-emitting diode at 300 K and currents of (*1*) 20, (*2*) 40, (*3*) 60, (*4*) 80, and (*5*) 120 mA (solid lines); dotted lines represent the corresponding current pulses.

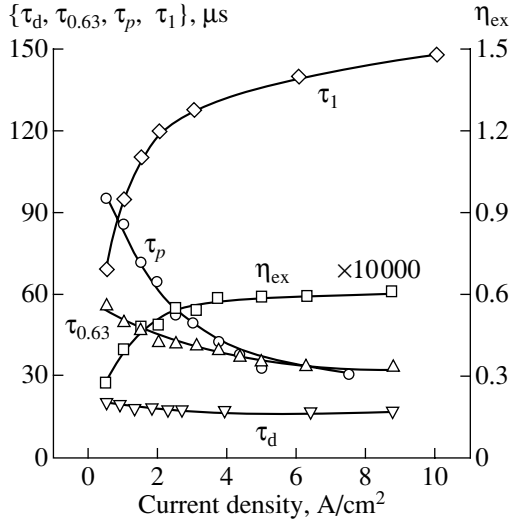

Fig. 4. Dependences of the time constant of the electroluminescence (EL) decay (τ_d), the time of the rise in EL intensity to $0.63I_m$ ($\tau_{0.63}$), the lifetime of minority charge carriers (τ_p), the external quantum efficiency (η_{ex}), and the time of existence of reverse current until it sharply decreases (τ_1) on the average current density.

measured at various amplitudes of current pulses and plotted using a logarithmic scale of the time axis. It can be seen from Fig. 3 that the onset of the sharp increase in the EL intensity in silicon LED correlates with the attainment of a steady-state current. The time lag of the rise in current with respect to voltage in diodes is typically caused by modulation of the base resistance in a diode [23]. Apparently, this effect also takes place in the diode under investigation and causes the time lag between the onset of the sharp increase in the EL intensity and the instant that corresponds to the application of a voltage pulse. The kinetics of the EL decay is adequately described using an exponential function with the decay constant τ_d. The dependence of τ_d on the average current density j (obtained by dividing the current by the area of the p–n junction) is shown in Fig. 4. It is noteworthy that the independence of the time of decay of EL intensity to zero from the current-pulse amplitude was also reported for the diode studied by Dittrich *et al.* [11]. As in [11], we observed a decrease in τ_d in the diode under investigation as a result of feeding a reverse voltage (V_R) to the diode immediately after termination of the forward-current pulse. However, the relative decrease in the EL decay time after the reverse biasing of the diode with $V_R = 0.5$ V was larger in [11] than in this study. The promotion of the EL decay as a result of biasing the diode with a reverse voltage after the forward-current pulse may be related to the widening of the space-charge region (SCR). An electric field in SCR is conducive to a rapid exit of minority charge carriers from the base and the cessation of EL. In order to relieve the diode base of charge carriers injected by forward current, it is necessary that the depth of penetration of these carriers into the base does not exceed the SCR width after cessation of the forward current. It is well known [23] that the above depth decreases as both the diffusion length of minority charge carriers and the duration of the forward-current flow decrease. All other factors being the same, the diffusion length decreases as the lifetime of minority charge carriers decreases, whereas the SCR width increases as both the concentration of the doping impurity in the base and the reverse voltage decrease. The difference between the aforementioned parameters may be the main reason for the differences between the effect of reverse voltage on the EL decay kinetics in this study and in [11]. It is noteworthy that the interband-EL decay time measured experimentally in [11] was ~0.1 μs. This value does not apparently represent the limiting response speed for Si LEDs with a band-to-band emission spectrum; the time it took to attain a steady-state forward current for the diode studied in [11] was no longer than 0.5 μs. Apparently, the small value of this quantity gave no way of measuring the time lag between the onset of the sharp increase in the EL intensity and the instant the voltage pulse was applied. The experimental data of our studies suggest that feeding the LED in the current-generator mode can be used to eliminate the time lag between the onset of the sharp increase in the interband EL intensity and the instant of biasing the Si LED with a forward-voltage pulse.

Since the kinetics of the rise in EL intensity in the diode under investigation was clearly not exponential, we used the time interval $\tau_{0.63}$ to evaluate the rate of the rise in EL; during this period, the PL intensity attained the value $0.63I_m$ (I_m is the maximum EL intensity). The results of measuring the quantity $\tau_{0.63}$ at various current densities j are shown in Fig. 4; the current-density dependence of the lifetime of minority charge carriers τ_p

determined using formula (1) is also shown. Variations in the quantities τ_p and $\tau_{0.63}$ are generally similar: both decrease with increasing current; however, the dependences $\tau_p(j)$ and $\tau_{0.63}(j)$ differ significantly from each other at relatively low current densities. Reverse current flows through the diode after the forward-bias voltage from an external source is switched off. The reverse current is caused by the exit of minority charge carriers to the external circuit; these carriers are accumulated in the diode base during the forward-current flow [23]. As can be seen from Fig. 2, the reverse current initially varies only slightly with time (for a time τ_1) in the diode under investigation; subsequently, this current decreases rapidly and practically vanishes over time τ_2. The value of τ_2 was almost independent of j and was equal to ~(15–20) μs. The dependence $\tau_1(j)$ is shown in Fig. 4. Comparing the kinetics of the EL decay with that of reverse current in Fig. 3 and also the current dependences of τ_1 and τ_d in Fig. 4, we may conclude that the EL (especially at fairly large values of j) almost ceases to be detected much earlier than is the case with reverse current. This behavior may be caused by the fact that the time during which the voltage across the diode is retained after the forward-bias voltage from an external source is much longer (severalfold) than the lifetime of minority charge carriers [23]. The above persistent voltage is caused by the build-up of the minority charge carriers in the base. The data obtained in this study are not consistent with the idea [11] that the quantity $\tau_1 + \tau_2$ is equivalent to the lifetime of charge carriers.

Figure 4 also shows the dependence of external quantum efficiency (η_{ex}) in the diode under investigation on the current density j. η_{ex} is the ratio between the number of photons emitted by the diode into the surrounding space and the number of charge carriers injected into the base. The quantity η_{ex} was determined from measurements of the current that flowed through the Si diode, the photocurrent of the Ge photodiode, the current–power sensitivity of this photodiode, and the value of the solid angle from which the LED emission was focused onto the entrance window of the Ge photodiode. It was assumed that the emission distribution was spatially isotropic. In addition, it was assumed that all the radiation focused onto the photodiode entrance window, which was fabricated in the form of a minilens built into the diode package, was collected in the active area of the photodiode. For a planar silicon diode, the ratio between the internal quantum efficiency (η_i) and the external quantum efficiency is very large due to the large value of the refractive index n in silicon. The result of calculation [24] for an LED that was similar in design to the LED studied by us (however, without a dielectric film at the surface) yielded $\eta_{ex}/\eta_i \approx 0.013$ at $n = 3.6$. As shown by Emel'yanov *et al.* [20], the value of η_{ex} can be several tens of percent smaller if there is an oxide film (through which the emission leaves the diode) in the diode under consideration than in the case where there is no such film. Thus, it is likely that the value of η_i in the diode under investigation can be larger than η_{ex} by a factor of 100, i.e., can be as large as ~0.6%. The use of diodes with a special configuration makes it theoretically possible to increase the ratio η_{ex}/η_i by more than a factor of 25 in comparison to this ratio for a planar diode [24]. According to our estimations, the average concentration of minority charge carriers injected into the base in the experiments described above varied from $N \approx 5.5 \times 10^{15}$ to ~1×10^{17} cm^{-3} (at $j = 10$ A/cm^2). The value of η_{ex} depends weakly on j even at $N \geq 3.6 \times 10^{16}$ cm^{-3}.

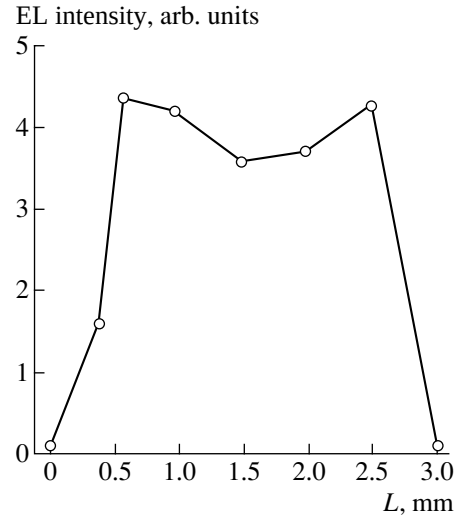

Fig. 5. Results of measuring the electroluminescence (EL) intensity distribution along the direction that is parallel to one of the sides (with a length of 2 mm) of a square p–n junction. The distance L is reckoned from the point $L = 0$, which is located outside the p–n-junction area.

The distribution of the interband-emission intensity over the area of p–n junctions in efficient silicon LEDs is of great interest. This distribution has not been studied so far. In this study, the Si LED was positioned within the field of view of a microscope. We studied the dependence of the intensity of radiation that was incident on the photosensitive area of the photodetector mounted on the eyepiece of the photodetector microscope on the position of the observation on the sample surface. The field of view was limited by a circle with a diameter of 0.4 mm. The results of measurements of the EL-intensity distribution along the direction parallel to one of the sides of the square sample are shown in Fig. 5. The results of measuring the EL intensity for several arbitrarily chosen directions within the p–n-junction area varied by no more than 25% under the experimental conditions described above.

It was shown previously [20] that the value of τ_p for the diode under investigation decreased severalfold as temperature decreased from 300 to 80 K. In Fig. 6, we show the results of studying the EL kinetics at 300 and 80 K and the current that flows through the diode for the amplitude-value current of 0.4 A. As the temperature of

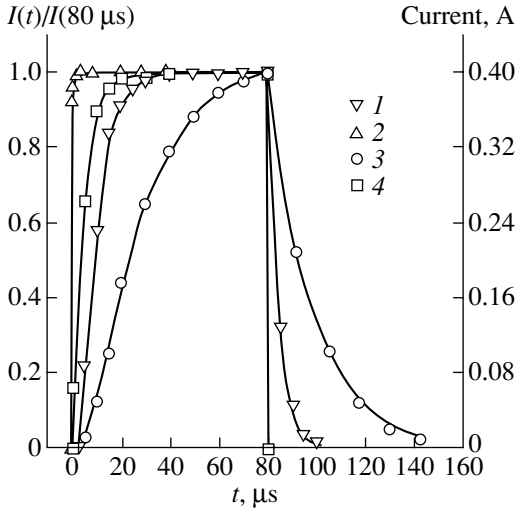

Fig. 6. (*1*, *3*) Kinetics of electroluminescence (EL) and (*2*, *4*) the corresponding current pulses at temperatures T = (*1*, *2*) 80 and (*3*, *4*) 300 K at a current-pulse amplitude of 0.4 A. I denotes the EL intensity.

measurements decreases, a significant decrease in the time of attaining the amplitude value of current, the time lag in the onset of the sharp increase in the EL intensity, and the rise and decay times of the EL intensity is observed.

4. CONCLUSION

In this paper, as originally in [20], we report the results of comprehensive studies of an efficient silicon light-emitting diode that features a high thermal stability of spectral characteristics of band-to-band electroluminescence (EL). We studied the kinetics of the rise and decay of EL, the kinetics of the current flow, and the lifetimes of minority charge carriers for various currents. We observed and explained the time lag between the onset of the sharp increase in EL intensity and the instant the voltage pulse was applied to the diode. The distribution of the interband EL intensity over the *p*–*n*-junction area was evaluated for the first time.

ACKNOWLEDGMENTS

We thank V.I. Vdovin for his help in studying extended structural defects.

This study was supported in part by INTAS (grant no. 2001-0194), the Russian Foundation for Basic Research (project no. 02-02-16374), and the Section of Physical Sciences of the Russian Academy of Sciences (the "Physics of Condensed Media: New Materials and Structures" program).

REFERENCES

1. M. A. Green, J. Zhao, A. Wang, *et al.*, Nature **412**, 805 (2001).
2. Wai Lek Ng, M. A. Lourenco, R. M. Gwilliam, *et al.*, Nature **410**, 192 (2001).
3. J. Michel, J. L. Benton, R. F. Ferrante, *et al.*, J. Appl. Phys. **70**, 2672 (1991).
4. N. A. Sobolev, A. M. Emel'yanov, and Yu. A. Nikolaev, Fiz. Tekh. Poluprovodn. (St. Petersburg) **35**, 1224 (2001) [Semiconductors **35**, 1171 (2001)].
5. N. A. Sobolev, A. M. Emel'yanov, Yu. A. Nikolaev, *et al.*, Mater. Sci. Eng. B **81**, 176 (2001).
6. E. Ö. Sveinbjörnsson and J. Weber, Appl. Phys. Lett. **69**, 2686 (1996).
7. N. A. Sobolev, O. B. Gusev, E. I. Shek, *et al.*, Appl. Phys. Lett. **72**, 3326 (1998).
8. S. Pizzini, M. Guzzi, E. Grilli, and G. Borionetti, J. Phys.: Condens. Matter **12**, 10131 (2000).
9. N. A. Sobolev, O. B. Gusev, E. I. Shek, *et al.*, J. Lumin. **80**, 357 (1999).
10. N. V. Vostokov, Yu. N. Drozdov, Z. F. Krasil'nik, *et al.*, in *Proceedings of Meeting on Nanophotonics* (Nizhni Novgorod, 2002), p. 14.
11. Th. Dittrich, V. Yu. Timoshenko, J. Rappich, and L. Tsybeskov, J. Appl. Phys. **90**, 2310 (2001).
12. W. Michaelis and M. H. Pilkuhn, Phys. Status Solidi **36**, 311 (1969).
13. T.-C. Ong, K. W. Terrill, S. Tam, and C. Hu, IEEE Electron Device Lett. **4**, 460 (1983).
14. A. M. Emel'yanov and A. N. Yakimenko, in *Proceedings of 7th International Meeting on Radiation Physics of Solids* (Sevastopol, 1997), p. 56.
15. V. Yu. Timoshenko, J. Rappich, and Th. Dittrich, Appl. Surf. Sci. **123–124**, 111 (1998).
16. R. D. Altukhov and E. G. Kuzminov, Solid State Commun. **111**, 379 (1999).
17. A. M. Emel'yanov, Yu. A. Nikolaev, and N. A. Sobolev, Fiz. Tekh. Poluprovodn. (St. Petersburg) **36**, 454 (2002) [Semiconductors **36**, 430 (2002)].
18. C. W. Liu, M. H. Lee, Miin-Jang Chen, *et al.*, Appl. Phys. Lett. **76**, 1516 (2000).
19. W. van Roosbroeck and W. Shockley, Phys. Rev. **94**, 1558 (1954).
20. A. M. Emel'yanov, N. A. Sobolev, T. M. Mel'nikova, and S. Pizzini, Fiz. Tekh. Poluprovodn. (St. Petersburg) **37**, 756 (2003) [Semiconductors **37**, 730 (2003)].
21. D. Lax and S. F. Neustadter, J. Appl. Phys. **25**, 1148 (1954).
22. I. M. Vikulin and V. I. Stafeev, *Physics of Semiconductor Devices* (Sovetskoe Radio, Moscow, 1980), Chap. 1, p. 50.
23. Yu. R. Nosov, *Switching in Semiconductor Diodes* (Nauka, Moscow, 1968; Plenum, New York, 1969).
24. A. A. Bergh and P. J. Dean, *Light Emitting Diodes* (Clarendon, Oxford, 1976; Mir, Moscow, 1979), Chap. 6.

Translated by A. Spitsyn